The University Of Sheffield.

Development of Ultrasonic Techniques for Rolling Element Bearing Monitoring

Benjamin Paul Clarke

A thesis submitted in partial fulfilment of the requirements for the degree of

Doctor of Philosophy

The University of Sheffield

Faculty of Engineering

Department of Mechanical Engineering

Submission Date

January 2022

Abstract

Ultrasound techniques cover almost the whole spectrum of performance criteria for rolling element bearings including lubrication and load measurements. Many areas that are not covered are also current areas of research. It is clearly attractive to be able to use the same data acquisition hardware and processing techniques to acquire multiple indicators of bearing performance. Of course, the technology has its advantages and disadvantages. Film thickness measurements are not as accurate as optical techniques, measurements of contact load are made indirectly through detection of raceway deflection and converting to load through knowledge of contact mechanics, and some minor modifications are often required to bearings in order for measurements to be made. There are also issues with distortion of signals with bonded sensors called fringe effects. However, instrumentation can be much less invasive than other measurement methods and it is arguable that film thickness measurement is most practical with ultrasound, in part due to the ease of calibration through naturally occurring reference signals. Additional insights into lubricant behaviour between roller passes can also be obtained from ultrasonic techniques.

The broad aim of this work was to develop ultrasonic rolling bearing techniques. There were several areas of development in this work. These were error in measurements, measurement of bearing load distribution, the use of shear sensors, investigation into distortion of bonded sensor signals (fringe effects) and development of focussing techniques using bonded sensors to eliminate fringe effects.

Quantification of error in ultrasonic measurements was used to identify possible transient events in data from an operational wind turbine, most likely caused by wind gusts. Movement of the loaded zone in this wind turbine was also observed and linked to these transient events. A method for detection and severity monitoring of rolling bearing misalignment was developed using ultrasonic techniques in a lab setting using a full scale

wind turbine bearing test rig. Shear sensors were used to observe areas of a contact that were fully separated and areas that were in mixed lubrication. They were also used to observe possible lubricant solidification in the bearing test rig. k-space modelling of the interaction of an ultrasonic wave with a contact determined that fringe effects were most likely a result of both reflections from either side of the contact interfering with each other when the beam width was larger than the contact, and scattering of the beam at the edges of the contact. Modelling also suggested that fringe effects could be removed from signals through focussing of the ultrasonic beam. Finally, the total focussing method was applied to bearing sized contacts, both through k-space modelling and experimentally, in order to remove fringe effects from signals. Convergence methods were also proposed to ensure sufficient focussing.

Acknowledgements

First and foremost I would like to thank my supervisor, Rob Dwyer-Joyce, both for the opportunity to undertake a PhD in such an interesting field and for your guidance and support throughout the years. I am very grateful for all of the doors you have opened for me and for the experiences I have gained.

Working as part of a cohort in the iT-CDT and within the wider tribology group has been a fun and supportive environment to work in. Thank you to everyone in the group who has supported me both technically and socially, particularly C4. Special thanks to Henry Brunskill and Andy Hunter who are a well of knowledge in triboacoustics and were very helpful in getting me up to speed in the area and supporting my work throughout my PhD. Also to Gary Nicholas for all of his insights into ultrasonic rolling bearing monitoring and working alongside me for a significant portion of my work. Finally, thank you to Artur Gower for useful discussions around ultrasound modelling.

Outside of the University of Sheffield I want to thank Michael Wheeldon and Jon Wheals from Ricardo for their help with SABR modelling, loan of the *MultiLife* rig, useful comments and insights into industry. Thank you to Ed Hart at the University of Strathclyde for his help in understanding wind turbine operation. I also want to thank Cédric Courbon at ENISE for his help with modelling ultrasound and Jie Zhang at the University of Bristol for helping me get to grips with the total focussing method.

This work was funded by the EPSRC and ORE Catapult so a big thank you to these institutions that made this research possible.

Last but not least I want to thank my parents for making me who I am today and enabling me to pursue work which interests and challenges me. And Carol, thank you for your love, patience and support over the last few years.

Contents

List of Figures

List of Tables

Nomenclature

Abbreviations

CAD	Computer aided design
CRB	Cylindrical roller bearing
EDM	Electrical discharge machining
EHL	Elaso-hydrodynamic lubrication
FFT	Fast Fourier transform
FMC	Full matrix capture
FMS	Film measurement system
GP	Gaussian process
HSS	High-speed shaft
NDT	Non-destructive testing
PE	Pulse echo
PI	Prediction interval
PRF	Pulse repetition frequency
PZT	Lead zirconate titanate
R	Reflection coefficient
RCF	Rolling contact fatigue
REB	Rolling element bearing
RMS	Root mean square
SoS	Speed of sound
SNR	Signal to noise ratio
TFM	Total focussing method
ToF	Time of flight
ΔToF	Change in time of flight
TRB	tapered roller bearing
UPR	Ultrasonic pulser receiver
US	Ultrasound
VG	Viscosity grade
WEC	White etching cracks
WSF	White structure flaking

Symbols

a	Major contact width	m
A	Area	m^2
b	Minor contact width	m
B	Bulk modulus	Pa
c	Speed of sound	m/s
c_A	Speed of sound in component A	m/s
c_p	Speed of sound at pressure p	m/s
c_0	Speed of sound at atmospheric pressure	m/s
$Cte1$	Curve fitting parameter dependent on k	1
$Cte2$	Curve fitting parameter dependent on k	1
d	Near field constant	1
dQ	Load difference line-point contact at transition	N
D	Transducer diameter / width	m
D_m	Pitch diameter	m
D_R	Roller diameter	m
E_A	Modulus of elasticity of body A	Pa
E'	Reduced modulus of elasticity	Pa
f	Frequency	Hz
f_{rpo}	Outer raceway roller pass frequency	Hz
f_{rpi}	Inner raceway roller pass frequency	Hz
F_a	Axial load	N
F_r	Radial load	N
h	Lubricant film thickness	m
h_c	Central lubricant film thickness	m
h_{min}	Minimum lubricant film thickness	m
i	Imaginary unit	1
J_a	Axial load integral	1
J_r	Radial load integral	1
k	Radius ratio	1
$\bar{k}$	Ellipticity parameter	1
$K_{LC_{inner}}$	Line contact load constant for the inner raceway	1
$K_{PC_{outer}}$	Point contact load constant for the outer raceway	1
K_d	Load distribution factor	1
l	Roller length	m
L	Acoustoelastic constant	1
p	Pressure	Pa
p_{avg}	Average contact pressure	Pa
p_{max}	Maximum contact pressure	Pa
n	Contact type factor	1

Q	Roller load	N
Q_{LC}	Roller load for a line contact	N
Q_{PC}	Roller load for a point contact	N
Q_{outer}	Roller load at the outer raceway	N
Q_{inner}	Roller load at the inner raceway	N
Q_{ψ}	Roller load at bearing angle ψ	N
r_q	RMS roughness	m
r_{qA}	RMS roughness of body A	m
R_{Ax}	Radius of body A in the x direction	m
R_{By}	Radius of body B in the y direction	m
R_{CW}	Value of reflection coefficient for contact width monitoring	1
R_{min}	Minimum reflection coefficient	1
R_x	Reduced radius in the x direction	m
R_y	Reduced radius in the y direction	m
R'	Reduced radius	m
$\mathbf{R}$	Reflection coefficient	1
u	Speed	m/s
u_r	Roller speed	m/s
u_{rw}	Raceway speed	m/s
U	Lubricant entrainment speed	m/s
w	Transducer width	m
z	Acoustic impedance	Pa s/m
z_A	Acoustic impedance of body A	Pa s/m
Z	Number of rolling elements	1

α	Lubricant pressure-viscosity coefficient	1
δ	Deflection	m
δ_{trans}	Transition deflection between point and line contacts	m
ϵ	Bearing preload / clearance factor	1
ε	Strain	1
η	Dynamic viscosity	Pa s
κ	Stiffness	N/m
φ_0	Transducer divergence angle	rad
ω	Angular frequency	rad/s
ω_i	Inner raceway speed	rpm
ω_m	Cage speed	rpm
ω_o	Outer raceway speed	rpm
λ	Wavelength	m
Λ	lambda ratio	1
ρ	Density	kg/m^3
υ	Kinematic viscosity	$m^2\ s^{-1}$
υ_A	Poisson's ratio of body A	1
$\bar{\varepsilon}$	Elliptical integral	1
$\bar{\xi}$	Simplified elliptical integral	1
γ	Contact angle	radians

Chapter 1

Introduction

This chapter introduces Rolling Element Bearings (REBs) and gives the example of wind turbines for an application in which monitoring of bearing performance is attractive. Wind turbines and the bearings they contain are briefly described as well as the different monitoring requirements in various bearing use cases. An overview of bearing performance parameters is then introduced and current techniques are appraised to cover the monitoring of these parameters, including ultrasound which is shown to be the most attractive option. This leads into the aim of this work: to develop existing ultrasonic techniques to improve bearing performance monitoring, which is split into more specific objectives.

1.1 Rolling Element Bearings

Rolling bearings are amongst the most common machine elements in the world. Their use ranges from simple applications such as skateboard wheels to much more complex machines like aircraft gas turbines. Bearings permit relative motion between two components while still allowing load to be transmitted. They also minimise frictional losses caused by relative motion and allow the motion to be constrained in a desired way. Unsurprisingly, rolling element bearings use rolling elements to do so. Examples of rolling element bearings can be seen in Figure 1.1. Other common types of bearing include journal bearings and thrust pad bearings.

1.2 Requirement for Monitoring

Rolling bearing selection and design processes are generally well established and life-time prediction is successful in the majority of use cases. If a REB is sufficiently lubri-

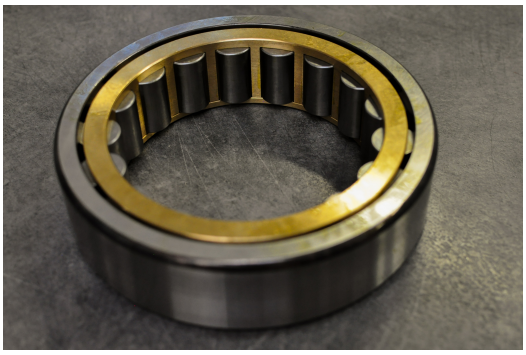

(a) Cylindrical roller bearing [1].

(b) Tapered roller bearing [2].

Figure 1.1: Examples of rolling element bearings.

cated, not overloaded, kept free of containments, adequately supported and properly installed then most causes of damage and failure are eliminated [3]. The only remaining cause of failure is material fatigue. Predictions for REB failure are therefore based around this mechanism which is known as Rolling Contact Fatigue (RCF). Key standards surrounding lifetime prediction are ISO 76, 281 and TS-16281 [4, 5, 6]. Rolling bearings are often designed to outlast the usable life of the machine they inhabit but can be designed for easy replacement should this not be the case. That being said, the deterioration of bearing performance can have significant effects on overall machine operation and unexpected failure of bearings can cause catastrophic damage to other machine components. There are also limitations to the calculations outlined in the standards listed above which can significantly effect lifetime predictions if they are not accounted for.

The requirement to monitor rolling bearings depends on several factors, including:

- Overall machine cost
- Consequences of reduced efficiency to the machine performance and viability
- Consequences of machine failure and downtime
- Ease and cost of bearing replacement
- Frequency, requirement for and cost of current inspection and maintenance schedule
- Likelihood of failure
- Likelihood of detection of onset of failure through other means

A good example of candidates for condition monitoring are the bearings in wind turbines. An example wind turbine can be seen in Figure 1.2.

Figure 1.2: An example wind turbine [7].

Industrial wind turbines are expensive machines - a 1 GW scale wind turbine can cost more than £1 million to produce and install and so a condition monitoring system would be inexpensive in comparison [8]. A reduction in efficiency of the machine would result in a low energy production rate for the turbine leading to slower return-on-investment for the turbine owner. The consequences of bearing failure are twofold: During the downtime of the turbine the owner has lost their income or lost their reduction in overhead costs as the turbine is no longer producing energy. Downtimes can be significant in length due to the requirement to wait for the correct weather conditions to conduct the repairs. The cost of repairing the turbine must also be taken into account. The cost of the replacement bearing will be fairly insignificant in relation to the overall turbine cost, however the complexity of disassembling and reassembling the turbine to access the bearings, together with the specialist equipment required means that the process is overall quite costly [9], particularly if the turbine is offshore. Catastrophic bearing failure may also damage other components within the turbine leading to further downtime and repair costs. An example of failed wind turbine bearings is shown in Figure 1.3

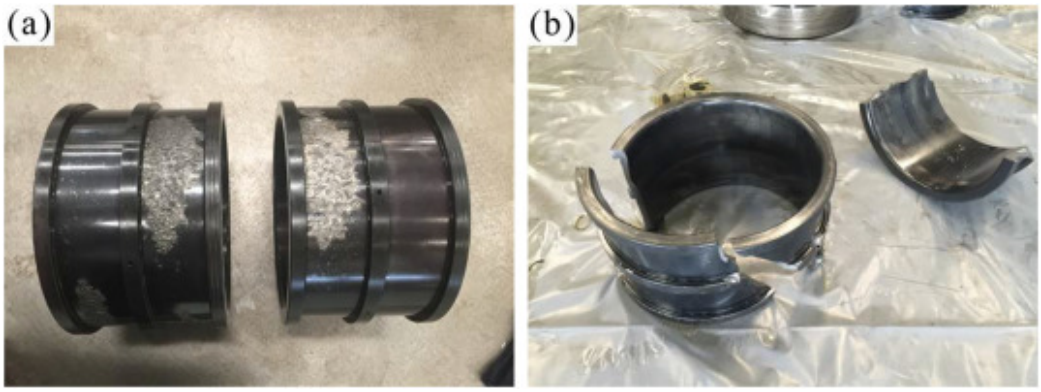

Figure 1.3: Example failed bearings from a wind turbine gearbox wind turbine. (a) Severely worn and (b) fractured raceways. Reproduced with permission from the publisher [10].

Wind turbines normally undergo regular inspection and maintenance, thus the onset of bearing failure is likely to be detected, although this depends heavily on the inspection techniques used. Due to the challenging environment and ever-increasing size of wind turbines, bearing failures are not uncommon [11] and bearing designs have required revision to suit this challenging application. Wind turbine bearings are already monitored in turbines [12] and methods are normally focused on early-warning signs of failure, which are indicated by lubrication or load monitoring. There are various ways in which this can be done which will be discussed in more detail in Section 1.4.

1.3 Rolling Element Bearings in Wind Turbines

Wind turbines harness energy in the wind to generate electrical energy. In 2020 wind turbines made up an average of 24% of the UK's energy demands [13], up from 18.8% in 2019 and 1.3% in 2009 [14]. Wind is the largest source of renewable electricity generation in the UK [15] and will continue to lead the growth of the renewable energy industry in the UK driven by both Government policy, such as the EU Renewables Directive [16] and the Climate Change Act 2008 [17], along with the decreasing price of wind-generated electricity [18]. Adoption of wind energy has been seen globally; China is the current the leading country for capacity of newly installed wind turbines in 2020, followed by the USA, Brazil, Netherlands and Germany [19].

There is a long-term trend of increasing wind turbine capacity, rotor diameter and hub height [20] meaning that wind turbine components are exposed to increasingly higher

loads and harsher environments. As a result, new materials, component designs and configurations, including bearing technologies, have been and continue to be developed to combat these challenges.

1.3.1 Wind Turbine Components

The following section, based on Manwell, McGowan and Rogers [21], splits up a wind turbine into its major components and explains their functions with a focus on those containing bearings. Figure 1.4 shows a typical configuration and the relative locations of these components within the turbine. One major difference in design that is commonly seen is that some designs do not include a gearbox and instead directly connect the generator with the hub. This omits some of the reliability issues that can be associated with the gearbox but makes generator design larger and more complex. Turbines without a gearbox are termed 'direct drive' turbines.

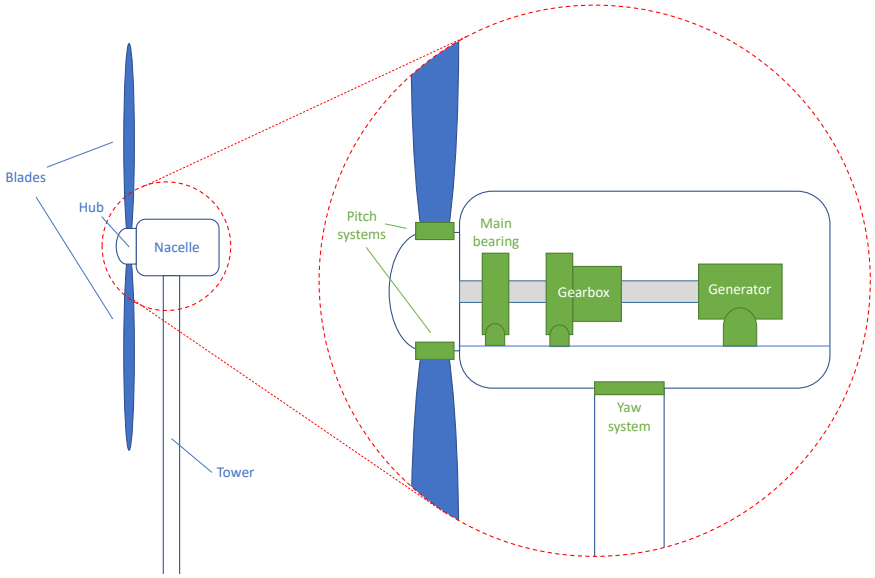

Figure 1.4: Wind turbine component overview, highlighting systems in which rolling element bearings are used.

1.3.1.1 Rotor

The rotor consists of the blades, pitch system and hub. The blades convert the motion of the wind into rotation of the main shaft in a similar manner to how aircraft convert thrust into lift. They do this by creating a pressure difference across an aerofoil through variations in air flow speeds across the upper and lower surfaces. Blades can be rotated to an optimal position for extracting energy from the wind or

away from this optimum position to, for example, maintain the power output of the turbine once the rated power of the generator has been reached. The rotation of the blades is controlled by the pitch systems which rotate the blades on pitch bearings through mechanical actuators. Some older turbines do not have pitch systems which reduces complexity of the wind turbine at the expense of the efficiency of the turbine. The hub connects the blades to the main shaft through the pitch systems. Figure 1.5 shows a turbine hub before the blades were attached through the pitch bearings. A pitch bearing can be seen as the inner ring around the visible opening.

Figure 1.5: A wind turbine hub prior to the attachment of the blades. A pitch bearing can be seen as the inner ring around the visible opening [22].

1.3.1.2 Nacelle

The nacelle contains the majority of remaining components: the main bearings, gearbox (if used) and generator, all connected through shafts. There are also various auxiliary systems such as control, lubrication and braking. The nacelle itself protects these components from the external environment and allows reaction loads and moments from components to be supported.

There are many different configurations and bearing types used in main bearings but their primary function is to support the rotor and react non-torque loads, preventing their transmission further down the drivetrain [23].

The gearbox functions to convert the low speed rotation of the rotor into high speed rotation more appropriate for traditional generator designs. As previously stated, the gearbox is not present in direct drive turbines. Gearboxes usually have multiple stages

including planetary and parallel. Gearboxes therefore have the highest concentration of bearings in a wind turbine and have a variety of bearing types to support the rotating components in each of the stages. Figure 1.6 shows a gearbox, rotor shaft and brake assembly being installed in a wind turbine nacelle.

Figure 1.6: A gearbox, rotor shaft and brake assembly being installed in a wind turbine nacelle [24].

The generator functions to convert the rotating energy of its input shaft into electrical energy to be transferred to the energy grid. Generator bearings are electrically isolated through non-conductive components such as ceramic rollers. Early turbine design connected the generator directly to the grid meaning the generator was required to rotate at a fixed speed to maintain the power line frequency. As a result the rotor had to spin at a fixed speed and consequently some efficiency was lost at lower wind speeds. Modern turbines have asynchronous generators connected to the grid through power electronics, which enable the speed of the generator to be adjusted to maintain optimum rotor speed, increasing overall turbine efficiency.

1.3.1.3 Tower

The tower structurally supports the turbine and enables transmission of unwanted reaction forces to the ground through a chosen fixation mechanism, most commonly foundations. The tower is connected to the nacelle through a yaw system which allows the direction of the rotor to be changed through rotation of the nacelle on yaw

bearings. This enables maximisation of the energy produced by the turbine as the direction of wind in a particular location can substantially change over time.

1.3.2 Bearing Monitoring for Wind Turbines

Wind turbine bearings can be monitored for several reasons, which are outlined in the sections below. Each reason has it's own considerations, for example how much detail is required, the cost of the monitoring system and the accessibility of the environment.

1.3.2.1 Design Verification

The first use case is to verify a design process. This could be to check existing processes function as intended with new applications or to verify that new design tools or processes such as models give appropriate results. Verification of a certain attribute of bearing performance may be required which in itself may narrow down available techniques. In this case bearings are normally tested on a test rig which simulates the real operational environment of a component or subset of components but they could also be tested on full scale prototype turbines. A laboratory environment lends itself to more complex and costly testing techniques where the environment is more closely controlled and higher levels of detail are required.

1.3.2.2 Installation

Whether a bearing is correctly installed or not can have a big impact on if the bearing will last its intended lifetime or fail early. The ability to check bearing performance after installation, where equipment is available to correct any errors, is therefore very attractive, particularly in the case of offshore wind turbines where equipment hire can be very expensive.

1.3.2.3 Condition Monitoring

Condition monitoring is used to allow early warning of failure for efficient scheduling of maintenance and replacement. Permanent monitoring of turbines requires a balance between the cost of using a monitoring system and the cost of additional maintenance and replacements required where it not used. More detailed inspection at regular intervals where bearing maintenance is already scheduled may also be attractive if permanent monitoring is too expensive.

1.3.2.4 Fault Diagnosis

In the case where bearings in operational wind turbines have seen early failures it is necessary to understand why these occur to prevent reoccurrence in replacement bearings or future turbine designs. Inspection of failed bearings may be sufficient to determine cause and necessary preventative action but where it is not monitoring of bearings in operational turbines or representative test rigs may be deemed necessary.

1.4 Bearing Monitoring Techniques

1.4.1 Measurement Parameters

The factors that affect rolling element bearing performance and failure are described in more detail in Chapter 2 but are summarised below. Bearing performance and failure factors can be categorised into loading and lubrication and are summarised in Figure 1.7.

1.4.2 Measurement Techniques

A range of measurement techniques have been developed in order to measure load and lubrication during bearing operation. An overview of these measurement techniques and their capabilities is shown in Table 1.1. These techniques are briefly described along with their advantages and disadvantages in the following sections.

Key	
x	possible
∼	partial / indirect
¿	area of research

Measurement technique	Used on full bearing assembly	Used in wind turbine	Load				Lubrication			
			Circumferential distribution	Roller distribution	Damage detection	Wear measurement	Film thickness	Lubricant distribution	Contamination	Degradation
Capacitance	Y [25, 26]	N	x [26]	∼ [26]			x [25]			
Optical	N	N					x [27]	x [28]		
Oil analysis	Y [29]	Y [29]			∼ [30]	∼ [30]			x [30]	x [29]
Electrostatic	Y [31]	N			x [31]	∼ [31]				
Vibration	Y [32, 33]	Y [34]			x [33]					
Acoustic emission	Y [35]	Y [36]			x [36]					
Temperature	Y [25]	Y [12]			x [12]					
Load cells	Y [37]	N		∼ [27]						
Strain gauges	Y [38]	N	x [38]							
Ultrasound	Y [39]	Y [40]	∼ [39]	¿ [41]	x [39]	¿ [42]	x [43]	x [44]	∼ [30]	¿ [30, 45]

Table 1.1: A comparison of the capabilities of various bearing measurement techniques.

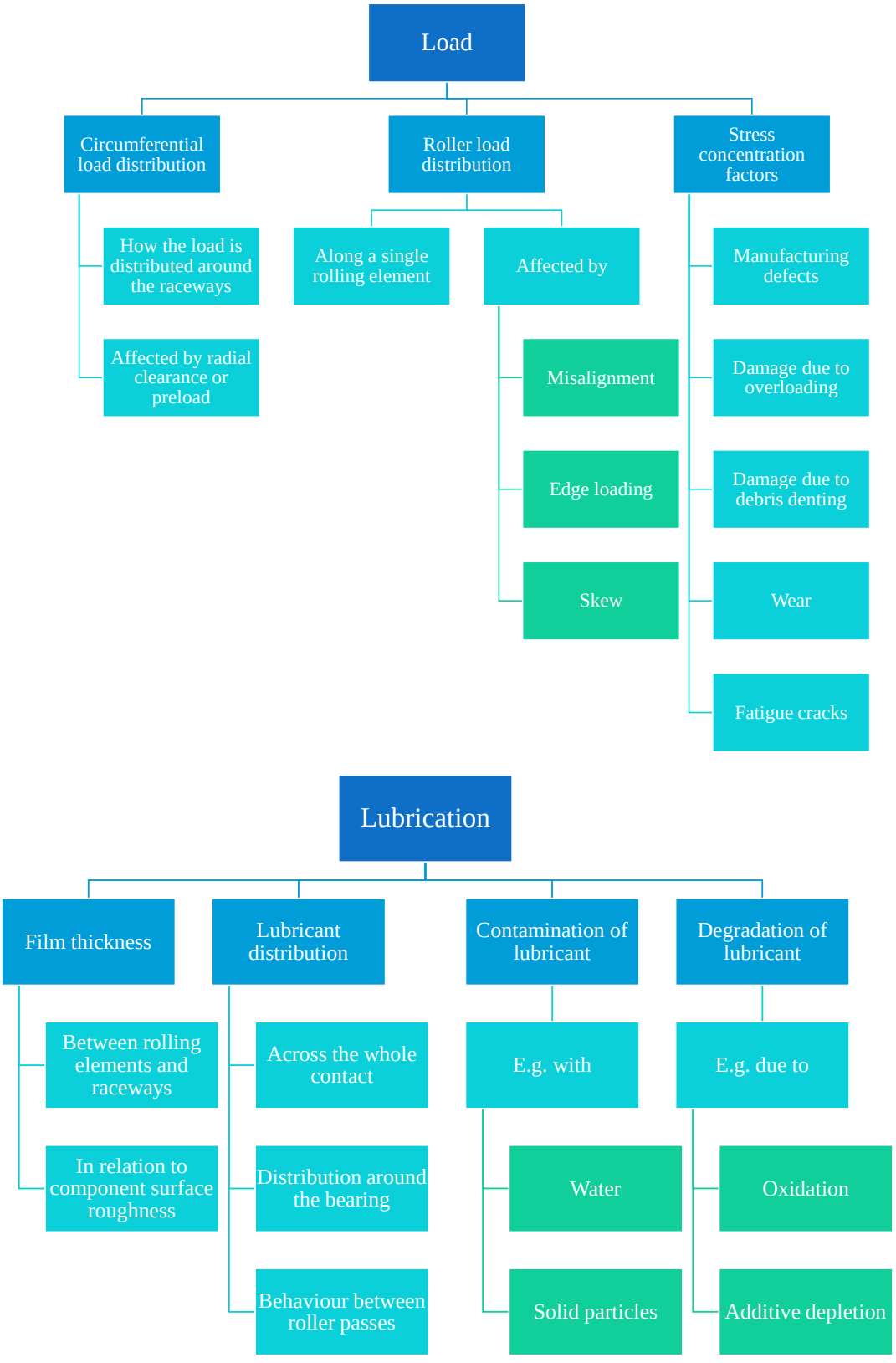

Figure 1.7: Rolling bearing performance hierarchy.

1.4.2.1 Capacitance

The lubricant film thickness between two components can be measured through capacitance measurements across bearing components [25] together with knowledge of the load distribution in the bearing, Hertzian contact areas and the dielectric properties of the lubricant. Metal-to-metal contact is also indicated by a drop to near-zero capacitance values. Capacitance measurements require electrical isolation of the bearing and capacitance is most often measured between the inner and outer raceways. These measurements can be used on functional steel bearings although there are drawbacks. These include the requirement for knowledge of load distribution and the nature of capacitance measures as an average of the inner race-roller and the outer race-roller contacts. Measurements can also be quite sensitive to lubricant purity and contact size and shape must be presumed [46]. Measurement of the lubricant distribution within the bearing or contacts is only possible by depositing a thin film on the surface of a raceway [46].

Cen and Lugt [25] used capacitance sensors to monitor the film thickness of an axially loaded ball bearing from start up with fresh grease. Figure 1.8 shows an example of data recorded. In their research the film thickness measurement was determined by dividing the overall capacitance divided by the number of balls to obtain an average film thickness measurement. In this case the churning phase was seen within the first hour, after which the grease entered the bleeding phase.

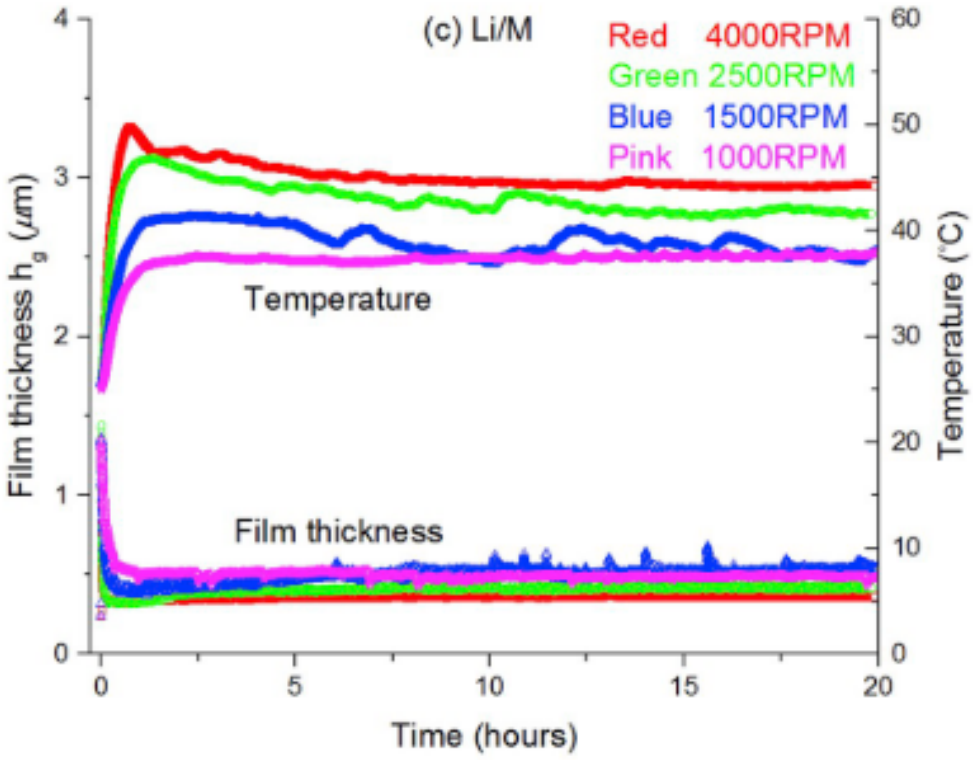

Figure 1.8: Li/M grease film thickness (hg) and temperature measurement results under load of 513 N and at a range of different speeds (c) [25].

Capacitance sensors have also been used to measure load [26]. This is the only instance of this type of measurement in the literature and example data is not given by the authors. A capacitor was fixed to a chosen bearing housing with a constant gap between the capacitor and the raceway. The sensor monitored changes in the gap between the sensor and the raceway. This measured deflection was then converted into load through calibration experiments or modelling [47]. Placement of these sensors at multiple locations could allow load distribution to be determined although the sensors may be too large to make roller load distribution measurements. There is a clear disadvantage to this method: the additional step of experimentally calibrating the installed sensors or the requirement for a model to convert measured values to load.

1.4.2.2 Optical

Optical film thickness measurements are made using the principle of interferometry. Light is directed at the contact and an interference pattern is formed by the interaction of the light which has travelled through the lubricant film and light that has not.

The observed fringe pattern can then be compared to results of calibration experiments to deduce film thicknesses. This technique enables accurate and high-resolution lubricant distributions to be observed but in order to do so one of the components of the bearing must be transparent, which is far from ideal; transparent components such as glass do not behave in the same way as steel bearing components and are not capable of withstanding the same loads. A calibration experiment is also required to determine the relationship between fringes and film thickness, although reference to literature may be sufficient. Most work using this technique has been on single contacts as opposed to full bearing analysis. Further details and sources can be found in [27] pg. 332.

An example of film thickness measurement on a ball bearing is shown in Figure 1.9:

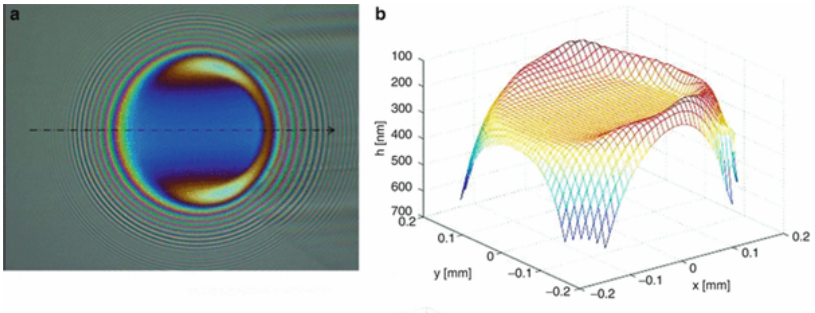

Figure 1.9: Optical film thickness measurements showing (a) the optical measurement with fringes and (b) data converted to film thickness through reference to calibration data [28].

1.4.2.3 Oil Analysis

Oil analysis encompasses a wide range of techniques which are used to analyse samples of oil to determine their properties and content. Offline analysis (i.e. a sample taken then analysed in a lab) can give detailed and comprehensive evaluations of oil condition but it takes a significant amount of time from sample to results and it is often impractical to obtain very regular samples [30]. Lab analysis techniques include spectrography and ferrography, amongst others [48]. Online methods have been developed to improve upon the drawbacks mentioned above, involving wear debris sensors, viscosity sensors and water content sensors, amongst others. These sensors use a mix of technologies including capacitive, inductive, optical, and acoustic technologies. A detailed overview has been written by Zhu et al. [30]. A significant disadvantage here is that the majority of methods analyse lubricant away from the

contacts of the bearing. Lubricant behaviour in the bearing can be inferred from results but not directly monitored.

1.4.2.4 Electrostatic

The electrostatic technique is based on the principle that electrostatic charge generation accompanies wear in bearings [31]. Sensors can be placed in bearing housing close to roller-raceway contacts so they may detect damage to the bearing caused by wear. These measurements are rather indirect and only give an indication of wear.

1.4.2.5 Vibration & Acoustic Emission

Vibration and acoustic emission monitoring are probably the most common techniques employed for condition monitoring of rolling bearings. Sensors are typically mounted to the outer casings of bearings or to components being monitored and the sensors are most commonly piezoelectric transducers or accelerometers. Signals obtained are in the form of amplitude measurement or impulses which are then further analysed to determine information about the state of a bearing. Vibration generally refers to lower frequency vibrations whereas acoustic emission refers to higher frequency impulses.

Data analysis methods operate in both the time and frequency domain and are continually being improved upon [32, 33, 35]. Examples of typical data can be seen in Figures 1.10 and 1.11. The detection, categorisation, and localisation of these defects are all possible although information surrounding the causes of these defects is much more difficult to infer from data. These techniques are most often used to inform maintenance requirements rather than other components of a bearing's performance.

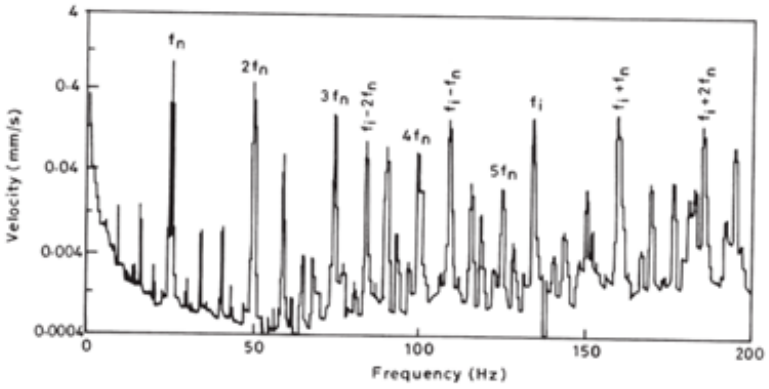

Figure 1.10: A typical vibration spectrum for a rolling bearing with an inner race defect [35].

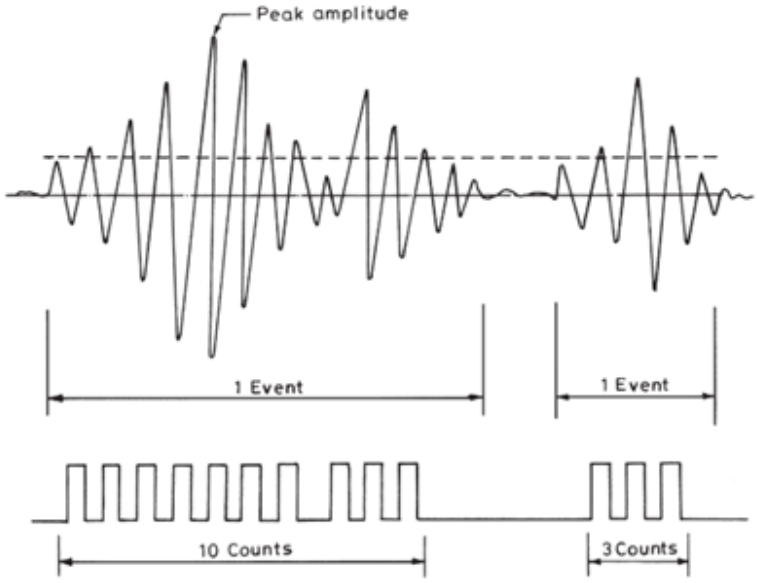

Figure 1.11: A typical acoustic emission signal [35].

1.4.2.6 Temperature

Temperature monitoring employs thermocouples or similar technology to monitor the temperature of a bearing. The closer to the bearing components the temperature sensor is situated, the more effective the technique is at detecting faults. The premise is that increases in operational temperature are associated with faults such as insufficient lubrication, misalignment, and excessive wear. This technique rarely gives any insight beyond establishing that there is a problem with the bearing, and can be slower to detect these problems than other methods [12]. These methods were employed in [25].

1.4.2.7 Strain Gauges

Strain gauges can be used to monitor the load through parts of a bearing and the distribution of load when several locations are monitored. Modifications to bearing structures are sometimes required for installation of strain gauges in the appropriate orientations. Figure 1.12 shows an example of modifications required to a tapered roller bearing raceway. In order to calibrate the sensors, strain measurements are taken at a range of known loads. A custom jig and compression rig are required to load the bearing. Further details can be found in [49]. Drawbacks of this method include the number of modifications required to the bearing and the complex calibration process.

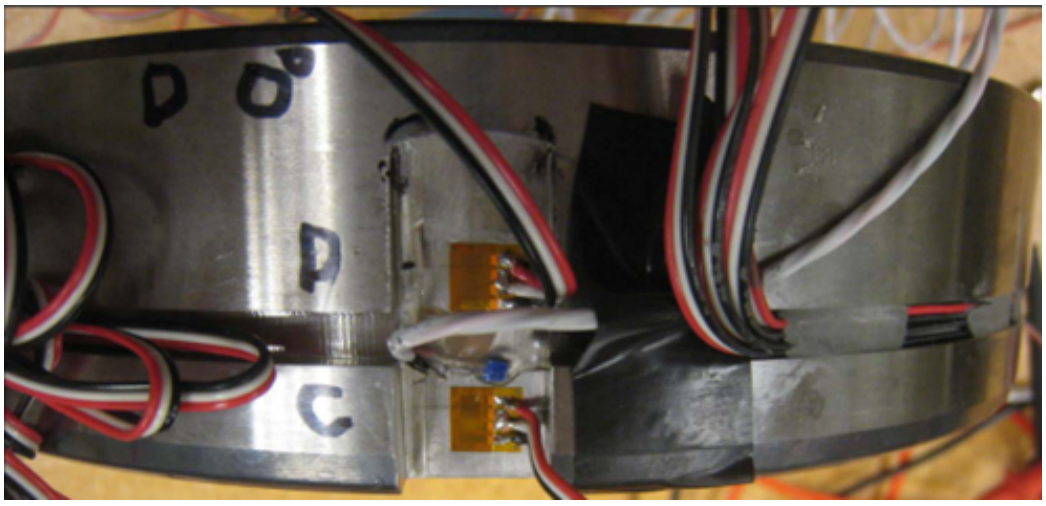

Figure 1.12: Strain gauges installed on a modified tapered roller bearing raceway [49].

Load measurement on a pair of wind turbine gearbox high speed shaft bearings have been undertaken using these methods on a test rig [50]. The instrumented tapered roller bearings (TRB) are shown in Figure 1.13 and some example results where points around the circumference off the bearing were measured during normal bearing operation and compared with simulation results are shown in Figure 1.14. Load variation due to simulated braking and grid loss events were also measured.

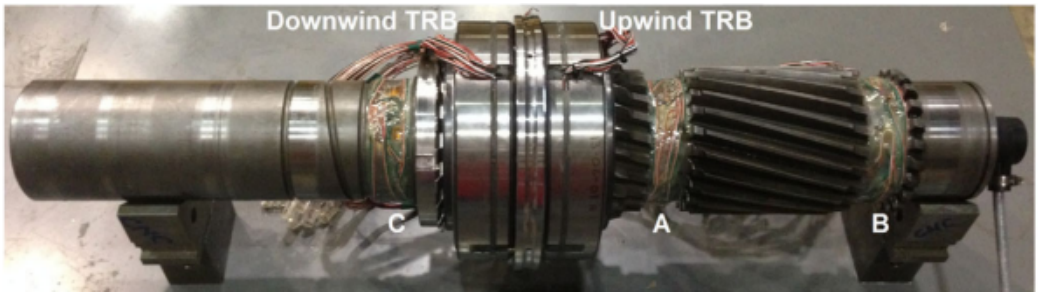

Figure 1.13: Instrumented bearings and high speed shaft [50].

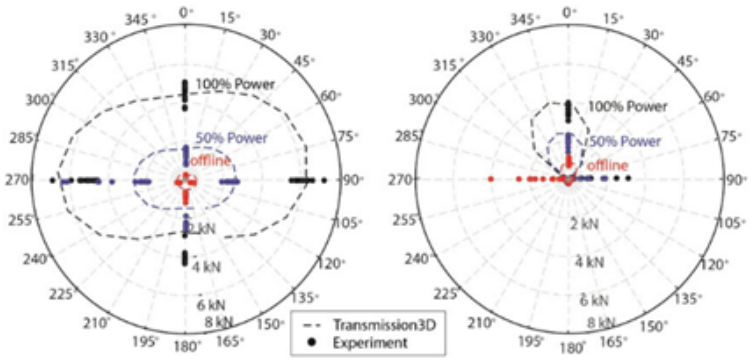

Figure 1.14: Experimentally measured and computationally modelled load zones for the downwind (left) and upwind (right) tapered roller bearings under pure-torque operation [50].

1.4.2.8 Load Cells

Incorporation of load cells into bearings has been demonstrated by Chen & Chen [37]. This allowed the authors to monitor the effect of preload on bearing performance. Although this technology can very accurately measure load, incorporating load cells into bearings is difficult and, in this case, only gave the overall load as opposed to the load distribution of the bearing. Incorporating load cells into bearing supports at various locations could allow low resolution load distribution measurements but would require custom bearing modifications. Load cell use for measurement of load distribution across rollers may be possible through similar designs to the "stress pins" described in [3], pg. 368 which appear to be only a concept at present. These are shown in Figure 1.15.

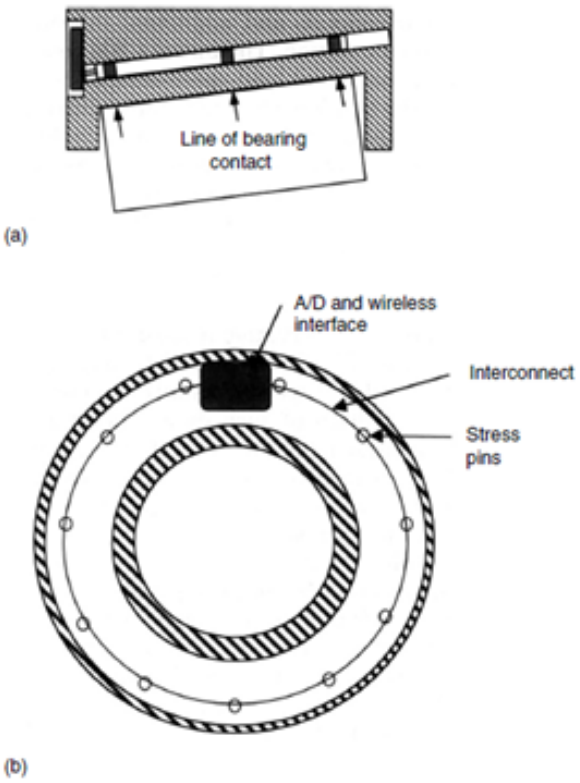

Figure 1.15: "Stress pins" distributed (a) axially and (b) circumferentially to determine load distribution [3].

1.4.2.9 Ultrasound

As can be seen from Table 1.1, ultrasound techniques cover almost the whole spectrum of measurement criteria, and the areas that are not covered (lubricant contamination and degradation) are current areas of research. It is clearly attractive to be able to use the same data acquisition hardware and processing techniques to acquire multiple indicators of bearing performance. Of course, the technology has its advantages and disadvantages. Film thickness measurements are not as accurate as optical techniques, measurements of contact load are made indirectly through detection of raceway deflection and converting to load through knowledge of contact mechanics, and some minor modifications are often required to bearings in order for measurements to be made. However, instrumentation can be much less invasive than other measurement methods and it is arguable that film thickness measurement is most practical with ultrasound, in part due to the ease of calibration through naturally occurring reference signals. Additional insights into lubricant behaviour between roller passes can also be obtained from ultrasonic techniques. Section 3.7 provides more detail around

these techniques.

1.5 Review

This section has made the case for why one might want to monitor the performance of a rolling element bearing with the example of wind turbine bearings being given as a good candidate. It outlined where bearings are found in wind turbines and their functions, then explored features of a bearing that require measurement to assess bearing performance and current technologies were assessed for their appropriateness. Resultantly the use of ultrasonic techniques appeared very attractive for this application.

1.6 Aims and Objectives

This research aims to develop ultrasonic rolling bearing techniques in the following ways.

- Understand the current error in ultrasonic measurement techniques on a rolling bearing.
- Assess the error of roller load measurements on an operational wind turbine bearing through comparison to a simple model, with knowledge of measurement error.
- Create a detection mechanism for misalignment of rolling bearings through ultrasonic measurements.
- Develop a method to detect a transition from mixed to fully separated lubricant regimes in a rolling bearing through use of shear sensors.
- Understand how finite sensor size and resulting fringe effects affect ultrasonic measurements.
- Develop bonded sensor technologies to enable more robust measurement.

1.7 Thesis Layout

The remainder of this thesis has the following layout:

Chapter 2 introduces rolling element bearing theory required to be able to interpret how an ultrasonic wave interacts with rolling bearing interfaces.

Chapter 3 explains the theory surrounding ultrasound and it's use for measuring interfaces, key details surround the equipment required to do so and the current state of these techniques for monitoring rolling element bearings.

Chapter 4 investigates the variability in ultrasonic measurements, as well as investigation of fringe effects (introduced in Chapter 3) and demonstration of measurement of misalignment using ultrasonic techniques.

Chapter 5 presents ultrasonic load measurements from an operational wind turbine and compares them to expected modelled loads using a simple model of the turbine drivetrain. It shows how these measurement can be used to identify transient events in data and indicate changes in the load distribution of the bearing.

Chapter 6 expanded ultrasonic techniques for the measurement or rolling contacts through the use of shear sensors. It shows how shear sensor may be able to dedifferentiate between mixed lubrication and fully separated contacts. It also highlights the problems caused by fringe effects and gives insight into their cause using data processing methods.

Chapter 7 uses finite element and k-space modelling techniques to investigate the cause of fringe effects in ultrasonic techniques. It also shows how focussing of the ultrasonic beam can be used to remove these effects from reflection coefficient signals but not change in time of flight signals.

Chapter 8 shows how the use of full matrix capture and the total focussing method can be used to focus ultrasound in post processing through k-space modelling. A method to determine whether sufficient focussing is achieved is proposed.

Chapter 9 demonstrates experimental inspection of a small contact using these methods and recommendations for progressing these techniques into use in actual bearings is suggested.

Finally, conclusions of the research and recommendations for future research are given in Chapter 10.

Chapter 2

Rolling Element Bearing Theory

This chapter describes the basics of rolling bearing analysis that will be used in Chapters 4 and 5 to convert deflection measurements to load, Chapter 5 to estimate bearing load distribution, Chapters 4, 6 and 7 to predict bearing contact widths, Chapter 6 to predict lubricant film thickness and in Chapters 5 and 6 to approximate speeds of different bearing components from cage speed measurements.

2.1 Types of Rolling Element Bearing

Rolling element bearings consist of an inner raceway and an outer raceway separated by a set of rolling elements. The spacing of the rolling elements is normally maintained by use of a cage. There are many different types of rolling element bearings, usually separated into categories based on the shape of the rolling elements. Simplified diagrams of the different types of bearings can be seen in Figure 2.1. It should be noted that the cages are missing from these diagrams.

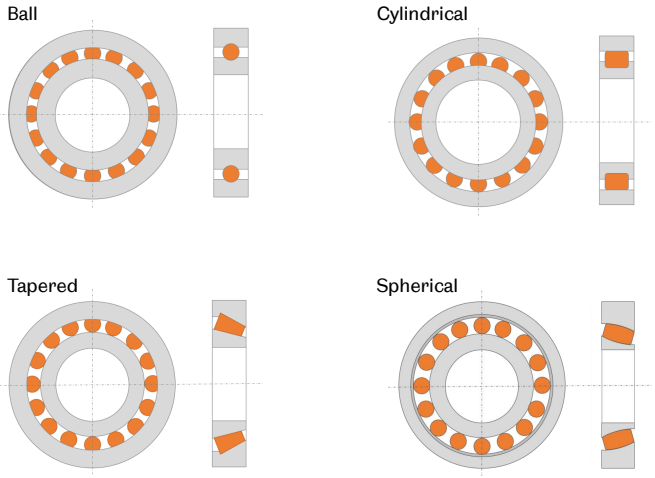

Figure 2.1: Different types of roller bearings. Axial views (left) and section radial views (right) are shown for each bearing. Cages are not shown.

Each roller type has its own strengths and weaknesses. They are selected for specific applications based on the load type, load severity and operational speed. The types of bearing outlined above can be further split into sub-types and wind turbine bearings often have specific adaptions to suit the application (not explored here).

2.2 Bearing Speed and Geometry

Standard bearing geometries can be seen in Figures 2.2 and 2.3. The nomenclature and symbols are used in subsequent sections.

In most use cases a rolling bearing has one static raceway and one rotating raceway. When one of these raceways rotates, the rollers in the bearing orbit at a speed of ω_m rpm (the cage speed) and roll on their own axes (at a speed of ω_R rpm). With knowledge of bearing geometry and the assumption that there is no slip in the bearing the cage speed can be calculated from inner or outer raceway speed:

$$\omega_m = \frac{1}{2}\left[\omega_i\left(1 - \frac{D_R}{D_m}\cos(\gamma)\right) + \omega_o\left(1 + \frac{D_R}{D_m}\cos(\gamma)\right)\right] \tag{2.1}$$

where ω_i is the inner raceway speed, ω_o is the outer raceway speed and D_m is the pitch diameter, as defined in Figure 2.2. D_R and γ are defined in Figure 2.3.

Similarly, roller speed can also be calculated:

$$\omega_R = \frac{D_m}{2D_R}\left(1 - \frac{D_R}{D_m}\cos(\gamma)\right)\left(1 + \frac{D_R}{D_m}\cos(\gamma)\right)(\omega_o - \omega_i) \tag{2.2}$$

The raceway speed can also be calculated from the roller pass frequency at the outer (f_{rpo}) or inner (f_{rpi}) raceway:

$$\omega_o = \frac{120 f_{rpo}}{Z[1 - \frac{D_R}{D_m}\cos(\gamma)]} \tag{2.3}$$

$$\omega_i = \frac{120 f_{rpi}}{Z[1 + \frac{D_R}{D_m}\cos(\gamma)]} \tag{2.4}$$

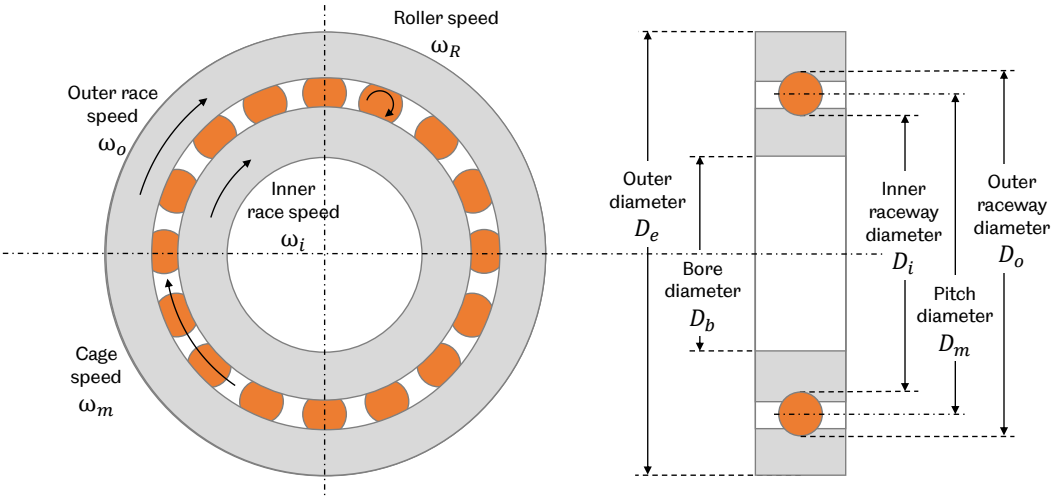

Figure 2.2: Bearing speeds and geometries for a ball bearing. An example of a ball bearing is used but the speeds and geometries can be transferred to other bearing types.

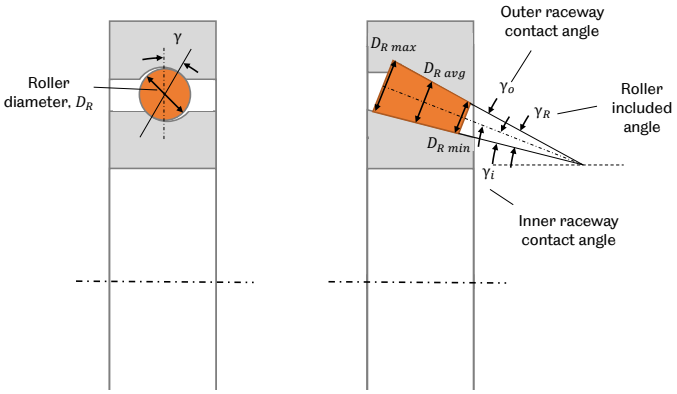

Figure 2.3: Bearing contact angles for (a) ball bearings and (b) tapered roller bearings.

2.3 Contacts in Bearings

Analytical evaluation of contacts in bearings often uses Hertzian [51] contact calculations or variations on this theory. Contact dimensions, surface pressure distributions and deflections can all be calculated if bearing geometries and material properties are known. The simplest form of contact to evaluate is a point contact where a circular contact patch is formed however contacts in rolling element bearings are typically line or elliptical contacts. Contact shapes for point, elliptical and line contacts along with their dimensions are shown in Figure 2.4.

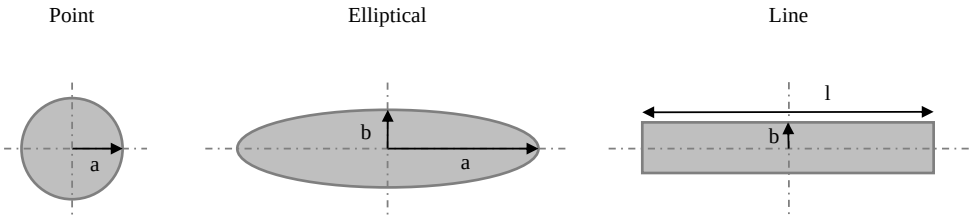

Figure 2.4: Different contact shapes and their dimensions.

Normal pressure distributions in contacts are assumed to be elliptical as shown in Figure 2.5.

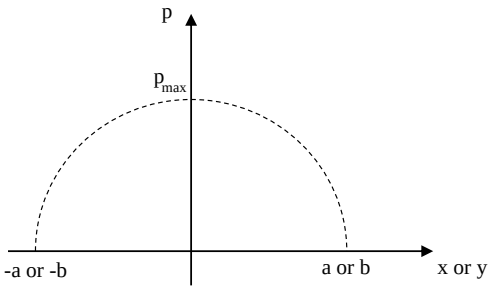

Figure 2.5: Different contact shapes and their dimensions.

General formulae for Hertzian contact calculations involve the calculation of a reduced modulus of elasticity and a reduced radius of curvature which define the material properties and geometry of the system and are outlined for line and elliptical contacts in the following Sections.

2.3.1 Line Contacts

For a line contact the following equation can be used to calculate contact width, b [27]:

$$b = \sqrt{\frac{8\ Q\ R'}{\pi\ l\ E'}} \tag{2.5}$$

where Q is roller load, and l is the roller length. The reduced radius R' and the reduced modulus E' are defined by:

$$\frac{1}{R'} = \frac{1}{R_x} + \frac{1}{R_y} = \left[\frac{1}{R_{Ax}} + \frac{1}{R_{Bx}}\right] + \left[\frac{1}{R_{Ay}} + \frac{1}{R_{By}}\right] \tag{2.6}$$

$$\frac{1}{E'} = \frac{1}{2}\left[\frac{1-{\upsilon_A}^2}{E_A} + \frac{1-{\upsilon_B}^2}{E_B}\right] \tag{2.7}$$

where R is a radius of body A or B in either the x or the y direction, E is the elastic modulus of either body A or B and υ is the Poisson's ratio of either body A or B.

Average and maximum contact pressures can be predicted using Equations 2.8 and 2.9 respectively.

$$p_{max} = \frac{2\ Q}{\pi\ b\ l} \tag{2.8}$$

$$p_{avg} = \frac{Q}{2\ b\ l} \tag{2.9}$$

Maximum line contact deflection (δ) can be calculated using Equation 2.10 [27]:

$$\delta = 0.319 \left(\frac{2\ Q}{E'\ l}\right)\ \left[\frac{2}{3} + \ln\left(\frac{4\ R_A\ R_B}{b^2}\right)\right] \tag{2.10}$$

2.3.2 Elliptical Contacts

Elliptical contact widths in both the axial direction (a) and rolling direction (b) can be calculated using Equations 2.11 and 2.12:

$$a = \left(\frac{6\ \bar{k}^2\ \bar{\varepsilon}\ Q\ R'}{\pi\ E'}\right)^{1/3} \tag{2.11}$$

$$b = \left(\frac{6\ \bar{\varepsilon}\ Q\ R'}{\pi\ \bar{k}\ E'}\right)^{1/3} \tag{2.12}$$

where simplified elliptical integral $\bar{\varepsilon}$ and ellipticity parameter $\bar{k}$ are calculated using Equations 2.13 and 2.14. Equations 2.6 and 2.7 are still applicable.

$$\bar{\varepsilon} = 1.0003 + \frac{0.5968\ R_x}{R_y} \tag{2.13}$$

$$\bar{k} = 1.0339\ \left(\frac{R_y}{R_x}\right)^{0.636} \tag{2.14}$$

Elliptical contact pressures can be calculated with Equations 2.15 and 2.16

$$p_{max} = \frac{3\ Q}{2\ \pi\ a\ b} \tag{2.15}$$

$$p_{avg} = \frac{Q}{\pi\ a\ b} \tag{2.16}$$

Maximum elliptical contact deflection (δ) can be calculated using Equation 2.17:

$$\delta = \bar{\xi}\left[\left(\frac{4.5}{\bar{\varepsilon}\ R'}\right)\left(\frac{Q}{\pi\ \bar{k}\ E'}\right)^2\right]^{1/3} \tag{2.17}$$

where simplified elliptical integral $\bar{\xi}$ is calculated using Equation 2.18:

$$\bar{\xi} = 1.5277 + 0.6023 \ \ln\left(\frac{R_y}{R_x}\right) \tag{2.18}$$

2.3.3 Other Deflection Calculations

It is sometimes beneficial to be able to separate these deflections, for example, the deflection of the raceway and not the rolling element might be of importance. Tripp [52] introduced these relationships for a line contact.

In general, elliptical contacts are seen in ball and spherical bearings whereas line contacts are seen in cylindrical and tapered roller bearings. That being said, cylindrical and tapered rollers almost always have some level of crowning in order to avoid edge loading [3] and so often transition from elliptical contacts at low load to line contacts at high loads. Therefore methods have been developed to account for these transitions. Palmgren [53] introduced a relationship between deflection and load based on laboratory testing of crowned rollers:

$$\delta = 3.84 \times 10^{-5} \ \frac{Q^{0.9}}{l^{0.8}} \tag{2.19}$$

Houpert [54] defines a transition deflection for bearing contacts. Below the transition deflection the contact is treated as a point contact and above this value the contact is treated as a line contact, corrected for a transitional region:

$$Q_{LC} = K_{LC} \ \delta^{1.078} \tag{2.20}$$

$$\begin{aligned} K_{LC_{outer}} &= 0.27835 \ E' \ l \ \left(\frac{1+\gamma}{t}\right)^{0.078} \\ K_{LC_{inner}} &= 0.2723 \ E' \ l \ \left(\frac{\cos(\beta)}{D_m}\right)^{0.074} \end{aligned} \tag{2.21}$$

$$Q_{PC} = K_{PC} \ \delta^{1.5} \tag{2.22}$$

$$K_{PC} = E' \ \sqrt{R_x} \ \left(\frac{1}{Cte1 \ k^{Cte2}}\right)^{1.5} \tag{2.23}$$

$$k = \frac{R_y}{R_x} \tag{2.24}$$

$$\begin{aligned} \delta_{trans_{outer}} &= \left(\frac{1.078}{1.5} \ \frac{K_{LC_{outer}}}{K_{PC}}\right)^{\frac{1}{0.426}} \\ \delta_{trans_{inner}} &= \left(\frac{1.074}{1.5} \ \frac{K_{LC_{inner}}}{K_{PC}}\right)^{\frac{1}{0.422}} \end{aligned} \tag{2.25}$$

$$
\begin{aligned}
&For\ \delta \leq \delta_{trans} \quad && Q = K_{PC}\ \delta^{1.5} \\
&For\ \delta \geq \delta_{trans} \quad && Q_{outer} = K_{LC}\ \delta^{1.078} - dQ_{outer} \\
& && Q_{inner} = K_{LC}\ \delta^{1.074} - dQ_{inner}
\end{aligned}
\tag{2.26}
$$

$$
\begin{aligned}
dQ_{outer} &= \left(\frac{1.078}{1.5}\ \frac{K_{LC_{outer}}}{K_{PC}}\right)^{\frac{1.1}{0.422}}\ \left(\frac{0.422}{1.5}\ K_{LC_{outer}}\right) \\
dQ_{inner} &= \left(\frac{1.074}{1.5}\ \frac{K_{LC_{inner}}}{K_{PC}}\right)^{\frac{1.1}{0.426}}\ \left(\frac{0.426}{1.5}\ K_{LC_{inner}}\right)
\end{aligned}
\tag{2.27}
$$

n.b. $Cte1$ and $Cte2$ are specific curve fitting parameters dependent on k.

2.4 Load Distribution

When a load is applied to a bearing the way this load is distributed across the rollers is not always uniform and is related to a variety of factors. This section summarises these relationships. For bearings under pure radial load, distribution of load can be described by the following equations [3]:

$$
Q_{max} = \frac{K_d \cdot F_r}{Z \cdot \cos(\gamma)} \tag{2.28}
$$

$$
Q_{\psi} = Q_{max}\left[1 - \frac{1}{2\epsilon}[1 - \cos(\psi)]\right]^n \tag{2.29}
$$

where the distribution is as shown in Figure 2.6.

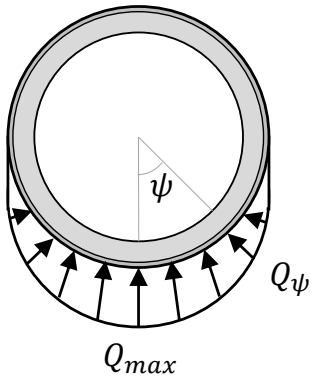

Figure 2.6: Example load distribution in a radially loaded rolling element bearing.

For ball bearings with no diametral clearance $K_d = 4.37$ and for roller bearings with no diametral clearance $K_d = 4.08$. For both types of bearings and nominal diametral clearance $K_d = 5$. For point contacts $n = 1.5$ and for line contacts $n = 1.11$. The value of ϵ is determined by the amount of clearance in the bearing. When there is clearance $0 < \epsilon < 0.5$, when there is no clearance $\epsilon = 0.5$ and if there is preload on the bearing $0.5 < \epsilon < 1$. [3]

For bearings under combined radial and thrust load the use of load integrals is necessary instead of the load factor in pure radial load equations [3]:

$$Q_{max} = \frac{F_r}{J_r(\epsilon) \cdot Z \cdot \cos(\gamma)} = \frac{F_a}{J_a(\epsilon) \cdot Z \cdot \cos(\gamma)} \tag{2.30}$$

Values of ϵ, $J_r(\epsilon)$ and $J_a(\epsilon)$ can be found through their relationship with $F_r \cdot \tan(\gamma)/F_a$ [3].

2.5 Lubrication

The function of a lubricant is to control friction and wear in a system. Lubricants used in wind turbines are normally oils or greases.

Oils can be sub-categorised based on their source into mineral, synthetic oils and biological oils. They are generally made up of a base oil and additives which improve specific aspects of the oil's performance. [27]

Greases are made up of a base oil and additives like oils but with the addition of a thickener which traps the oil in small pockets [27]. These thickeners are often soaps (a compound of a fatty acid and a metal) but can also be non-soaps [3]. Grease provides lubrication by releasing the base oil and additives contained within the grease onto the bearing surfaces.

2.5.1 Lubricant Viscosity

The viscosity of a lubricant is critical to its performance and it is therefore important to understand how the environment in which the lubricant operates may affect its viscosity [27]. The viscosity of a lubricant depends largely on the chemical composition of the base oil but can also be modified with additives [27]. Viscosity can be defined as dynamic viscosity, η:

$$\eta = (F/A)/(u/h) \tag{2.31}$$

where F is contact force, A is contact area, u is surface speed and h is lubricant thickness.

Or kinematic viscosity:

$$\upsilon = \eta/\rho \tag{2.32}$$

where rho is the density of the lubricant.

The thickness of a lubricant film is proportional to the lubricant viscosity. A minimum viscosity is therefore required for a film thick enough to separate the two surfaces of a contact. As viscosity, and therefore film thickness, increases beyond this point more energy is required to shear the lubricant and so energy is lost and heat is generated at the contact. There is therefore an optimum viscosity for each system. [27]

Optimising lubricant viscosity for a system can be a challenging prospect as viscosity changes with temperature, pressure and shear rate of the lubricant. Viscosity will generally decrease with increasing temperature and increase with increasing pressure [27]. Shear rate dependence only occurs in non-Newtonian fluids. Examples of lubricants behaving as non-Newtonian fluids include mineral oils at high shear rates and greases [27]. The most common non-Newtonian behaviour is shear thinning where viscosity decreases with increased shear rate.

2.5.2 Lubricant Degradation

Degradation of a lubricant is inevitable due to chemical reaction with atmospheric oxygen and water. Additives also deplete during oxidation as they react with the environment and the metallic surfaces in the bearing. In the case of greases, the base oil gradually separates from the thickener over the lifetime of the oil and the thickener can also become too soft or too hard through heating or mechanical working. Lubricants used must therefore maintain the required properties for its desired service life. Viscosity of lubricants can decrease due to degradation. [27]

2.5.3 Elastohydrodynamic Lubrication

Elastohydrodynamic lubrication (EHL) is a form of hydrodynamic lubrication in the presence of high-pressure contacts like those seen in rolling element bearings. In order to understand EHL an understanding of hydrodynamic lubrication is therefore necessary. Hydrodynamic films are formed where lubricant fills a gap between converging geometries and motion between the converging surfaces occurs. Lubricant is

drawn into the gap and the resulting increase in pressure forces the surfaces apart. In the case of EHL the effect of elastic deformation of the converging surfaces and the changes in viscosity of the lubricant with pressure are significant. [27]

The pressure distribution in a Hertzian contact is elliptical. This changes when the surfaces move against each other in the presence of a lubricant. The difference between the pressure profile of a Hertzian and EHL contact can be seen in Figure 2.7. The contact area enlarges and so the pressure profile spreads out slightly. The contacting surfaces are mostly parallel and planar, resulting in a central region with film thickness h_c but a constriction is formed near the exit of the contact resulting in a minimum film thickness, h_0 and a corresponding pressure peak. The lubricant viscosity increases as it enters the contact and decreases as it leaves the contact however the relative velocity of the surfaces remains constant. This constriction forms to maintain continuity of flow with the loss of lubricant viscosity at the exit. [27]

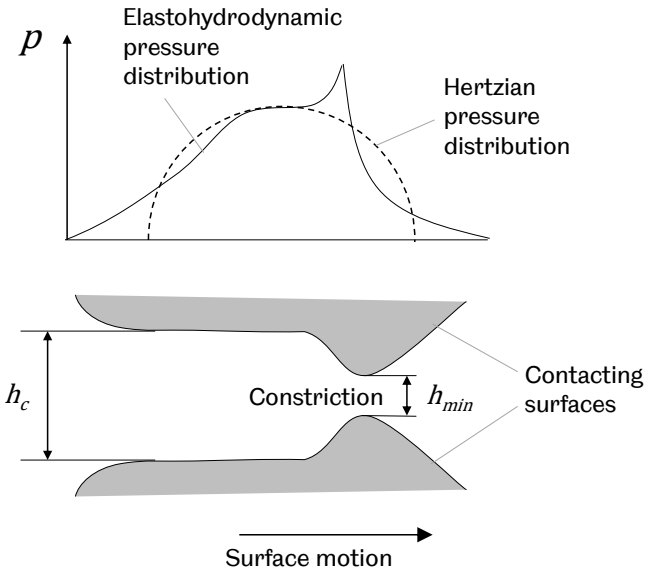

Figure 2.7: Pressure and film thickness distribution in an EHL contact. Adapted from [27].

The above pressure distribution describes a line contact. In a point contact the end constriction is curved to fit the contact boundary and is known as the 'horseshoe' constriction [27], as show in Figure 1.9.

Many factors can influence the thickness of the lubricant film including geometry, speed, load and lubricant properties. The central and minimum film thicknesses can

be calculated using formulae derived by Hamrock and Dowson [55] through Equations 2.33 and 2.34 respectively [27]:

$$\frac{h_c}{R'} = 2.69 \left(\frac{U\eta_0}{E'R'}\right)^{0.67} (\alpha E')^{0.53} \left(\frac{Q}{E'R'^2}\right)^{-0.067} \left(1 - 0.61e^{-0.73k}\right) \tag{2.33}$$

$$\frac{h_{min}}{R'} = 3.63 \left(\frac{U\eta_0}{E'R'}\right)^{0.68} (\alpha E')^{0.49} \left(\frac{Q}{E'R'^2}\right)^{-0.073} \left(1 - 0.61e^{-0.68k}\right) \tag{2.34}$$

Mean lubricant entrainment speed U can be calculated through Equation 2.35.

$$U = \frac{u_{rw} + u_r}{2} \tag{2.35}$$

η_0 is the lubricant dynamic viscosity and α is the lubricant pressure-viscosity coefficient. The above calculations assume that the contacting surfaces separating the lubricant films are flat, however in reality there is no such thing as a flat surface. EHL films can be very thin and there are occurrences at which the film thickness approaches the roughness of the contacting surfaces. One way to define the roughness of a surface is the RMS roughness:

$$r_q = \sqrt{\frac{1}{x}} \int_0^x z^2 dx \tag{2.36}$$

where x is the surface plane and z is the height plane.

The lambda ratio [56] is used to define the film variation as a function of local surface roughness:

$$\Lambda = \frac{h_{min}}{\sqrt{{r_{qA}}^2 + {r_{qB}}^2}} \tag{2.37}$$

where r_{qA} is the RMS roughness of body A and r_{qB} is the RMS roughness of body B.

The lambda ratio has been found to correlate closely with the limits of EHL – wear and surfaces alteration has been seen all the way up to $\Lambda = 4$ with decreasing severity as lambda ratio increases. However, a large number of machine elements have been known to operate well even though $\Lambda < 1$. This region is known as mixed or partial EHL and the contact load is shared between contacting asperities and the lubricant film. It is thought that the asperity contacts themselves form EHL contacts in a process known as micro-EHL. [27]

2.6 Performance and Failure

There are many factors that can affect the performance of a bearing over its lifetime and eventually lead to bearing failure. The criticality of lubricant film thickness to prevent wear has already been mentioned in Section 2.4.3 and this and other factors will now be discussed.

The most classical failure mode for a rolling contact bearing is through rolling contact fatigue (RCF). If the sub-surface shear stress exceeds the endurance limit of the material, over time cracks will form and propagate to the surface resulting in loss of material. Crack initiation normally occurs at the sub surface maximum shear stress location and initiation and propagation can take many cycles. The bearing life due to RCF can be predicted using ISO standards [5] [6] and bearings are normally designed such that they should fail after their design life – for wind turbines this is usually in the region of 25 years. With high surface shear stresses (due to sliding) or surface damage (due to other failure modes) cracks can also be surface initiated. The resulting damage from RCF is most commonly referred to as spalling [57].

Other causes of failure can arise from improper bearing mounting and alignment, overloading, insufficient lubrication and lubrication contamination with abrasives, moisture or corrosive agents [57]:

- Improper bearing mounting, misalignment and overloading
  - increases contact pressures, resulting in:
    - increased sub-surface shear stresses
    - and accelerated RCF.
- Insufficient lubrication.
  - Most commonly as a result of interruption of lubricant supply.
    - The lubricant film thickness and therefore the value of Λ is reduced.
  - Lubricant film thickness can also be reduced through increased temperatures in the bearing leading to a reduction in lubricant viscosity.
    - Increases in temperature are often a result of increased friction due to other damage mechanisms.
- Lubricant contamination

  - can cause stress concentrations which can initiate or accelerate surface initiated RCF.
    * Hard particles introduced through seals or from wear debris can cause dents in surfaces as they are rolled over.
    * Ingress of moisture or other corrosive substances in lubricants can result in oxidation of rolling contacts and corrosion pitting.
- Other events can also cause stress concentrations leading to surface initiated RCF.
  - Sudden impacts can cause plastic deformation resulting in indentation of raceways known as brinelling.
  - Vibration or oscillations in bearings, sometimes prior to installation but also seen in operation, can cause fretting wear of rolling surfaces called false brinelling which can progress to fretting corrosion.
    * The oscillatory motion enables this damage by pushing lubricant out of the contact.
  - If bearings are not properly insulated, electrical currents can pass through contacts causing pitting.

A failure mode that has been an issue for wind turbine bearings over recent years is white structure flaking (WSF) caused by axial cracks and white etching cracks (WEC). This failure mode is associated with microstructural changes in the region just below bearing contacts known as the white etching area (WEA). There is evidence of many drivers and mechanisms for WSF including hydrogen embrittlement, electrical and thermal effects and stress induced factors. Some of these can be related back to impaired lubrication and high contact pressures. [58]

Another failure mode that has received attention for failures in wind turbine bearings is micropitting, particularly in spherical roller bearings. Micropitting occurs when asperity contact occurs between the two contacting surfaces, i.e. the bearing is insufficiently lubricated. The additional shear stress causes the maximum stress values to move closer to the surface of the contact meaning that localised stresses under asperity contacts become significant, causing material to break away and form very small pits. [59]

The result of wear due to these damage mechanisms is an increased clearance in bearings which can further deteriorate bearing operating conditions through load distribution across a smaller proportion of the bearing. Increases in temperature and vibration and subsequent bearing failure often follow [57].

2.7 Conclusions

This section has introduced some key theory for rolling element bearings that require understanding in order to interpret how an ultrasonic wave interacts with rolling bearing interfaces. This includes bearing types and their intended operating conditions, prediction of characteristics of a bearing contact (including contact dimensions, pressure distribution and deflection), how load is distributed in a rolling element bearing and details of lubrication in bearing contacts, including contribution factors to pressure distribution and how film thickness can be predicted. The criticality of proper lubrication conditions and RCF accelerators to prevent early bearing failure has also been highlighted.

Chapter 3

Ultrasound

3.1 Introduction

In this chapter the theory behind propagation of ultrasound and how it interacts with interfaces is introduced. Key concepts of equipment, transducers and processing techniques necessary for ultrasonic data acquisition are then outlined. Finally, a review of work to date using ultrasonic transducers to monitor rolling element bearings is presented which shows gaps in current research and areas that required development which will be the focus of the following chapters.

Ultrasound is a specific type of acoustic signal; the propagation of sound waves or mechanical vibrations through a medium [60]. Ultrasound is high frequency vibration greater than the human ear can detect, typically quoted as above 20 kHz. Propagation of elastic waves is enabled through the elastic nature of a medium; if a material is not stressed beyond its elastic limit, then the particles can elastically oscillate. When particles are displaced from their equilibrium, electrostatic restoration forces, along with the inertia of the particles, cause vibrations in the medium [61]. Ultrasound has many uses, the most well-known of which is medical scans during pregnancy. Within mechanical engineering ultrasound has traditionally been used for non-destructive testing (NDT) [60] but more recently techniques have been developed for tribological interfaces [42, 62, 63].

3.2 Propagation Modes

There are several types of ultrasonic waves including bulk waves, surface waves and plate waves. This work focuses on the use of bulk waves which can be split into

longitudinal and shear waves. Longitudinal waves propagate in the direction of their vibration whereas shear waves propagate perpendicular to their direction of vibration, as shown in Figure 3.1 [64].

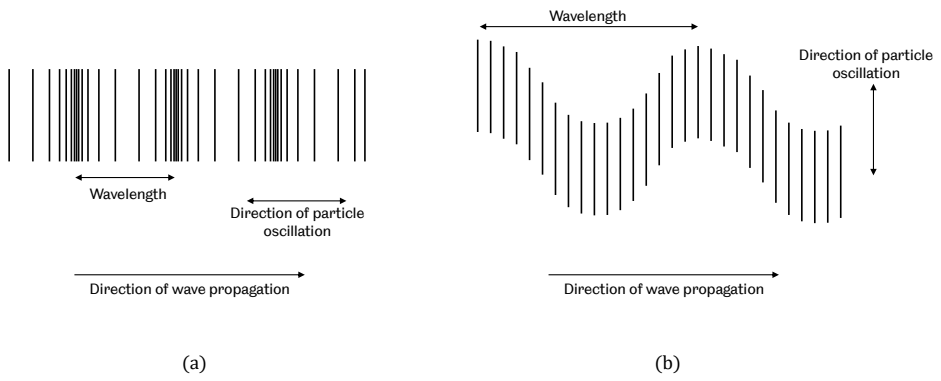

Figure 3.1: Propagation of bulk (a) longitudinal and (b) shear waves.

3.3 Factors Affecting Propagation

Important concepts in sound propagation are the speed of sound, attenuation, reflection and refraction.

3.3.1 Speed of Sound

The speed of sound is linked with the wavelength and frequency of the sound as described by Equation 3.1:

$$c = f \cdot \lambda \tag{3.1}$$

Longitudinal and shear waves travel at different speeds [65] and in solids longitudinal waves tend to travel almost twice as fast as shear waves. Changes in the temperature of a material can also affect the speed of sound.

A stress field can change the speed of sound of an acoustic wave. This is known as the acoustoelastic effect. When a material is in compression the speed of sound increases

and when it is in tension the speed of sound decreases. An acoustoelastic constant can be defined to describe this behaviour:

$$L = \frac{dc_p/c_0}{d\varepsilon} \tag{3.2}$$

A different acoustoelastic constant is defined depending on wave mode, its propagation direction relative to the stress field, and its particle oscillation direction relative to the stress field [66].

3.3.2 Attenuation

Attenuation of ultrasound is the reduction in acoustic energy as the wave propagates through a medium which cannot be prevented. Attenuation is the combined effect of absorption (conversion of acoustic energy to thermal energy) and scattering (reflection of sound energy away from its original direction of propagation) [67]. The rate at which a signal attenuates depends on the characteristics of the sound wave as well as material properties and the structure of the medium. Sound attenuates faster at higher frequencies and therefore lower frequency sound will travel further through a component [67]. A more porous material will scatter more of the acoustic energy so ultrasound will attenuate faster in, for example, metal castings than forged metals. Material properties can also have an effect: steel will generally attenuate sound faster than aluminium if similar production routes have been taken. The rate of signal amplitude decay due to attenuation is generally defined as an exponential decay which is a function of distance travelled [67].

3.3.3 Interaction with Interfaces

When a sound wave hits an interface some of the wave is reflected from the interface and some of the sound is transmitted through the interface, as shown in Figure 3.2.

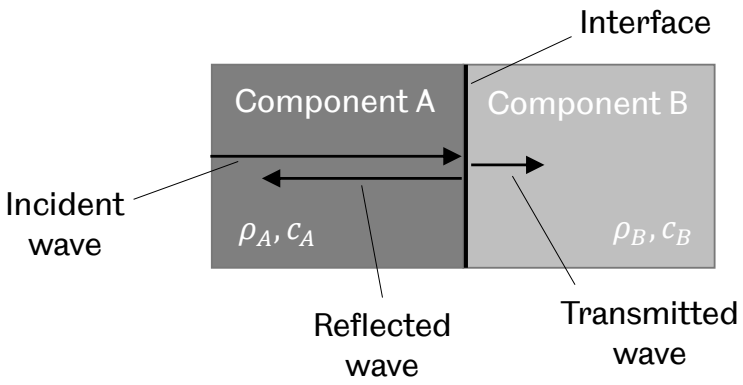

Figure 3.2: Sound reflection and transmission at an interface.

If we consider a perfectly bonded planar interface the proportion of the acoustic wave reflected from the interface depends on the acoustic impedance of the materials that share the interface [65]:

$$\mathbf{R} = \frac{z_B - z_A}{z_B + z_A} \tag{3.3}$$

$$z = \rho \cdot c \tag{3.4}$$

$\mathbf{R}$ is the reflection coefficient and is a value between -1 and 1. $\mathbf{R} = 1$ means that all of the wave is reflected and $\mathbf{R} = 0$ means that none is reflected. A negative value indicates that the phase of the reflected signal will be inverted. For a steel-air interface here $z_{steel} = 4.710^7\ kg/m^2s$ and $z_{air} = 0.410^3\ kg/m^2s$ [34] then $\mathbf{R}$ = -0.99998. Almost all of the wave is reflected. In this way the reflection coefficient can be experimentally obtained by dividing the amplitude of the received reflection with an interface (measurement) by that received when there is only air present(reference), as shown in Figure 3.3. Equation 3.5 follows.

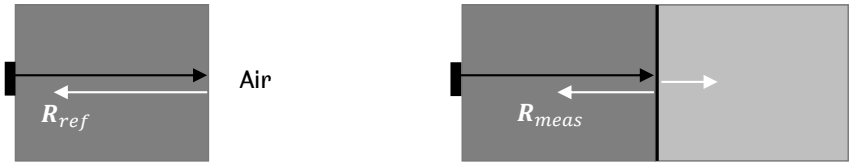

Figure 3.3: Ultrasonic measurement (a) without and (b) with the presence of an interface, demonstrating referencing with air.

$$|\mathbf{R}| = \frac{|\mathbf{R}_{meas}|}{|\mathbf{R}_{ref}|} \tag{3.5}$$

Equation 3.3 is not entirely realistic (if two bodies are in contact, they will not be perfectly bonded, and the interface will never be entirely flat) but gives a reasonable approximation. Tattersall [68] used the 'spring model' for an interface to expand the expression for reflection coefficient to include the effect of contact stiffness:

$$\mathbf{R} = \frac{z_B - z_A + i\,\omega(z_A z_B/\kappa)}{z_B + z_A + i\,\omega(z_A z_B/\kappa)} \tag{3.6}$$

$$\omega = 2\pi f \tag{3.7}$$

The magnitude of reflection coefficient through trigonometry is then:

$$|\mathbf{R}| = \sqrt{\frac{(z_B - z_A)^2 + (\omega z_A z_B/\kappa)^2}{(z_B + z_A)^2 + (\omega z_A z_B/\kappa)^2}} \tag{3.8}$$

If the two materials in contact are made of the same material and therefore have the same acoustic impedance, as is often the case with rolling bearings, then Equation 3.8 can be simplified and rearranged to define contact stiffness as a function of reflection coefficient [69]:

$$\kappa = \frac{\omega z}{2}\sqrt{\frac{1}{|\mathbf{R}|^2} - 1} \tag{3.9}$$

The stiffness of a very thin layer of lubricant is governed by the following relationship:

$$\kappa = \frac{\rho\, c^2}{h} \tag{3.10}$$

And so combining Equation 3.8 or 3.9 with Equation 3.10 and rearranging the lubricant film thickness can be defined as a function of reflection coefficient [70]:

$$h = \frac{\rho\, c^2}{\omega\, z_A\, z_B} \sqrt{\frac{|\mathbf{R}|^2\,(z_A + z_B)^2 - (z_A - z_B)^2}{1 - |\mathbf{R}|^2}} \tag{3.11}$$

$$h = \frac{\rho\, c^2}{\omega\, z} \sqrt{\frac{|\mathbf{R}|^2}{1 - |\mathbf{R}|^2}} \tag{3.12}$$

The bulk modulus of a lubricant is defined as:

$$B = \rho\, c^2 \tag{3.13}$$

Knowledge of the bulk modulus of the lubricant is therefore essential to find the lubricant film thickness from measurement of the reflection coefficient, however the bulk modulus of a lubricant is known to change under pressure. Values of pressure can be estimated through Hertzian calculations and values of bulk modulus at these pressures can be ascertained either experimentally or through theoretical relationships.

If sound waves hit an interface at an angle they will be reflected or transmitted at an angle according to Snell's law [71], which can be explained with the help of Equation 3.14 and Figure 3.4. The sound that is transmitted into component B is refracted at an angle dependent in the incident angle and the properties of both component A and B.

$$\frac{\sin(\theta_1)}{\sin(\theta_2)} = \frac{c_A}{c_B} \tag{3.14}$$

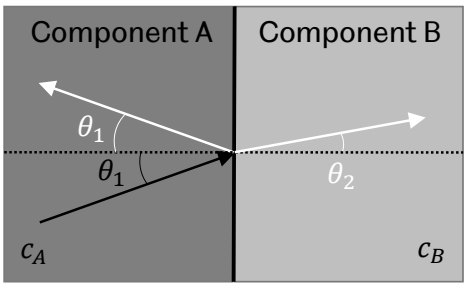

Figure 3.4: Snell's law: how a sound wave reflects and refracts from an interface when the incident wave is not perpendicular to the interface.

The presence of unwanted interfaces in a component, such as cracks, can be determined using ultrasound, which is the basis of ultrasonic NDT techniques. Crack location can be determined by the time of flight (ToF) of a reflection and their size and orientation can be determined by capturing reflections from several locations along the crack length. Through similar methodologies, changes in ToF can be used to measure deflection [72] and wear [42] of interfaces.

3.4 Wavefronts and Beam Shape

Huygens' principal states that any wave front can be constructed from a large number of spherical waves of the same frequency [60]. This is useful for the visualisation of sources, propagation and reflection of sound waves. Figure 3.5 shows how this principle can be applied to the source of an ultrasonic wave to visualise the shape of the wavefront. Assuming the transducer acts as a piston shaped generator, five spherical wavefronts are shown. The wavefront shown results when these spherical waves, and those from all points between, interfere. The resultant wavefront in front of the transducer is a plane wave, whereas at the edge of the transducer an annular wavefront is formed.

Huygens' principle can also be applied to reflected sound where each point on the wavefront that hits the interface also acts as a spherical emitter. This is visualised in Figure 3.6.

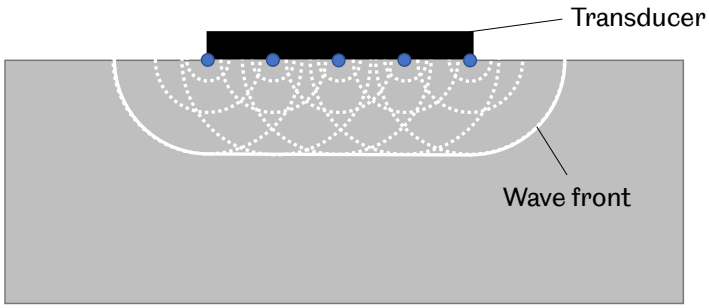

Figure 3.5: Visualisation of a wave source using Huygens's principle.

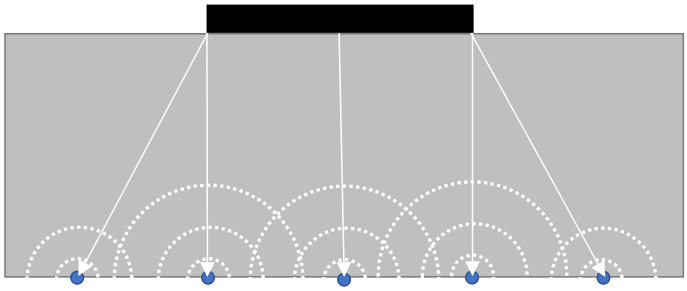

Figure 3.6: Visualisation of a reflected wave using Huygens's principle.

Huygens' principle describes how a sound field propagates from a source but does not describe how strong the excitation becomes at a given point in the field. Cross sections of the pressure field resulting from an ideal oscillator can be seen in Figure 3.7.

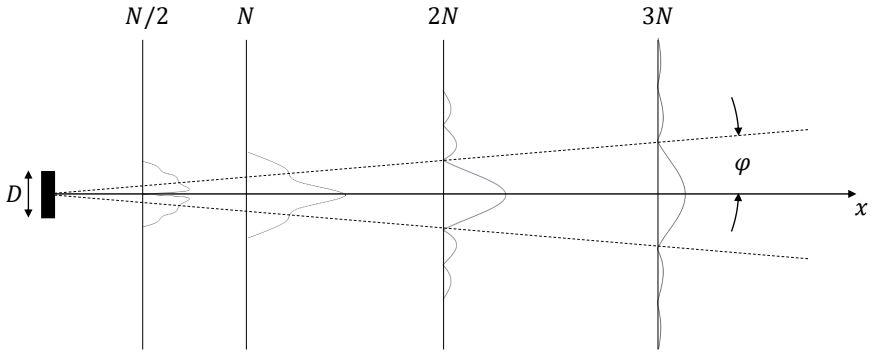

Figure 3.7: Cross sections of sound pressure distributions for a circular oscillator. Adapted from [60].

To fully explain Figure 3.7 the concept of near field distance is required [60]:

$$N = d\,\frac{D^2}{4\lambda} \tag{3.15}$$

where d is 1 for circular oscillators or is dependent on the ratio of side lengths for rectangular oscillators and D is the length of the larger side. Values for d for various side length ratios are given in [60].

The near field is the sound field up to the near field length and has quite a complicated structure due to constructive and destructive interference of waves from the oscillator. Measurements in this range can be problematic [73] and should be avoided where possible. At the near field length there is a single maximum pressure, after which a simpler field is formed: the far field. In the far field the pressure amplitude gradually decreases as the beam diverges. The angle of divergence is shown in Figure 3.7. [60]

The angle of divergence for circular oscillators can be calculated using:

$$\sin(\varphi_0) = 1.22\,\frac{\lambda}{D} \tag{3.16}$$

For rectangular oscillators there are two beam divergence angles, one for each orientation of the transducer [60]. For each case the oscillator width in each plane is used. The beam width can be found by simple trigonometry:

$$w = 2L\tan(\varphi_0) \tag{3.17}$$

where L is the distance from the source.

These equations are only valid when D is much greater than λ. With decreasing $\frac{D}{\lambda}$ the angle of divergence approaches 90^{o} and at $\frac{D}{\lambda} = 1$ the pressure field is nearly spherical [60].

3.5 Measurement Systems

A typical ultrasound system includes one or more transducers, an ultrasonic pulser receiver (UPR), a digitiser, a PC and cabling to connect all of these together. All of these elements are described in more detail in the following sub-sections. A system diagram for a typical ultrasound system in pulse-echo mode can be seen in Figure 3.8. Pulse-echo mode is where the same transducer emits and receives ultrasonic waves.

In pulse-receive (also known as pitch-catch) mode, a different transducer receives to the transducer that emits the ultrasonic waves.

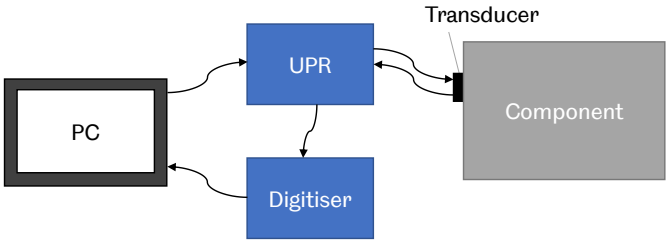

Figure 3.8: Ultrasonic system diagram - pulse-echo configuration.

3.5.1 Transducers

An ultrasonic transducer converts electrical signals into sound waves and vice versa and are referred to as sensors and transducers interchangeably in this thesis. Transducers used in this work function through the piezoelectric effect [74]. These types of transducer have a Curie temperature [75] and if this temperature is exceeded they will no longer function, even if temperature is brought back below this threshold. For PZT materials the Curie temperature is around 300 °C but can vary significantly depending on composition.

Transducers normally consist of a piezoelectric material sandwiched between two electrodes, as shown in Figure 3.9. Application of an oscillating voltage across the ground and live (or positive and negative) electrodes enables excitation of the transducer, causing it to vibrate. Equally, external vibrations that cause the transducer to vibrate are converted into an electrical signal. Some transducers have 'wrap-around' electrodes which enable cables to be attached to one face of the transducer but this reduces the active area. Standard transducers can be grounded through electrically conductive components.

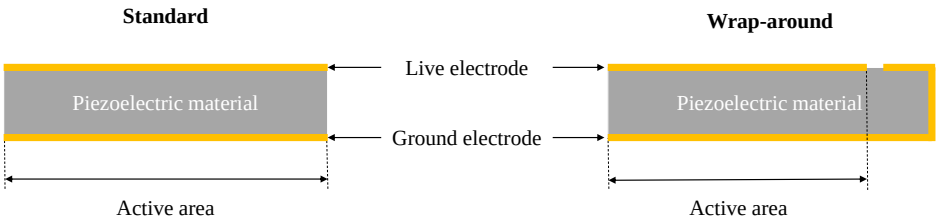

Figure 3.9: Transducer schematics. Left is a standard element and right is a wrap-around element.

NDT applications typically use ultrasonic probes to transmit sound into a component. These are made up of a transducer with backing material encased in a protective case. The function of the backing signal is to damp the signal [76] so that the signal emitted has a large bandwidth (i.e. contains a large range of frequencies) and is short in duration.

The size of the ultrasonic transducer is limited by its thickness, which also controls the transducer frequency. As a rule of thumb, the smallest dimension of the transducer should not be less than three times the thickness [73]. For example, a 10 MHz transducer is typically around 0.2 mm thick. The smallest dimension this transducer can be normally operated at is therefore 0.6 mm. If the transducer were cut to a smaller size, then the edge effects of the transducer become dominant and the transducer will no longer oscillate in its desired mode. A larger transducer will create a larger excitation with the same excitation voltage, resulting in larger amplitude reflections and thus a larger signal to noise ratio (SNR).

Transducer beam spread is also important to consider. The measurement area of a bonded transducer has previously been described as the area of the ultrasound transducer where the measured surface is parallel to the transducer surface [73]. Figure 3.10 helps to explain this reasoning. In a pulse-echo configuration the sound which is emitted perpendicular to the surface is reflected directly back at the sensor and is detected. The sound which is emitted from the edges of the transducer hits the measured surface and is reflected away from the transducer according to Snell's law. Due to the presence of fringe effects in past results [39, 77], further discussed in Section 3.7.4, this theory is questionable.

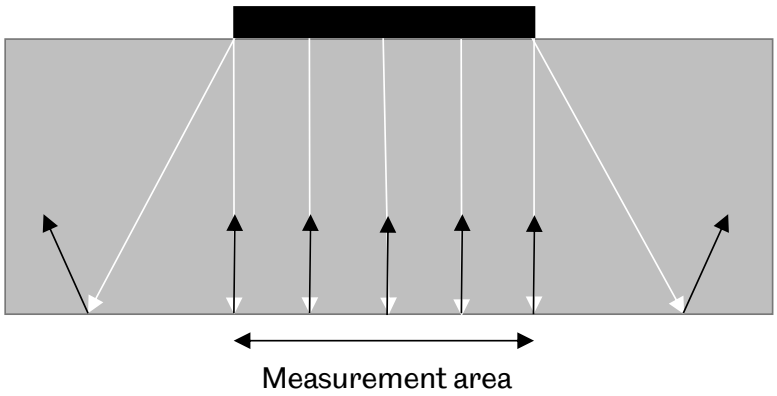

Figure 3.10: Transducer measurement area

In reality the area measured by the transducer is likely to be closer to the spot size.

For an unfocussed transducer the area measured can be approximated using Equations 3.16 and 3.17 in accordance with the assumptions described in Section 3.4. It can also be measured given the correct equipment. Howard [39] measured the wavefront of a 1.5 × 7 mm sensor bonded to a bearing raceway using a system of stepper motors and an ultrasonic probe. The results in Figure 3.11 show a 3.8 mm beam width at -6 dB and approximately a 5 mm beam width to the first minima. Beam width calculations for this sensor size indicate the beam width should have been 9.7 mm at -6 dB and 16.9 mm at the first minima. With the size of the sensor approaching the wavelength of the ultrasound (0.6 mm) one would expect that this beam spread would be even further increased than these equations predicted. The behaviour may have been affected by the geometry of the raceway, though more likely by the bonding of the transducer to the raceway, but these results question the applicability of these equations. Excitation of only the edge of a transducer has been known to cause focussing effects [60]. Due to the geometry of the raceway the sensors are likely to have been best grounded at the their edges.

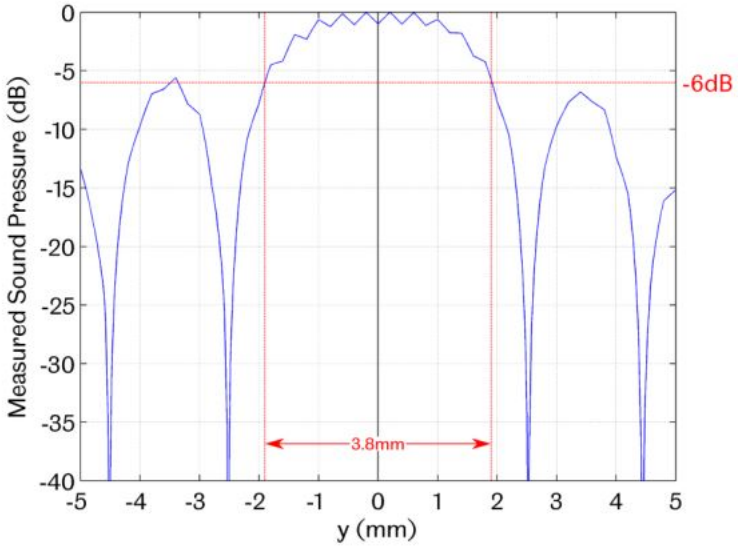

Figure 3.11: Example transducer wavefront measurement. From [39].

3.5.2 Coupling

NDT transducers require coupling to the component the sound wave is to be transmitted through. This coupling is normally some form of gel or rubber and functions to eliminate air gaps in between the transducer and component [78]. A large amount of work has also made use of immersion transducers, where water is typically used

to couple transducers with a component. The use of immersion transducers enabled focussing but also requires bulky equipment to be attached to the test bearing.

Alternatively, transducers can be bonded directly to the component which eliminates the requirement for coupling and gives the effect of damping the transducer [79]. Some other advantages include better performance at elevated temperatures and a much more repeatable signal [39]. Their overall form factor is also significantly smaller, enabling much less invasive instrumentation. Previous work has identified high temperature strain gauge adhesives as suitable for bonding transducers and highlighted the importance of achieving a thin bond layer [79].

Ideally ultrasonic waves should be transmitted parallel to the interface of interest in order to receive enough energy back from reflections. Some error can be tolerated due to the divergence of beams but this has meant that grooves or channels cut into parts are often required to create a parallel surface to the roller-raceway interface, for example in a tapered roller bearing.

3.5.3 Cabling

Due to the low-voltage signals received from ultrasound transducers the signals carried through connecting cables are susceptible to noise. It is therefore necessary to use shielded cables to connect to transducers. Coaxial cable is normally used, an example of which can be seen in Figure 3.12.

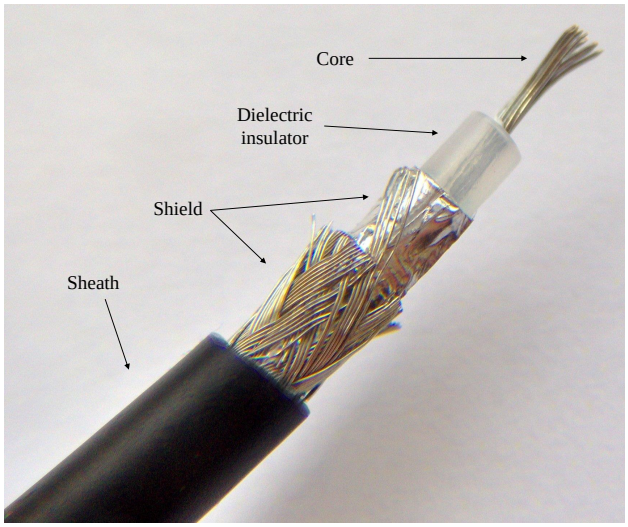

Figure 3.12: Composition of a coaxial cable. Adapted from [80].

3.5.4 Ultrasonic Pulser Receiver

The Ultrasonic Pulser Receiver (UPR) generates the excitation pulse that is sent to the ultrasonic transducer. Depending on the capability of the UPR this pulse can be as complex as a chirp (a sinusoidal wave which sweeps through a range of frequencies) and as simple as an impulse generated by capacitor discharge.

Ideally, the largest possible amplitude pulse will be transmitted into the component of interest so that the signal to noise ratio is as high as possible, reducing error in measurements. In order to do so a higher pulse voltage can be used, though if the pulse voltage is too high then the transducer may be depolarised; limits are normally supplied by transducer manufacturers and generally, a smaller transducer has a lower voltage limit than a larger one. Some other tweaks can also be used in terms of excitation pulse shape, for example a sine excitation of the same voltage better excites a traducer than an impulse. Another consideration when selecting a UPR is the pulse repetition frequency (PRF). This is the frequency with which the UPR can send a pulse and therefore limits the resolution of measurements in time.

Filters can also be used to increase signal quality, for example to remove high or low frequency noise, or to tune signal gain to make proper use of digitiser range. More complex pulsing capabilities, increased pulse voltage, higher PRFs and more complex signal amplification and filtering all come with an associated increase in cost to the system. The UPR normally makes up a considerable amount of the overall cost.

3.5.5 Digitiser

A digitiser converts the analogue ultrasonic signal into a digital one for storage and further processing. The main considerations when selecting a digitiser are its sample frequency and its resolution. Sampling frequency determines resolution for time based measurements and digitiser resolution determines the resolution of amplitude based measurements. This device is generally the other considerable cost of a measurement system.

3.5.6 Multiplexing

One additional component, not mentioned previously, that can be included in an ultrasonic system is a multiplexer. A multiplexer is chiefly a set of high-speed switches that enable one ultrasonic system to interact with many transducers. These can be

useful when using arrays of transducers and are often much cheaper than using several UPRs, although they split the PRF of the UPR between the number of channels used.

3.5.7 Focussing

The size of the ultrasound beam directed at the area of interface is an important consideration and will be discussed in further detail in Chapter 8. Essentially, the smaller the beam width, the higher the lateral resolution of measurements. There are several methods of focussing transducers, but these can generally be split into passive and active techniques. Passive techniques include the use of transducers with curved faces, lenses (most commonly immersion transducers) and phase plates [60]. Active techniques require arrays of transducers which are pulsed at varying time points through means of electronic delays. The interference of the waves from each of the transducers forms a focussed beam [60]. Active focussing requires more complex and costly UPR and digitiser equipment as the number of channels increases. To date only passive immersion focussed transducers have been used on rolling element bearings.

Resolution improvements in NDT systems have also been implemented using the Full Matrix Capture (FMC) technique. This involves the use of an array of transducers and capturing reflections for the full range of transducer pairs. i.e. transducer 1 is pulsed and data is received from transducer 1 and then each of the other transducers in the array. This is repeated pulsing each of the transducers. The result is a 'full matrix' of captured data. Post processing techniques allow greater resolution to be obtained than traditional techniques, notably the Total Focussing Method (TFM) [81]. There are clearly challenges with the use of this technique in dynamic testing due to the amount of time this large number of captures requires but it may be useful in static environments or where the speed of acoustic equipment is sufficiently fast compared to the movement of the dynamic objects being tested. Where bearings are under static loads and at constant speeds, synchronisation of pulsing with bearing rotation may also be possible.

3.6 Data Processing

An example of a reference signal and a measurement signal for ultrasonic data is shown in Figure 3.13. Each signal is called an A-scan.

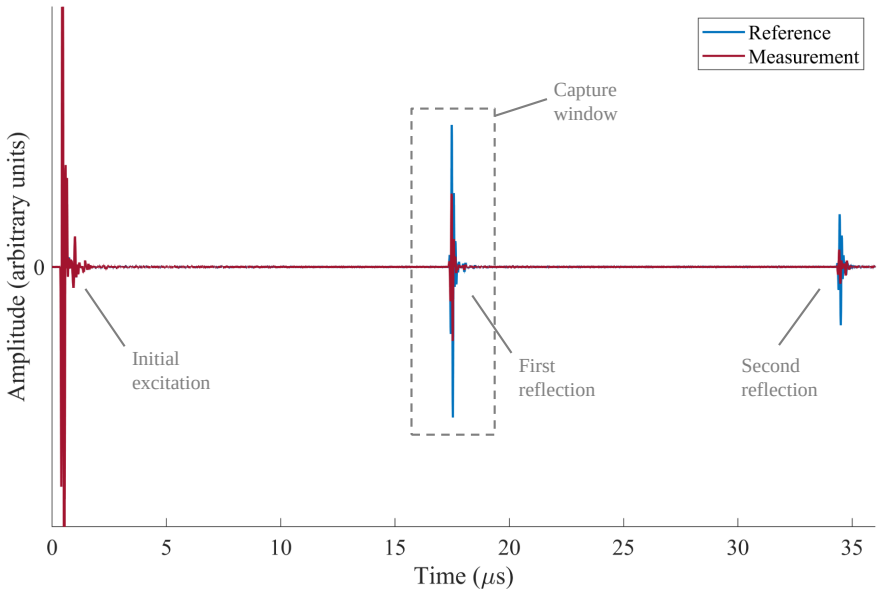

Figure 3.13: Typical ultrasound signals (A-scans) including reference and measurement signals.

Typically, the first reflection is used as it has the greatest SNR and is sometimes the only section of the A-scan recorded in order to reduce file size. This is shown as the capture window in Figure 3.13. The reference signal is taken once or can be periodically taken to account for changes in environment (e.g. temperature). Alternatively, referencing can be pre-calibrated by, for example, placing the component in an oven and recording a set of references over a range of temperatures. The corresponding reference signal can then be selected in post processing through use of simultaneous temperature data from a thermocouple close to the sensor. Measurement signals are continually taken and are compared to the reference signal. The two features most commonly monitored are change in amplitude and change in ToF.

3.6.1 Amplitude Monitoring

Changes in amplitude are normally monitored in the frequency domain as frequency dependence is sometimes a consideration, for example when calculating film thickness. The windowed first reflection (capture window) can be converted to the frequency domain through use of the fast Fourier transform (FFT). The change in amplitude is generally monitored at the centre frequency of the transducer, as shown in Figure

3.14(b), because this frequency has the greatest SNR. The amplitude of the measurement and reference are then compared to obtain the reflection coefficient as described in Equation 3.5.

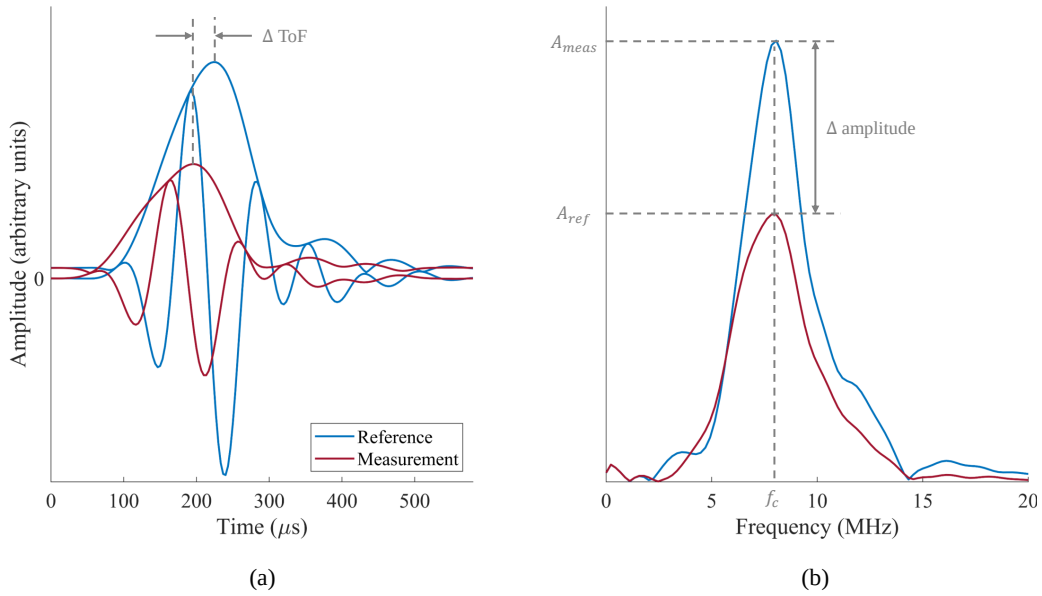

Figure 3.14: First refection (capture window). (a) In the time domain, showing windowed A-scans of the first reflection for both reference and measurement signals. The Hilbert envelope of each of these signals is also shown. (b) In the frequency domain. The frequency amplitude of the time domain signals is shown, along with the centre frequency (f_c) and reference and measured amplitudes (A_{ref} and A_{meas}) at the centre frequency.

3.6.2 Time of Flight Monitoring

There are several methods of measuring ToF of an ultrasonic pulse, which were mostly developed for NDT purposes. These include zero crossing and cross correlation. The most robust method for measuring changes in time of flight with the presence of a tribological interface was developed by Chen et al. [82] and Nicholas et al. [40]. Where sampling frequency is insufficient for the desired precision in ΔToF the signal can be interpolated to improve this. The envelopes of the signals are found using the Hilbert transform, as shown in Figure 3.14(a), which eliminates any unwanted phase shift resulting from contact stiffness. The envelopes are then normalised and cross correlated to find the change in time of flight.

3.7 Ultrasound in Rolling Element Bearings

The first work using ultrasonic techniques to monitor rolling bearings was published by Dwyer-Joyce et al. in 2003 [83]. In this paper the central film thickness of contacts were measured. Since then these techniques have been extensively developed and a summary of the literature up to the date of this review is show in Table 3.1. Aspects of a selection of these papers are further explored in the following sections.

Year	Reference	Transducer	Summary
2003	Dwyer-Joyce et al.[83]	Focussed immersion	The first published measurements of lubricant film thickness using ultrasonic methods in a rolling bearing. Results compared well with EHL calculations.
2004	Dwyer-Joyce et al. [62]	Focussed immersion	A study into the limitations of the ultrasonic method for measuring film thicknesses. Films down to 50 nm were measurable in a ball on flat configuration. Other limitations were associated with attenuation, spatial resolution and contact patch speed.
2005	Zhang et al. [84]	Focussed immersion	Results of film thickness measurements compared well with a rig measuring film thickness by the movement of a digital piezo translator.
2006	Zhang et al. [85]	Focussed immersion	The first published work to measure the film thickness profile as ball rolled past an ultrasonic transducer. Reflection coefficient results show a parabola shape as expected. Film thickness results were corrected using the theoretical acoustic energy distribution of the transducer.
2006	Zhang et al. [43]	Focussed immersion	Water, acetone, and sand were added to the lubricant whilst the bearing was being monitored by ultrasonic techniques. In all three cases the addition of contaminant was detectable. Total film collapse was seen with the addition of water and acetone.
2009	Takeuchi [86]	Coupled with housing	Measurement of the width of an indentation on the bearing raceway was done in this study.
2009	Drinkwater et al. [87]	Deposited thin film	The first measurements with a transducer bonded to the raceway instead of using an immersion transducer. The high frequency of the transducer gave some improvements in resolution. The first “W shape” in reflection coefficient plots was seen here and was explained by deflection of contact changing the shape of the reflected beam.
2012	Wan Imbrahim et al. [88]	Focussed immersion	This paper goes into increased detail on factors affecting ultrasonic film thickness measurements. The effect of measuring in front and behind the focal length of the transducer was shown. Interestingly the W shape was seen when measurements were taken in the near field. Operation a long way into the far field also resulted in distorted reflection coefficient roller profiles. A ’sweet spot’ in the focal zone was demonstrated.

Year	Reference	Transducer	Summary
2014	Zhang et al. [89]	Bonded transducer	This paper used a transducer bonded to the raceway of a bearing and monitored lubricant film thickness. The transducer measurement area was larger than the contact and so Hertzian contact calculations in combination with ray modelling of the contact was used to correct results fairly successfully, although no reflection coefficient or film thickness profiles were shown, only minima.
2014	Li et al. [90]	Focussed immersion	A method for increasing accuracy of lubricant film thickness measurements when the spot size of the transducer is similar to the contact size was proposed. The method used the areas between successive measurements (non-overlapping areas) when high PRF is used.
2015	Zhang et al. [91]	Bonded transducer	This paper is largely the same as [89] with a slightly different transducer.
2015	[82]	Bonded transducer	This work introduced the possibility of measuring the load at a roller-raceway contact. The technique directly measured deflection of the raceway, removed the contributions of phase shift and acoustoelastic effects and converted the deflection to load through a Hertzian contact model.
2016	Howard [39]	Bonded transducer	This work highlights fringe effects and the W shape in reflection coefficient measurements of rolling element contact passing an ultrasonic transducer. It also shows how defects in bearings can be monitored to failure although this was found to give no more warning than temperature monitoring methods for indication of damage. The possibility of identifying lubricant starvation with ultrasonic techniques was also introduced here.
2018	Avcioglu [92]	Focussed immersion	This work showed the indentations in rollers can be detected by anomalies in results when time of flight is used as a monitoring technique.
2020	Nicholas et al. [40]	Bonded transducers	Results from this work were enabled by [39]. This data was from a bearing in an operational wind turbine. Fringe effects were seen in reflection coefficient data and the W shape was seen in both reflection coefficient and load measurements. The behaviour of lubricant between roller passes was analysed. Variations in load and lubrication behaviour across the full roller compliment were seen and suggested to be due to slight geometrical differences in rollers.
2021	Nicholas et al. [44]	Bonded transducers	This work expanded on the observed lubricant behaviour between roller passes in [40]. It showed that variation in lubricant reflow time could be monitored and associated with changes in bearing speed, load and lubricant viscosity. It was also possible to observe whether a bearing was sufficiently lubricated or not.
2021	Nicholas [41]	Bonded transducers	This included work published in the previous two papers [40, 44]. Areas of this work were also complete in collaboration with the author. In particular, measurements from a full-scale CRB test rig, results of which are shown in Chapter 6 of this thesis. Within this work, misalignment of rollers using ultrasound was observed for the first time.

Table 3.1: Summary of literature relating to ultrasonic measurement of rolling element bearings.

3.7.1 Instrumentation

Throughout previous works two main techniques of coupling transducers with bearing components have been employed. The use of immersion transducers was initially used. An example experimental setup is shown in Figure 3.15. This arrangement allowed

focussed transducers to be used and smaller spot sizes (measurement areas) to be formed. It is obvious however that this setup requires severe bearing modification and would be difficult to employ on an operational bearing.

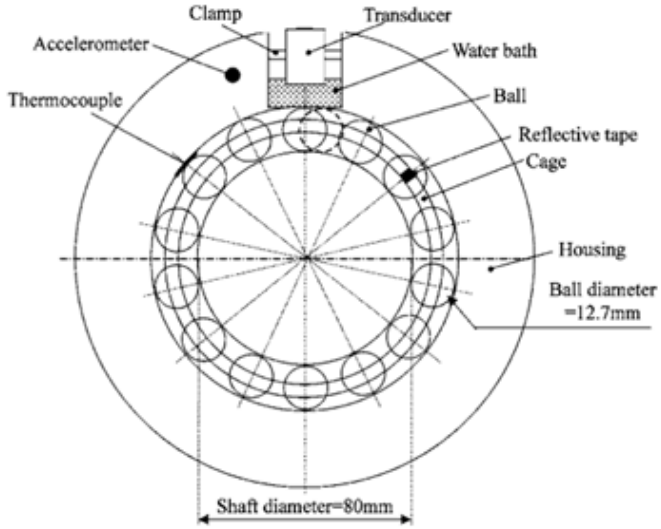

Figure 3.15: A schematic of an immersion transducer coupled with a rolling bearing [43].

Later work bonded transducers directly to parts of the bearing, typically the static raceway. This was far easier to implement, especially on operational bearings, but came with drawbacks which will be discussed in the following sections. An example of a bearing instrumented in this fashion is shown in Figure 3.16.

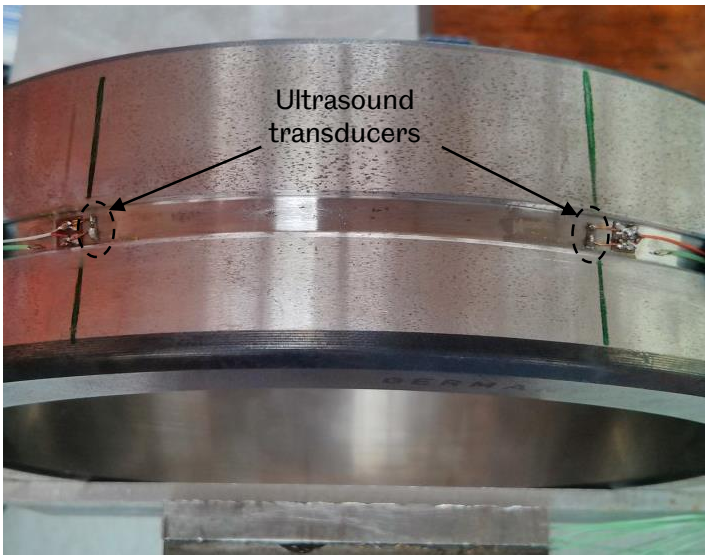

Figure 3.16: An example of transducers (piezoelectric elements) bonded to a rolling bearing raceway. Adapted from [39].

3.7.2 Referencing

Ultrasound is used in rolling element bearings to monitor the interfaces between rolling elements and raceways. When obtaining a reference, rolling bearings have an advantage in that references naturally occur during the operation of the bearings. Steel-air interfaces occur between roller passes which means that any changes in sensor response, which may for example occur due to changes in operating temperature, can be calibrated out.

The most practical way to obtain this reference from an ultrasonic data stream is to obtain the modal waveform [39]. The data processing method is illustrated in Figure 3.17. The data stream refers to a stack of successive windowed A-scans typically windowed around the first reflection, one for each measurement. These are the blue waveforms in Figure 3.17. The single most frequently occurring (modal) value for each data point in the ultrasonic signal (i.e. each point in one of the blue waveforms) across the full data stream is found and used to construct the modal reference waveform. This results in the red waveform where each point is the modal value of the corresponding point all of the blue waveforms. Where signal capture frequency is too low data may require thresholding before finding the modal waveform [93].

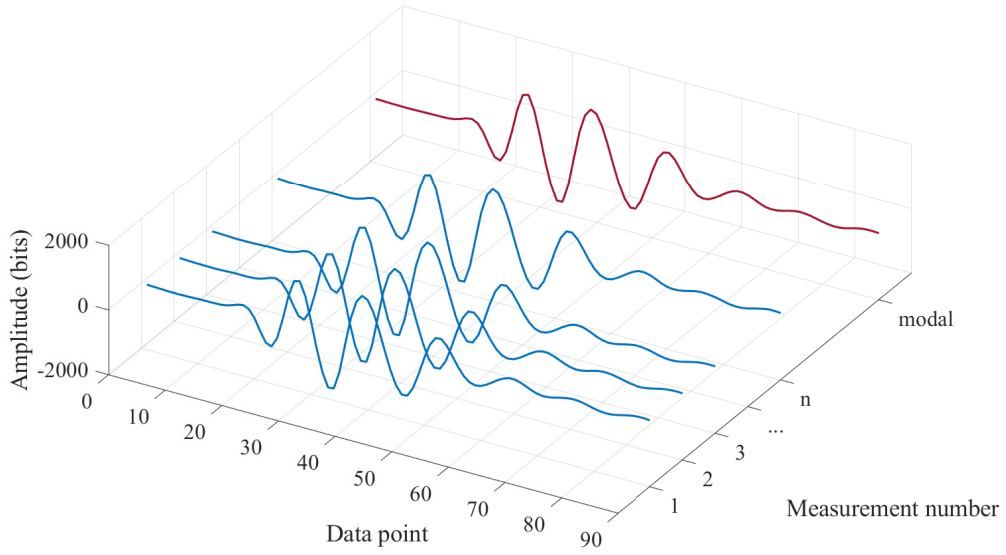

Figure 3.17: Obtaining the modal reference waveform from an ultrasonic data stream. For each of the data points the modal value is found across n measurements to construct the modal reference.

3.7.3 Bearing Speed

An ultrasound sensor on a static raceway can monitor the ball or roller pass frequency in either the time domain, as shown by Figure 3.18, or in the frequency domain, as described in [40]. Roller pass frequency can then be converted to bearing speed through knowledge of bearing geometry, as described in Section 2.2.

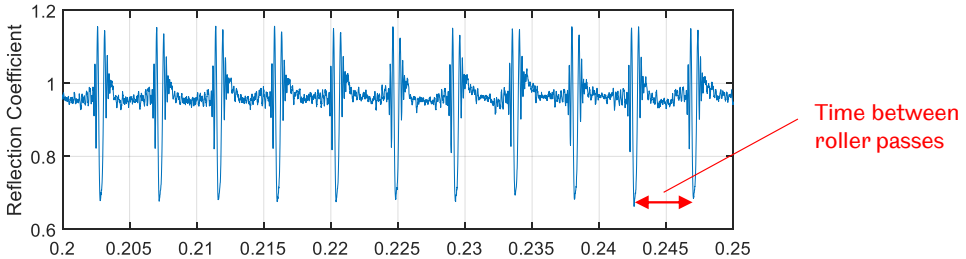

Figure 3.18: Features used for bearing speed monitoring.

3.7.4 Contact Patch Characterisation

Early contact patch characterisation used immersion transducers to focus a beam on the contact patch. Dwyer-Joyce and Drinkwater [94] showed that reflection coefficient plots over-predicted contact sizes at low ultrasound frequencies when compared with

Hertzian calculations. This was caused by a relatively large spot size compared to the contact size, resulting in a blurring effect. Dwyer-Joyce and Drinkwater [94] also demonstrated the possibility of deconvolution to negate some of the blurring using a response function of $\sin(x)/x$ for the transducer, although the majority of the useful information was high frequency low amplitude data which was susceptible to error from noise. Deconvolution was undertaken by dividing the Fourier transform of the reflection coefficient data by the Fourier transform of the response function. The result was then inverse transformed.

Howard [39] analysed the reflection coefficient plots obtained when a cylindrical roller passed over an area of raceway monitored by a single ultrasound transducer bonded to the raceway. Typical examples of these plots are shown in Figure 3.19, labelled with features of interest.

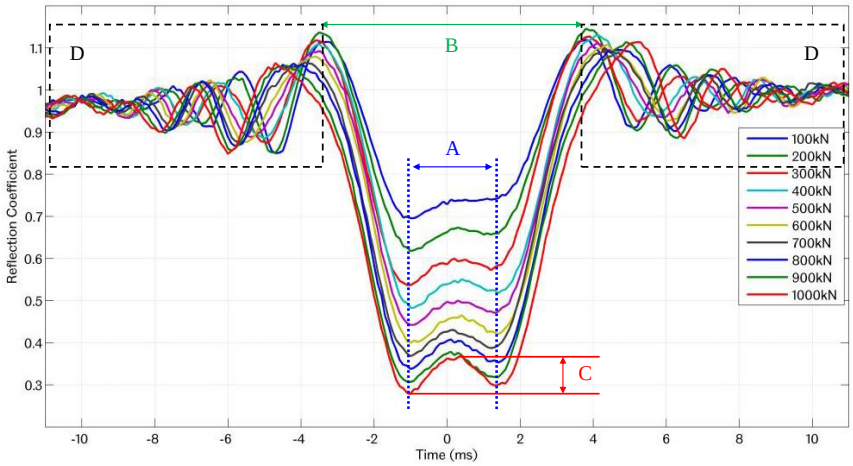

Figure 3.19: Reflection coefficient curves for a single roller pass at bearing loads between 100 and 1000 kN, with features A, B, C and D highlighted. Adapted from [39].

The central W profile (which includes features A, B and C) is enclosed with 'side fringes' (feature D) either side. Of all the features, Feature B is the most promising for determining contact width 2b although the blurring effect of the measurement area of the transducer (as discussed previously) will mean this width will be over-predicted. Were this the only issue with these measurements, then deconvolution of the results may give sufficiently accurate contact patch measurements but unfortunately there

are other drawbacks. The dependency of this feature width on fringe effects makes its use for contact width measurement difficult to justify.

Howard [39] did however suggest a solution to this problem. Figure 3.20 shows how it is possible to observe reflections from the back face of the roller indicated in (b). He suggests that these reflections are more suitable for contact patch characterisation as they are not susceptible to fringe effects.

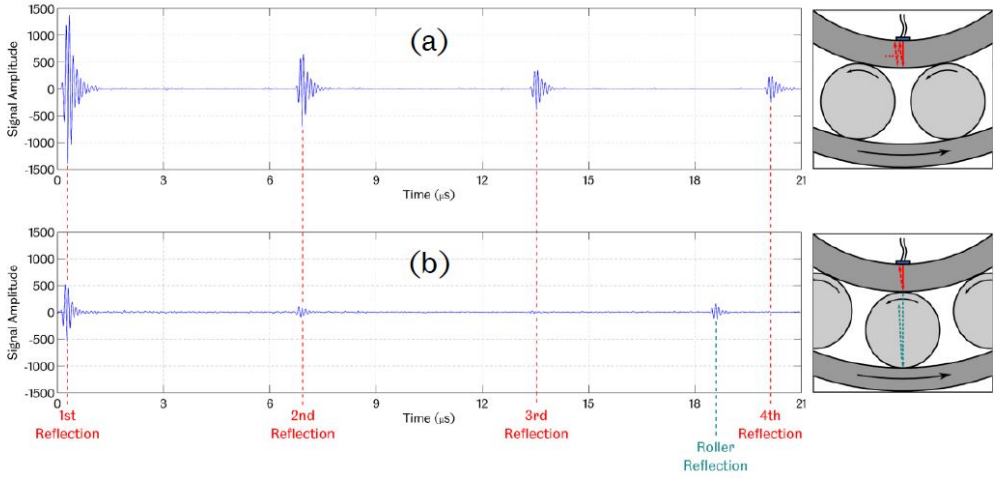

Figure 3.20: Reflections (a) with no roller in the sensor line-of-sight and (b) when a roller is directly aligned with the sensor. From [39].

Howard [39] suggested that:

1. the central peak of the W shape could be caused by either the acoustoelastic effect or the reduced attenuation of sound waves when they are under compressive stress and
2. that the fringe effects were caused by the divergence of the ultrasonic beam through the raceway.

Similar patterns in reflection coefficient were seen by Hunter [77] when monitoring cold rolling of steel, although only one maxima was seen either side of the W shape as opposed to the fringe effects seen by Howard [39]. Hunter [77] showed that when the contact width increased the overall width of the W increased but also that additional minima were introduced in the lower section of the W, as shown in Figure 3.21. Furthermore Hunter [77] observed additional reflections which interfered with the main reflection from the interface and presented compelling evidence that the additional reflections were from the contact exit and entry. He suggested that these additional

reflections are a result of acoustoelastic effects where the high stress gradients at the entry and exit have a lensing effect causing concentrated beams to emanate from the contact entry and exit.

Hunter [77] suggested that the contact width could be defined by taking the distance between the two points where the reflection coefficient plot crosses the point halfway between the minimum value and 1, calculated using Equation 3.18, although the value of R used could be anywhere between the maxima and minima either side of the W shape due to fringe effects.

$$R_{CW} = \frac{1 + R_{min}}{2} \tag{3.18}$$

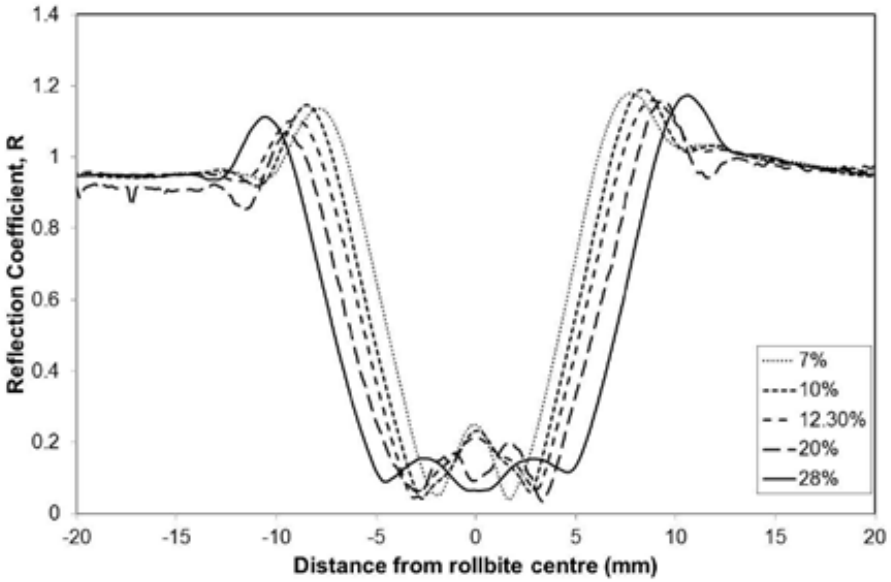

Figure 3.21: Reflection coefficient pattern for varying cold rolling strip elongations. Contact width increases with increased strip elongation. From [77].

These effects are not mentioned in the majority literature where focussed ultrasound beams are used [83, 90, 86, 91] and so focussing may also be an avenue to reducing or removing fringe effects from signals. Wan Ibrahim et al. [88] show how moving in and out of the focal zone causes similar patterns in reflection coefficient to those seen by Howard [39] and Hunter [77] which can be seen in Figure 3.22. Several factors may be at play here, including the spot size of the transducer and the shape of the beam.

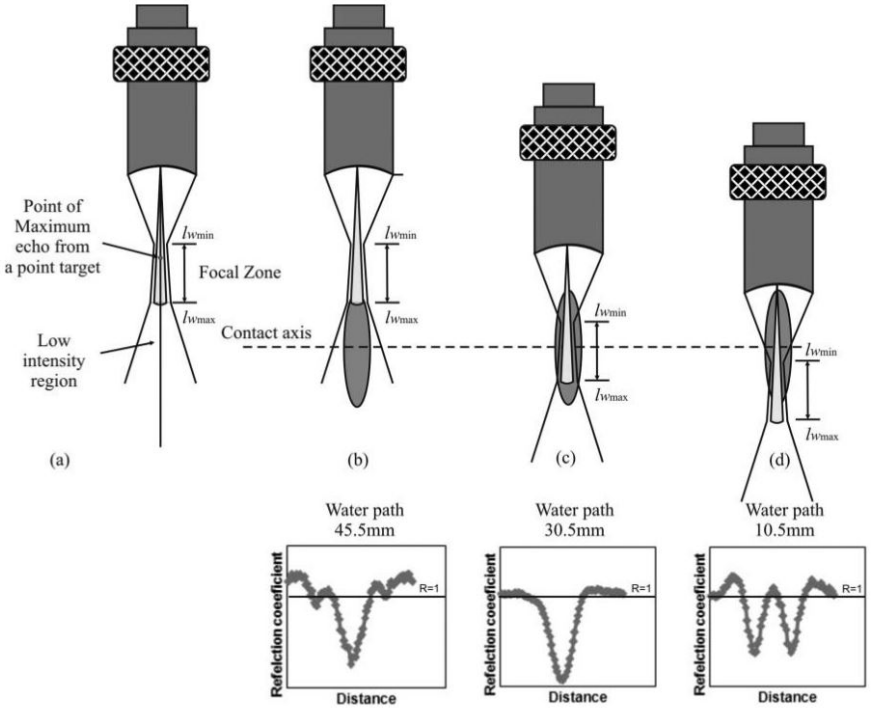

Figure 3.22: The effect of focal length on measured reflection coefficient with a focused immersion transducer. (a) schematic of the transducer beam (b) from the region before the focal zone (c) from the focal zone (d) from the region after the focal zone. From [88].

3.7.5 Lubricant Film Thickness

The method described in Section 3.3.3 has been used extensively to determine film thicknesses in rolling bearings [83, 90, 86, 91], although a lot of work uses focussed ultrasound through use of immersion transducers in water baths coupled to bearings. In the case of permanently bonded sensors, from Figure 3.19 it is clear that the expected film thicknesses distribution, as shown in Figure 2.7, is not predicted by reflection coefficient plots. Two phenomena have been suggested here which prevent the expected distribution being seen by ultrasound. The first is the blurring effect when the measurement zone is not small in comparison to the contact width. The second is the interference in the reflections described in Section 3.7.4, suggested to be caused by either a large beam width or the acoustoelastic effect.

3.7.6 Presence of Lubricant

Another observation made by Howard [39] is that lubricant starvation in a bearing can be identified via ultrasound. In flooded lubrication conditions reflection coefficients of

between 0.9 and 1 are seen between roller passes. In this region reflection coefficients of less than 1 indicate the presence of lubricant on the surface as some of the sound is transmitted to the lubricant layer. The absence of lubricant is indicated by a constant reflection coefficient of 1 between roller passes, as shown in Figure 3.23.

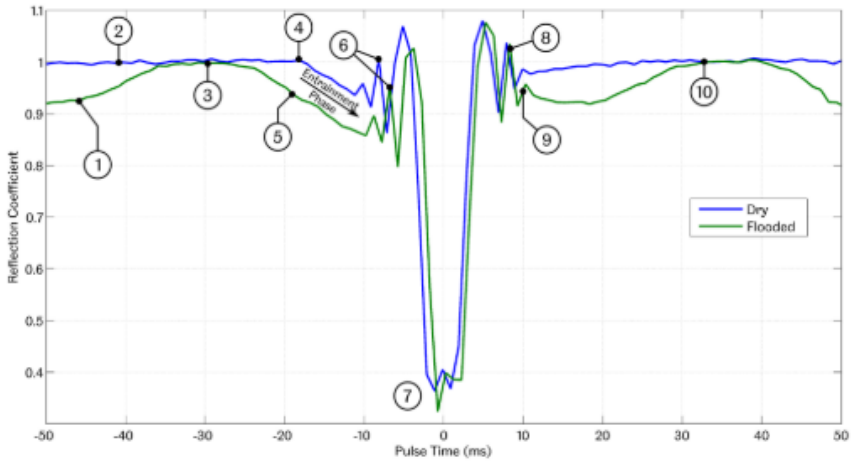

Figure 3.23: The difference in reflection coefficient trends in flooded and dry (starved) conditions. From [39].

These techniques have been further developed by Nicholas et al. [40] where different lubricant reflow mechanisms were observed at low and high speeds of a tapered roller bearing in an operational wind turbine gearbox, and different lubricant reflow speeds were seen for different lubricant viscosities, bearing speeds and loads in a cylindrical bearing test rig [44].

3.7.7 Load

Load monitoring of rolling element bearings using ultrasound was developed by Chen et al. [82] and involves measuring the reduced change in ToF of an ultrasound reflection in a raceway due to the presence of a roller under load. In this situation three factors contribute to the change in ToF: the deflection of the raceway, the change in speed of sound due to the acoustoelastic effect and the apparent phase change in the signal caused by interaction with the interface. The apparent phase change can be eliminated by use of the Hilbert transform and so the deflection can be found through knowledge of the acoustoelastic constant of the raceway material and the change in ToF:

$$\delta = \frac{\Delta ToF c_0}{(1 - L)} \tag{3.19}$$

This deflection can then be converted to contact load through use of a contact model. These techniques have been further developed by Nicholas et al. and applied to an operational wind turbine [40]. Example data is shown in Figure 3.24. This paper used the most up-to-date contact model through application of Houpert's [54] equations which account for transition between point and line contacts.

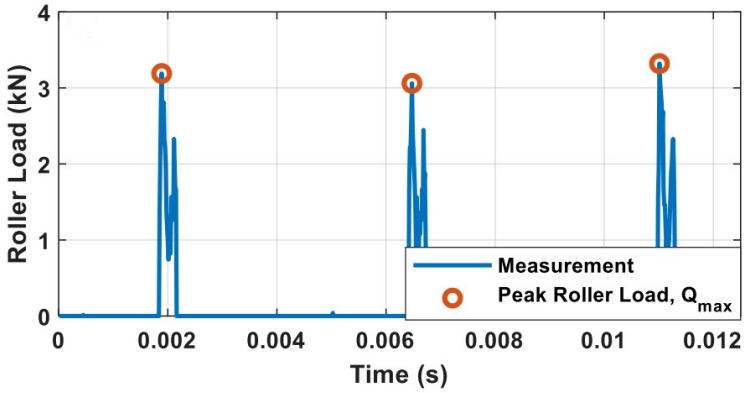

Figure 3.24: Roller load measurements for 3 roller passes in an operational wind turbine high speed shaft TRB. From [40].

Although ultrasonic load measurements line up well with loads applied during testing ultrasound ToF plots often have two peaks, similar to the reflection coefficient plots shown in Figure 3.19 but inverted. This can be seen in Figure 3.25 where change in ToF has been converted to deflection using Equation 3.19. This suggests that the additional reflections which cause fringe effects in reflection coefficient measurement may also interfere with ToF measurements and should be a subject of further investigation.

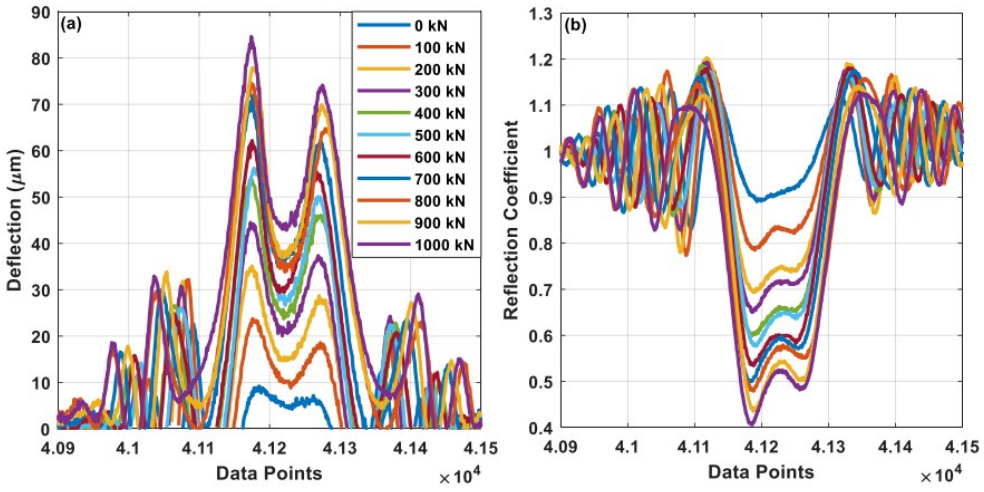

Figure 3.25: Comparison of roller pass (a) deflection and (b) reflection coefficient measurements with varying load. From [41].

To date, load measurement of bearings has mainly focused on one measurement point. There is a gap here of expanding load measurement into distribution within a bearing. Another gap in knowledge is the level of error in ultrasonic load measurements.

3.7.8 Shear Sensors

In other applications shear sensors have been used for viscosity measurements [95, 96] and friction measurements [97], although these techniques do not suit themselves to measurement in bearings in their current state. Shear sensors have also been used in combination with longitudinal sensors for mixed lubrication film thickness measurement in large cold rolling contacts [77]. The theory behind these measurements is that longitudinal sensors measure the combined normal stiffness of both the solid contact and the lubricant layer in mixed lubrication. Shear sensors should only measure the shear stiffness of the solid contact as shear waves are not supported by liquids. The liquid stiffness can therefore be determined by the difference between the longitudinally measured total stiffness and the shear measured solid stiffness. The measured shear stiffness of the solid contact is different to the longitudinal stiffness of the contact, however this can be converted through knowledge of the relationship between the two. The ratio of shear to longitudinal stiffness in steel was calculated to be 0.824 by Hunter [77] and therefore the stiffness of the liquid layer in a mixed lubrication contact can be defined through Equation 3.20.

$$\kappa_{longitudinal_{liquid}} = \kappa_{longitudinal} - \kappa_{shear}/0.824 \tag{3.20}$$

Stiffness can be calculated from either Equation 3.8 or 3.9 using the spring model and therefore film thickness can be calculated using Equation 3.10. What has never been observed using shear ultrasound is a transition from mixed lubrication to fully separated contacts. This should be noticeable as a fully separated contact has no asperity contact and thus the shear reflection coefficient should remain at 1 regardless of the presence of a contact.

Mixed film lubrication has previously been measured in roller bearings with only longitudinal sensors but these studies required calibration measurements or model predictions to predict the portion of the contact stiffness due to solid contact [98, 99] which is not ideal.

3.8 Conclusions

Theory behind the propagation of ultrasound and how it interacts with interfaces was first discussed in this chapter. Key concepts of equipment, transducers and processing techniques necessary for ultrasonic data acquisition were then introduced. Finally, a review of work to date using ultrasonic transducers to monitor rolling element bearings was presented. The current capabilities of ultrasound to monitor bearings was outlined which included lubricant film thickness, lubricant re-flow behaviour and load monitoring. Gaps in technology highlighted were lack of investigation of load distribution, lack of knowledge of error in load measurements and inability to monitor mixed lubricant film thicknesses. The effect of fringe effects on results was also highlighted as a major obstacle.

Chapter 4

Quasi-Statically Loaded Roller Contact Measurements

4.1 Introduction

This chapter contains investigations of a roller-raceway contact using ultrasonic methods. This was done using quasi-static experiments, which is a series of static experiments that replicate dynamic movement, in this case the rolling of an element across a raceway. Figure 4.1 helps to explain this. Instead of the element rolling over the raceway with constant applied load, the raceway was moved in increments and the roller load removed before each movement and reapplied after movement. In this way we can build up the same signal response for the dynamic and quasi-static sensor measurements, albeit with different resolutions. Resolution for the dynamic case depends on PRF and for the quasi-static case depends on raceway movement step size.

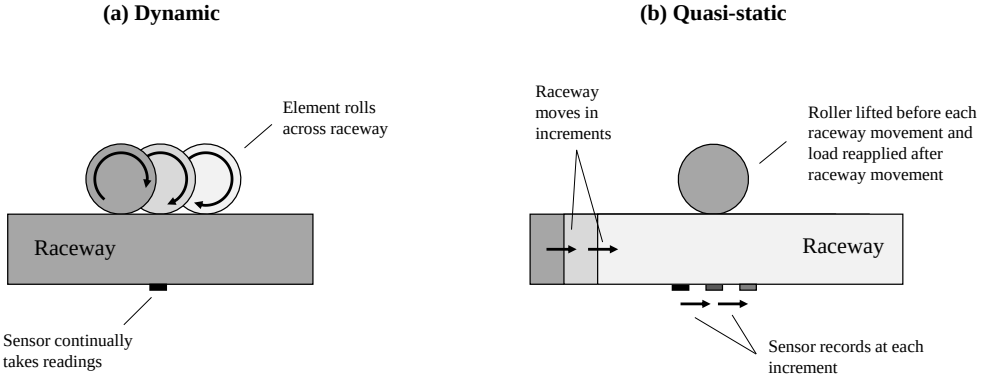

Figure 4.1: A schematic to describe the difference between (a) dynamic and (b) quasi-static experiments.

Quasi-static experiments offered some potential for insights into ultrasonic measurements that dynamic measurements could not. Firstly, the opportunity to make multiple measurements at the same contact point and at the same load offered the opportunity to investigate measurement error through statistical analysis which has not previously been explored. Secondly, non-dynamic measurements offered the opportunity to determine whether fringe effects are a result of some dynamic effect, for example interference between residual reflections from the previous pulse with the signal from the current pulse. Quasi-static experiments also offered the opportunity to see whether fringe effects would occur in a non-lubricated contact. Finally, these experiments enabled a trial of instrumentation with multiple sensors for measurement across the axis of the roller and possible misalignment monitoring with less challenging accessibility requirements than instrumentation of an operational bearing.

4.2 Experimental Apparatus

4.2.1 Roller Static Loading Rig

An existing jig was used which was previously used in conjunction with the *MultiLife* rig described in Section 6 and was repurposed for this work. Computer aided design (CAD) renders of the jig in both fully assembled and part-assembled states can be seen in Figure 4.2. The jig enabled a single roller to be pressed against the inner raceway of an NU2244 cylindrical roller bearing, the chosen test bearings for the

MultiLife rig. The parameters of the NU2244 bearing are shown in Table 4.1. The original purpose of the jig was to allow overloading of the raceway prior to testing on the *MultiLife* rig in order to 'seed' damage and induce accelerated bearing failure. The jig has since been modified to allow ultrasonic monitoring of the contact through the addition of a slot on the bearing carrier, approximately 10 mm wide and 3 mm deep. This allowed space for sensors to be bonded to the inner face of the raceway and cables to be routed out of the jig. By indexing the raceway through several known positions, a quasi-static ultrasonic dataset of the roller-raceway contact could be acquired.

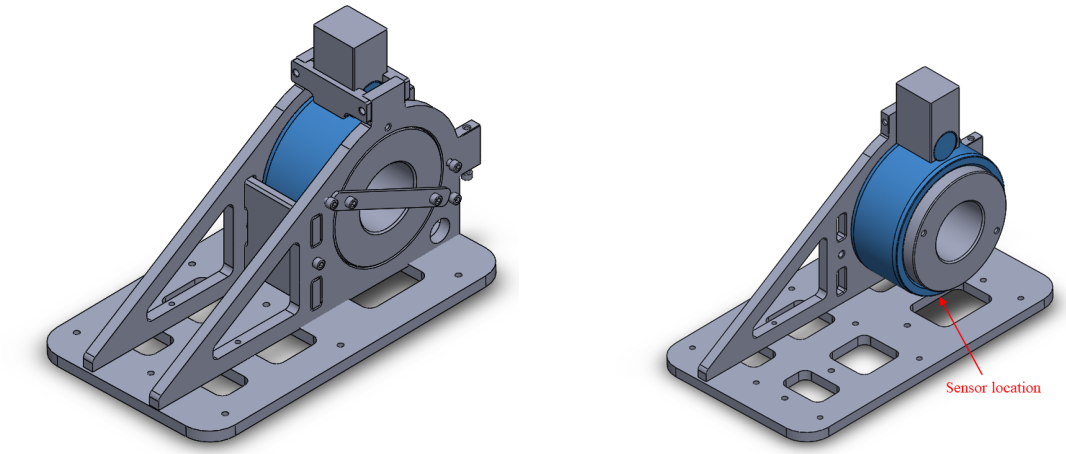

(a) Fully assembled (b) Part-disabssembled

Figure 4.2: Seeding jig CAD renders. The inner raceway and a roller from an NU2244 bearing are highlighted in blue.

Bearing Parameter	Symbol	Value
Inner raceway diameter	D_i	259 mm
Pitch diameter	D_m	313 mm
Width	-	108 mm
Roller diameter	D_R	54 mm
Roller length	l	82 mm
Number of rollers	Z	15
Dynamic load rating	C_ω	1600 kN
Fatigue load limit	C_u	250 kN

Table 4.1: Bearing parameters for the NU2244 cylindrical roller bearing used in the *MultiLife* rig.

4.2.2 Instrumentation

Seven longitudinal sensors were bonded to the raceway in the configuration shown in Figure 4.3. The number of sensors was selected so that one sensor was aligned with the centre of the roller (resulting in an odd number of sensors) and additionally so that all sensors could be used on 8 channel acquisition hardware. The number of channels was limited by the size of the slot in the seeding jig for cable routing; seven cables was close to the limit for standard gauge coaxial cable.

Sensors were aligned such that the centre point of the middle sensor was positioned at the centre of the raceway and the sensors were spaced axially from the centre line at 11 mm even spacing. Sensor positions marked on the raceway prior to instrumentation can be seen in Figure 4.4 (a). Sensors were cut to 5x1 mm strips and bonded to the raceway with strain gauge adhesive. Custom instrumentation jigs which matched the curvature of the raceway were used to hold the sensors in place during the curing process. These were made from EN31 steel and curved surfaces were wire EDM cut. Jig drawings can be seen in Appendix A.

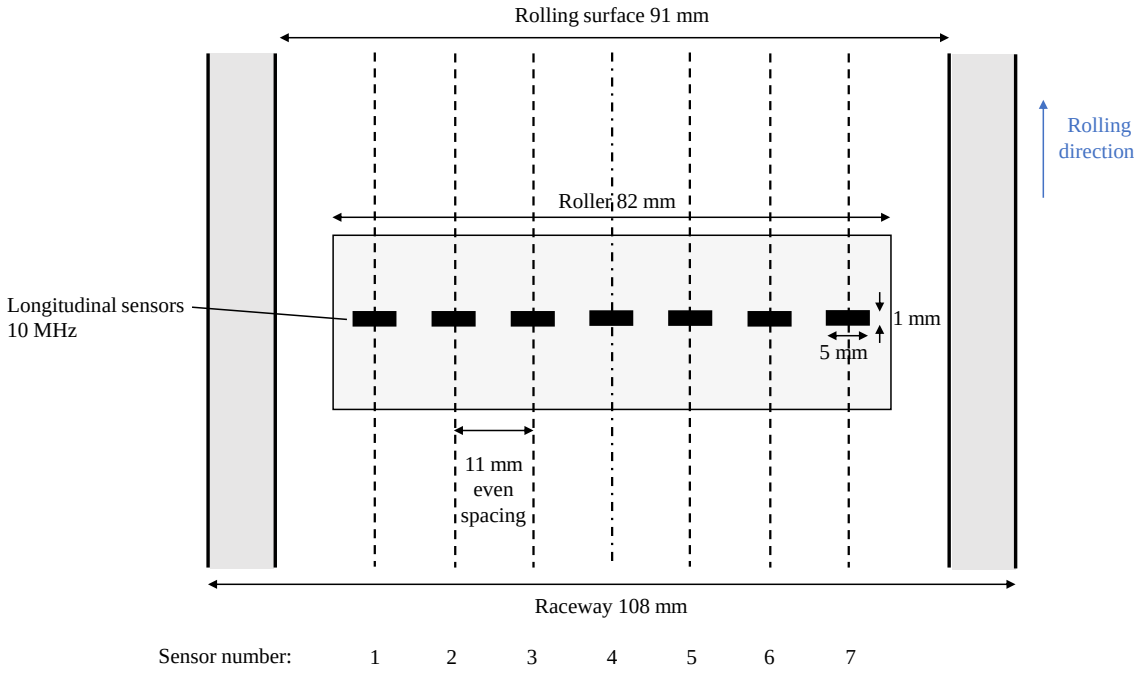

Figure 4.3: Seeding jig instrumentation schematic.

Coaxial cables with SMB connectors were then attached to the sensors. Live terminals were soldered to the electrode of the sensors and grounds were epoxied to the raceway.

Cabled sensors were then potted with epoxy potting compound to protect them from damage when the raceway was installed in the seeding jig. The instrumented raceway is shown in Figure 4.4 (b). This image also shows green 1 mm spaced markings which were used to aid the alignment and indexing of the contact with respect to the sensor array. Intermediate steps of a very similar instrumentation can be seen in Figure 6.4.

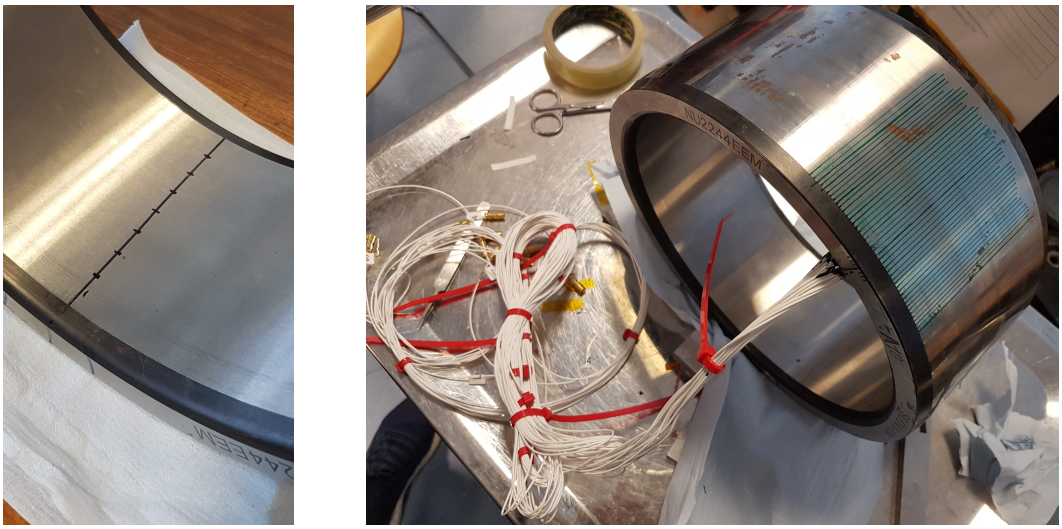

(a) (b)

Figure 4.4: (a) Sensor locations for the seeding jig instrumentation marked on the bearing raceway prior to instrumentation (b) Instrumented bearing for the seeding jig. Green 1 mm spaced markings which were used to aid the alignment and indexing of the contact with respect to the sensor array can also be seen.

4.2.3 Acquisition Hardware

This testing used a Film Measurement System (FMS) for ultrasonic acquisition. For measurement system basics and terminology refer to Section 3.5. The FMS is a single-unit ultrasonic measurement system from *Tribosonics Ltd.* It is compromised of a PC with two bespoke PCI cards, one for the UPR and one for the digitiser, as shown in Figure 4.5. The two PCI cards are used through LabVIEW interface software. The UPR uses an inverse top hat shape excitation pulse which has tunable voltage (up to 300 V), pulse width (equivalent 1-20 MHz) and PRF (up to 80 kHz). It has a built-in multiplexer which splits the PRF across the number of active channels, up to a maximum of 8. The digitiser samples data to a resolution of 12 bits in amplitude and 10 ns in the time domain.

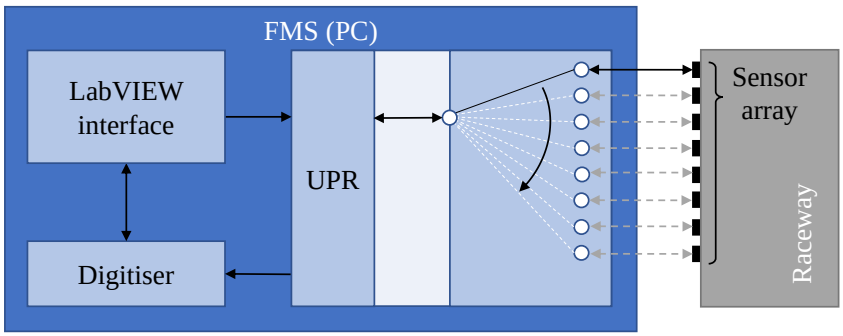

Figure 4.5: FMS schematic.

4.2.4 Methodology

Compression testing was carried out on a 1000 kN hydraulic machine. The seeding jig was aligned centrally on the test bed and a spherical seat was attached to the top head to minimise any effects of misalignment. The load applied was accurate to ±0.05 kN. The jig in the test rig can be seen in Figure 4.6.

Figure 4.6: Seeding jig in test rig.

For each index position, ultrasonic measurements were taken from 0 - 300 kN in 50 kN increments, 0 kN being the reference case with no roller present. The raceway was indexed in 0.5 mm increments over a 14 mm window, from -7 mm to +7 mm

alignment of the sensor array and the centre of the contact patch. A total of 90 tests were completed: 6 per position, or 15 per load.

FMS settings were tuned to the 10 MHz sensor frequency and to maximise the amplitude of the first reflection within the digitiser range. PRF was set at 125 Hz and each data set was captured for 2 s, meaning a total of 250 A-scans were taken for each data set. This low PRF also gave plenty of time for signal attenuation between pulses, ensuring that no residual signals from the previous pulse would be present when the subsequent pulse was triggered.

Data was processed to obtain reflection coefficient (R) and change in ToF as described in Section 3.6. To assess the variability of ultrasound signals each reference A-scan was compared to each measurement A-scan. 250 A-scans were taken for each load case (including the reference case) and so 62,500 pairs of A-scans were compared for each load and sensor location.

The variation in each of these data points incorporated several sources of error. These included noise in the signal, digitisation error, error implicit in processing methods and variation in load during the 2 s capture period. The error caused by load variation can be calculated through Equation 3.19. Using deflection values from Appendix B, where $L = -2.26$ and $c = 5960m/s$ [44], this error equates to approximately 0.012-0.025 ns, which is a low but not insignificant proportion of the overall variation (3-13%), as will be shown the following section. The following estimates of measurement variability were therefore slight overestimates.

Deflection was converted to change in time of flight (ΔToF) using Equation 3.19 where L = -2.26 and c_0 = 5960 m/s [44]. Load was calculated using Houpert relationships (Equations 2.20 - 2.27) and the geometry and material properties described in Table 4.2:

Material property / geometry	Symbol	Value
Young's modulus (GPa)	$E_A = E_B$	210
Poisson's ratio (1)	$\upsilon_A = \upsilon_B$	0.3
Roller radius (mm)	R_{Ax}	27
Raceway radius (mm)	R_{Bx}	129.5
Axial roller curvature (m)	R_{Ay}	17.15 [44]
Axial raceway curvature (mm)	R_{By}	-198.81 [44]
Roller length (mm)	l	82

Table 4.2: Material properties and geometries for Houpert deflection calculations.

4.3 Results & Discussion

4.3.1 Trends in Measurement Parameters

4.3.1.1 Reflection Coefficient Trends

The frequency response of the sensors is shown in Figure 4.7. It can be seen that the central frequency of the sensors is around the intended frequency of 10 MHz, with some sensors having slightly higher central frequencies. The -6 dB bandwidth of the sensors (50% drop from peak amplitude) was around 8 to 13 MHz and the -20 dB bandwidth (90% drop from peak amplitude) was around 5 to 15 MHz.

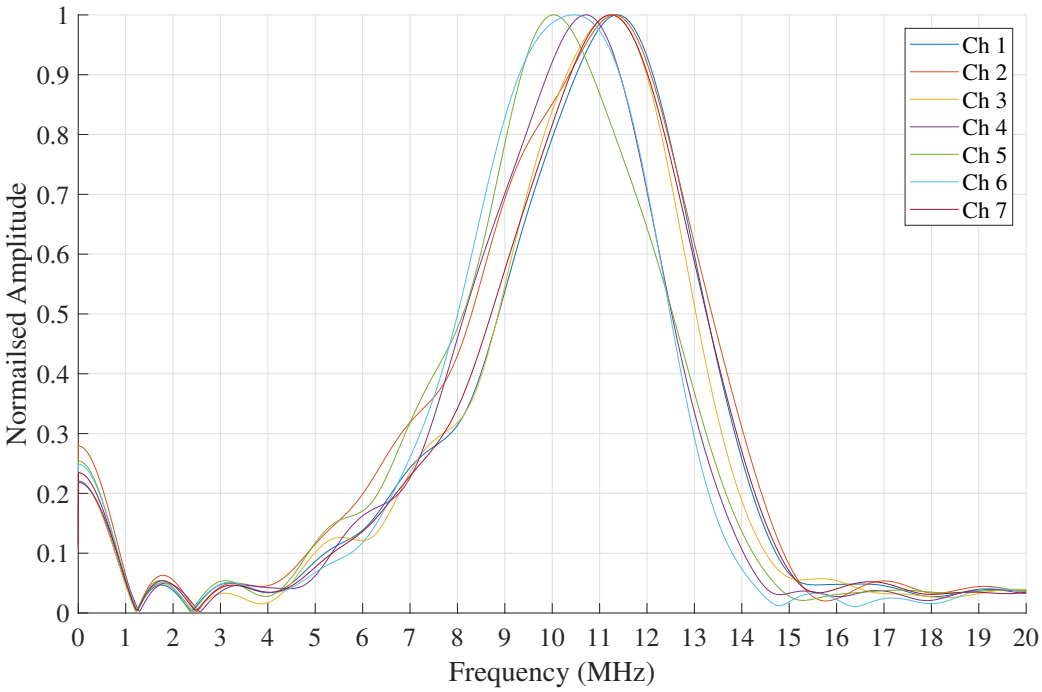

Figure 4.7: Sensor frequency responses for all 7 sensors from the reference signals when the sensor was aligned with the centre of the contact.

Spectrograms of reflection coefficient for both a low load contact and a high load contact across the -20 dB bandwidth can be seen in Figures 4.8 and 4.9 for the central sensor (channel 4) at 50 kN and 300 kN respectively. The first observation here was that fringe effects can be see in both spectrograms, but were more clearly seen in 4.8 as the yellow bands. Fringe effects were also present across the full range of frequencies.

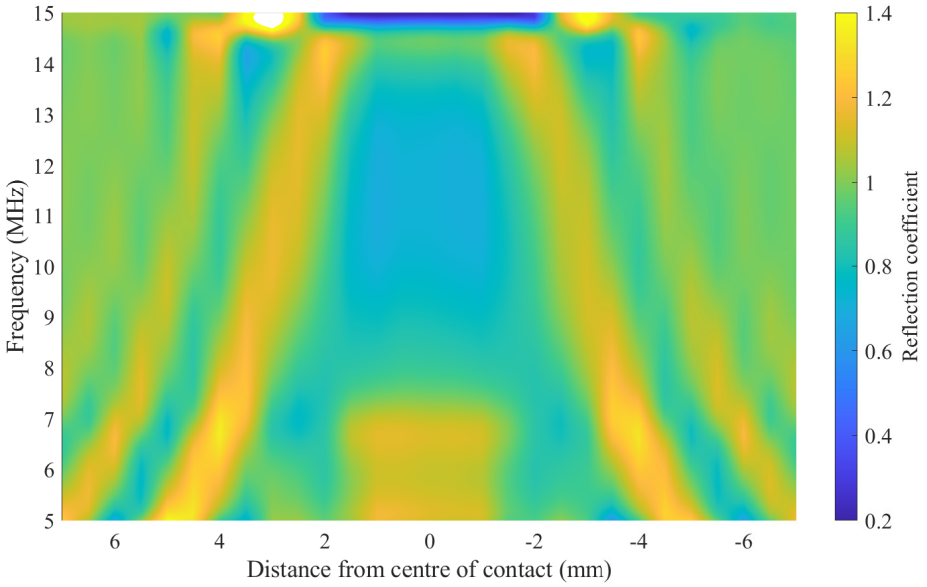

Figure 4.8: Spectrogram, 50 kN, channel 4 (centre sensor).

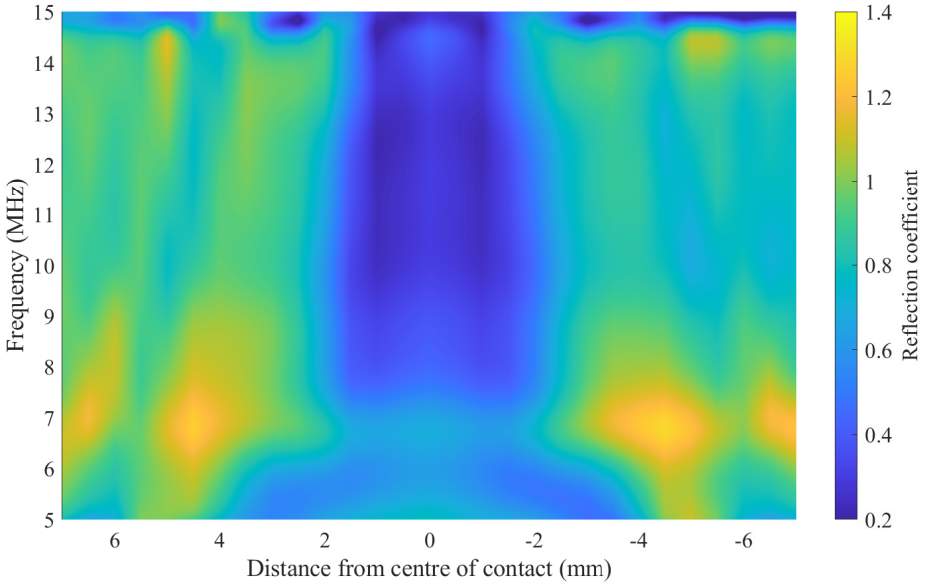

Figure 4.9: Spectrogram, 300 kN, channel 4 (centre sensor).

One sensor (4) and one frequency (10 MHz) were selected in order to more easily show fringe effects over the full range of loads applied (see Figure 4.10). Fringe effects are clearly present across the full range of loads. Reflection coefficient decreases with increasing load in very similar trends to those seen in dynamic experiments [39]. The

major discrepancy is that reflection coefficient on the negative side of the contact is offset from 1 with increasing load, whereas on the right side there is no obvious offset.

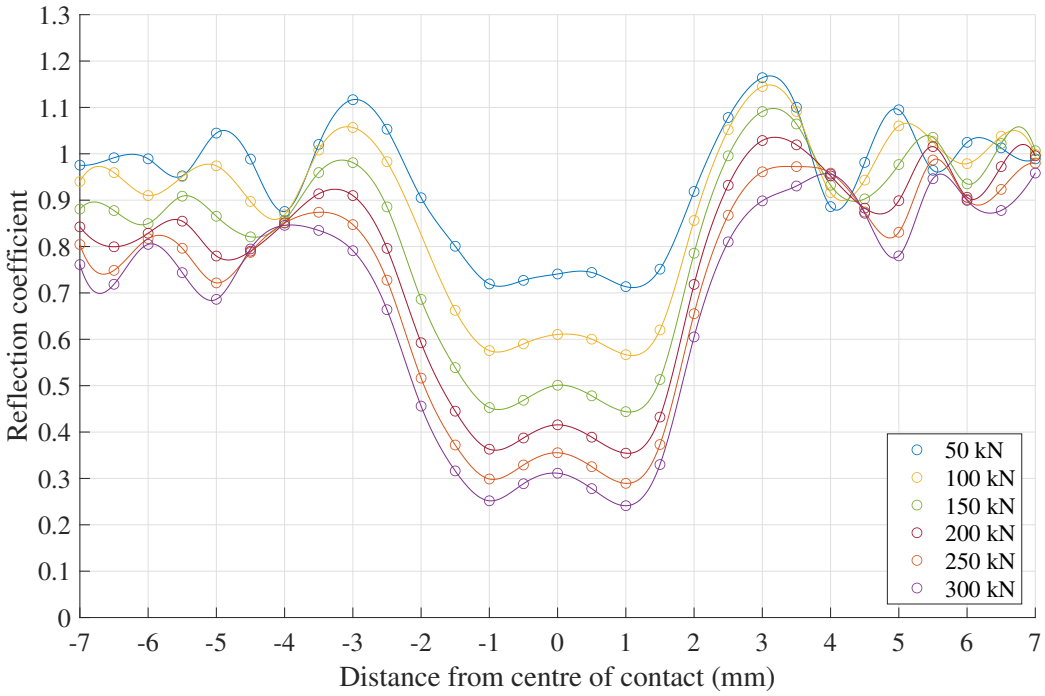

Figure 4.10: Reflection coefficient data from sensor 4 across all measured loads. The fitted lines are cubic spline interpolations of the results.

It was initially thought that this offset was due to temperature changes in the raceway across the duration of the tests. References were taken in each position but prior to the 50 kN and the remaining measurements followed in 50 kN increments. It therefore makes sense that the offset increased with load and perhaps also that the negative position readings had a larger offset as they were taken earlier in the day when the ambient temperature was cooler and the room may have been heating up at a faster rate. This has, however, been proven not to be the case by Figure 4.11 where the reference has been shifted such that the measurements were compared with the reference from the following roller position, almost straight after the 300 kN reading.

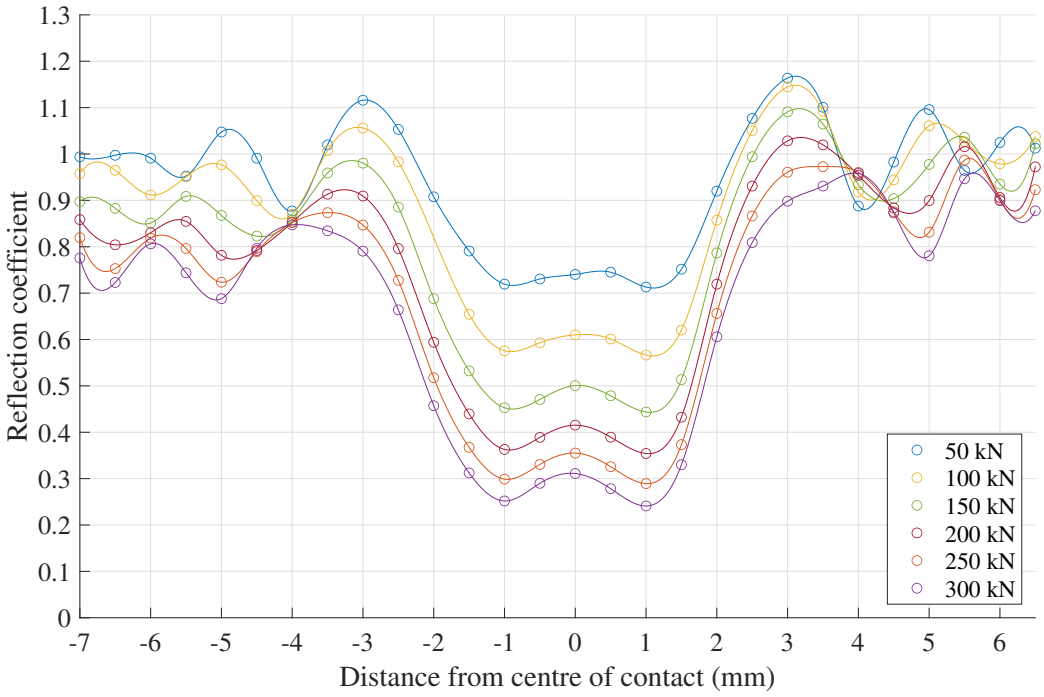

Figure 4.11: Reflection coefficient data from sensor 4 across all measured loads with shifted reference. The fitted lines are cubic spline interpolations of the results.

If the hypothesis described were true then 300 kN measurements would have an R value closer to one and the rest would be shifted upwards such that the 50 kN reading would be the furthest from one. This was not the case. In fact, the results looked almost identical evidencing some other factor affecting the results. One explanation could be the directivity of the beam not being perpendicular with the raceway, as depicted by Figure 4.12, which could be caused by the sensor not being perfectly perpendicularly bonded to the raceway. This is unlikely though as one would expect to see the signal affected on both sides of the contact. What is more likely is that some surface damage affected the results. Due to a shortage of stock of the raceway inner bearings from previous testing, an opened bearing was used which had some areas of corroded surface as shown in Figure 4.4(b). Care was taken to test an area with as little imperfection as possible but complete elimination from the test area was not possible.

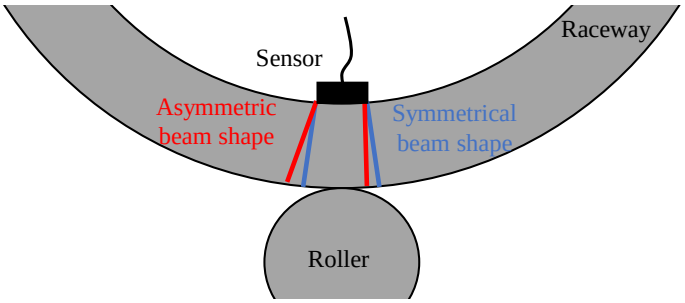

Figure 4.12: Asymmetric beam from ultrasound sensor.

Figure 4.13 shows a surface plot of reflection coefficient against sensor number and distance from the centre of the contact. Without the presence of fringe effects this would be an excellent way to approximate contact patch dimensions, however this is more difficult where they are present. This contact patch appears not to have much misalignment - reflection coefficient trends are reasonably uniform across the sensors with minima which increased towards the edges of the roller. This was expected due to the logarithmic profile on the rollers. One noticeable exception to this trend was sensor 3. This sensor had a noticeably higher minimum reflection coefficient which persisted across all measured loads, as shown in Figure 4.14. This could have a few causes including debris trapped in the contact, corrosion of the raceway or roller in this region, misalignment of this sensor and insufficient resolution accuracy in the rolling direction to catch the minima.

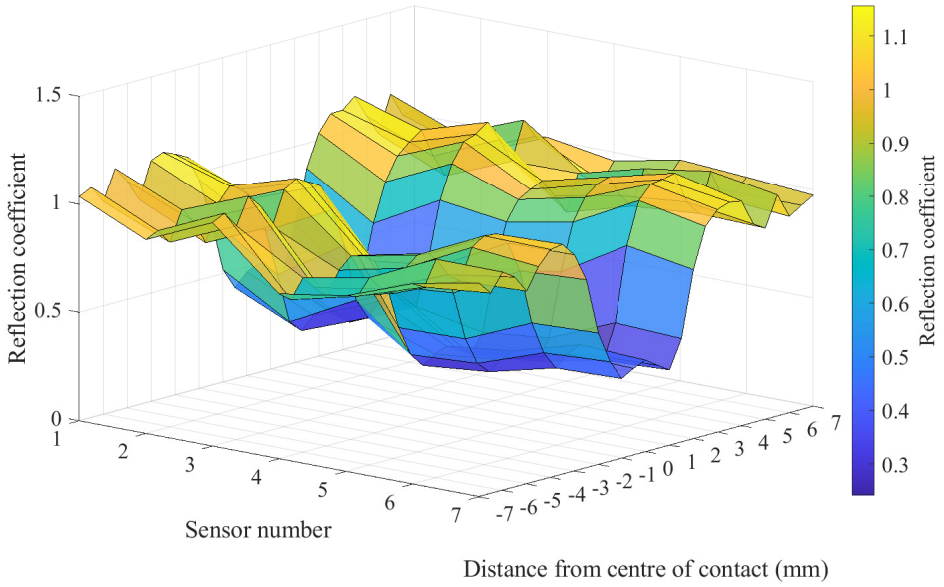

Figure 4.13: Reflection coefficient across all 7 sensors at 300 kN load.

Of course, it may have been the case that sensor 2 was the outlier and the contact was slightly misaligned towards sensor 7, or a combination of both sensor 2 and 3 experiencing influence form unknown factors. Another interesting trend is that of sensor 7 which more closely approaches the value of sensor 6 with increasing load. This may indicate the onset of edge loading on the sensor 7 end of the raceway as sensor 2 does not follow this trend with respect to sensor 1.

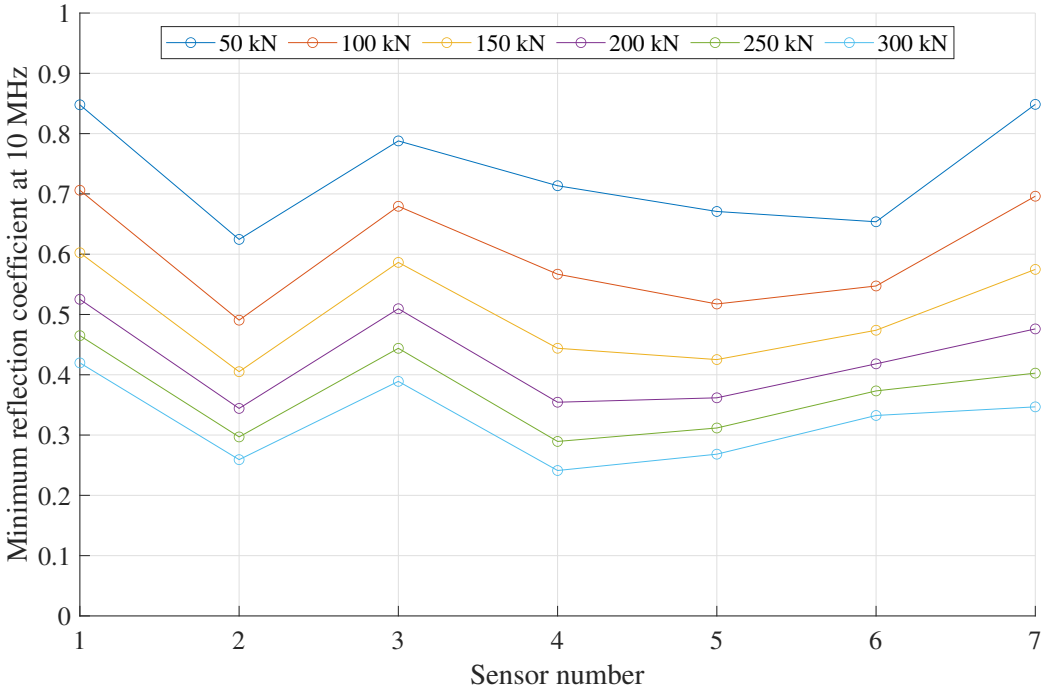

Figure 4.14: Minimum reflection coefficient across all sensor locations and loads.

Figure 4.15 shows estimations of ultrasonically measured contact widths for each sensor across the measured loads compared with predictions from elliptical contact width calculations using Equations 2.11 and 2.12. The ultrasonically measured contact width was estimated by finding the two points at which the minimum reflection coefficient value returned halfway from its minimum in Figure 4.10 but across all channels. The values were found through linear interpolation between the two neighbouring data points at the half-minimum values (calculated using Equation 3.18). Figure 4.16 helps to visualise this process.

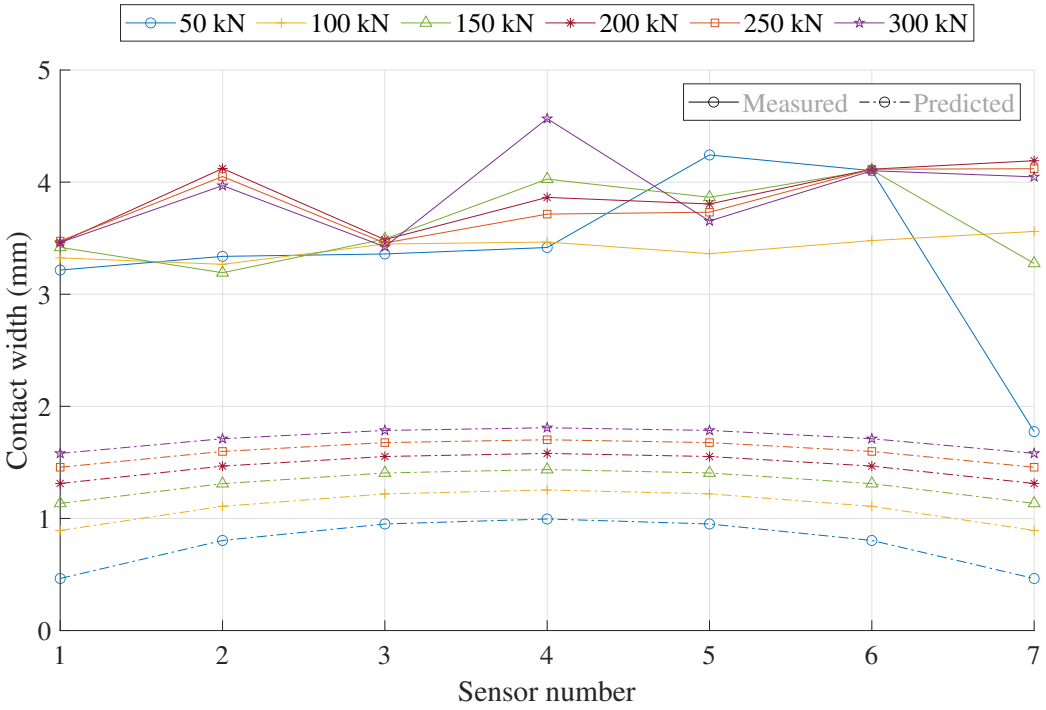

Figure 4.15: Estimated ultrasonically measured contact width across all sensor locations and loads compared with contact width predictions from elliptical contact calculations.

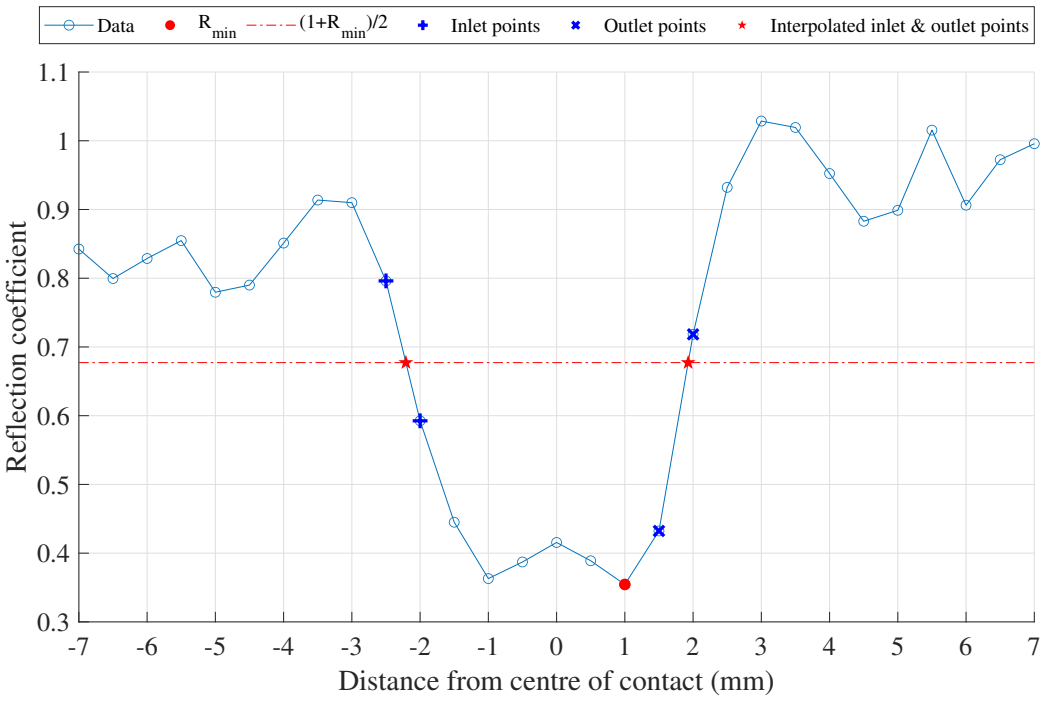

Figure 4.16: Contact width processing mechanism for a single roller pass.

At first glance Figure 4.15 looks chaotic and not very informative, but this in itself gives us some useful information. Measurements showed contact widths in the region of 3.5 to 4.5 mm whereas Hertzian calculations estimate that the contacts should have been in the region of 0.8 to 1.9 mm (see Appendix B). Measurement approximations were around three times the expected value and do not seem to follow any obvious trend with load or sensor position. This over-prediction was likely due to the transducer beam width being larger than the contact size. Measurement may improve with increased resolution in the rolling direction but it is also likely that the cause of fringe effects significantly compromised the results.

4.3.2 Time of Flight Trends

Much the same as Figure 4.10, Figure 4.17 shows the trend of change in ToF (ΔToF) with applied load. These measurements were clearly also effected by the cause of fringe effects, in fact the trends were remarkably similar to those seen in Figure 4.10 if they were inverted. This is significant as it suggests that the same phenomenon that caused fringe effects in reflection coefficient measurements also caused these distortions in change in ToF.

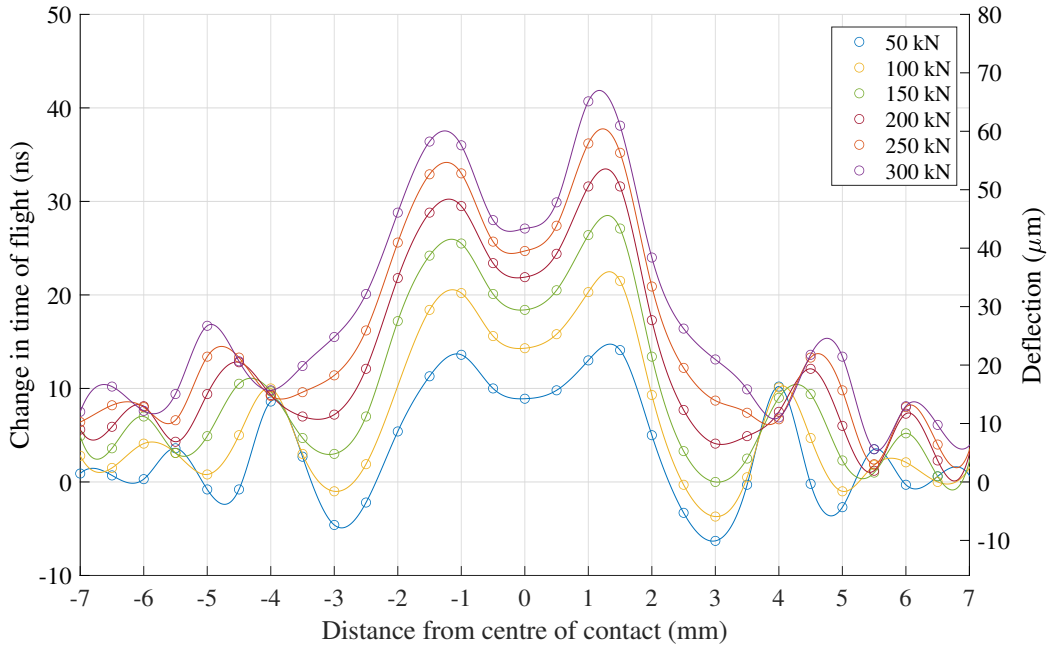

Figure 4.17: Change in time of flight data from sensor 4 across all measured loads, also converted to deflection using Equation 3.19. The fitted lines are cubic spline interpolations of the results.

Figure 4.18 shows the deflection values in Figure 4.17 converted to load using Equations 2.20 - 2.27. The peak values were approximately 1.67 times lower than the applied load which is a substantially difference. One possibility is that the low resolution in the rolling direction meant that peak ΔToF measurements were artificially low. The difference may also be attributed to the fact that Houpert's equations were developed for a raceway-roller-raceway configuration and not a raceway-roller-roller holder configuration and thus are not valid in this situation due to the difference in load distribution through the roller, although the author wouldn't expect this to make such a significant difference. Misalignment of the contact could also have affected the results. Nicholas has shown reasonable agreement between ultrasonically measured deflection and applied deflection (through knowledge of applied bearing load) with this same bearing and technique on an operational test rig [44]. Chen et al. [82] also showed good agreement between applied and ultrasonically measured load on a different bearing. It is interesting however that the presence of fringe effects in reflection coefficient trends significantly effects the validity of results but does not in time of flight measurements. It is clear that better understanding of the cause of fringe effects would be beneficial.

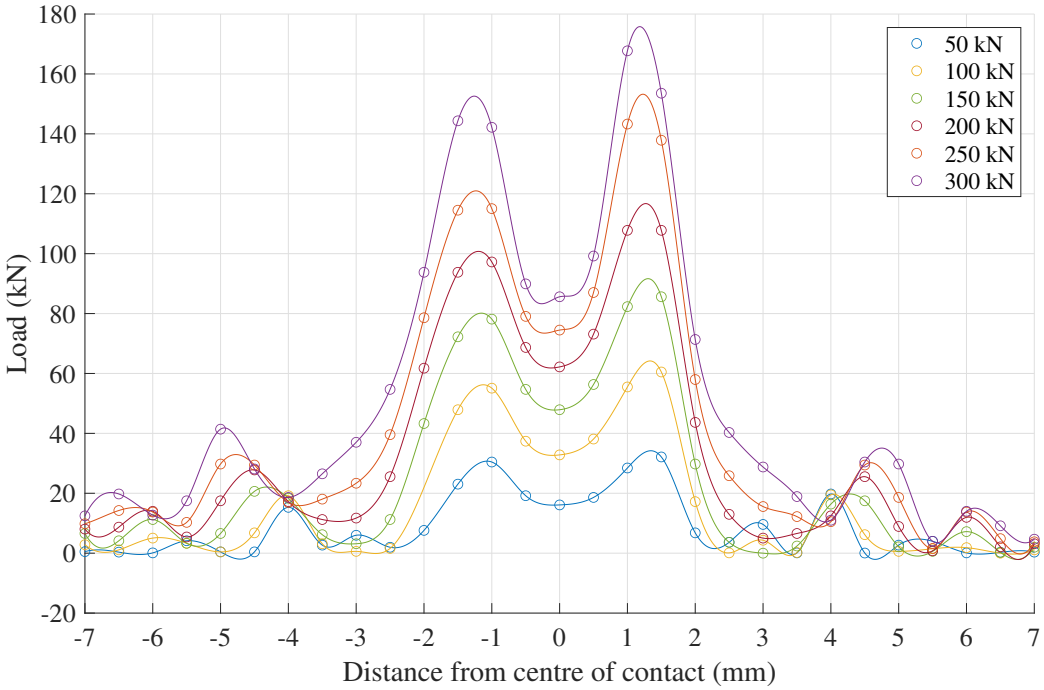

Figure 4.18: Predicted load data from sensor 4 across all measured loads. The fitted lines are cubic spline interpolations of the results.

Change in time of flight across all 7 sensors at 300 kN load is shown in Figure 4.19.

When compared with Figure 4.13 the anomaly at sensor 3 was not present, suggesting that change in time of flight was a more robust way of assessing contact misalignment. Figure 4.20 shows a clearer indication of contact misalignment. This seems to suggest a slight misalignment towards sensor 7.

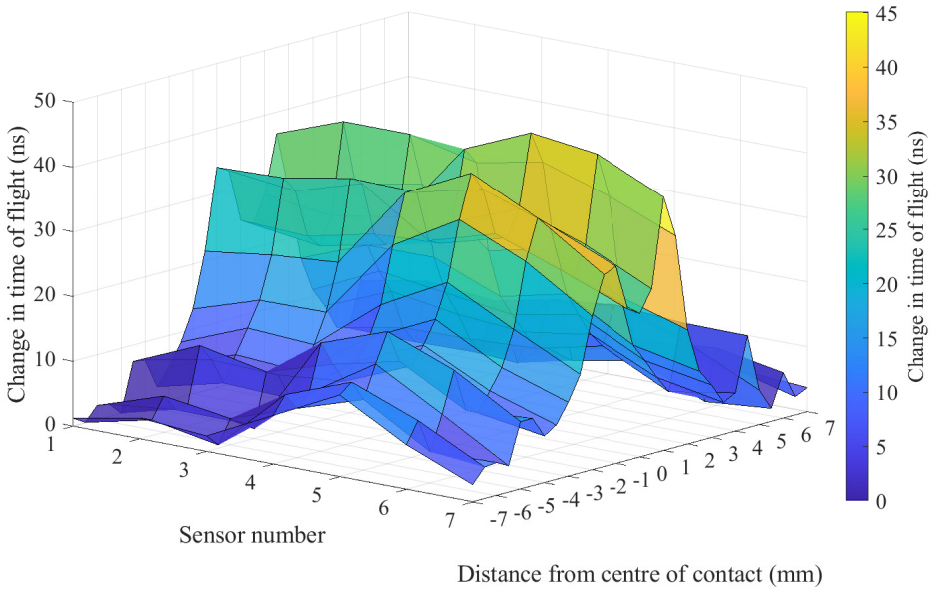

Figure 4.19: Change in time of flight across all 7 sensors at 300 kN load.

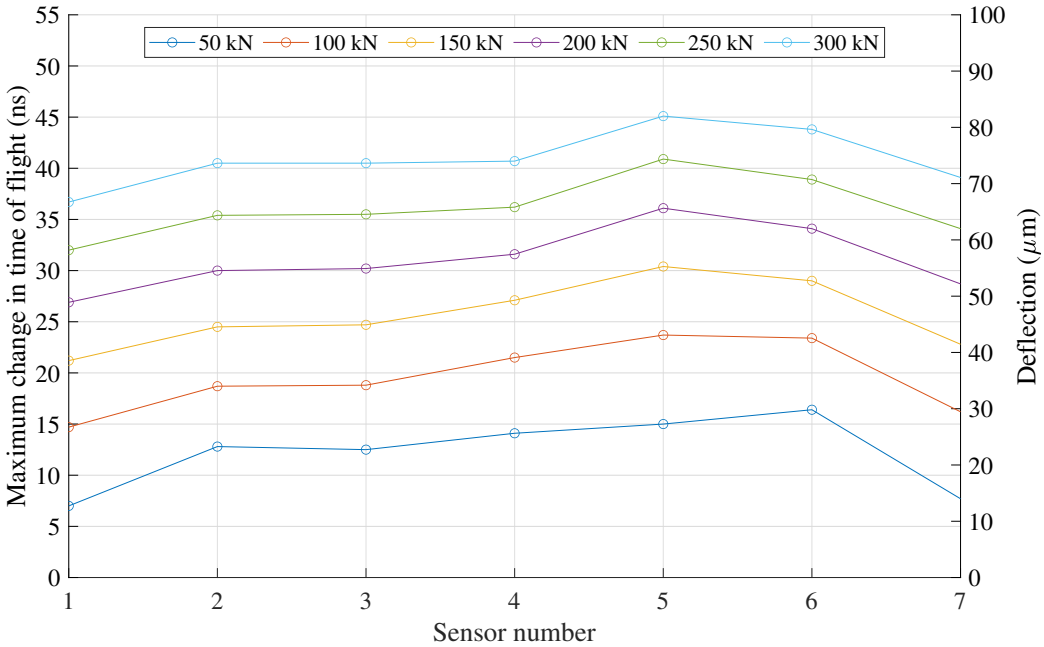

Figure 4.20: Maximum change in time of flight across all sensor locations and loads, also converted to deflection using Equation 3.19.

4.3.3 Variability in Measurement Parameters

With 250 repeats for both the measurement and reference signal a large quantity of comparisons could be made to obtain both reflection coefficient and change in time of flight - 62,500 comparisons for each load and sensor to be exact. This allowed robust statistical analysis on the amount of variability in both of these measurement parameters to be undertaken. Data from multiple locations was taken for both reflection coefficient and time of flight data. These were across all 7 sensors and at 5 different different distances from the centre of the contact in the rolling direction, selected as features of interest across the full half-range of data collected. From Figure 4.10 it can be seen that 0.0 mm was at the centre, 1.0 and 1.5 mm were close to the minimum value, 2.5 mm was approximately the edge of the W shape and 5.0 mm was part way through the fringe effects. These also correspond with similar (inverted) features in Figure 4.17. Taking data from these five locations allowed a greater range of variability to be analysed than looking at maximum and minimum points in isolation.

Arguably, analysing values across this full range did not follow the normal data processing route where the minima or maxima would be used to further calculate film thickness from R or load from ΔToF, however the processing method from raw A-scans is exactly the same. The effect of fringe effects on variability is also of interest and therefore analysis across the full contact gave valuable insight here.

4.3.3.1 Reflection Coefficient Variability

Before analysis could be conducted, the normality of the data required checking to ensure the techniques used were appropriate to the datasets. Data was both checked visually, as shown in Figure 4.21, and through one-sample Kolmogorov-Smirnov tests, all of which confirmed normal distribution of the data with a 5% significance level.

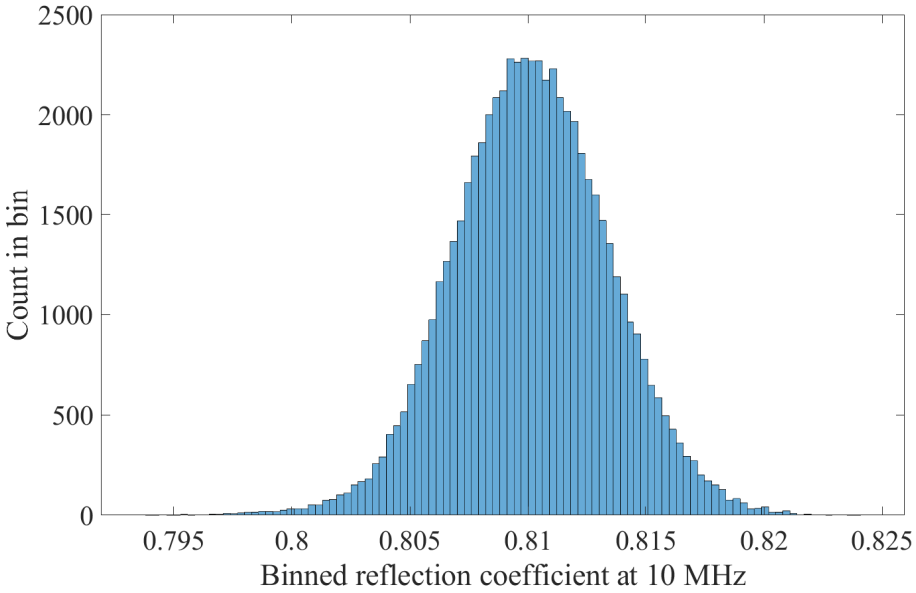

Figure 4.21: Example histogram of data distribution for one set of reflection coefficient comparisons. Data set was 300kN, ch4, position 0.0.

Figure 4.22 shows mean against standard deviation values of reflection coefficient for each of the data sets. The standard deviation of reflection coefficient increased with mean value for reflection coefficient and scatter of this data was similar across all five distances from the centre of the contact. The increasing standard deviation with mean R is the opposite of what would be expected if this error were dominated by signal to noise ratio (SNR), as the SNR would decrease with lower reflection coefficient values. The cause of this is not clear but it was possibly a result of the cause of fringe effects.

Figure 4.22 shows the same relationship but with standard deviation as a percentage of the mean. This shows that variability in reflection coefficient is fairly insignificant over the measured values of R, although this may become more of an issue at much lower R values which would be expected if fringe effects were not present.

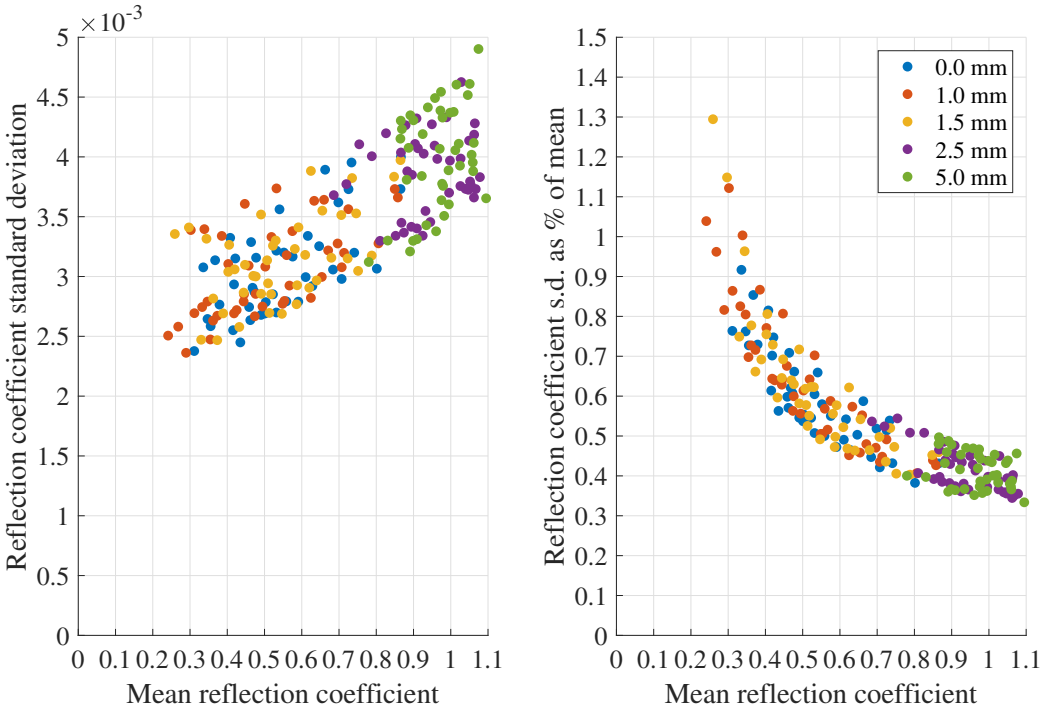

Figure 4.22: Comparison of mean and standard deviation value (left) and percentage of the mean (right) reflection coefficients.

Multiples of standard deviations from a mean can be used to create prediction intervals (PI) for how far points are likely to lie from the mean value. Figure 4.23 shows three prediction intervals at one, two and three standard deviations which create 68, 95 and 99.7% either side of the mean. Results show fairly acceptable levels of predicted error in measurements.

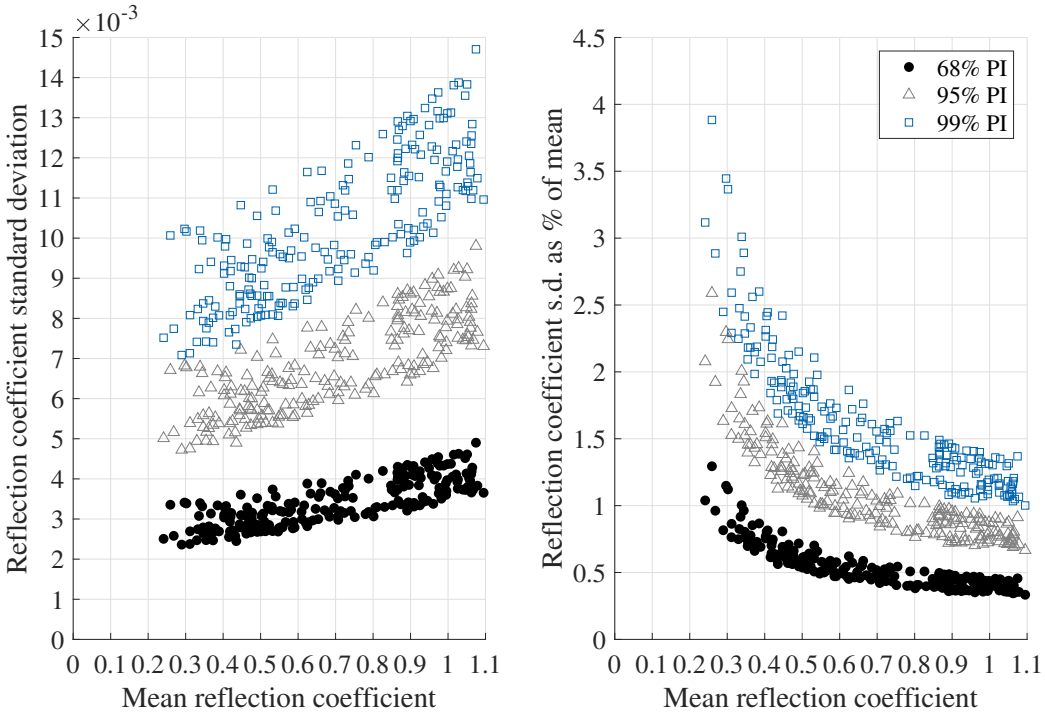

Figure 4.23: Comparison of mean and standard deviation value (left) and percentage of the mean (right) reflection coefficients as prediction intervals (PIs).

4.3.3.2 Time of Flight Variability

As with reflection coefficient data, change in time of flight data was also checked for normality. An example histogram can be seen in Figure 4.24 and all one-sample Kolmogorov-Smirnov tests confirmed normal distribution of the data with a 5% significance level.

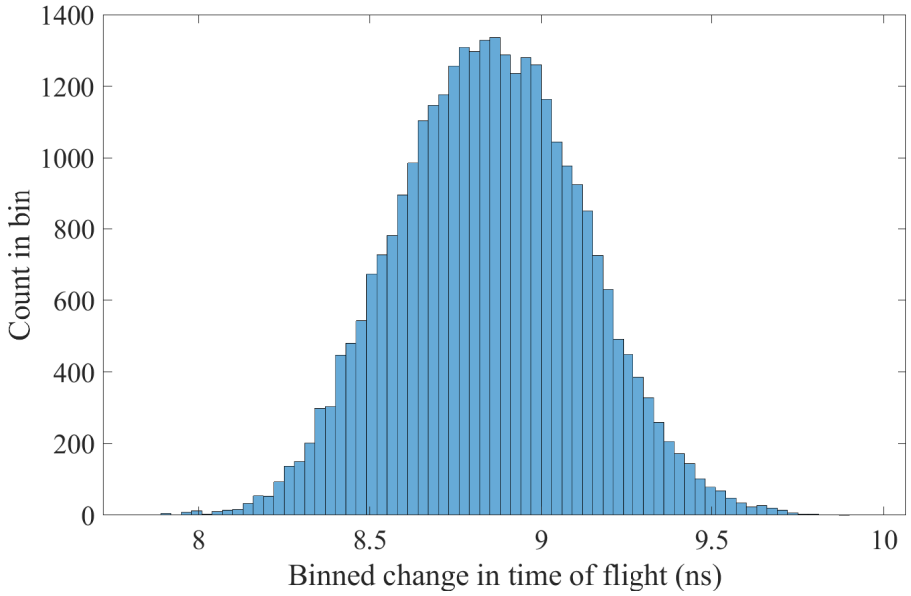

Figure 4.24: Example histogram of data distribution for one set of reflection coefficient comparisons. Data set was 50kN, ch2, position 0.0.

Figure 4.25 shows mean ΔToF against standard deviation values of ΔToF for each of the data sets for four different distances from the centre of the contact. As with R, the standard deviation of ΔToF increased with mean value of ΔToF however this time scatter of this data was not similar across all five distances from the centre of the contact. The increase in standard deviation with mean value can be explained by the accompanied decrease in signal to noise ratio when ΔToF increases. As more load is applied through a contact, deflection of the bodies in contact increases but so does the stiffness of the contact. This means more ultrasound is transmitted through the contact and so the amplitude of the reflected signals decreases while the noise level remains constant.

As previously stated, the error associated with fluctuating load applied by the compression rig was 0.012-0.025 ns. Across the 0.2-0.47 ns range of standard deviation values this equated to approximately 3-13%.

Figure 4.25 also shows the same relationship but with standard deviation as a percentage of the mean. This time variability in change in time of flight was much more significant over the measured values of ΔToF, particularly when converted into prediction intervals, as shown in Figure 4.26.

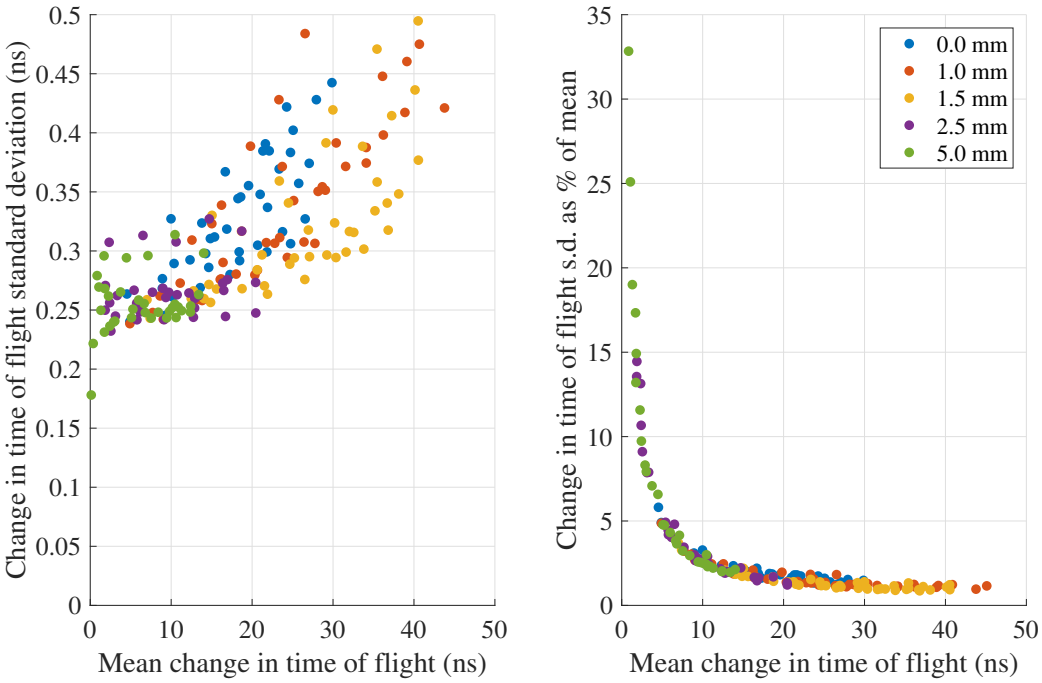

Figure 4.25: Comparison of mean and standard deviation value (left) and percentage of the mean (right) reflection coefficients.

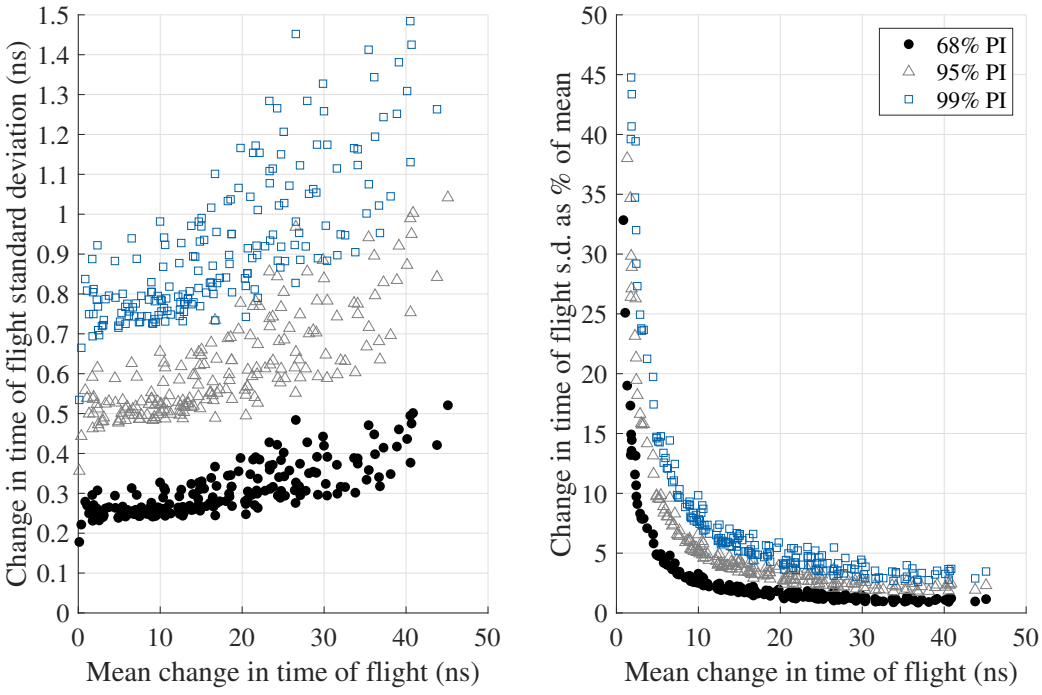

Figure 4.26: Comparison of mean and standard deviation value (left) and percentage of the mean (right) reflection coefficients as prediction intervals (PIs).

This shows that ΔToF monitoring of bearings is better suited to heavily loaded

bearings where the deflection is large. An example of how this ΔToF error could carry through into measurement of load variation on a fairly lightly loaded bearing is shown in Chapter 5. There were two likely reasons for this larger error. The first reason was the digitisation rate of the signal in the time domain relative to the changes being measured. The digitisation interval of raw signals was 10 ns. Even though interpolation of the A-scan improved the precision of measurements, measured ΔToFs were a maximum of 50 ns, therefore improvement of acquisition hardware to reduce this 10 ns time interval would likely be beneficial. The second reason for the large error was likely inherent in the processing method. There was often a slight change in the pulse shape between the reference and measured signals. Cross correlation of these dissimilarly shaped pulse envelopes during processing also likely caused some error.

4.4 Conclusions

This work has used an array of longitudinal transducers along the axis of a rolling contact to investigate various factors in ultrasonic measurements through quasi-static experiments. The following conclusions can be taken from this chapter:

- Fringe effects were visible in both reflection coefficient and change in time-of flight data and were not due to dynamic effects, high PRFs or lubricant in the contact.
- It appears that misalignment of rollers can be detected using longitudinal ultrasonic techniques, although reflection coefficient measurements may be distorted by surface damage or distress. A combination of the two processing techniques is recommended for a thorough analysis of the contact.
- Error due to variability in ultrasonic signals was estimated using a statistical approach and prediction intervals.
  - The variation in each of these data points incorporated several sources of error. The sources of error were not exhaustive and did not include those which would offset data, such as the acoustoelastic constant. The errors in the analysis included noise in the signal, digitisation error, error implicit in processing methods and variation in load during the 2 s test capture period. The error caused by load variation was calculated to be approximately 3-13% and therefore the prediction intervals of measurement variability were slight overestimates.

  - Error in reflection coefficient measurements was generally good with 95% prediction intervals giving between ± 0.7 and 2.6% error between reflection coefficients of 0.2 to 1.
  - Error in change in time of flight measurements was significantly higher than reflection coefficient with 95% prediction intervals giving between ± 1 and 39% error between ΔToF of 46 to 1 ns. The increase in error was likely caused by a combination of decreased digitisation interval in relation to the measured change in the time as well as a more complex data processing routine.

- Ultrasonic sensors over-predicted contact width by approximately three times the predicted value from both line and elliptical contact Hertzian calculations. This over-prediction was likely due to the transducer beam width being larger than the contact width and the resulting interference phenomena which significantly compromised the results. No obvious trend in ultrasonically measured contact width was seen with increasing load which may have been due to limited resolution in the rolling direction.

Chapter 5

Measured and Modelled Wind Turbine Gearbox Bearing Roller Loads Under Field Operating Conditions

5.1 Introduction

This chapter contains analysis of ultrasonic data from an operational wind turbine. A static multi-body model model of the wind turbine drivetrain was also used to appraise ultrasonic data. This work aimed to assess how previously measured error in load contributed to the overall load variation in an industrial application. A secondary aim was to explore whether changes in the load distribution of the bearing could be measured ultrasonically.

5.2 Background

Instrumentation and data acquisition work outlined in this section was done by Howard [39] and Ferguson [100] and not by the author. It is included as details are required for understanding of results from processing and analysis of the data which were undertaken by the author.

In previous work, a high-speed shaft bearing from a 600 kW Vestas V42 turbine located in the Barnesmore wind farm in the Republic of Ireland was instrumented with various sensors [39]. Further details about the turbine can be found in Table 5.1. Two condition monitoring systems were installed; CMS1 included conventional

monitoring techniques and CMS2 included ultrasonic transducers on the bearing. Figure 5.1 shows a schematic of the turbine nacelle and CMS; only the systems from which data was used in this project are shown, many other components were instrumented.

Rated power (kW)	Cut-in/ rated/ cut-out wind speed (m/s)	Rotor diameter (m)	Hub height (m)	Turbine type	Power control	Generator
600	14/ 16/ 25	42	50	Fixed speed	Pitch	Asynchro-nous

Table 5.1: Details of the instrumented Vestas V42 turbine.

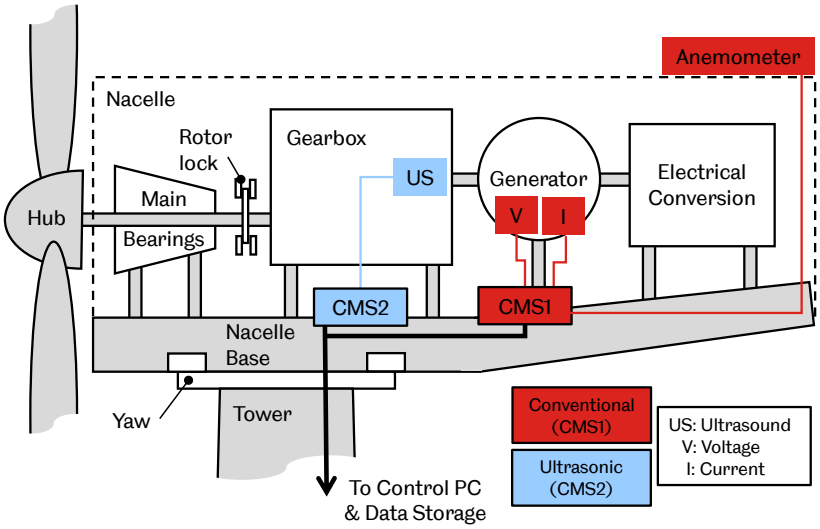

Figure 5.1: Simplified overview of condition monitoring systems installed in the wind turbine. Adapted from [39].

5.2.1 Conventional Instrumentation

Conventional data sets used were wind speed, generator voltage and generator current. Wind speed was measured using an anemometer mounted to the nacelle, as shown in Figure 5.2 (a). Generator voltage and current were measured using voltage sensors fitted over terminal bolts and Rogowski coils looped around each of the three phases which can be seen in Figure 5.2 (b).

Figure 5.2: (a) Anemometer as part of weather station installed on roof of nacelle (b) Rogowski coils looped around each of the three phases and voltage sensors fitted to each of the terminal bolts of the generator. Images reproduced with permission from [100].

5.2.2 Ultrasound Instrumentation

The ultrasonic transducers were installed on the rotor side high-speed shaft (HSS) bearing as shown in Figure 5.3. Primarily the HSS bearings were chosen for study because of relative ease of access when the gearbox was swapped out for maintenance. It was possible to change the bearing for an instrumented one without major modification. Some preliminary analysis (using SABR , see Section 5.4.1) had suggested that bearing B (a 32222-type tapered roller bearing) was the most highly loaded; and also identified the circumferential location which would experience the maximum load zone at rated power. This was selected as the sensor location. To avoid the necessity of slip rings, only the stationary outer raceway of the bearing was instrumented. Geometries and other bearing parameters of the 32222 tapered roller bearing are summarised in Table 5.2.

Bearing Parameter	Symbol	Value
Bore diameter	-	110 mm
Outer diameter	-	200 mm
Pitch diameter	D_m	154.26 mm
Width	-	56 mm
Maximum roller diameter	$D_{R_{max}}$	24.20 mm
Mean roller diameter	$D_{R_{mean}}$	22.92 mm
Minimum roller diameter	$D_{R_{min}}$	21.64 mm
Roller length	l	37 mm
Number of rollers	Z	20
Contact angle for outer race	γ_o	15.64°
Dynamic load rating	C_ω	402 kN
Fatigue load limit	C_u	61 kN

Table 5.2: Bearing parameters for the instrumented 32222 tapered roller bearing in the Barnesmore wind turbine gearbox.

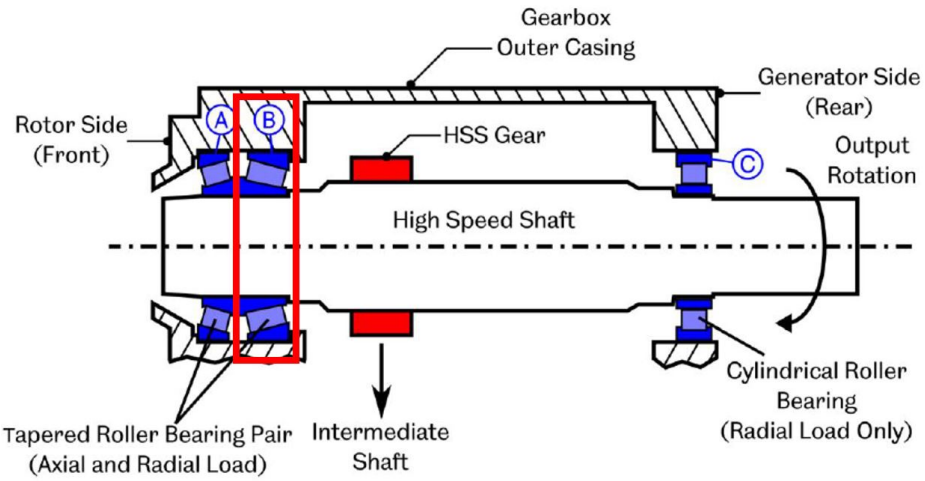

Figure 5.3: HSS bearing configuration for instrumented Vestas V42 wind turbine. The instrumented turbine was bearing B. From [39].

In order for the transducer to be parallel with the roller raceway interface a channel was machined in the raceway, as shown in Figure 5. The positioning of the machined channel was such that the transducer measurement area was axially central in order to measure at the centre of the roller-raceway contact.

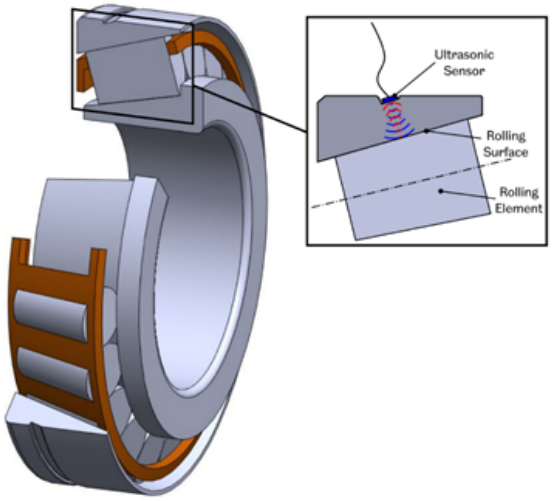

Figure 5.4: Illustration of the channel machined in the bearing for ultrasonic instrumentation.

Two ultrasound transducers were installed on the raceway, one at the outer boundary of the expected loaded region (as identified by SABR) at approximately 90% of the peak load (channel 1), and one at the centre of the loaded region (channel 2), as shown in Figure 5.5. This 100 – 90% of maximum load region will be referred to as the'peak loaded regio'.

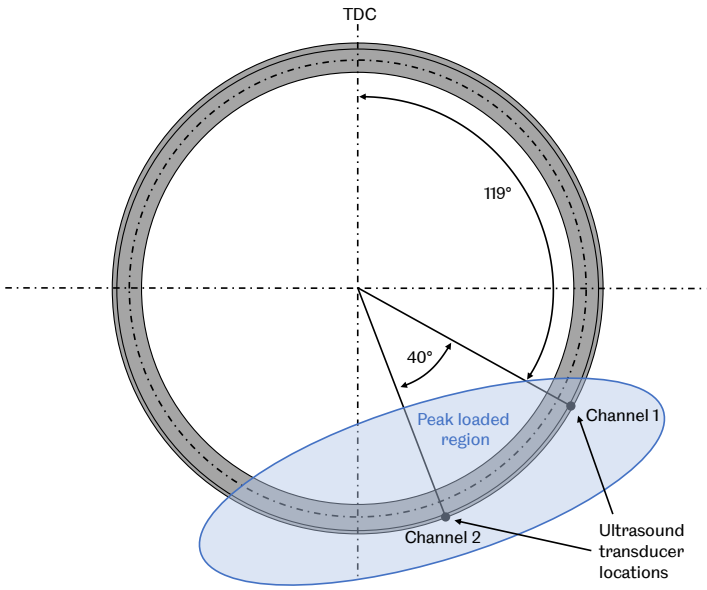

Figure 5.5: Radial locations of ultrasound transducers on the instrumented bearing.

The ultrasonic transducers were elements of piezoelectric material bonded to the raceway using high temperature strain gauge adhesive. Each of the transducers produced

longitudinal waves, had a centre frequency of 10 MHz and were cut to 5x1 mm. The transducer was installed such that the 1mm side was aligned with the minor contact width (rolling direction), and the 5mm with the major contact radius (transverse direction). A coaxial cable connected each of the transducers to an ultrasonic data acquisition system in order to minimise noise in the transmitted signals. Images of the installed sensors can be seen in Figure 5.6.

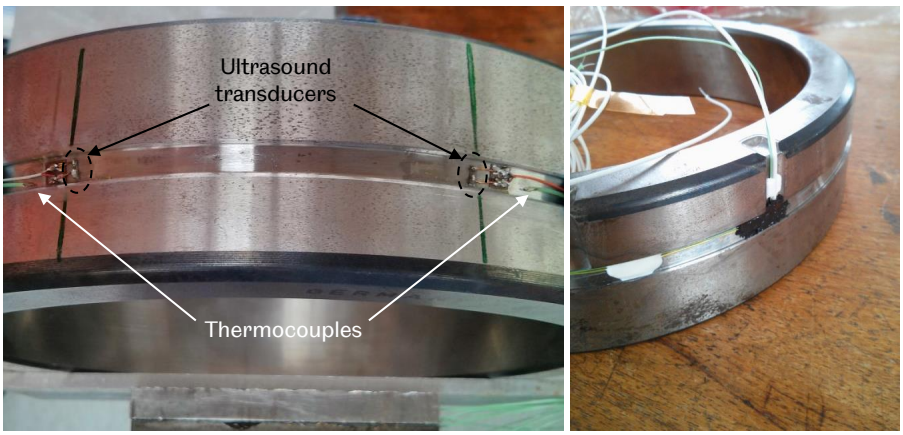

Figure 5.6: Images of bearing outer raceway instrumentation (a) piezoelectric transducers and thermocouples bonded in the machined groove (b) routing of cables out of the bearing raceway. Adapted from [39].

5.2.3 Data Acquisition

A summary of data used in this study is shown in Table 5.3. All data except ultrasound was captured using CMS1. Ultrasound was captured by CMS2. CMS2 used FMS data acquisition hardware, as described in Section 4.2.3.

Data	Sensor	Number of sensors	Sample duration	Unit	Sample rate	Acquisition rate
V	Voltage sensor	3	60s	V	Every 1 minute	10.24 kHz
I	Rogowski coil	3	60s	A	Every 1 minute	10.24 kHz
Wind speed	Anemometer	1	60s	m/s	Every 1 minute	50 Hz
US	Piezoelectric transducer	2	2s of 80 kHz PRF (160,000 A-scans)	Arbitrary amplitude	Every 20 minutes	100 MHz

Table 5.3: Summary of Barnesmore data used.

5.3 Data Processing

5.3.1 Ultrasound Data

Processing of ultrasonic data to obtain bearing speed, roller load and MRC for this data set had previously been undertaken by Nicholas [40] and so duplication of this work was unnecessary. Roller pass frequency was monitored in the frequency domain as described in Section 3.7.3 and converted to bearing speed using Equation 2.3. Change in time of flight was monitored through cross correlation as described in Section 3.6.2, converted to deflection using Equation 3.19 and then converted to roller load using Houpert's equations, as described in Section 2.3. More specifically, Equations 2.22 and 2.23 were used as transitional values of deflection for line contacts (as defined by Equation 2.25) were not reached at any point in this study, indicating that the bearing was lightly loaded. Reflection coefficient was obtained through spectral amplitude monitoring at the central frequency of the transducers as described in Section 3.6.1. A modal reference was used, as described in Section 3.7.2. Speed, load and MRC were mean values from each of the two second data captures.

From this point onwards all work was undertaken by the author.

5.3.2 Conventional Data

Anemometer signals were directly converted to wind speed however some simple processing was required to obtain generator power from voltage and current signals. A sinusoidal signal for each of the three generator phases was present. Power was calculated using voltage and current signals, with a generator power factor of 0.89.

5.3.3 Combined Data

For each of the data sets the mean value was found across the sample durations shown in Table 5.3. The sample rate of ultrasound data was lower than the conventional data sample rate due to the larger amount of data required for an ultrasound signal. Conventional data was therefore linearly interpolated to match with the timestamp of the ultrasonic data.

In this study bearing conditions were only studied during normal operation of the turbine. Thresholding was applied to remove data from start-up or shut down. The turbine cut-in and cut-out wind speeds of 4 m/s and 25 m/s were therefore used to threshold data. The generator for this turbine also appears to have a minimum

operating power just above 100 kW. This was used as a threshold in order to eliminate any start-up or shut-down events from the data as well as times where the turbine was not in operation. These thresholds can be seen in Figure 5.7.

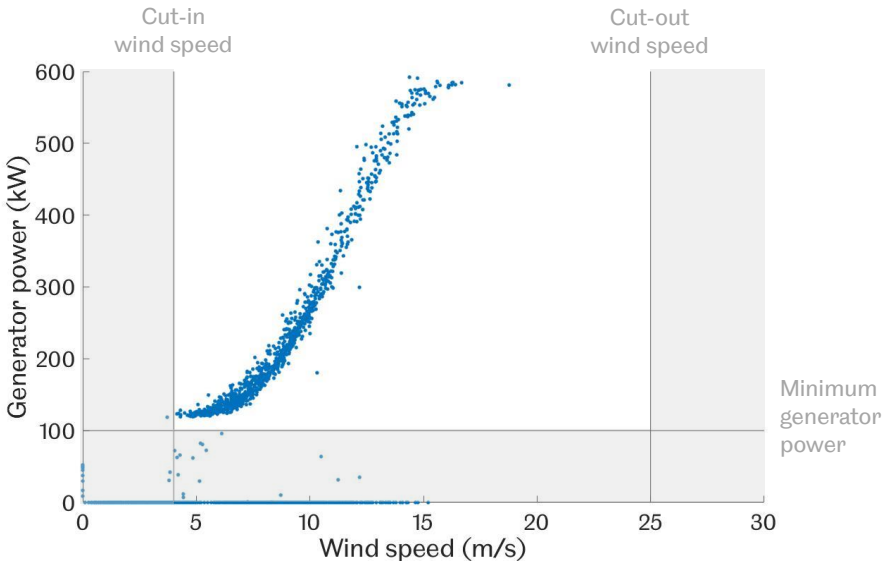

Figure 5.7: Wind turbine power curve thresholding. Cut-in and cut-out wind speeds of 4 and 25 m/s and generator power of 100 kW were used as thresholds to eliminate data outside the normal operating behaviour of the turbine.

The turbine had a control system that meant the turbine rotor span at constant speed and therefore data points outside of the normal speed range of the HSS were eliminated, as shown in Figure 5.8. Data outside of this range was likely to have been obtained during start-up, shut down, or when the turbine was not operational.

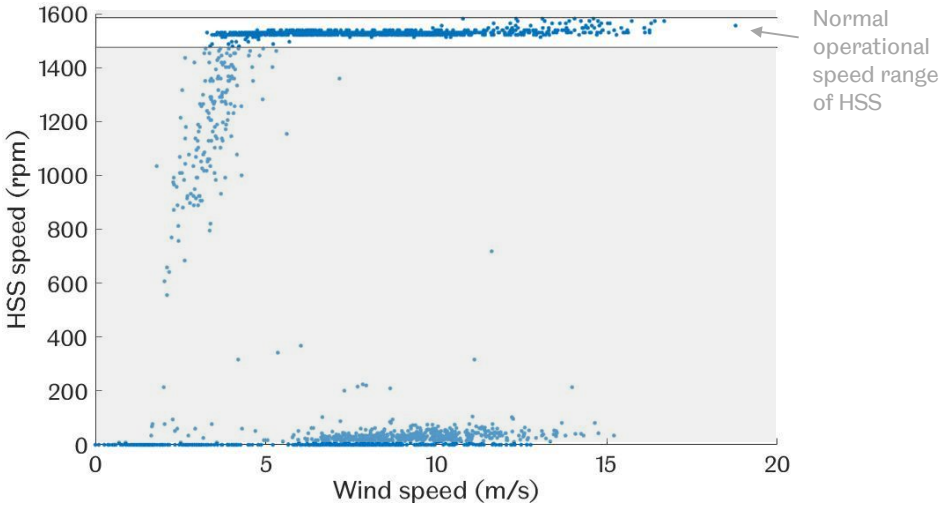

Figure 5.8: HSS speed thresholding. The turbine used a fixed speed control strategy and so data points outside the indicated region are data outside the normal operating behaviour of the turbine.

After thresholding, ultrasonic load measurements for both channels plotted against wind speed and turbine power can be seen in Figures 5.9 and 5.10 respectively.

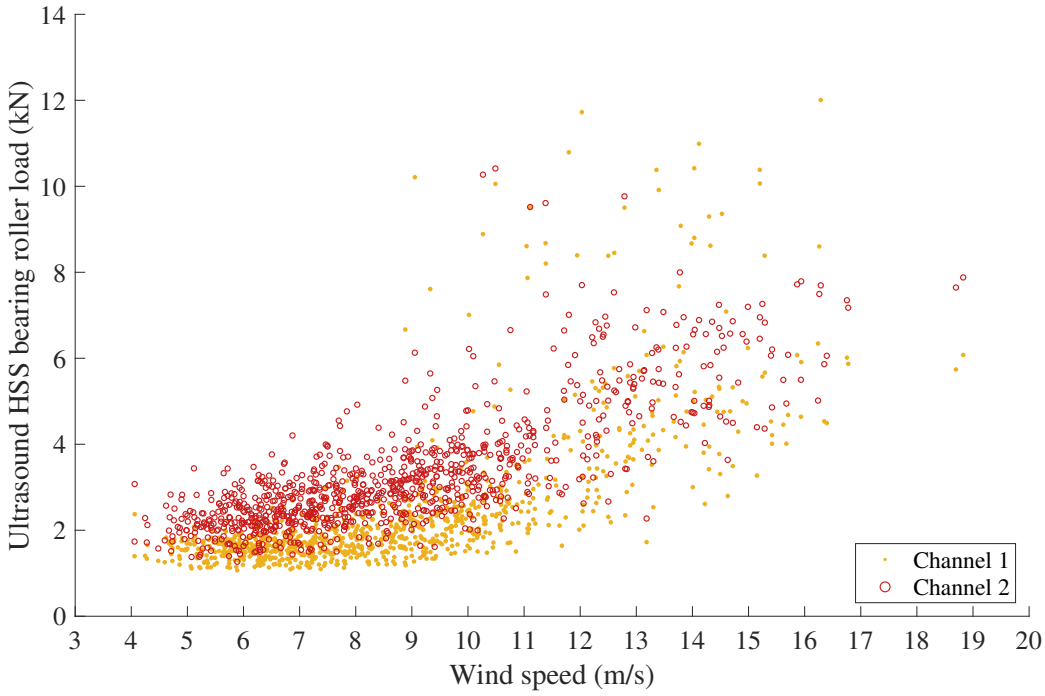

Figure 5.9: Ultrasonic roller load measurements vs wind speed for both channel 1 (edge of the loaded zone) and channel 2 (centre of the load zone) after thresholding.

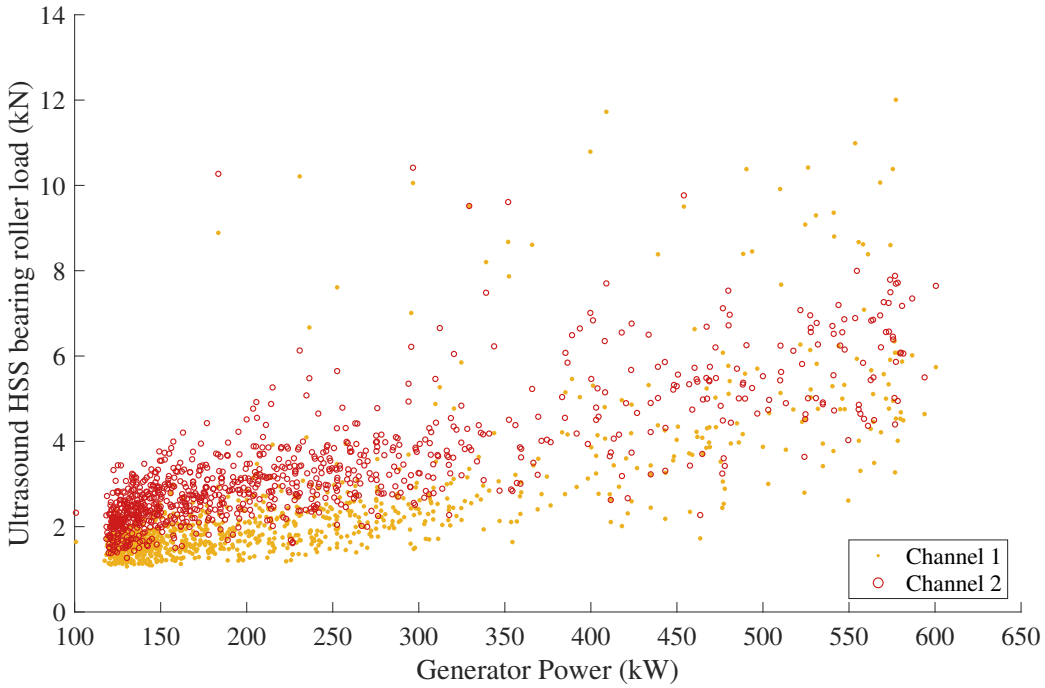

Figure 5.10: Ultrasonic roller load measurements vs turbine power for both channel 1 (edge of the loaded zone) and channel 2 (centre of the load zone) after thresholding.

Figure 5.9 shows that ultrasonically measured roller load increased with increasing wind speed for both channels and Figure 5.10 shows that ultrasonically measured roller load increased with increasing turbine power. In both cases scatter of the data increased with increasing measured roller load. For the majority of the data channel 2 loads were larger than channel 1 loads and there was less scatter in channel 1 data than channel 2 data. All of these observations were expected, at least in part.

Higher wind speeds mean that more torque will be transmitted through the shafts and a higher axial load will on the rotor. The increased torque in the shaft increases generator power. The increased torque in the shafts, as well as the increased axial load on the rotor will also mean that bearing loading will increase. Increased scatter at higher loads was expected due to increased wind gusts at higher wind speeds, although scatter is larger than expected.

Channel 1 was predicted to be further from the peak load than channel 2 and thus the lower load was expected. This also meant that channel 1 was expected to have less scatter as it would be less prone to changes in load due to movement of the loaded zone and any transient loading would likely be of lower amplitude. Also note that

loads were quite low in comparison to the load ratings of the 32222 tapered roller bearing (see Table 5.2).

5.4 Multibody Modelling

5.4.1 SABR Model of Gearbox

SABR is a shaft, gear and bearing conception and design package based on engineering standards (such as ISO 281 [5] and ISO/TS 16281 [6]) as well as Ricardo's product design, manufacturing and testing experience [101]. The software uses power flow to resolve the system. Ricardo optimised beam models are used to calculate shaft loads and bearing load models are dependent on bearing type but are based on relationships well summarised by Harris and Kotzalas [3].

SABR was used to create a model of the gearbox installed in the instrumented Vestas V42 turbine, as shown in Figure 5.11. Shaft, bearing and gear geometries and interfaces were recreated for all three stages of the gearbox and material properties defined. Zero deflection boundary conditions were set using infinitely thin bearings where appropriate. SABR requires either input or output shaft torque and speed as boundary conditions.

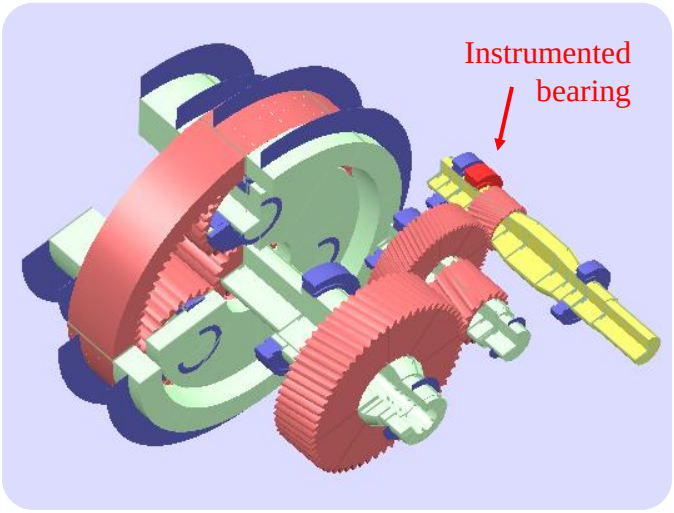

Figure 5.11: Ultrasonic roller load measurements vs turbine power for both channel 1 (edge of the loaded zone) and channel 2 (centre of the load zone) after thresholding.

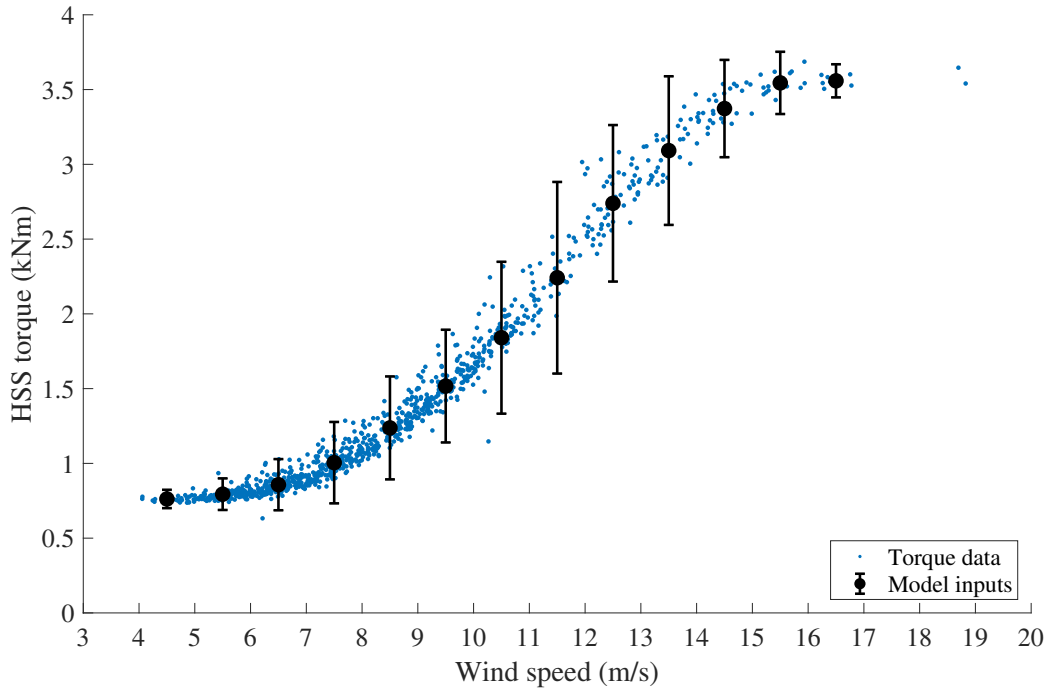

Figure 5.12: High speed shaft torque curve with model inputs. Central points of model inputs are mean values, and extremities of error bars show ±3 standard deviations of binned values. Binned values are every 1 m/s ±0.5 m/s.

5.4.2 Model Input Generation

Data collected from the turbine was used to define the boundary conditions of the model. The HSS torque was found by dividing the generator power by the rotational speed. As wind turbine generators have very high efficiencies [102], it has been assumed that generator losses are negligible. Since the bearing investigated is on the high speed shaft, gearbox efficiency need not be accounted for.

Figure 5.12 shows how data was binned into sets across the range of wind speed values between integers of wind speeds (i.e. between 4 and 5 m/s, between 5 and 6 m/s, etc.). Very little data was available above 17 m/s therefore these points were not evaluated. The rated power of the turbine is 16 m/s and so any results at wind speeds above 17 m/s would likely have similar torque values to the 16-17 m/s bin, although variability in measurements may differ. For each of the 13 bins, mean values were found and error bars were established at ±3 standard deviations from the mean, indicating 99% prediction intervals. These torque values were used to generate input torques for the model. With the addition of evaluating the range of torques at each wind speed a total of 39 torque cases were evaluated by the model.

HSS speeds were evaluated in a similar manner where the mean operational value ± 3 standard deviations value was 1480 ± 5 rpm. The range of HSS torques shown in 5.12 along with these HSS speeds were combined as boundary conditions to the model. Each boundary condition case was then solved by resolving shaft loads until all loads were balanced to within 0.1 mN. The model was used to output the radial and axial load acting on the bearing previously instrumented in the trials.

5.5 Prediction of Individual Roller Load

To allow for comparison with ultrasound load measurements, Equations 2.30 and 2.29 were used to convert the bearing axial and radial loads predicted by the multibody model into the load directly on the roller-raceway interface at the locations of both sensors (channel 1 and channel 2), as depicted by Figure 5.13. The resulting model loads are shown in Figure 5.14. Error bars correspond to the range of shaft torques and speeds used as boundary conditions.

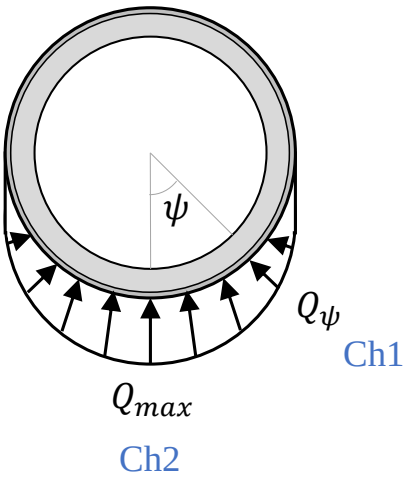

Figure 5.13: Radial load distribution of a rolling element bearing labelled with the approximate position of channel 1 and 2 ultrasound sensors.

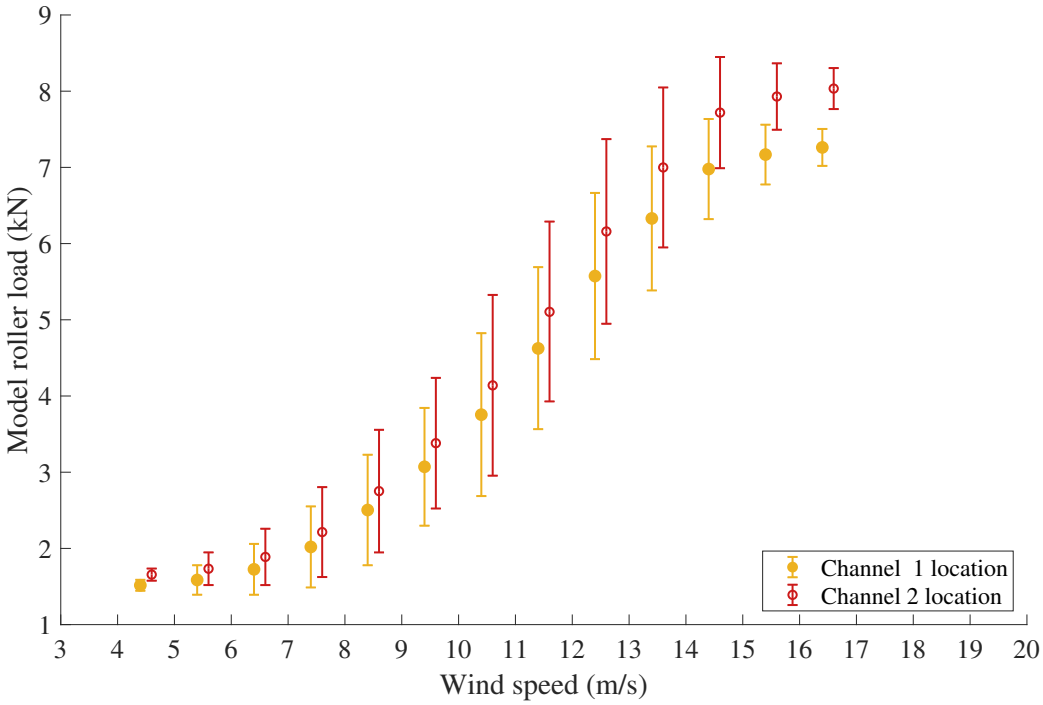

Figure 5.14: Model predicted roller loads at channel 1 and channel 2 locations. Error bars correspond to the range of model input torques and speeds. Chanel 1 results have been offset slightly to the left and channel 2 results have been offset slightly to the right for clarity.

5.6 Comparison of Measured and Modelled Bearing Load

Comparisons of ultrasound predicted load and model predicted load for both channel 1 and 2 are shown in Figure 5.15. There is a reasonable amount of scatter in ultrasonic load measurements but both channels show good agreement between ultrasound and model predicted loads.

The model load for channel 1 slightly over predicts in comparison to measured load; whereas for channel 2 the model slightly under predicts. This could be explained by a change in the load distribution of the bearing. The effect of introducing diametral clearance in the bearing is shown in Figure 5.16. If the load distribution is changed so that it is distributed over a smaller area than predicted, then the load at channel 1 would be smaller than predicted and the load at channel 2 would be slightly larger. It is likely that this bearing had some preload and therefore unlikely that there was any diametral clearance in the bearing. Prediction of load distribution by the load integrals was therefore slightly inaccurate for some other unknown reason.

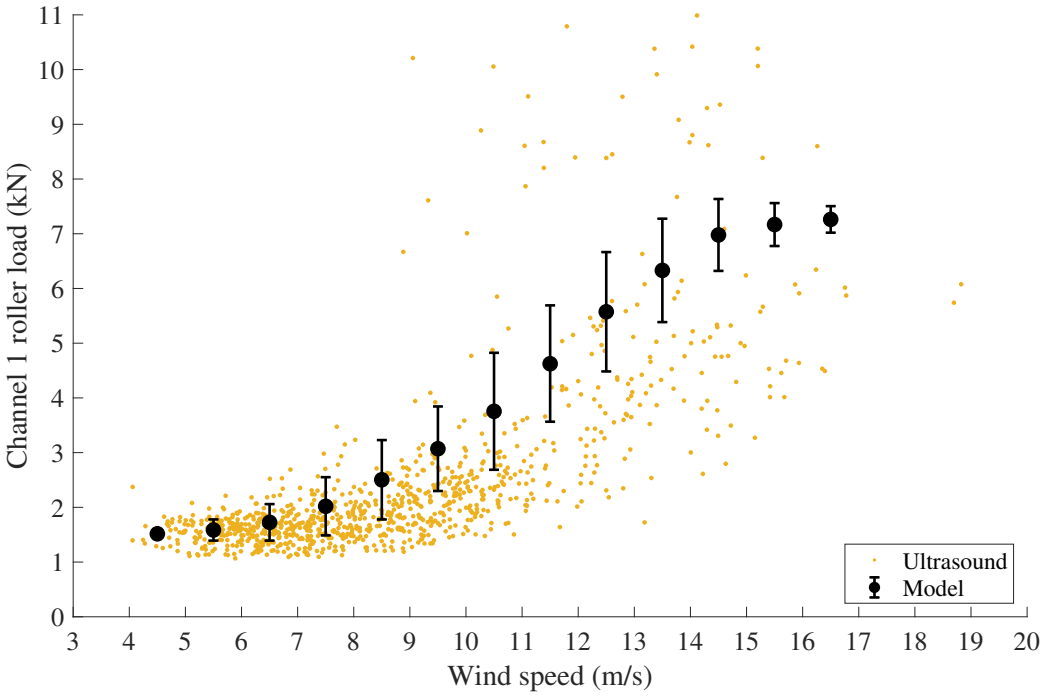

(a) Channel 1: edge of the peak loaded region.

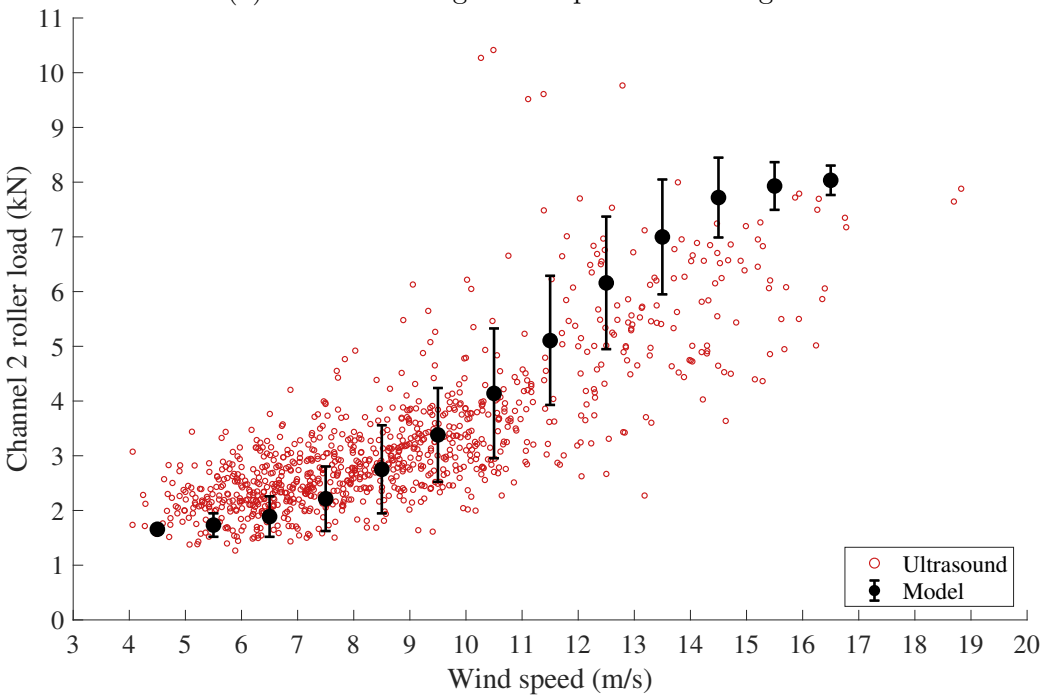

(b) Channel 2: centre of the peak loaded region.

Figure 5.15: Load comparison between ultrasound and model predicted roller loads for (a) channel 1 and (b) channel 2 . Error bars correspond to the range of input torques shown in Figure 5.14. High load data points which were inconsistent with the general data trend are enclosed with dashed lines.

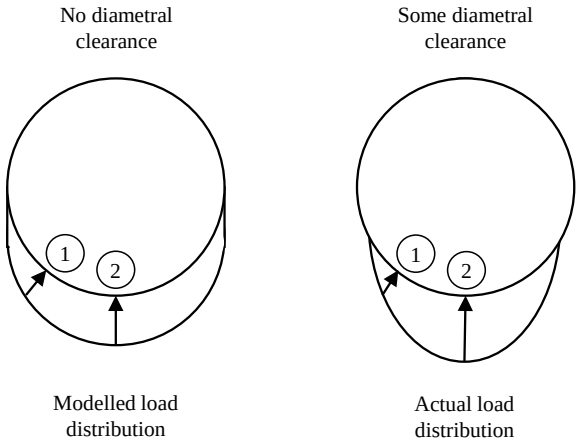

Figure 5.16: Effect of change in bearing load distribution with different internal clearances – an explanation for model under and over prediction.

5.7 Analysis of Load Variability

The level of scatter in the ultrasound measurements was such that a proportion of the data fell outside of the expected error associated with operational variations in shaft torque and speed (shown in Figure 5.15). An investigation into potential causes of this scatter was therefore performed. Variability in wind speed measurements, non-synchronous data sets and variability in ultrasound data were evaluated as potential sources of scatter. These were sources of variability that were able to be investigated with the available data and were not exhaustive.

5.7.1 Variability in Wind Speed Measurement

When power curve fitting, it is often assumed that the data represented by wind speed and power measurements can be regressed on to form the power curve [103, 104]. In the current context we are interested in the fact that measuring wind speed is difficult due to the turbine seeing an effective (non-point) wind speed which can be thought of as a rotor average value. As such, there is significant 'noise' present when this wind speed is assumed to be a measurement of effective wind speed. For the purposes of power curve modelling this is less of an issue as the goal is normally to determine the link between measured wind speeds and output power for certification and production estimates. In these cases, regression is performed to identify an

underlying relationship, with wind measurements tending to be interpreted as non-noisy input values and regression noise attributed to power values. Arguably, to properly capture the high noise values on measured wind speeds, regression should consider the noise on this input variable also. For the purposes of the current work the key question is then "are the high noise levels on wind speed measurements the underlying cause of the scatter seen in Figure 5.15?". In order to investigate this question it is proposed that a regression should be performed to smooth out the apparent noise on wind speed measurements so that Figure 5.15 can be replotted with 'corrected' wind speed values to see whether this reduces observed scatter (with an affirmative answer indicating that wind speed noise is indeed a contributor).

The turbine in question operated at constant speed with pitch control to maintain rated power once it was reached. Data points above a wind speed of 14 m/s were first eliminated from the dataset in order to ensure only data from the one operational region remained (turbine rated wind speed was 16 m/s). For the remaining measurements (seen in Figure 5.17(a)) a regression was performed to smooth out noise on wind speed values. Note that it was assumed that the major noise contribution is the wind speed variable (rather than power) and hence regression was performed with power treated as the input variable and wind speed as output variable, which is equivalent to a standard regression having swapped the x and y axes of Figure 5.17(a). A Gaussian process (GP) regression [105] was performed since the underlying function is not expected to have a parametric form due to the fact that, although power in the wind increases cubically with wind speed, factors such as aerodynamic efficiency cause deviation from this simple form [103, 104]. GP regression offers a non-parametric and flexible regression technique which fits a smooth curve to the data having optimised the fitting parameters using the data itself. Other non-parametric fitting techniques would be equally valid here, the aim being to smooth out wind speed measurement noise, and so there is nothing unique about the particular choice of fitting algorithm with respect to this problem. The outputs of this regression can also be seen in Figure 5.17(a). The fitted curve was then used to adjust measured wind speed values by taking the fitted wind speed corresponding to measured power at each measurement point.

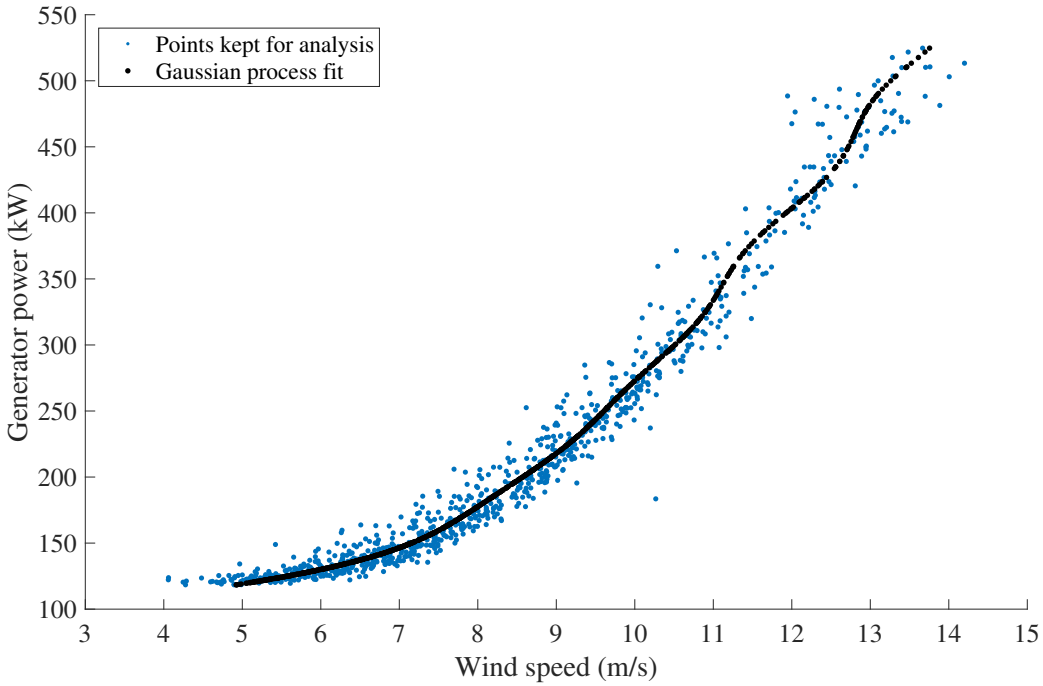

(a)

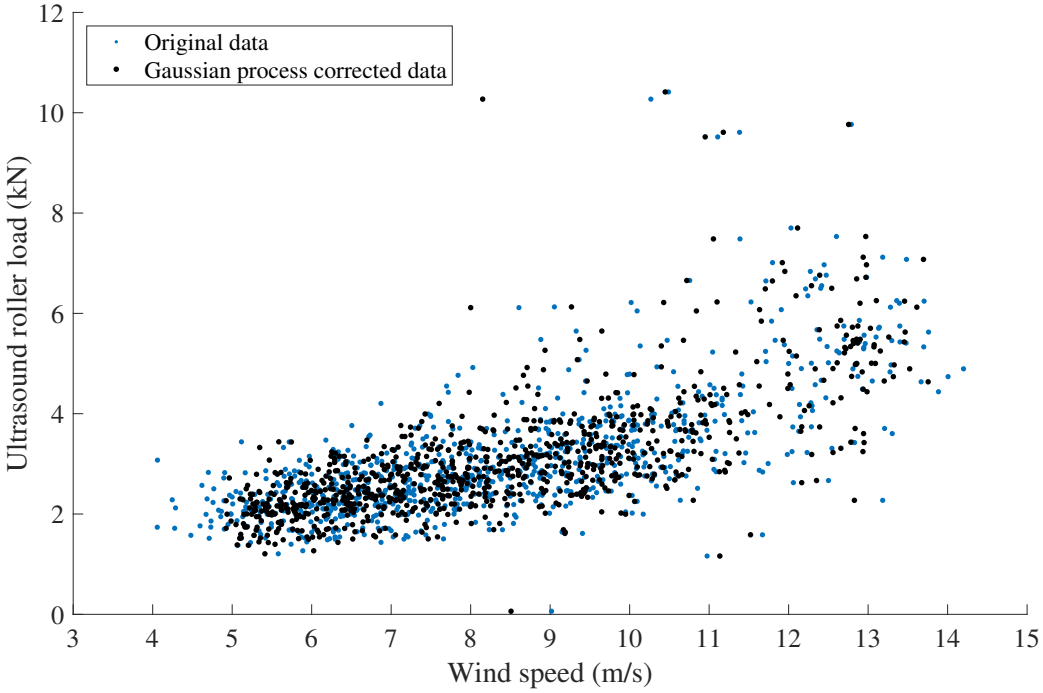

(b)

Figure 5.17: (a) Gaussian process regression on the wind speed - generator power relationship (b) US channel 2 bearing load before and after Gaussian process regression

Channel 2 ultrasound results with the Gaussian process corrected wind speed values

are shown in Figure 5.17(b). There was no significant reduction in scatter due to the correction which suggests that noise in wind speed measurement was not a significant factor in scatter of ultrasound results. The fact that the scatter in load measurement against generator power was similar to the scatter against wind speed support this conclusion (see Figures 5.10 and 5.9). The underlying causes of this scatter should therefore be explored further.

At this stage it seems prudent to state that other factors in the wind field may be the cause of variability in the ultrasound results. Variability in the wind field from features such as wind shear or turbulence may still cause variations in out of plane loading. This is less likely to have caused variation due to the fact that the instrumented bearing is reasonably far from the rotor but is possible, nonetheless. To investigate such phenomena further, knowledge of the wind field would be necessary, for which data was not available.

5.7.2 Error from Non-Synchronous Data Sets

Another possible cause of the scatter in measured loads was thought to be a result of non-synchronous data between conventional and ultrasound datasets (see Section 5.3.3). If this were the case, data where there was a longer duration between the time of ultrasound data capture and the closest time of conventional data capture would be expected at the extremities of the scatter and data captured more closely together would be expected at the centre of the scatter. Figure 5.18 shows that this was not the case. The extent of the scatter was mostly evident when the difference in capture time was 4 s and as the difference increased values appeared within this range.

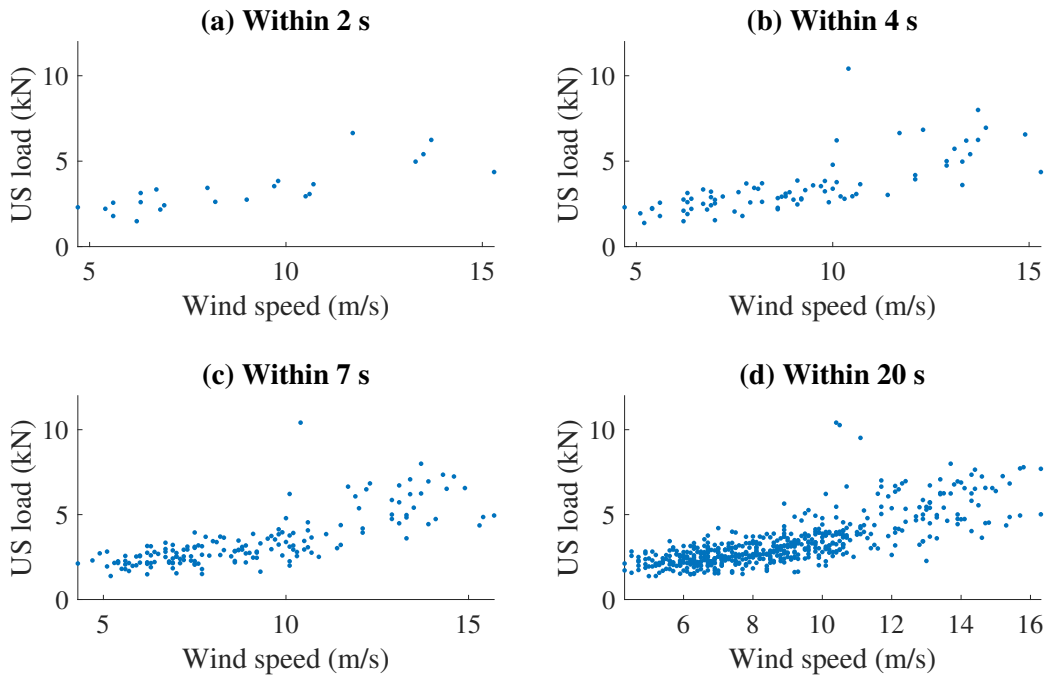

Figure 5.18: Effect of non-synchronised data channels on US channel 2 roller load scatter showing data points where CMS1 data was captured within (a) 2 s, (b) 4 s, (c) 7 s and (d) 20 s of CMS2 data.

5.7.3 Variability from Ultrasound Data Acquisition and Processing

To determine the amount of variability possible in ultrasound load measurements some simple experiments were undertaken with an acquisition system of the same specification as that installed in the Barnesmore turbine. Static compression tests were done with a single roller against a raceway at a range of loads in order to obtain deflections of a similar magnitude to those seen in the instrumented HSS bearing. These experiments were described in more detail in Section 4.

The ToF data from Figure 4.25 was converted into load using the geometry of the instrumented bearing and is shown in Figure 5.19. The trend changes shape slightly due to the relationship between load and deflection being non-linear (see Equation 2.22).

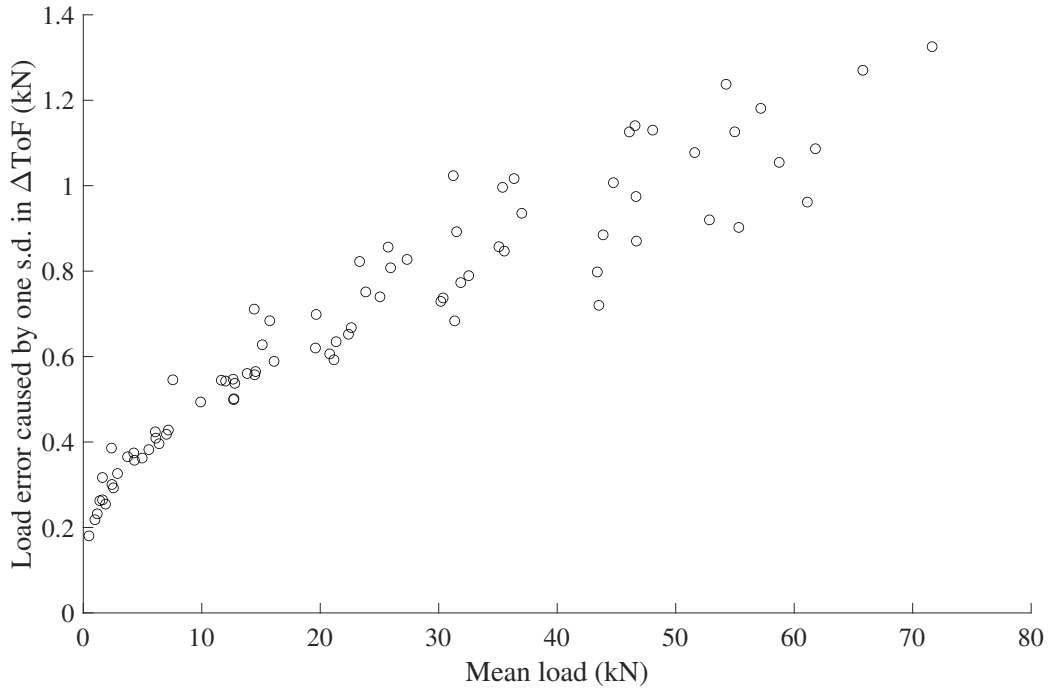

Figure 5.19: The effect of one standard deviation change in time of flight on US load prediction

Carrying through the change in time of flight prediction intervals from Figure 4.26 for the range of loads predicted by ultrasound for the instrumented bearing (1-12 kN) three load prediction intervals can be seen in Figure 5.20.

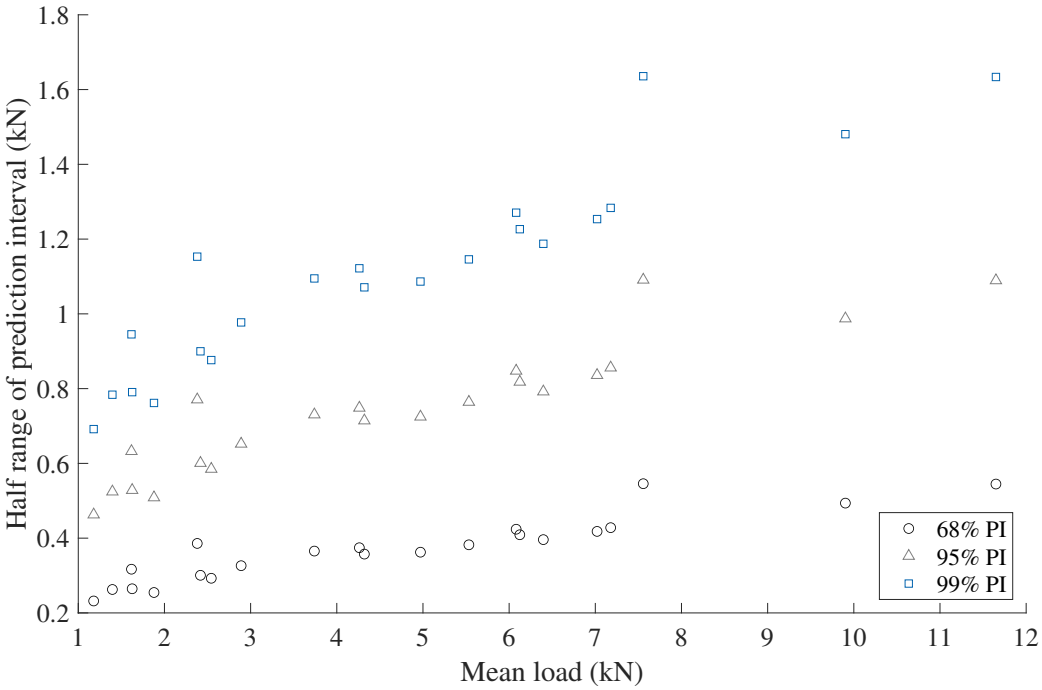

Figure 5.20: Load prediction intervals (PI) for 1-12 kN

This shows a reasonably large amount of data scatter expected due to errors in time of flight readings. It would therefore be reasonable to attribute the majority of the remaining scatter to variability in ultrasonic measurements.

This is visualised in Figure 5.21 by adding the prediction interval values from Figure 5.20 to the error bars from Figure 5.15 to give a prediction of where load values should lie within the measured data.

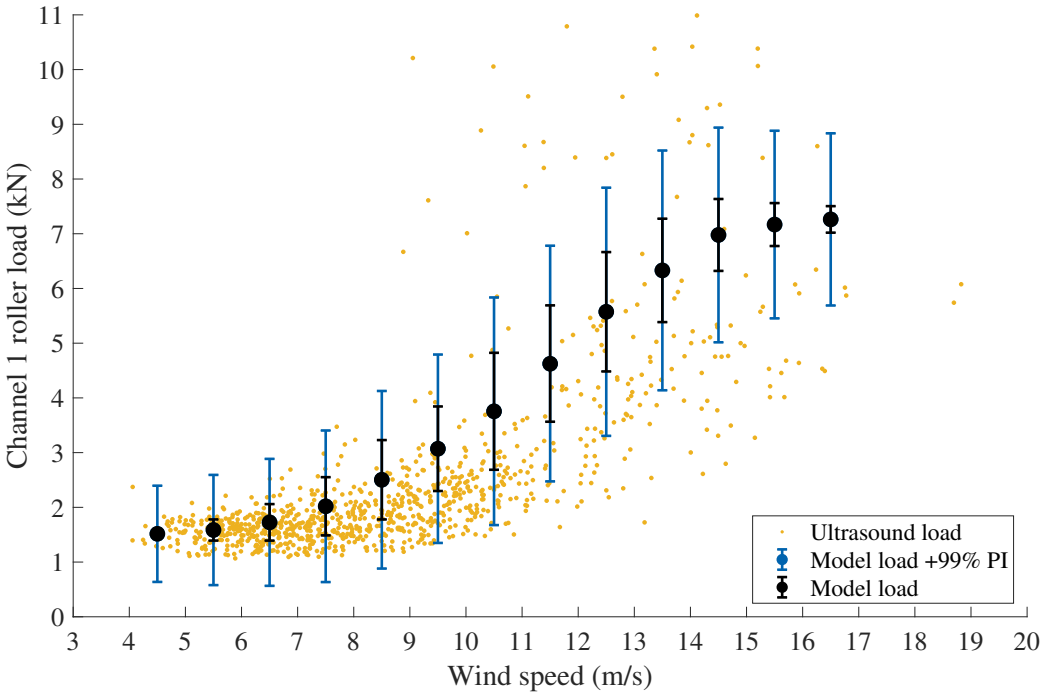

(a) Channel 1: edge of the peak loaded region.

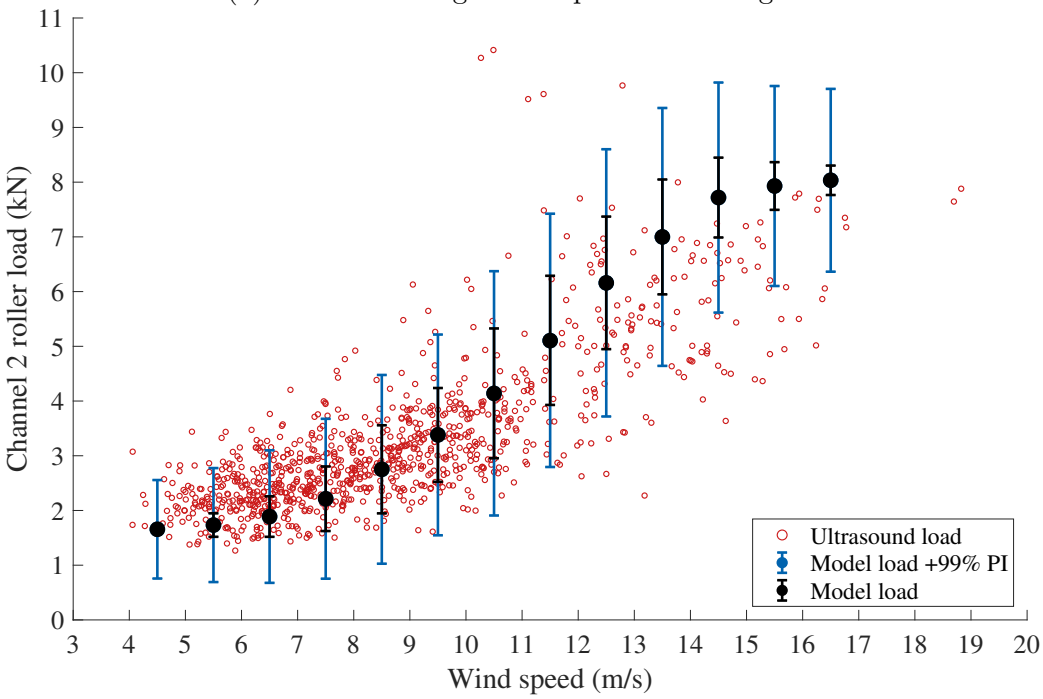

(b) Channel 2: centre of the peak loaded region.

Figure 5.21: Load comparison between ultrasound and model predicted loads for (a) channel 1 (edge of and (b) channel 2. Error bars correspond to the range of input torques shown in Figure 5.12 plus a 99% prediction interval from Figure 5.20.

Even though there is a trend of increasing signal error with load, if this error is

plotted as a percentage of the mean, the levels of error at higher loads was much more acceptable, as shown in Figure 5.22.

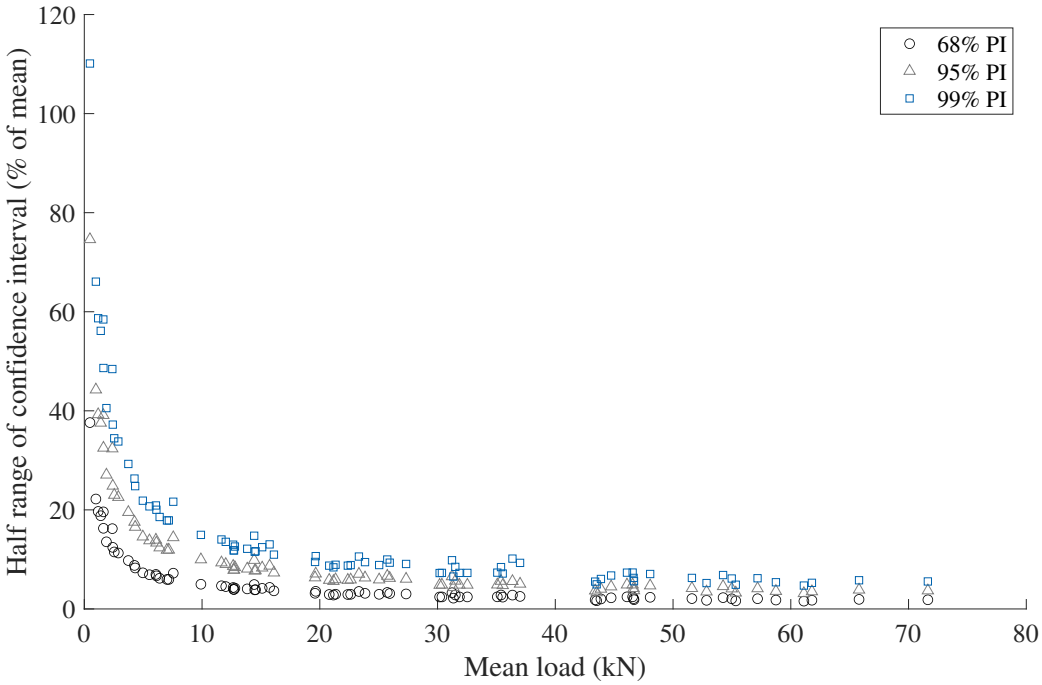

Figure 5.22: Load prediction intervals (PI) as a percentage of mean load

The more acceptable percentage error at higher loads shows that these techniques are better suited to bearings under larger loads where the level of scatter is small in comparison to the measured load. That being said, there are some ways in which the scatter at lower loads can be reduced, of which the most likely to have the greatest impact would be to improve the digitiser sampling rate. Load scatter may also be improved through removal of fringe effects from signals.

If we again turn our attention to Figure 5.21 we can see that in both sets of data there are points where ultrasonically measured loads are outside of the expected variation of load measurement. These points are both above and below the expected range and are likely to be a response to some transient event. More high load outliers are present in the data from channel 1 (edge of peak loaded region) than channel 2 (centre of peak loaded region) which suggests these events may shift the loaded region towards channel 1. Shifting of the loaded zone can also be thought of as changing the load distribution in the bearing and not rotation of any of the static components of the bearing. Shifting of the loaded region in a HSS tapered roller bearing due to grid loss events has been seen in other work [50], however these events were not seen in our

current dataset. It could, perhaps, have been caused by wind gusts instead. Figure 5.23 shows instances where channel 1 US measured loads were greater than those from channel 2, which confirms that the load zone was shifted for the majority of these points. For a better understanding of movement of the loaded zone in future bearing testing, more than two circumferential measurement sensors would be required to give insight into the changed load distribution.

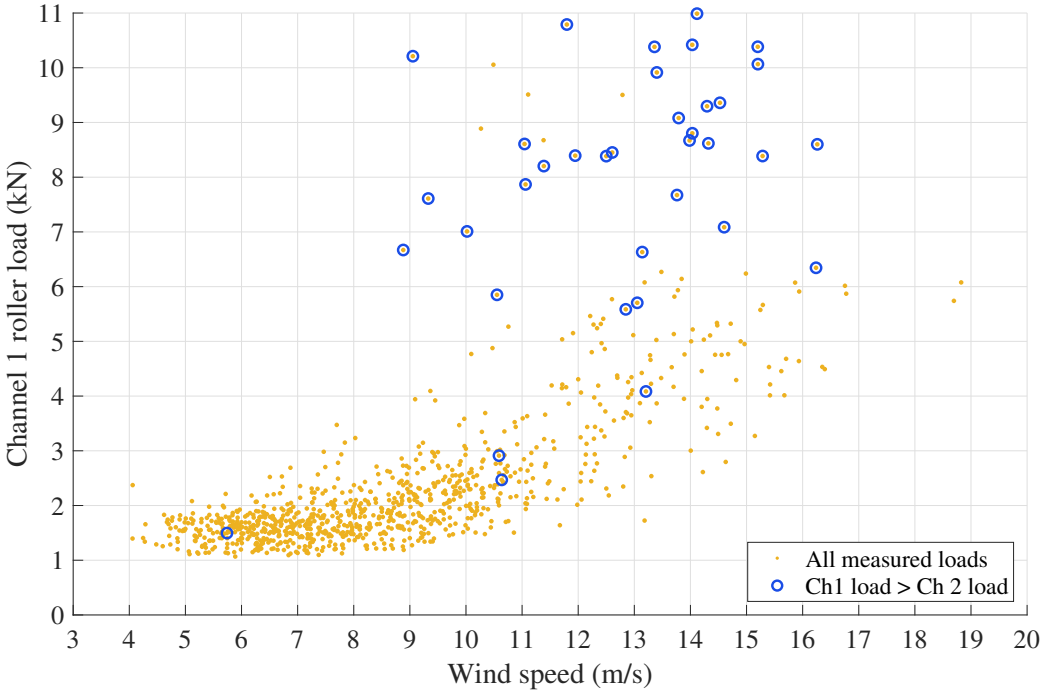

Figure 5.23: Measurements where channel 1 load was greater than channel 2 load.

These shifting of the loaded zone can also be seen in reflection coefficient data where channel 1 MRC values are lower than channel 2 MRC values, as shown in Figure 5.24.

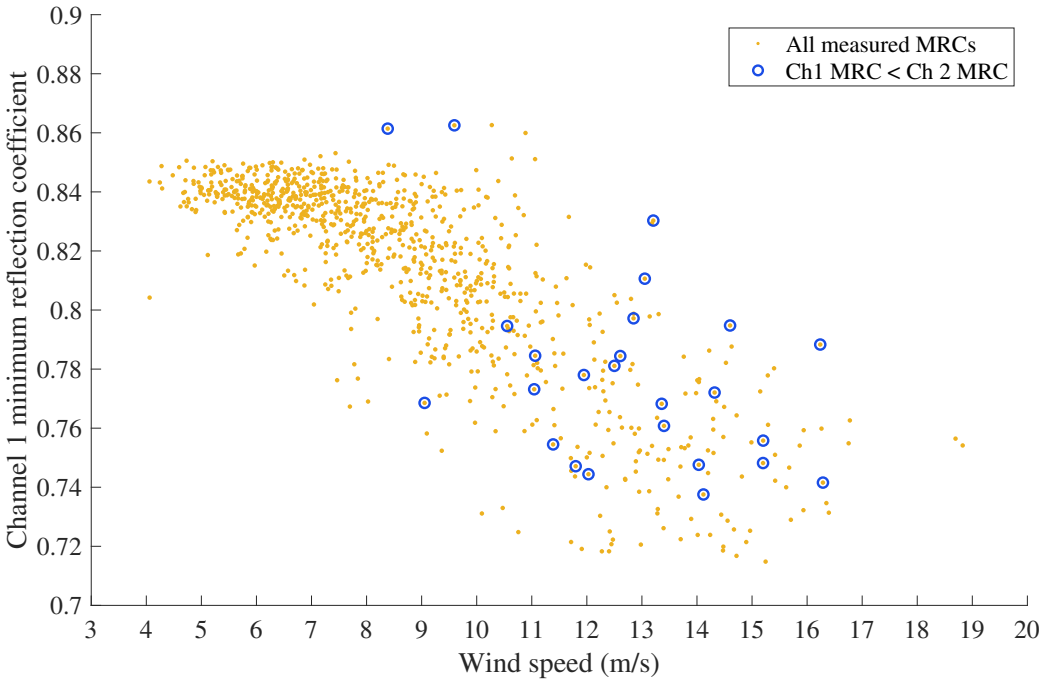

Figure 5.24: Measurements where channel 1 MRC was less than channel 2 MRC.

5.7.4 Other Factors

Although the factors assessed in this work can explain a large proportion of the scatter in ultrasonic load measurements, they are not the only possible reasons for the scatter. One way in which scatter may have been reduced in the modelling process is the use of generator power to back calculate shaft torque. This may have had the effect of hiding fluctuations in torque that would have explained the variability in load measurements, as well as the high load outliers. The model also does not account for dynamic effects in the system which would likely be required for a comparison during transient events.

While variability in wind speed measurement has been shown to be insignificant in causing scatter of ultrasonic load measurements, it is noticeable that scatter in load measurements increases at higher wind speeds. It is likely that the wind is more turbulent at these speeds which would explain the larger variation in load measurements on the bearing but there is no evidence to support this theory from the available data.

5.8 Conclusions

This work has shown that roller load measurement on an operational model compares well to those predicted by a static multi-body model of the gearbox. This increases

confidence that the ultrasonic technique predicts loads of the correct amplitude.

That being said, a significant portion of load variation has been attributed to error in ultrasonic load measurement by comparison to variation in quasi-static experiments. The high level of scatter in measurements was shown to be partially due to the fact that the bearing was under a light load. The measurement variability as a percentage of the mean would decrease when measuring more heavily loaded bearings. This percentage error would also likely decrease with improved measurement hardware.

Quantification of error in ultrasonic measurements was used to identify possible transient events in data. These events were most likely caused by wind gusts as no grid disconnection or braking events were observed in the data. Shifting of the load zone was detected through ultrasonic sensors for the first time, likely as a result of the identified transient events. For a better understanding of movement of the loaded zone in future bearing testing, more than two circumferential measurement sensors would be required to give insight into the changed load distribution.

Chapter 6

Measurements From a Wind Turbine Gearbox Bearing Test Rig

6.1 Introduction

This work used ultrasonic techniques to monitor rolling bearing performance of a bearing in a Cylindrical Roller Bearing (CRB) test rig. Experimental setup and data gathering for this work was done in collaboration with Nicholas [44]. Data processing and analysis methods were conducted independently. Both shear and longitudinal sensors were used to monitor bearing performance over a range of loads, speeds and lubricant viscosities.

There were several aims of this work, all of which filled previously identified gaps in research. The first aim was investigation of fringe effects and their causes. The second was to use shear sensors to gain any additional insights into the bearing operation, in particular to determine whether the lubrication regime was mixed or fully separated. The final aim was to measure load distribution along the roller raceway contact with the possibility of detecting misalignment in an operational bearing.

6.2 Experimental Setup

6.2.1 Test Rig

The MultiLife test rig was originally designed and commissioned by Ricardo UK Ltd. to provide validation of their *MultiLife* bearing concept [39]. Integration of ultrasonic sensors was enabled through collaboration with the University of Sheffield. The rig purpose was to replicate the operation of a CRB from the pinion bearing of a epicyclic

wind turbine gearbox bearing. Test bearings were NU2244 type bearings and were representative of those within a typical 2.5-3 MW turbine. The rig applied uniaxial radial load between 0 and 1400 kN to the test bearings using a hydraulic Enerpac to apply load through the static shaft shown in Figure 6.1 via the load arms. The outer raceway of the bearing could be rotated between 20 to 100 rpm and was driven by a 3 phase motor through drive belts. The lubrication system consisted of a pump, filter and sump from which oil was fed through an inlet at the top of the bearing and subsequently returned to the sump as shown in Figure 6.1 (c). The rig was controlled using a custom LabVIEW interface.

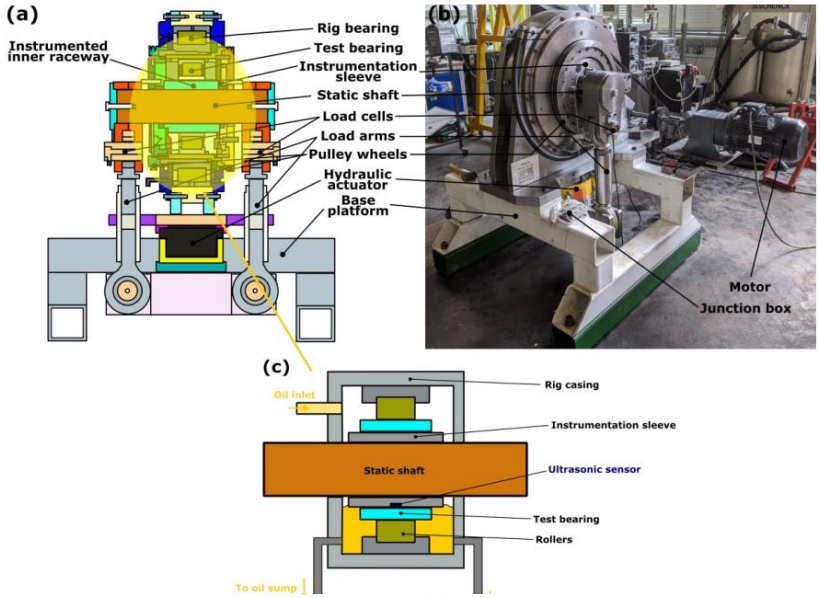

Figure 6.1: Multilife test rig (a) schematic (b) photo of the front side (c) sketch illustrating the lubricant inlet and outlet region. From [44].

An image of the slots, which were machined in the inner raceway housing to enable ultrasonic instrumentation of the bearing, are shown in Figure 6.2. Only the axial slot could be used for permanently bonded sensors due to the assembly process of the rig.

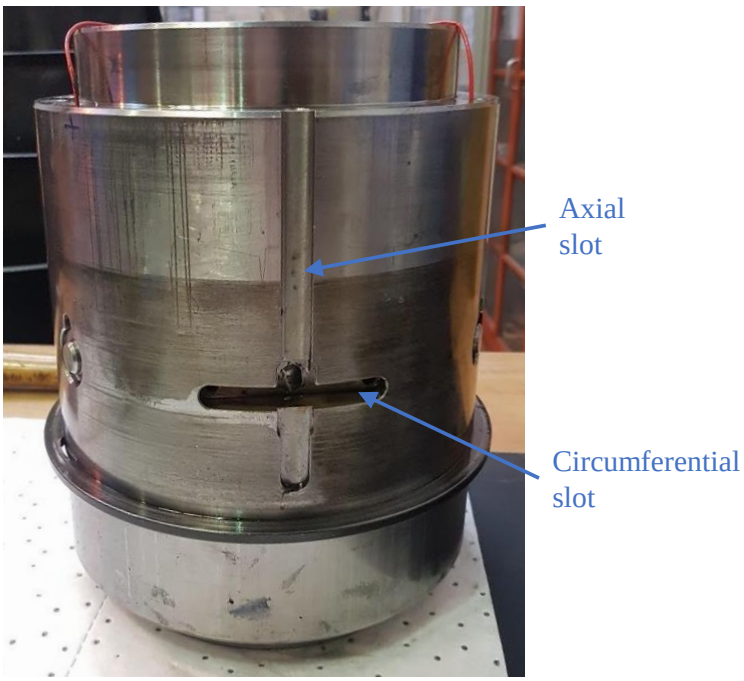

Figure 6.2: Bearing housing for the MuliLife rig showing the axial and circumferential slots to allow ultrasonic instrumentation.

6.2.2 Ultrasound Instrumentation and Data Acquisition

Much like the instrumentation in Section 4 but with the addition of shear sensors, 7 longitudinal sensors and 7 shear sensors were bonded to the raceway in the configuration shown in Figure 6.3. The number of sensors was based on limitations of acquisition hardware. The FMS is limited to eight channels and it was desirable to have a sensor aligned with the centre of the roller which requires an odd number of sensors. 7 sensors gave the maximum number of data points while fulfilling this requirement.

Sensors were aligned such that the centre point of the middle sensor was positioned at the centre of the raceway and the sensors were evenly spaced axially from this centre 11 mm apart. Spacing between the centre points of the row of longitudinal sensors and the row of shear sensors was approximately 2 mm.

10 MHz longitudinal sensors were selected so that results collected here were comparable to previous testing. Due to the shear speed of sound being approximately half of the longitudinal speed of sound, the frequency of the shear sensors was selected to be half that of the longitudinal (5 MHz) such that the wavelength, and thus the beam shape, were as similar as possible.

Both sets of sensors were cut to 5x1 mm strips and bonded to the raceway with strain gauge adhesive. Custom instrumentation jigs which matched the curvature of the raceway were used to hold the sensors in place during the curing process. These were made from EN31 steel and were wire EDM cut. Jig drawings can be seen in Appendix A. Bonded sensors can be seen in Figure 6.4 (a).

To allow for all of the cables to fit within the slot in the housing, micro-coaxial cable (0.4 mm diameter) was used. Live cables were soldered to the sensor electrode and ground cables were bonded directly to the raceway using silver epoxy. Following cabling, sensors were potted using an epoxy compound to protect them from damage during handling and installation, as shown in Figure 6.4 (b). Each of the 14 cables were connected to a thicker gauge coaxial cable to allow the use of SMB connectors on each end. Micro-coaxial and standard gauge coaxial cables were connected through a shielded junction box with a series of terminal connectors. The junction box can be seen in Figure 6.4 (c) circled in red.

The instrumented raceway was installed onto the bearing housing shown in Figure 6.2 such that the instrumented sensors sat inside the axial slot. This axial slot was located at bottom-dead-centre of the bearing when installed in the rig which coincided with the maximally loaded region of the bearing.

Unfortunately, after installation of the bearing into the rig it was discovered that shear sensor 5, as indicated by the red sensor in Figure 6.3, had short circuited. This was likely due to the more delicate electrode material on the shear sensors which is a result of slightly different manufacturing processes for the two sensor types. Measurements were taken using the 13 remaining functional sensors.

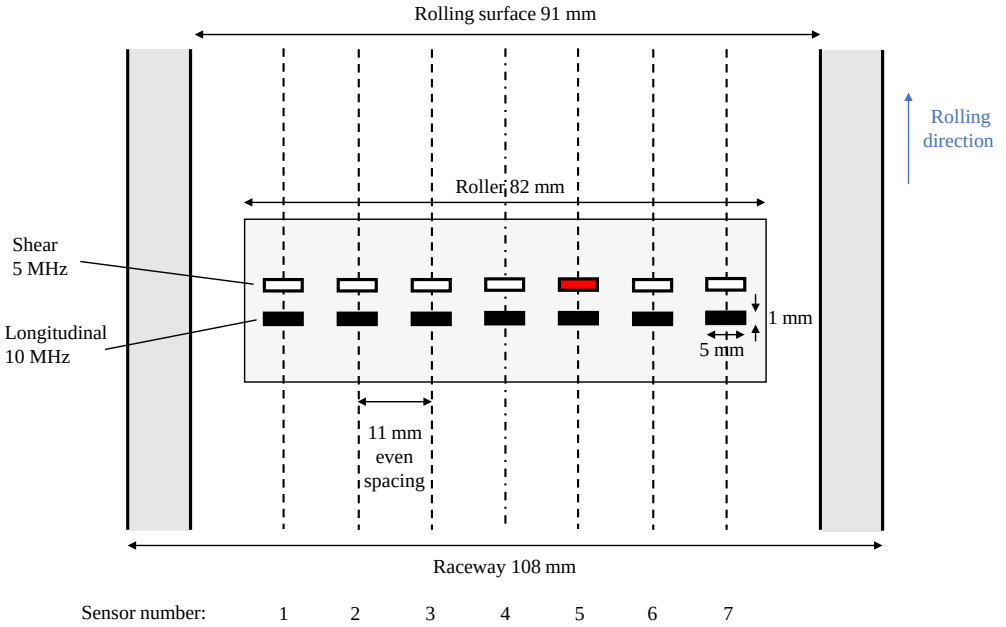

Figure 6.3: MultiLife bearing instrumentation schematic. The red sensor indicates that this sensor was not functional after installation into the rig.

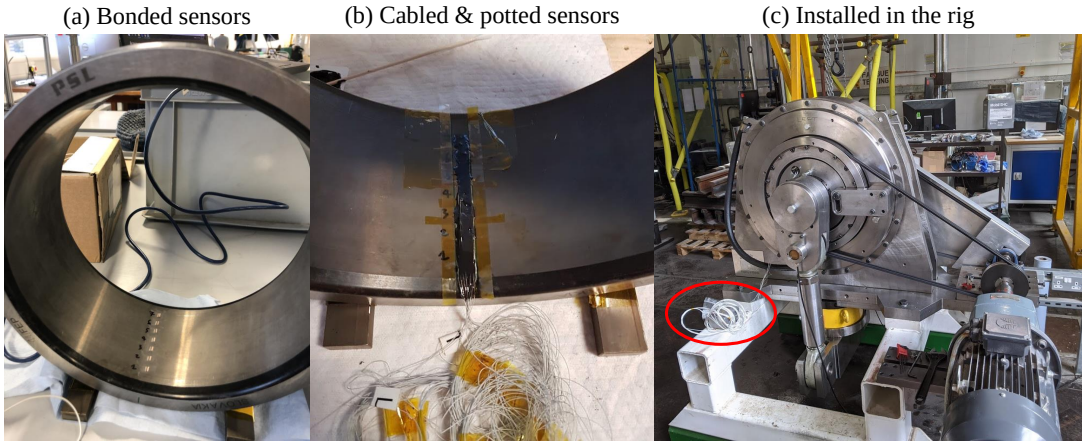

Figure 6.4: MultiLife bearing instrumentation process stages. (a) Sensors bonded to the raceway (b) Cabled and potted sensors (c) Instrumented raceway installed in the rig with junction box circled in red.

For measurement system basics and terminology refer to Section 3.5. This testing used an FMS for ultrasonic acquisition which was previously described in Section

4.2.3. The single difference here is the addition of a junction box between the UPR and sensor array in 4.5.

FMS settings were tuned to maximise the amplitude of the first reflection within the digitiser range. PRF was maximised to provide the best signal resolution in the rolling direction and each data set was captured for 10 s to allow several rotations of the full complement of rollers.

6.2.3 Test Matrix

Testing on the rig was split into three sets based on the three different lubricants tested. These were: Castrol Hyspin VG 32, Castrol Alpha SP 150 and Castrol Alpha SP 320. Their properties are summarised in Table 6.1 below.

Lubricant	Viscosity Grade	Density at 15 °C (kg/m^3)	Kinematic Viscosity at 40 °C (mm^2/s)	Kinematic Viscosity at 100 °C (mm^2/s)	Pressure-viscosity coefficient (Pa^{-1} $\times 10^{-3}$)
Castrol Hyspin VG 32	VG32	870 [106]	32 [106]	5.4 [106]	1.670 [41]
Castrol Alpha SP 150	VG150	890 [107]	150 [107]	14.5 [107]	2.057 [41]
Castrol Alpha SP 320	VG320	900 [107]	320 [107]	24.0 [107]	2.279 [41]

Table 6.1: Properties of lubricants used in testing.

For each of these sets of testing, load was varied from 0 to 1000 kN in 100 kN increments and speed was varied from 20 to 100 rpm in 20 rpm increments. For each of these increments the three sensor configurations in Table 6.2 were used to capture data. For each of these configurations, 3 repeats were taken. Overall a total of 1,485 tests were conducted.

Configuration	Ch 1	Ch 2	Ch 3	Ch 4	Ch 5	Ch 6	Ch 7	Ch 8
Longitudinal	L1	L2	L3	L4	L5	L6	L7	not used
Shear	S1	S2	S3	S4	S5	S6	S7	not used
Combination	L2	L3	L4	L6	S2	S3	S4	S6

Table 6.2: Sensor configurations.

6.3 Data Processing

Data was processed to obtain reflection coefficient and change in time of flight as described in Section 3.6. Other processing methods are described as they are introduced in the results.

6.4 Results and Discussion Layout

Much of the longitudinal data has been analysed in some detail already by Nicholas [41] who in investigated the following:

- How minimum reflection coefficient was affected by bearing load, speed and lubricant viscosity.
- The validity of converting MRC to lubricant film thickness.
- The ability of ultrasound sensors to detect lubricant behaviour between roller passes.
- The measurement of bearing speed through ultrasonic methods.
- Detection of misalignment using an array of ultrasonic sensors.
- Comparison of ultrasonic load measurements to applied bearing loads.

Nicholas' conclusions were:

- Minimum reflection coefficient decreased with increased load but showed no obvious trend with changing speed or lubricant.
- Reflection coefficient conversion to lubricant film thickness was not possible due to reflection coefficient dependence on frequency. It was suggested that this was due to the beam width of the transducer being larger than the contact width.
- Reflection coefficient pattern between roller passes can be used to indicate the lubrication condition of each roller and subsequently the whole bearing. Lubricant re-flow time was measured and found to be influenced directly by bearing load, and inversely by bearing speed and lubricant viscosity.
- Measurement of bearing speed through reflection coefficient trends was able to show instances with the higher viscosity lubricant (VG320) where the motor could not supply sufficient torque to maintain the desired speed. It may be

possible to use these techniques in combination with another method of bearing speed measurement to allow measurement of roller slip.

- Misalignment was perceivable from deflection measurements across the roller.
- Load measurements compared well with bearing applied load although the rig was slightly misaligned meaning that perfect agreement was not possible.

Because of Nicholas' [41] analysis, in this work some aspects of results were not analysed in such detail, however some of the presented work here duplicates the data presented by Nicholas. This was for comparative purposes for previous quasi-static testing (Chapter 4), data from shear sensors from this testing campaign, and further investigations using modelling in a following chapter (See Chapter 7).

The following sections are split into their aims:

- Investigation of fringe effects and their causes.
- The use of shear sensors to gain additional insight into bearing performance.
- Assessment of the ability of ultrasound sensors to detect misalignment.

6.5 Fringe Effect Investigation

In order for fringe effects to be fully defined their behaviour with varying experimental factors first requires definition. Reflection coefficient results will first be introduced, followed by ΔToF.

6.5.1 Reflection Coefficient

For ease of comparison to the following results Figure 3.19 is repeated as Figure 6.5 below.

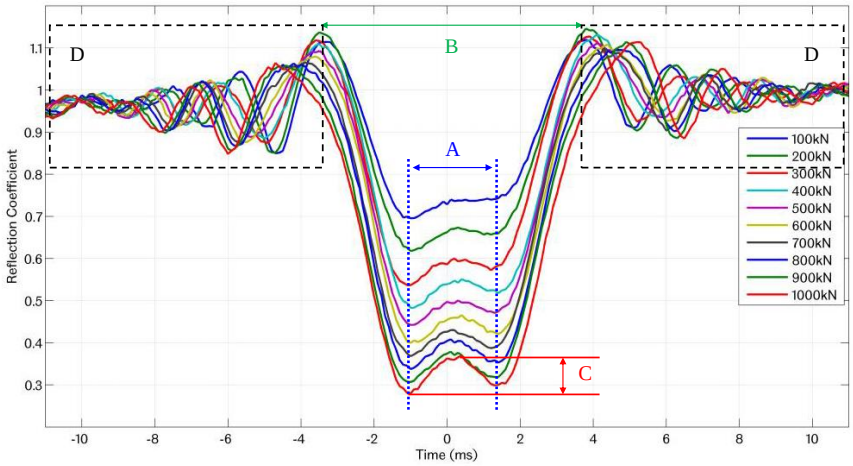

Figure 6.5: Reflection coefficient curves for a single roller pass at bearing loads between 100 and 1000 kN from previous testing [39]. Features A, B, C and D highlighted. Figure adapted from [39]

In Howard's [39] data increasing load resulted in a larger value for the width of the W shape (feature B) and an increase in magnitude of the central peak (feature C). The width between the two minima in the W shape (feature A) and the decay rate of the side fringes (feature D) were independent on load. Howard [39] makes no mention of the relationship of any of these features with speed and only tested with one lubricant (VG32).

6.5.1.1 Effect of Frequency

The frequency response of the longitudinal sensors is shown in Figure 6.6. It can be seen that the central frequency of the sensors was slightly less than the intended frequency of 10 MHz, with most sensors having central frequencies of around 8 MHz. The -6 dB bandwidth of the sensors (50% drop from peak amplitude) was around 6 to 10 MHz and the -20 dB bandwidth (90% drop from peak amplitude) was around 4 to 13 MHz. The full frequency bandwidth was around 2 to 14 MHz.

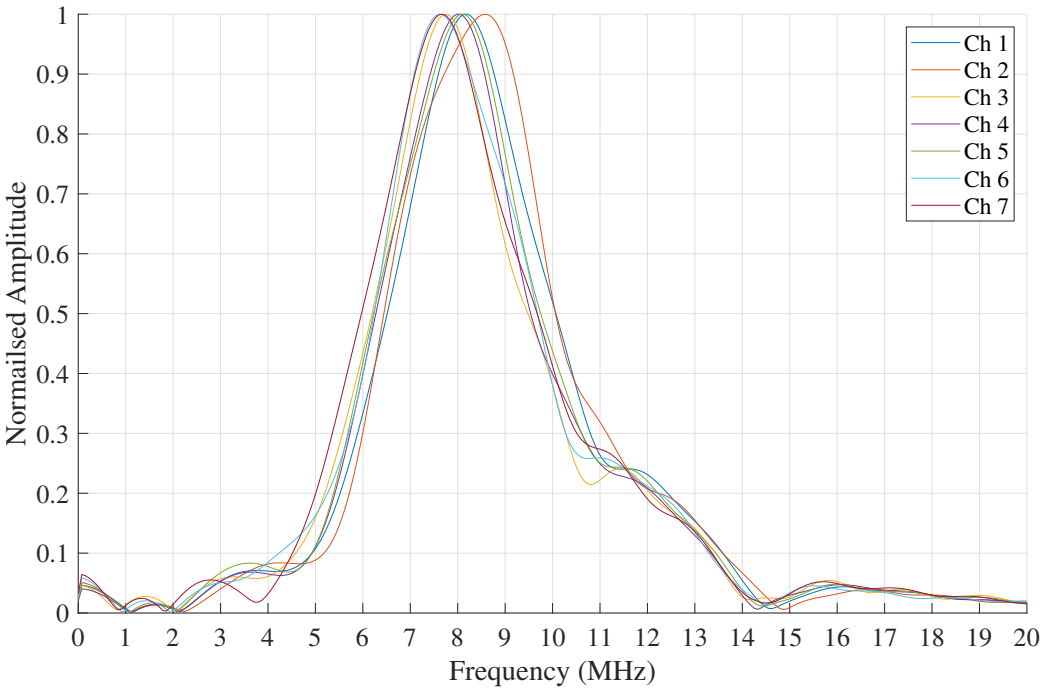

Figure 6.6: Sensor frequency responses for all 7 sensors from the reference signals of longitudinal data from the MutiLife rig.

Figure 6.7 shows an example spectrogram across the full bandwidth of a longitudinal sensor. Fringe effects are clearly visible in this plot across the full range of frequencies and this was the case across all lubricants, loads, speeds, and sensor channels tested.

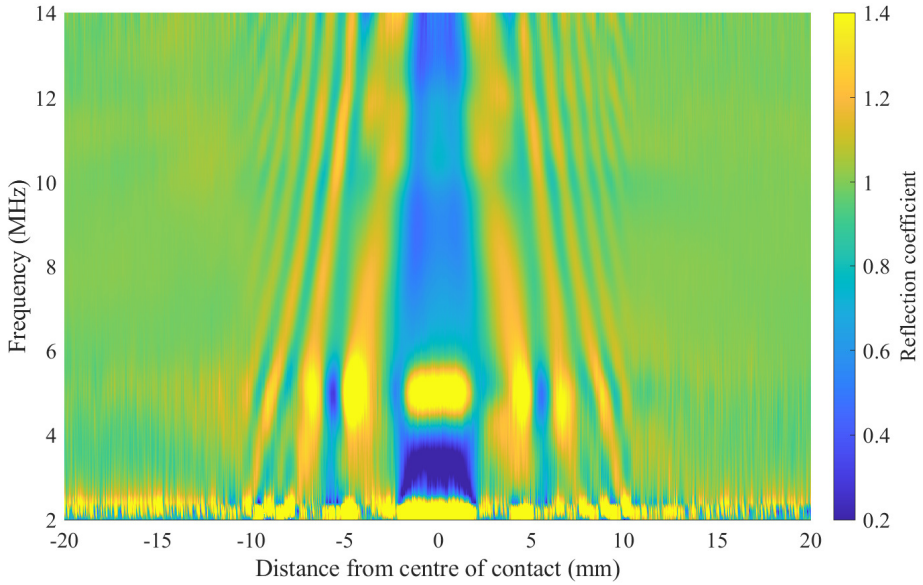

Figure 6.7: Spectrogram, VG150 lubricant, 500 kN, 60 rpm, repeat 2, channel 2.

The frequency response of the shear sensors is shown in Figure 6.8. It can be seen that the central frequency of the sensors was slightly higher than the intended frequency of 5 MHz, with most sensors having central frequencies of around 6 MHz. The -6 dB bandwidth of the sensors (50% drop from peak amplitude) was around 5 to 8 MHz and the -20 dB bandwidth (90% drop from peak amplitude) was around 3 to 9 MHz. The full frequency bandwidth was around 2 to 10 MHz.

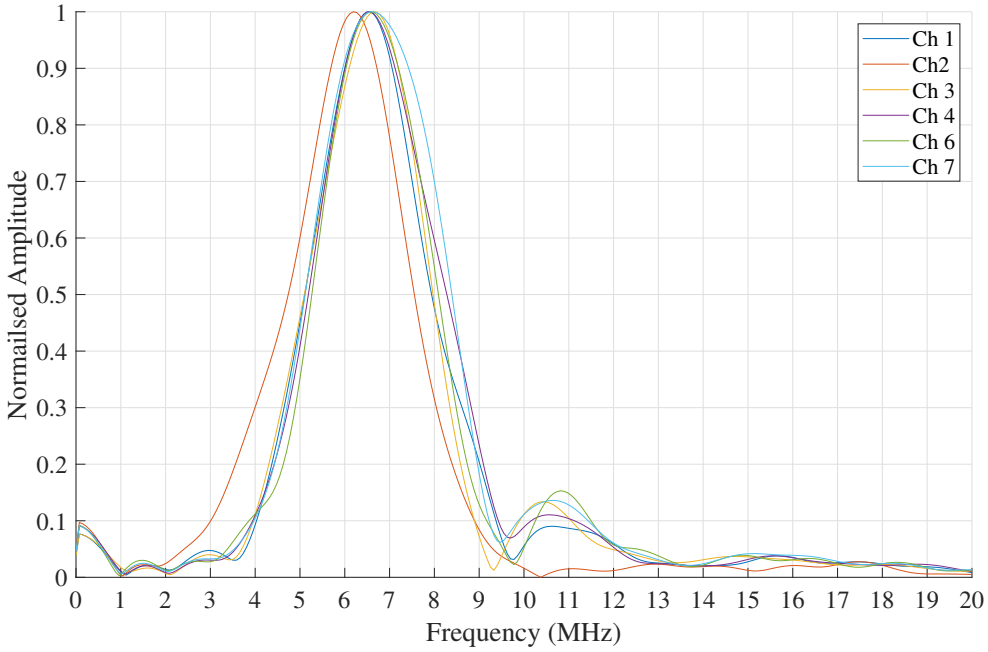

Figure 6.8: Sensor frequency responses for all 7 sensors from the reference signals of shear data from the MutiLife rig.

Figure 6.9 shows an example spectrogram across the full bandwidth of a shear sensor. This figure was from the same test as Figure 6.7. As with longitudinal data, fringe effects are clearly visible in this plot across the full range of frequencies and this was the case across all lubricants, loads, speeds, and sensor channels tested.

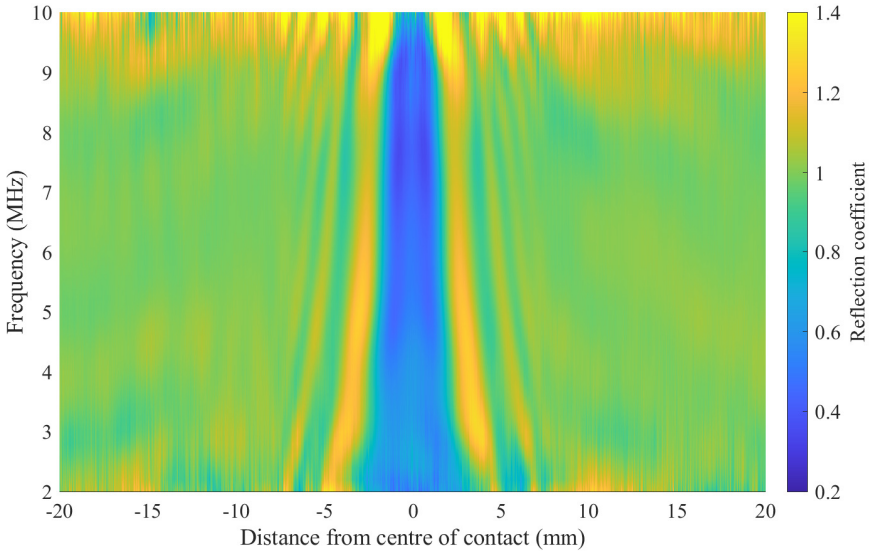

Figure 6.9: Spectrogram, VG150 lubricant, 500 kN, 60 rpm, repeat 2, channel 2.

The first noticeable difference between the longitudinal and shear spectrograms was the peak in reflection coefficient in the longitudinal data at around 5 MHz which was not present in the shear data, the cause of which is unclear. The other difference between these two figures is the widths of the features which are narrower in the shear case, which is addressed below.

A section across Figures 6.7 and 6.9 at their central frequencies shows the reflection coefficient trend for a single roller pass, as shown in Figure 6.10. In this case the central W shape width (both feature A and B) was larger for the longitudinal sensor.

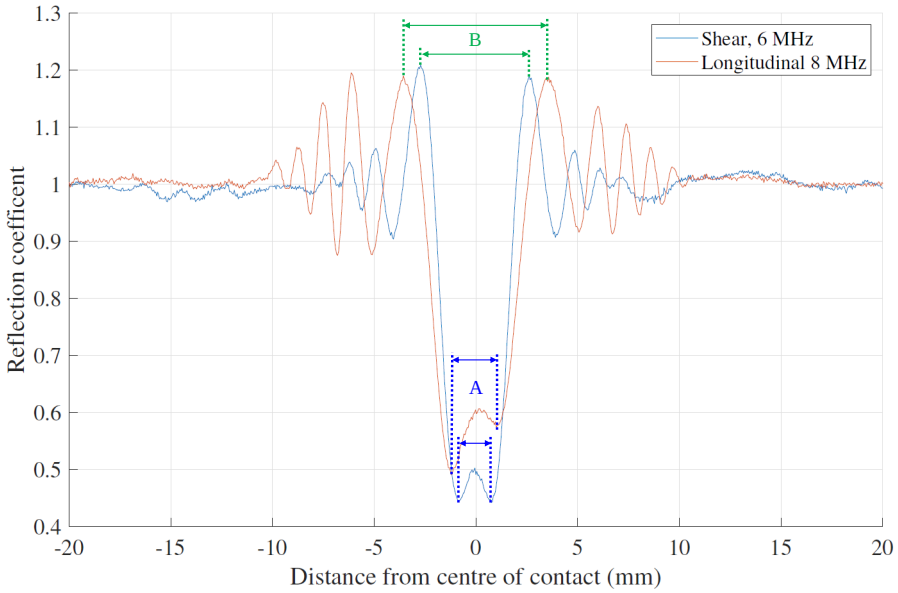

Figure 6.10: Example data to show how frequency affects the trend in reflection coefficient for a single roller pass. VG150 lubricant, 500 kN, 60 rpm, repeat 2, channel 2.

If this graph is re-plotted and instead of cutting through Figures 6.7 and 6.9 at 8 and 6 MHz, the cut is at 10 and 5 MHz then the central W shape is now almost the same width for the shear and longitudinal sensors, as shown in Figure 6.11.

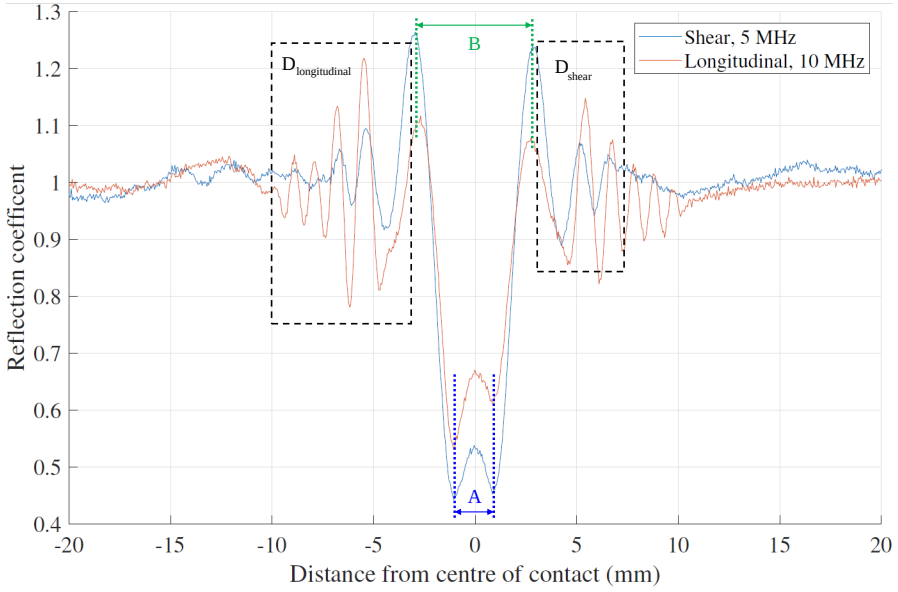

Figure 6.11: Example data to show how frequency affects the trend in reflection coefficient for a single roller pass. VG150 lubricant, 500 kN, 60 rpm, repeat 2, channel 2.

This shows that the width of the W shape (features A and B) is frequency dependent but also that this is likely due to the width of the sensor beam. At 10 and 5 MHz the sensor beam of the longitudinal and shear sensors were similar as the decrease in frequency offset the decrease in speed of sound of the shear sensor. It does not, however, explain why the fringes either side of the W shape (feature D) continue further for the longitudinal sensor than for the shear sensor.

Other noticeable differences between Figures 6.10 and 6.11 are the changes in amplitudes. With increasing frequency the minimum value for reflection coefficient increased for the longitudinal sensor, but did not significantly change for the shear sensor. Side fringe amplitude increased with increasing frequency for the longitudinal sensor but did the opposite for the shear sensor. The closest of the side fringes to the contact, both at the inlet and outlet also behaved differently from the rest of the side fringes. For both the longitudinal and shear sensors the amplitude of this fringe decreased with increasing frequency. These complex changes suggest that there are multiple mechanisms which interact to form fringe effects.

In order for comparison to ΔToF to be possible, the following reflection coefficient plots are plotted at the central frequencies of 8MHz for longitudinal sensors and 6 MHz for shear sensors.

6.5.1.2 Single Roller Pass Trends

Longitudinal: Figure 6.12(a), (b) and (c) shows how reflection coefficient changed with load, speed and lubricant respectively for a single roller pass monitored by a longitudinal sensor. Distance was calculated from bearing speed and known bearing geometry as described in Section 2.2 and roller passes were manually aligned. A clear trend of decreasing reflection coefficient at the centre of the contact with increasing load was seen, however no clear trend was evident with changing speed. There was also no clear trend with changing lubricant viscosity.

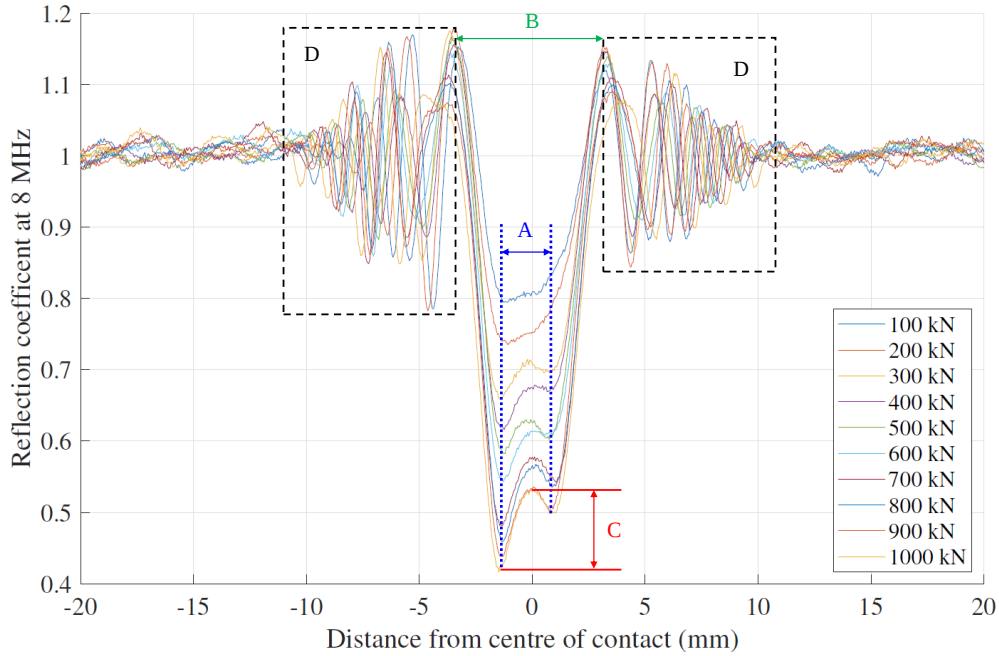

(a) VG150 oil, 60 rpm, repeat 2, channel 4. Labelled with featured A, B, C and D.

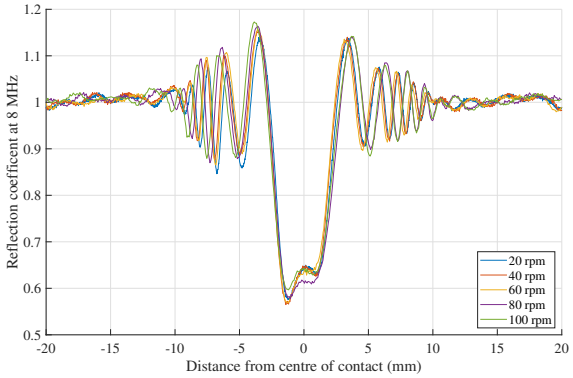

(b) VG150 oil, 500 kN, repeat 2, channel 4.

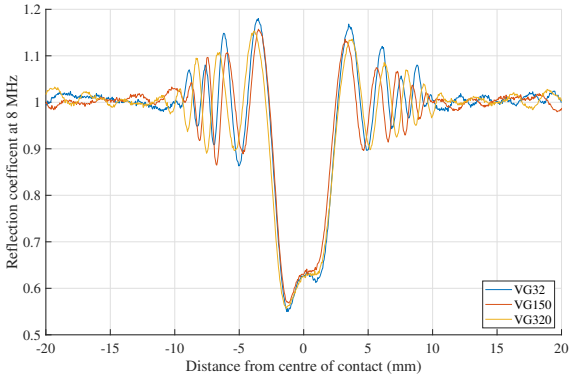

(c) 60 rpm, 500 kN, repeat 2, channel 4.

Figure 6.12: Example data from a longitudinal sensor to show the trend in reflection coefficient for a single roller pass was affected by changing (a) load, (b) speed and (c) lubricant viscosity.

The shape of the reflection coefficient plots seen in Figure 6.12(a) are closely comparable to those seen previously on the same rig, shown in Figure 6.5 [39]. The signal shape was largely the same and features of the signal mostly behaved in the same manner with changing load. There were, however, some slight differences.

One notable difference was the symmetrically of the central W shaped dip. The W shape was less symmetrical in these results (Figure 6.12(a)) than in previous testing (Figure 6.5). That is, there was a greater difference in amplitude between the two minima that make up the boundaries of feature A. This asymmetry was

present regardless of load, lubricant or speed. The asymmetry was also evident in the amplitude of the side fringes (feature D). The inlet side fringes were larger in magnitude than the outlet side fringes. It is difficult to comment on the cause of this asymmetry as the cause of fringe effects are not yet fully understood. The cause could have been differences in contact conditions or those around the contact. Asymmetric distribution of lubricant either side of the contact was the most likely cause of the difference.

Another difference between data in Figures 6.5 and 6.12(a) was that the width of feature B was far more dependent on load in Figure 6.5 than in Figure 6.12(a). In fact, in Figure 6.12(a) all of the B widths are almost exactly the same other than the 1000 kN case. This is likely to be as a result of the different frequency response of the sensors in the two studies and the effect this change in frequency has on the mechanism(s) which cause fringe effects.

Shear: Figure 6.13(a), (b) and (c) shows how reflection coefficient changed with load, speed and lubricant respectively for a single roller pass monitored by a shear sensor.

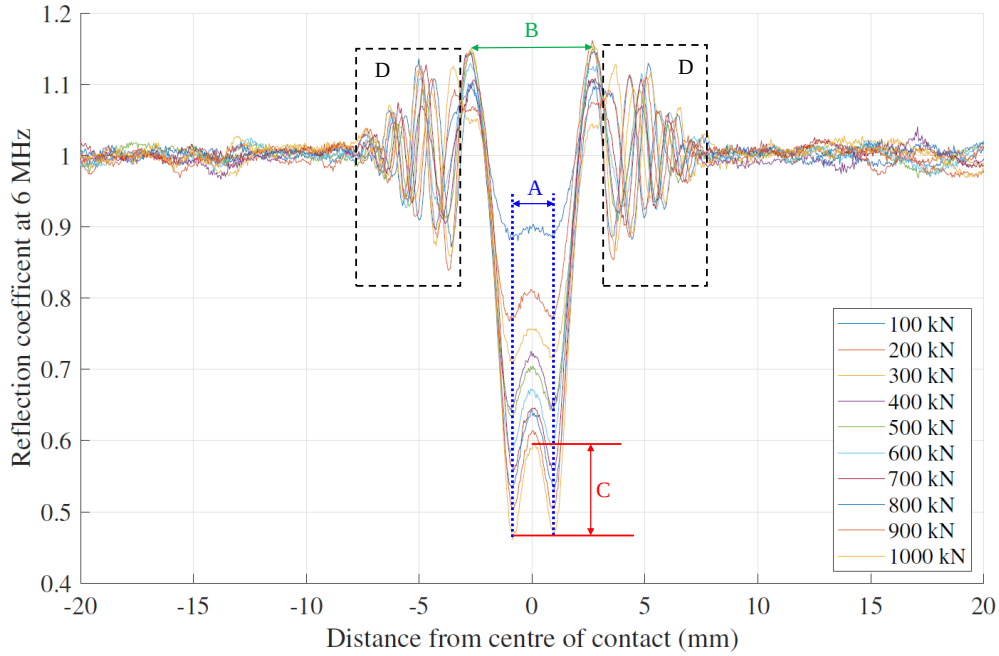

(a) VG150 oil, 60 rpm, repeat 2, channel 4. Labelled with featured A, B, C and D.

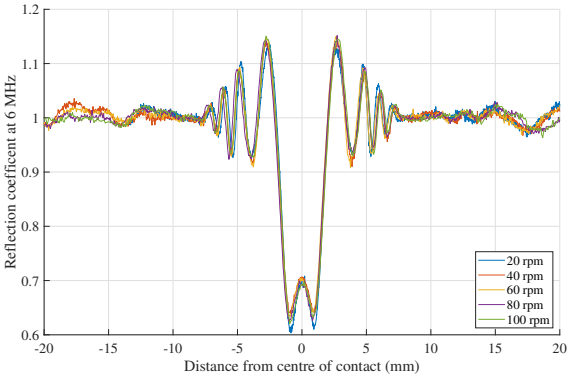

(b) VG150 oil, 500 kN, repeat 2, channel 4.

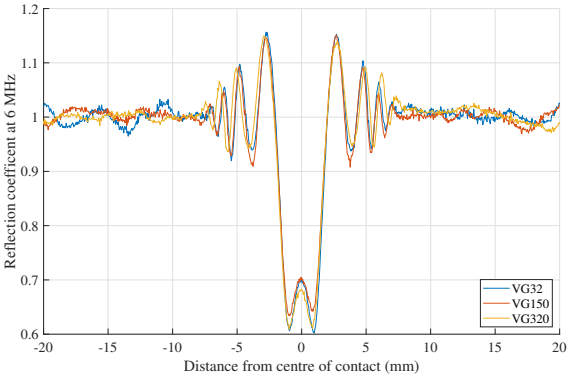

(c) 60 rpm, 500 kN, repeat 2, channel 4.

Figure 6.13: Example data from a shear sensor to show the trend in reflection coefficient for a single roller pass was affected by changing (a) load, (b) speed and (c) lubricant viscosity.

The same trends were visible here as with the longitudinal sensors: a trend of decreasing reflection coefficient at the centre of the contact with increasing load was seen and no clear trend was evident with changing speed or lubricant viscosity. The features A, B, C and D of the signal in Figure 6.13(a) also behaved in much the same way as the longitudinal data in Figure 6.12(a) with changing load. One notable difference between Figures 6.12 and 6.13 is that the central W shape was much more symmetrical for the shear data, as were the amplitudes of the side fringes (feature D). Again, the reason for this is unknown, but points to the asymmetry in the longi-

tudinal being due to some lubricant effect as shear sensors would be less sensitive to changes in lubricant than longitudinal ones.

The fact that shear and longitudinal sensors show very similar fringe effects suggests that the same mechanisms cause these interference pattern in both sensor types. Differences between longitudinal and shear signals are likely due to the inherent differences in the sound modes, i.e. that shear sound waves are not supported in liquids. This means that mechanisms which can remove fringe effects from longitudinal signals would also be very likely to remove them from shear signals.

This much more detailed overview of trends in interference patterns also enabled a model based investigation into fringe effects to be undertaken in Chapter 7.

6.5.1.3 Effect of Changing Window Length

Figure 6.14 shows example reference Ascans windowed around the first reflection for both a longitudinal and a shear sensor. It was discovered that by reducing the amount of the Ascan used, the severity of the fringe effects in the signal was reduced, up to a point. The following figures show reflection coefficient plots for a single roller pass where the first reflection was trimmed to 30, 50, 70 and 90% of its original length during processing.

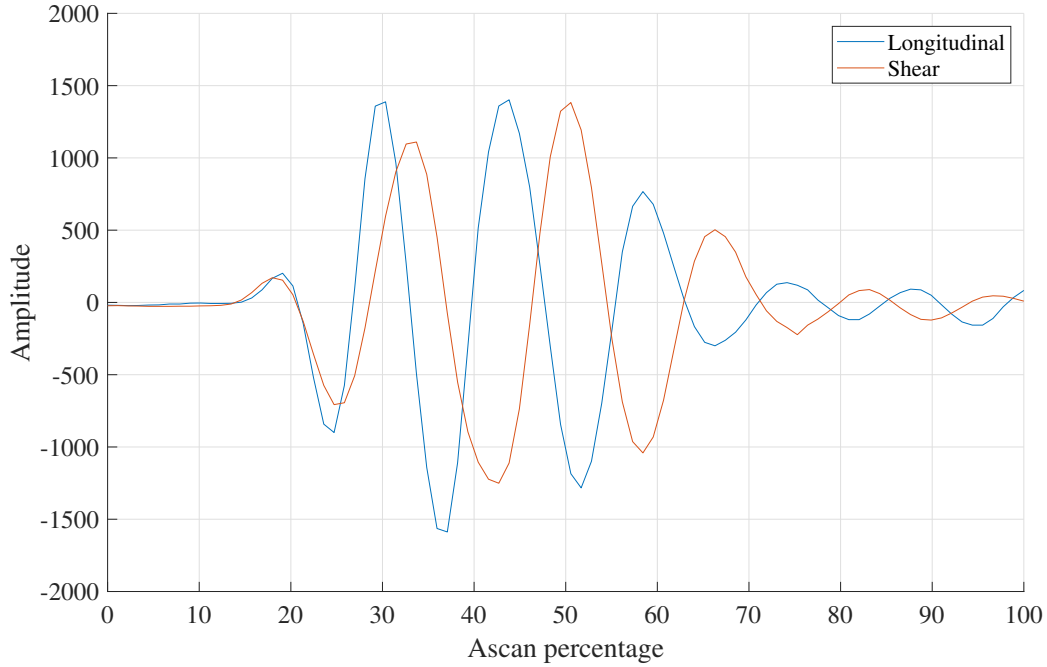

Figure 6.14: Ascans percentage.

Figures 6.15 and 6.16 show how this affected typical longitudinal and shear data respectively.

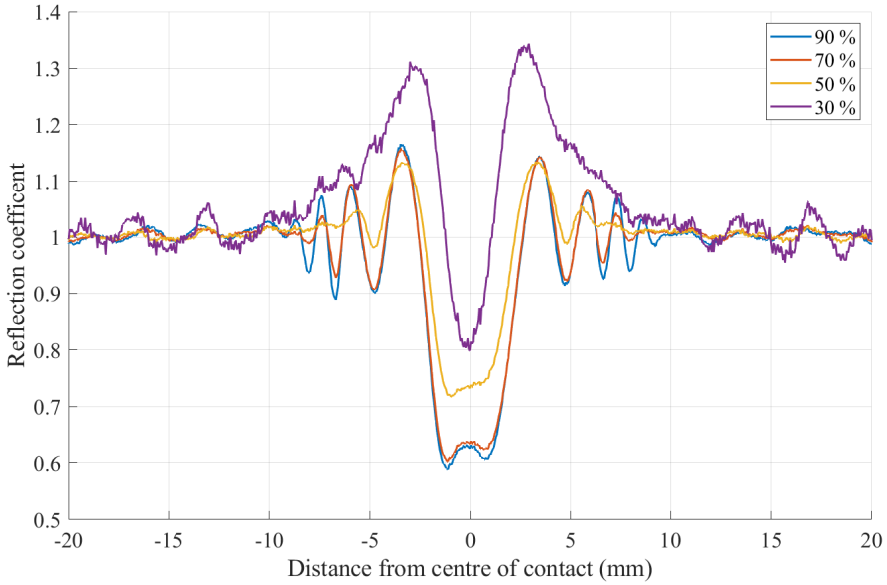

Figure 6.15: The effect of changing A-scan percentage on longitudinal, VG150, 500 kN, 60 rpm, channel 4 data.

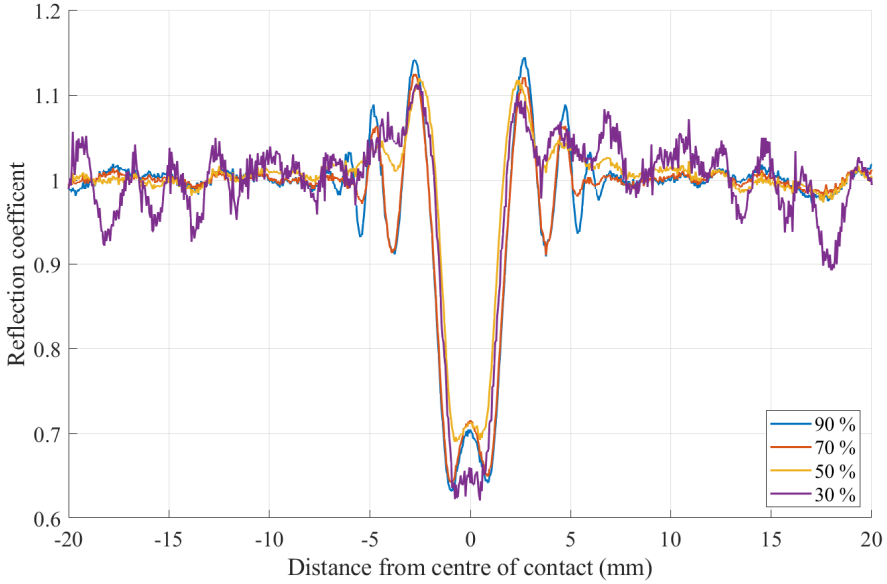

Figure 6.16: The effect of changing A-scan percentage on shear, VG150, 500 kN, 60 rpm, channel 4 data.

Both show how the magnitude and width of the side fringes (feature D) were reduced

with a shorter window length, along with the magnitude of the central peak in the W shape (feature C). This was, however, only up to a point. The 30% window shows how data quality quickly deteriorated once there was an insufficient proportion of the first reflection remaining.

The fact that these features can be partially removed from signals by cropping the latter part of the signal means that these features appear more strongly in the latter part of the reflection, meaning that they are all likely to be caused, at least in part, by beam spread. Figure 6.17 shows how portions of the ultrasound beam that spread further away from the transducer will have longer path lengths and thus will take longer to return to the sensor and appear in the latter part of the signal.

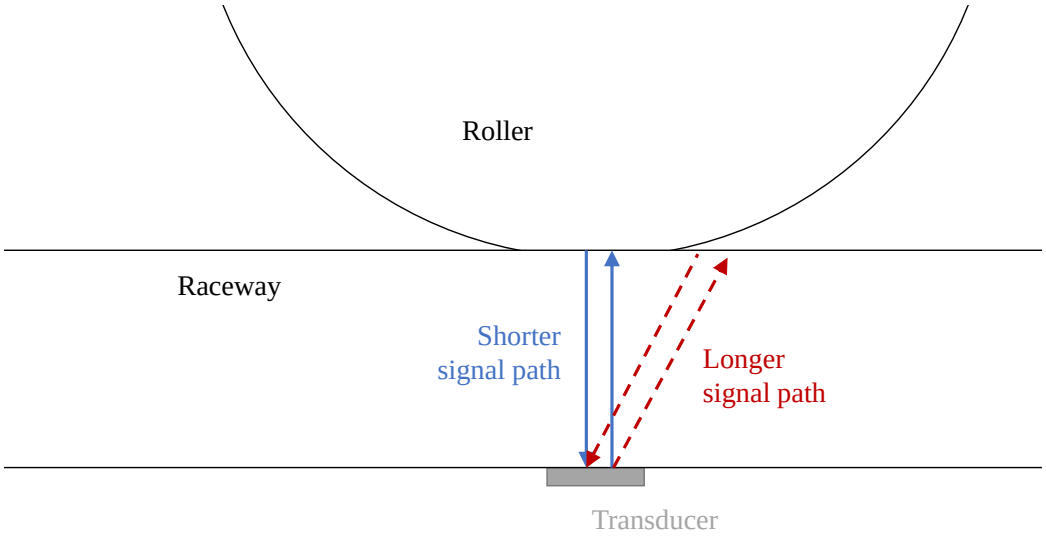

Figure 6.17: Illustrating the different path lengths caused by beam spread of an ultrasonic transducer.

6.5.2 Change in Time of Flight

Interference patterns (fringe effects) in ΔToF plots have not previously been addressed or compared with the interference patterns in reflection coefficient results. This section investigates whether fringe effects in ΔToF significantly affect the measurements.

6.5.2.1 Single Roller Pass Trends

With both longitudinal and shear sensors, ΔToF trends across a single roller pass largely resembled those seen with reflection coefficient, only inverted. They also

followed the same inverted trends with changing load, speed and lubricant. Instead of a central W shape, ΔToF plots had a central M shape.

Longitudinal: Figure 6.18(a) shows that the maximum change in time of flight increased with load. Figures 6.18(b) and 6.18(c) show that there was minimal change with speed and lubricant.

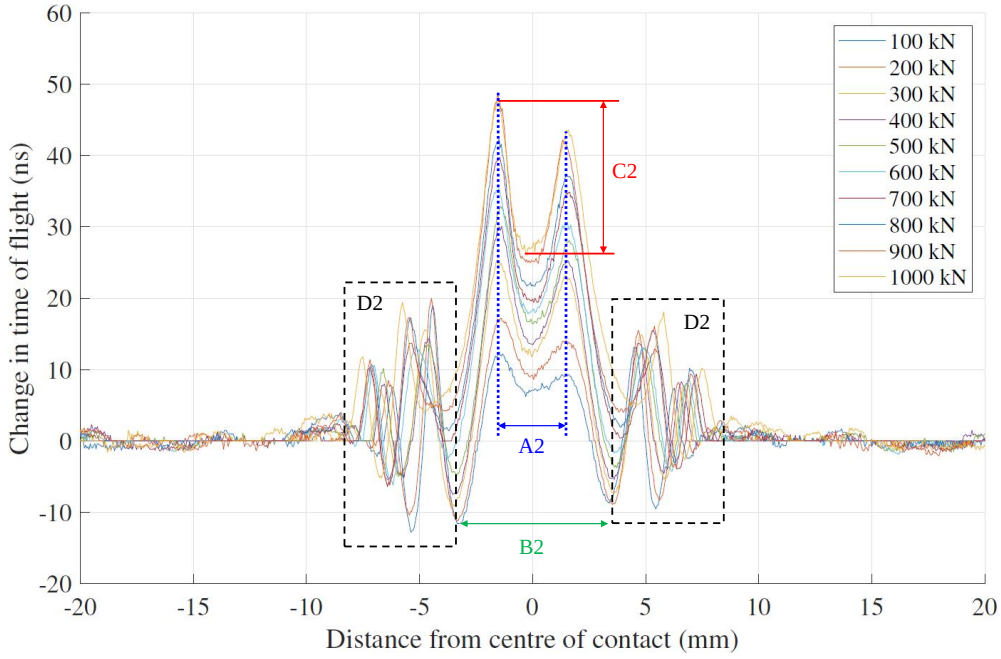

(a) VG150 oil, 60 rpm, repeat 2, channel 4. Labelled with featured A2, B2, C2 and D2.

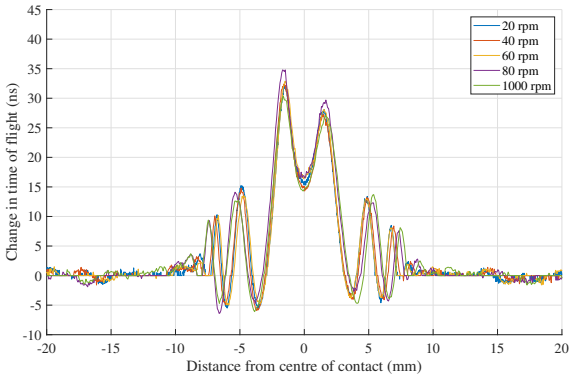

(b) VG150 oil, 500 kN, repeat 2, channel 4.

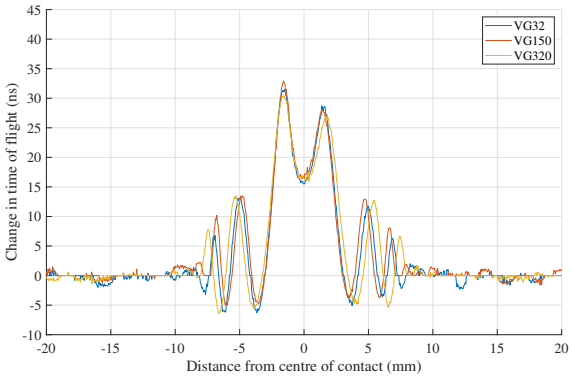

(c) 60 rpm, 500 kN, repeat 2, channel 4.

Figure 6.18: Example data from a longitudinal sensor to show the trend in change in time of flight for a single roller pass was affected by changing (a) load, (b) speed and (c) lubricant viscosity.

Differences between reflection coefficient and ΔToF load trends can be seen by comparing Figures 6.12(a) and 6.18(a). Feature A in 6.12(a) corresponds to Feature A2

in Figure 6.18(a), and the same applies to features B, C, D, B2, C2 and D2.

As with feature A, the width of feature A2 remained constant with increasing load. Feature C2 also behaved in a similar manner to feature C. The height increased with increasing load, although by a greater relative amplitude. This difference cannot currently be explained.

Feature B2 widened with increasing load, whereas feature B was mostly constant. This was likely caused by slight changes in the frequency spectrum of reflections at differing loads as these cannot be accounted for in ΔToF processing whereas they were with R processing. A reduction in frequency would increase the width of feature B but would also effect feature A so must only be present at the contact entry and exit.

Feature D2 was narrower than feature D but the relative amplitude of feature D2 compared to the maximum ΔToF was similar to the amplitude of feature D compared to MRC. The narrower side fringes (feature D/D2) cannot be explained with current knowledge of fringe effects. The side fringe amplitudes were asymmetrical in D2 in the same way as seen with feature D. Similarly, the ΔToF M shape was asymmetrical in the same direction as the reflection coefficient W shape.

Shear: As with longitudinal data, Figure 6.19(a) shows that the maximum change in time of flight increased with load. Figures 6.19(b) and 6.19(c) show that there was minimal change with speed and lubricant.

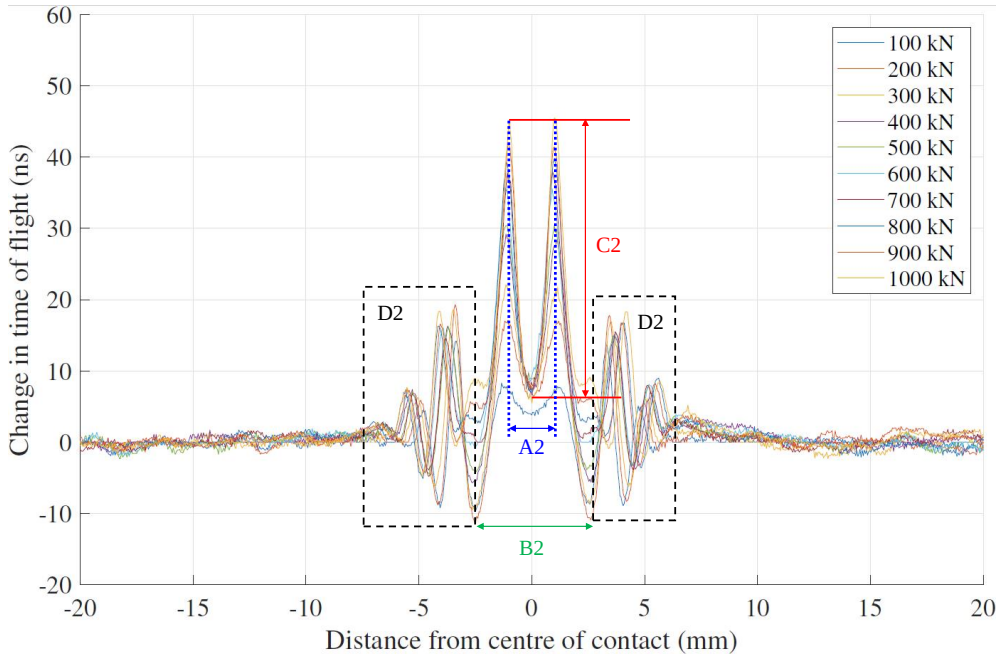

(a) VG150 oil, 60 rpm, repeat 2, channel 4. Labelled with featured A2, B2, C2 and D2.

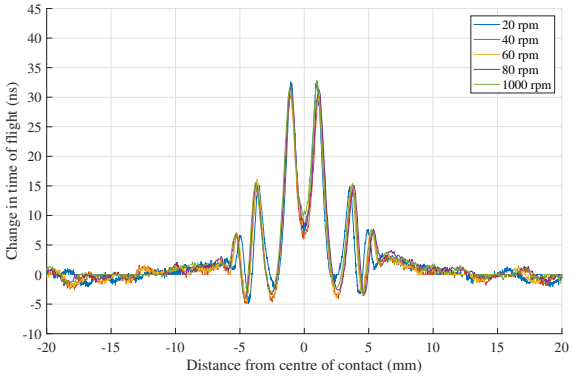

(b) VG150 oil, 500 kN, repeat 2, channel 4.

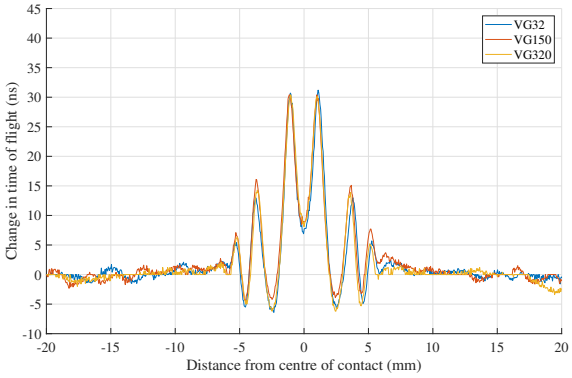

(c) 60 rpm, 500 kN, repeat 2, channel 4.

Figure 6.19: Example data from a shear sensor to show the trend in change in time of flight for a single roller pass was affected by changing (a) load, (b) speed and (c) lubricant viscosity.

The width of the shear M shape was narrower than in the longitudinal graph which may be explained by the same reasoning as previously described: the beam widths were likely different at the central frequency of the sensors. As with reflection coefficient results, the M shape was more symmetrical for shear results than longitudinal results.

Differences between reflection coefficient and ΔToF load trends can be seen by comparing Figures 6.13(a) and 6.19(a). Features A2, B2, C2 and, D2 differed from features A, B, C and D in exactly the same ways as with the longitudinal data.

Summary: The strong similarity of interference patterns in ΔToF with fringe effects in reflection coefficient plots is compelling evidence that the same phenomena cause both sets of interference. The overall shape and changes with load speed and lubricant were the same and any differences were small. The majority of these differences have also been explained.

This casts serious doubt on ΔToF and subsequent deflection and load measurement. It has been shown that fringe effects seriously distort reflection coefficient measurements so it is very likely that ΔToF measurements were distorted by fringe effects too.

6.5.2.2 Maximum Change in Time of Flight

Plotting maximum ΔToF against all of the test variables enables us to see a good overview of the testing. Figure 6.20 shows that maximum ΔToF increased with bearing load for both the longitudinal and shear sensors and was not significantly affected by lubricant viscosity. Figure 6.21 shows that maximum ΔToF was not significantly affected by speed either. These trends were expected although it is worth noting that these were the exact same inverse trends as with minimum reflection coefficient, which will be introduced later in this chapter (see Figures 6.22 and 6.23).

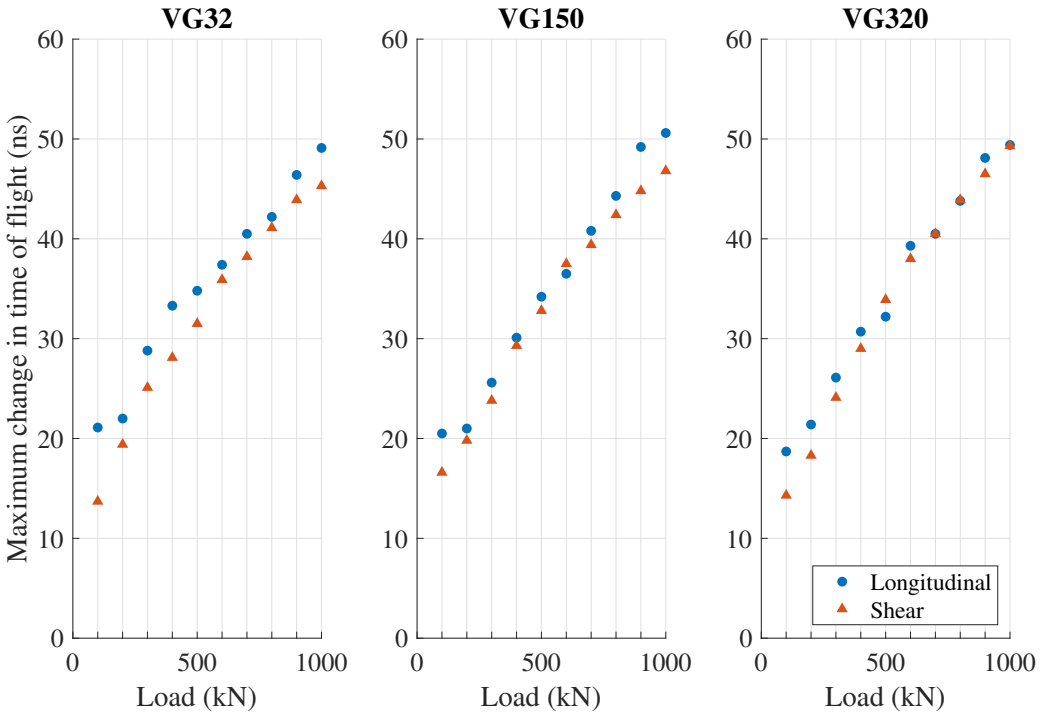

Figure 6.20: Maximum change in time of fight with changing load. VG320 lubricant, 60 rpm, repeat 2.

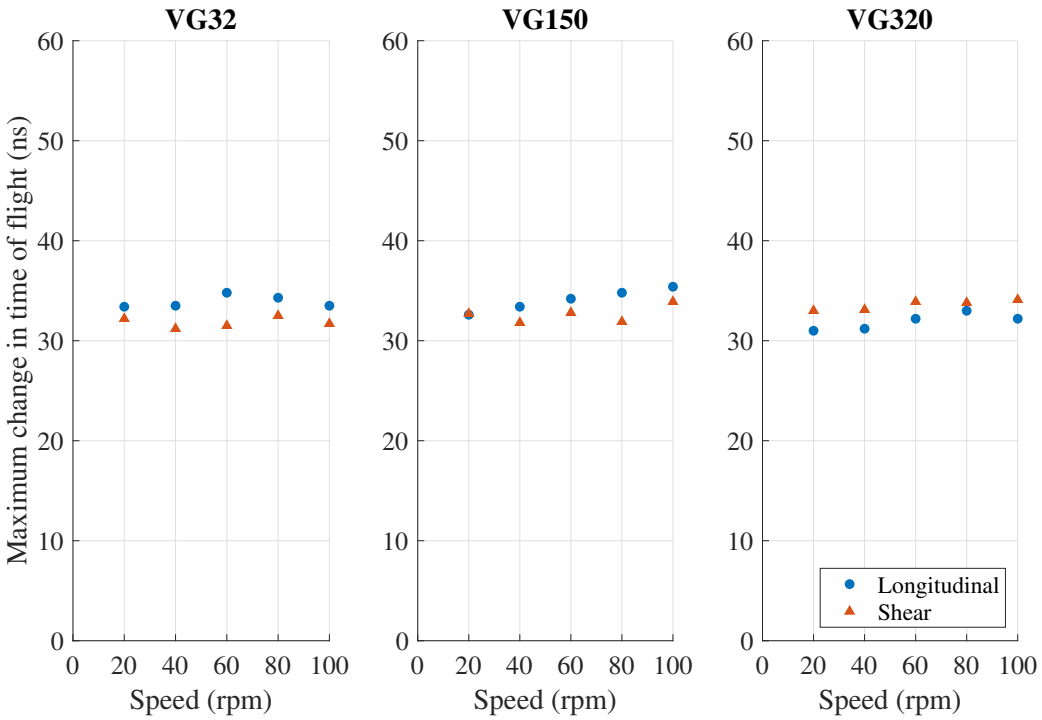

Figure 6.21: Maximum change in time of fight with changing load. VG320 lubricant, 60 rpm, repeat 2.

What was not expected was that maximum shear values were very similar to maximum longitudinal values. Using Equation 3.19 we can convert both longitudinal and shear change in time of flight values to deflection. For the longitudinal sensors L = -2.26 [41] and c_0 = 5960 m/s. This gives a multiplication factor of approximately 1828 for conversion to deflection. For the shear sensors L = -0.25 [41] and c_0 = 3220 m/s which gives a multiplication factor of 2576. This is 1.4 times the longitudinal factor and therefore shear values would be expected to be around 70% of longitudinal values. Shear values would therefore significantly over-predict when converted to load, as Nicholas [41] showed that longitudinal values were in reasonable agreement with rig applied bearing loads.

This poses the question of whether change in time of flight measurements were significantly affected by fringe effects. Perhaps shear measurements were more significantly affected than longitudinal measurements, but without fully understanding their cause it is difficult to say why this would be the case. What is more likely is that fringe effects dominate the signal and there is only a small contribution to the overall signal by actual deflection.

Ultrasound predicted loads have agreed well with applied loads in the past [82, 41]

so there is clearly some correlation between the magnitude of fringe effects in ΔToF measurements and load. Perhaps, instead of measuring deflection, these methods relate to some other contact parameter that directly influences the magnitude of fringe effects. The most likely contender is contact width.

6.6 Additional Insights Into Bearing Performance Through the Use of Shear Sensors

The aim of this section of work was to use shear sensors to gain any additional insights into bearing operation, in particular to determine whether the lubrication regime was mixed or fully separated.

6.6.1 Indication of Lubrication Regime

As previously mentioned, the concept behind the use of shear waves is that a fully separated contact should give a reflection coefficient of 1 for a shear sensor and a reflection coefficient of less than 1 for a mixed lubrication contact. This is based on the assumption that a liquid film cannot support a shear wave.

6.6.1.1 Testing Overview

Plotting MRC against all of the test variables provides an overview of the testing. Figure 6.22 shows how MRC decreased with increasing load for both longitudinal and shear data at sensor 4.

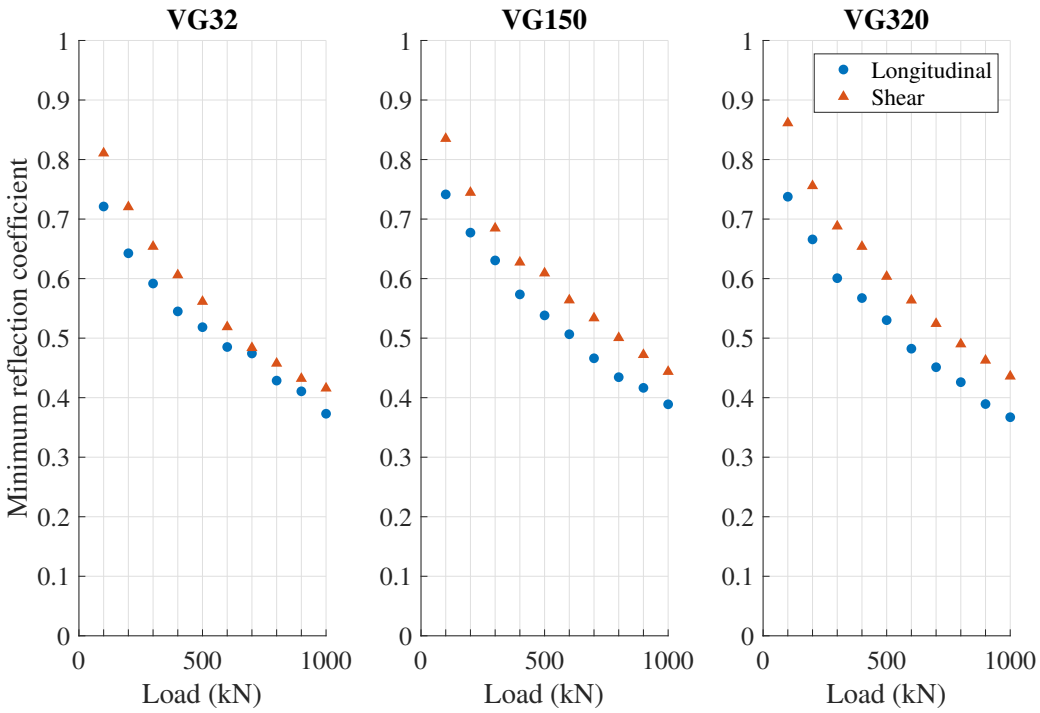

Figure 6.22: Data overview with changing load. Sensor 4, longitudinal 8 MHz, shear 6 MHz.

Figure 6.23 shows that speed did not significantly change the MRC values of either longitudinal or shear data.

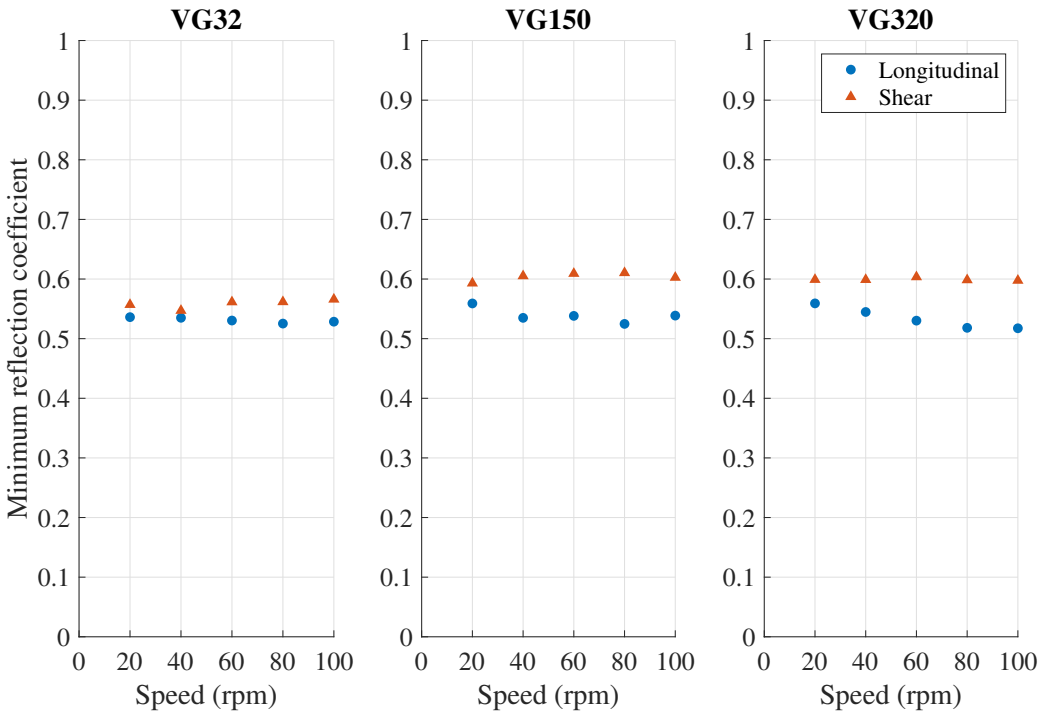

Figure 6.23: Data overview with changing speed. Sensor 4, longitudinal 8 MHz, shear 6 MHz.

MRC can also be seen to have no significant trend with increasing lubricant viscosity for both the longitudinal and shear data, although a slight increase in shear MRC can be seen from both of the previous figures.

To enable assessment of what additional information the shear sensors provide, first the insights longitudinal sensors provide must be summarised.

Longitudinal: For the longitudinal data, increasing load should have decreased film thickness and increased asperity contact in mixed lubrication. This should have increased contact stiffness whether the contacts were fully separated or in a mixed lubrication regime, therefore reducing reflection coefficient. This trend was observed in all of the data.

Film thickness should increase with increasing speed and therefore longitudinal MRC values should have increased whether the surfaces were fully separated or in a mixed regime. In actuality MRC slightly decreased and thus the trend is difficult to explain.

An increased lubricant viscosity should increase the film thickness. In the case of fully separated surfaces this should have increased MRC values of the longitudinal sensors. If the contact were in mixed lubrication, the longitudinal data should have

seen increasing MRC values because the number of asperity contacts should have been reduced. This trend of increasing MRC with increased lubricant viscosity was not seen.

Overall, longitudinal sensors did not behave as expected. Results suggest that all of the measurements were in the mixed lubrication regime and that contact stiffness was dominated by contact pressure. An alternative theory is that reflection coefficients were distorted by the cause of fringe effects such that some other contact parameter was being measured instead of contact stiffness. One possibility for this parameter is contact width.

Shear: If the contacts were fully separated, shear MRC should not have changed with load and should have remained at 1. In the case of mixed lubrication, MRC was expected to decrease with load due to increased asperity contact. The mixed film trend was seen in the collected data, which indicates that all of these tests had mixed film lubrication.

With increasing speed shear MRC values should not have significantly changed if the surfaces were fully separated and should have increased if they were in a mixed film regime. As shear values did not significantly change with speed, this indicates the contacts were all fully separated, in contrast to the load trend.

With increased lubricant viscosity shear MRC values should not have significantly changed if the surfaces were fully separated. If the contact was in mixed lubrication, the shear data should have seen increasing MRC values because the number of asperity contacts should have been reduced. The slight increase in shear MRC with increasing load indicates the bearing is in mixed mode lubrication.

Like longitudinal sensors, shear sensors did not entirely behave as expected. This may also be explained by reflection coefficient distortion due to the cause of fringe effects. An alternative explanation may also be that the lubricant was under sufficient pressure in the contacts to support shear waves.

6.6.1.2 The Presence of a Dip in Reflection Coefficient

One major observation here is that there were almost no cases of a longitudinal sensor observing a signal from a roller pass where a shear sensor did not. This was a very strong indicator that all of the contacts were in a mixed lubrication mode. There were, however, a few occasions where a longitudinal sensor observed a signal from a

roller pass where a shear sensor did not. Figure 6.24 shows observations where the bearing was solely loaded under the weight of the central shaft and load arms, i.e. no load was applied. Data here was used from testing where a combination of both shear and longitudinal sensors were tested at the same time. It can be seen at sensor 6 that no signal for a roller pass was obtained by the shear sensor where a signal was obtained for the longitudinal sensor. In contrast, both a longitudinal and shear signal were obtained from the more heavily loaded sensor 2. This gives tentative confirmation that full surface separation can be seen by the absence of signal in a shear sensor, even though this observation only occurred at low load, at the edge of the contact and was present with all measured lubricants and bearing speeds.

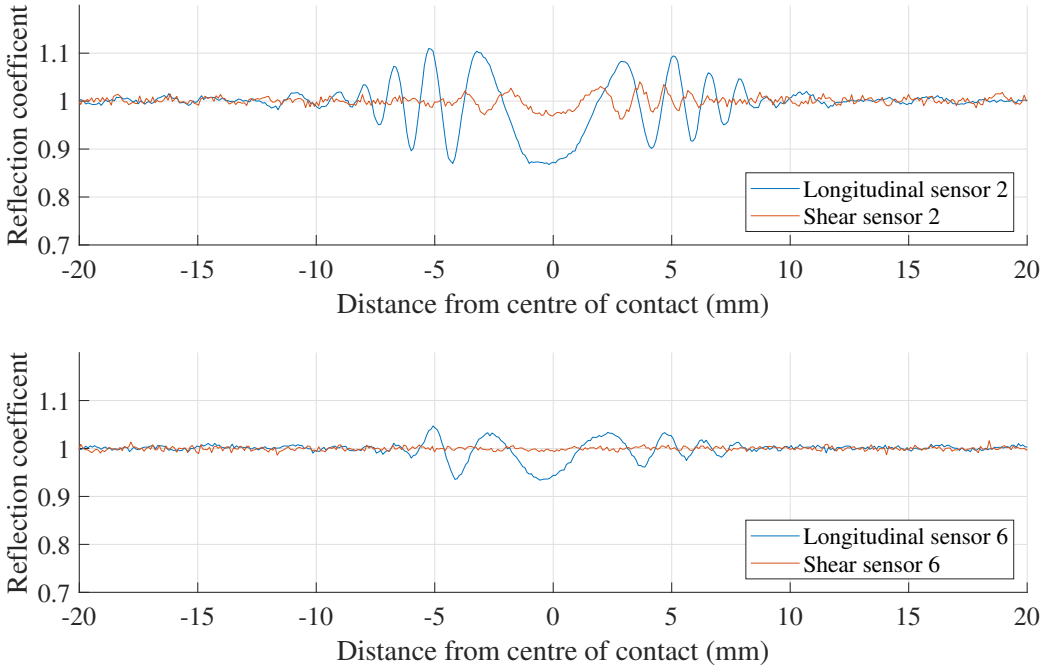

Figure 6.24: No load, VG320, 100rpm, longitudinal 8 MHz, shear 6 MHz

Predictions of lubricant film thickness can be made through knowledge of bearing performance parameters; example calculations can be seen in Appendix C. At a lubricant temperature of 40°C these calculations predicted a transition from mixed to fully separated lubrication in both the VG150 data and the VG320 data. The misalignment of the contact (which is shown in Section 6.7), causing higher contact pressures and greater lubricant heating, was likely the reason why all of the data remained in a mixed lubrication mode, as far as can be seen from ultrasonic data.

6.6.2 Lubricant Behaviour

Nicholas [41] has previously shown that differencing lubricant behaviours can be seen between roller passes. These behaviours, notably lubricant re-flow speed, varied with bearing load, bearing speed and lubricant viscosity. These behaviours will first be introduced in this data, after which they will be compared to similar behaviours in shear data.

6.6.2.1 Longitudinal

Figure 6.25 shows an expanded view of Figure 6.12(c) with another roller pass included. Noticeably, the second roller passes are not aligned. This has two likely causes. One is that the motor was not rotating the bearing at the specified speeds due to increased resistance in the system with increasing lubricant viscosity. This was shown to occur in this dataset by Nicholas [41]. The other possible cause is that there were differing amounts of slip within the bearing with different lubricants, which Nicholas suggested could be ultrasonically measured in future work if bearing speed could be measured externally [41].

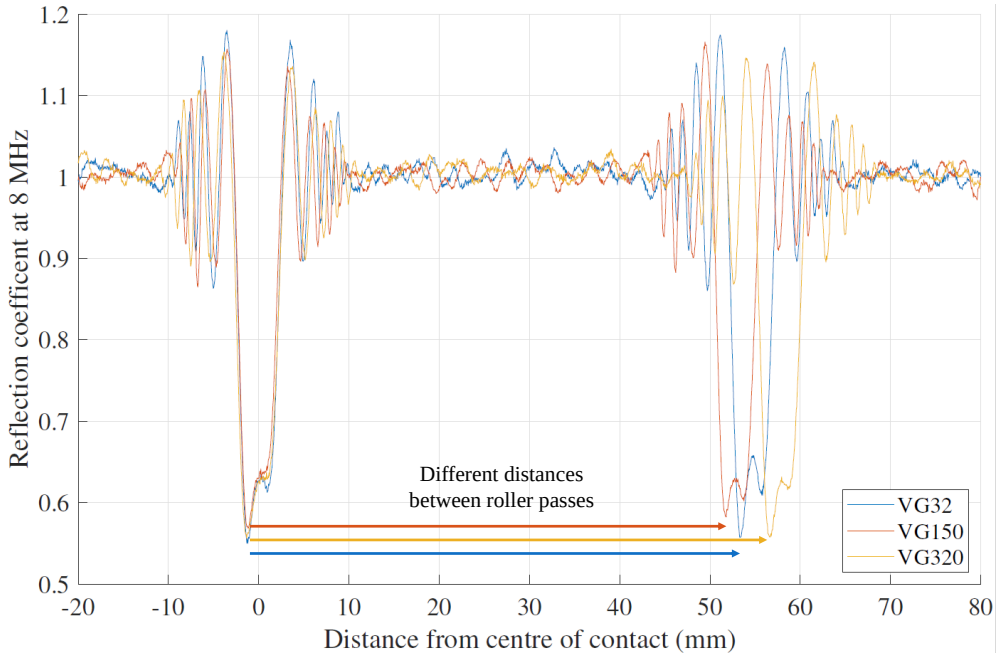

Figure 6.25: Example data to show the trend in reflection coefficient for a single roller pass with changing lubricant. 60 rpm, 500 kN, repeat 2, channel 4.

Figure 6.26 shows the same data but with ultrasonically measured bearing speed used to determine distance from the centre of the contact. This alleviated the first problem

of incorrectly estimated bearing speed but did not completely correct the offset due to the remaining problem of differing amounts of slip in the bearing with different lubricants. All of the distances in the graphs that follow in this section use distances calculated using ultrasonically measured bearing speed.

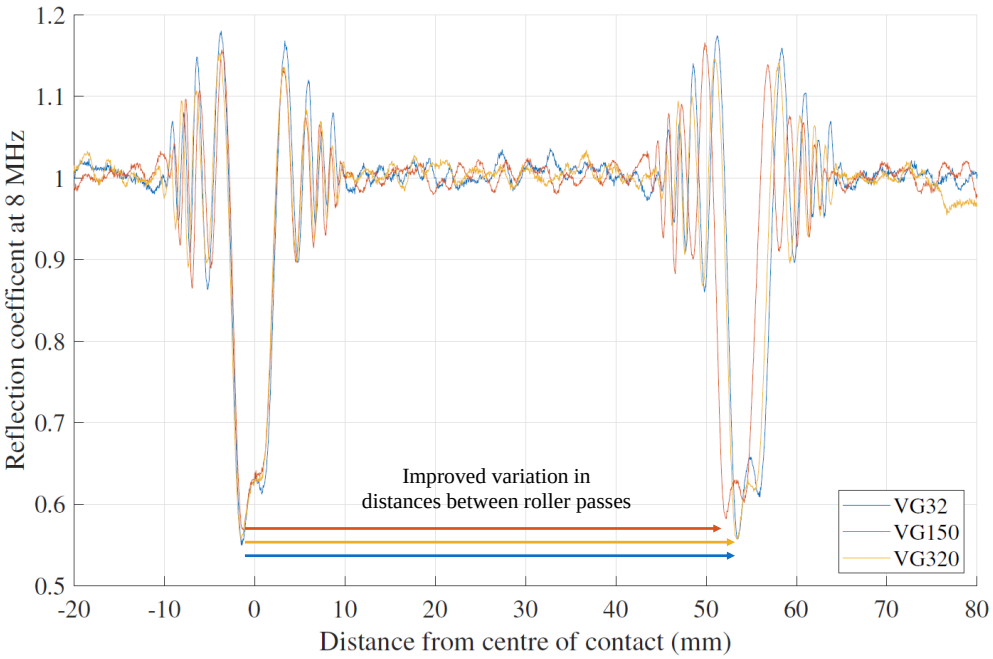

Figure 6.26: Example data to show the trend in reflection coefficient for a single roller pass with changing lubricant. 60 rpm, 500 kN, repeat 2, channel 4.

Additionally, it is noticeable that the trends between roller passes of $R = 1$ indicate a 'fully unlubricated' condition [44] in these experiments and at this sensor location and processing frequency. Whether this is due to lack of lubricant in the system or the sensors' inability to detect the surface film and its re-flow at these conditions is unknown and should be a subject of future research but is beyond the scope of this work. Figure 6.27 shows a data set where typical lubricant behaviour between roller passes was observed. Note that this time the more highly loaded sensor 2 is shown (instead of sensor 4 in Figure 6.25) for higher SNR. However, these trends were still visible at sensor 4 for this data set.

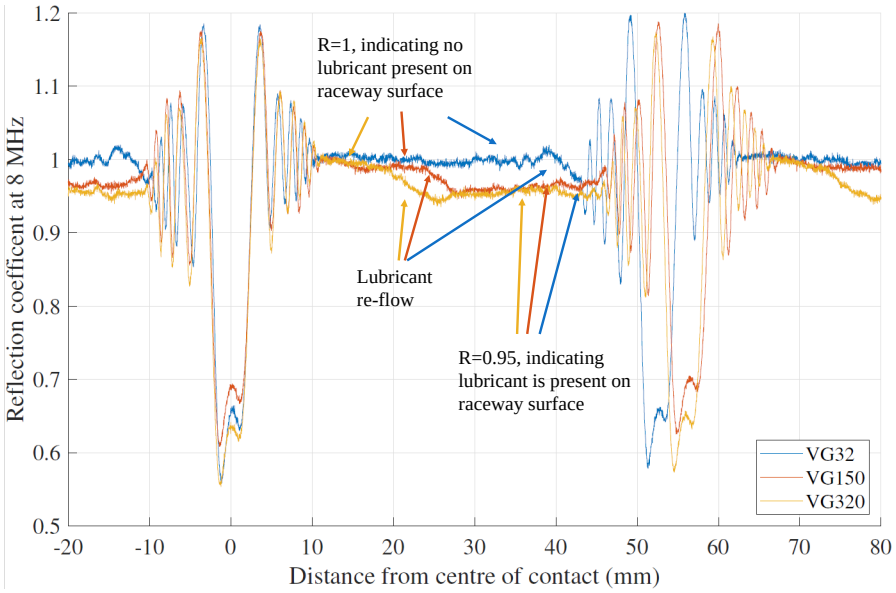

Figure 6.27: Example data to show the trend in reflection coefficient for a single roller pass with changing lubricant. 20 rpm, 300 kN, repeat 2, channel 2.

If we look between the two roller passes there were three regions of behaviour. The first, labelled R=1, indicated that there was no lubricant present on the raceway after the roller had pushed it from the contact. The second labelled region indicates the lubricant re-flowing onto the raceway and the third region, labelled R=0.95, indicated that the raceway was fully flooded with lubricant. These regimes were identified and explained by Nicholas [44].

6.6.2.2 Shear

Figure 6.28 shows the equivalent shear data for the longitudinal data shown in Figure 6.26. In this case the pattern between roller passes was very similar; there was no real deviation from a value of 1.

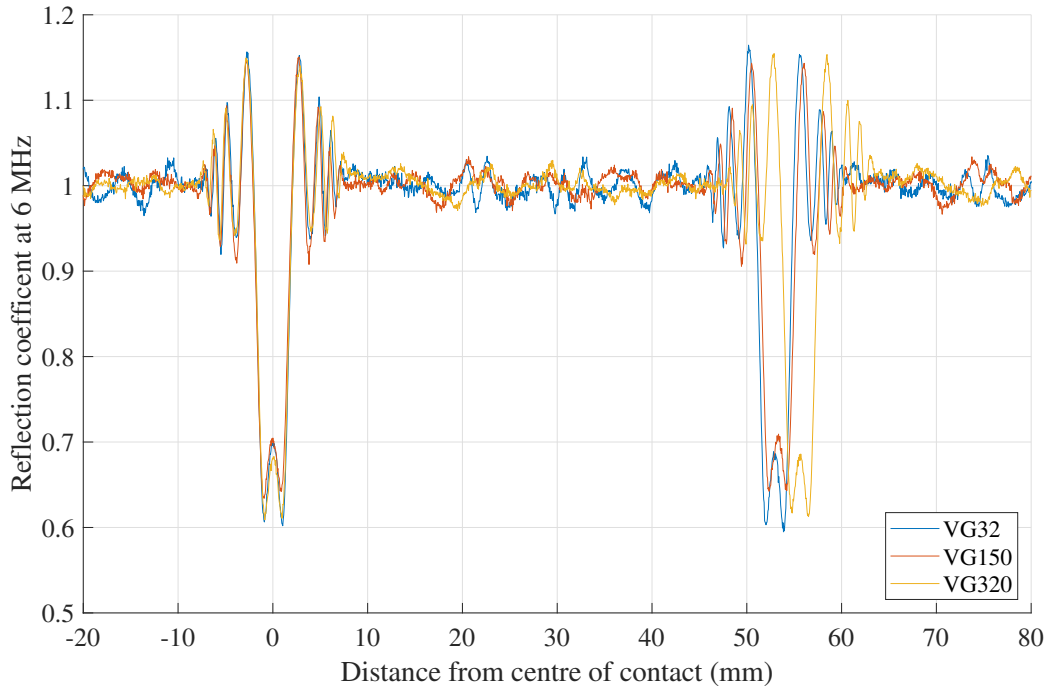

Figure 6.28: Example data to show the trend in reflection coefficient for a single roller pass with changing lubricant. 60 rpm, 500 kN, repeat 2, channel 4.

Figure 6.29 shows the equivalent shear data for the longitudinal data shown in Figure 6.27. This shows a mostly similar trend to Figure 6.28 in that values stayed around the value of 1.

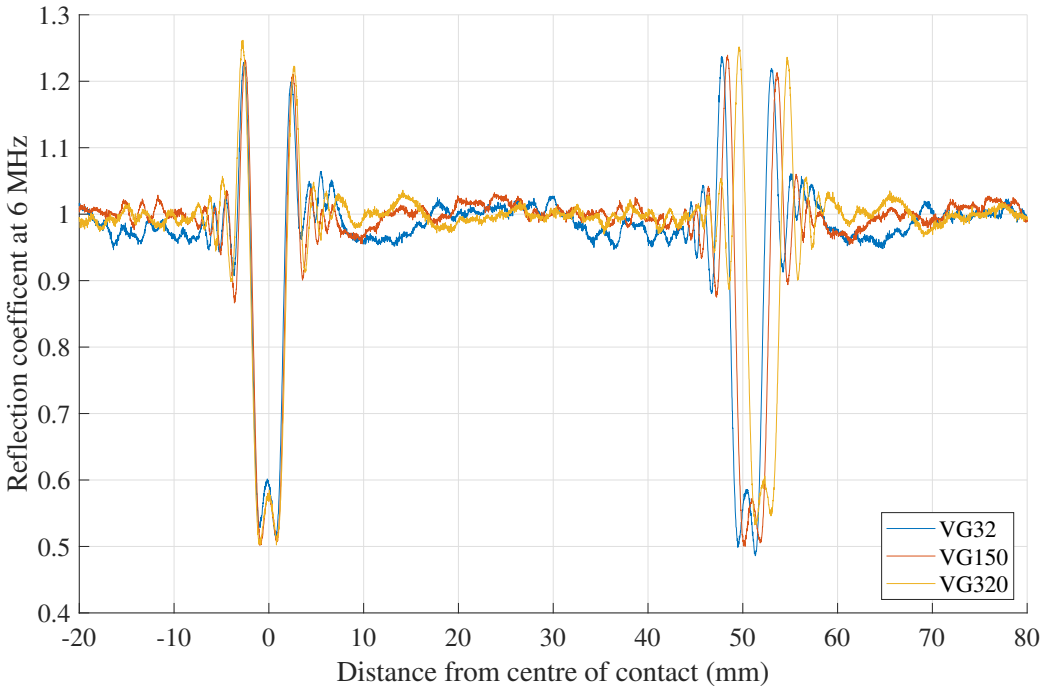

Figure 6.29: Example data to show the trend in reflection coefficient for a single roller pass with changing lubricant. 20 rpm, 300 kN, repeat 2, channel 2.

The exception to this was the VG32 data which slightly dipped below 1 before and after contact. This suggests that that shear sensors are not capable of monitoring lubricant flow between roller passes which was expected as liquids cannot typically support shear waves. The fact that we do not see the lubricant re-flow behaviour with shear sensors adds confidence to the technique using longitudinal sensors.

The shear data becomes more interesting when we look at sensor 3. Figure 6.30 shows the same dataset as Figure 6.29 but at channel 3 instead of 2. This shows a more obvious trend of decreasing reflection coefficient at the contact entry and exit, particularly with the higher viscosity lubricants.

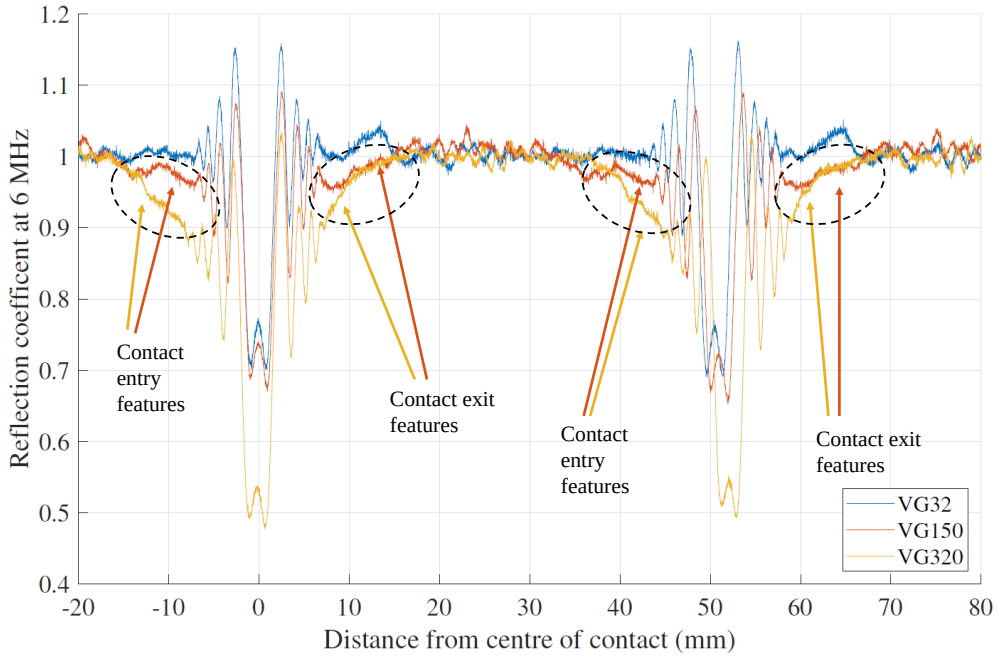

Figure 6.30: Example data to show the trend in reflection coefficient for a single roller pass with changing lubricant. 20 rpm, 300 kN, repeat 2, channel 3.

The contact entry and exit features are even more evident if we look at Figure 6.31, which shows the same dataset as Figure 6.28 but at channel 3 instead of 4.

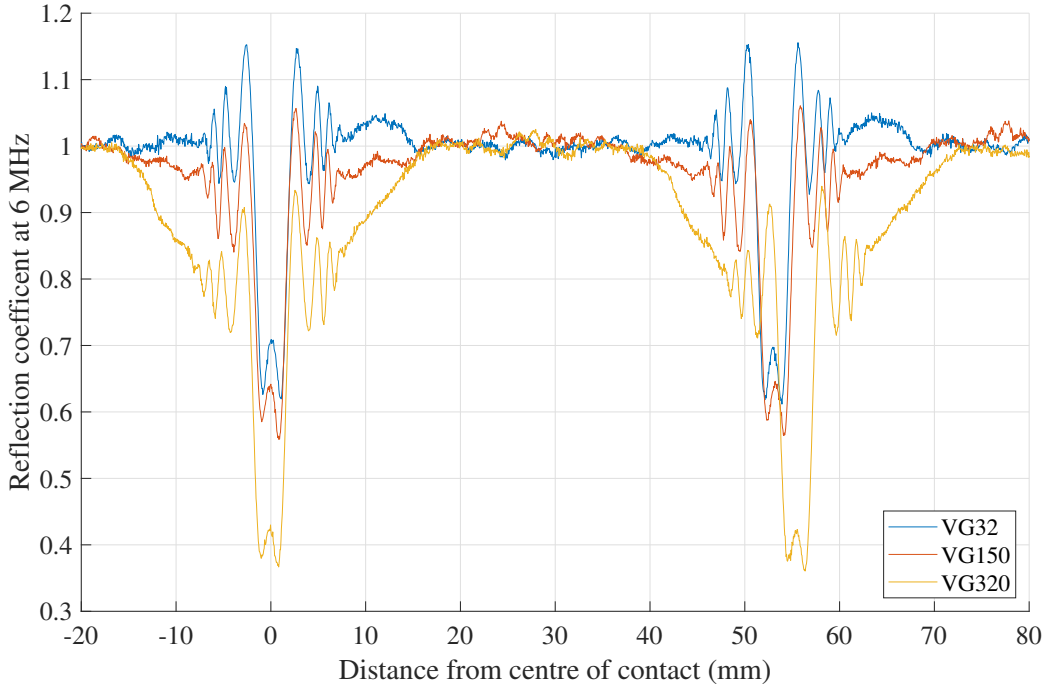

Figure 6.31: Example data to show the trend in reflection coefficient for a single roller pass with changing lubricant. 60 rpm, 500 kN, repeat 2, channel 3.

These features at the contact entry and exit were mainly seen in data from sensor 3 but also occasionally from sensor 2. In general they became more prominent with increased lubricant viscosity (as seen in Figures 6.30 and 6.31) and with increased load, as shown by Figure 6.32.

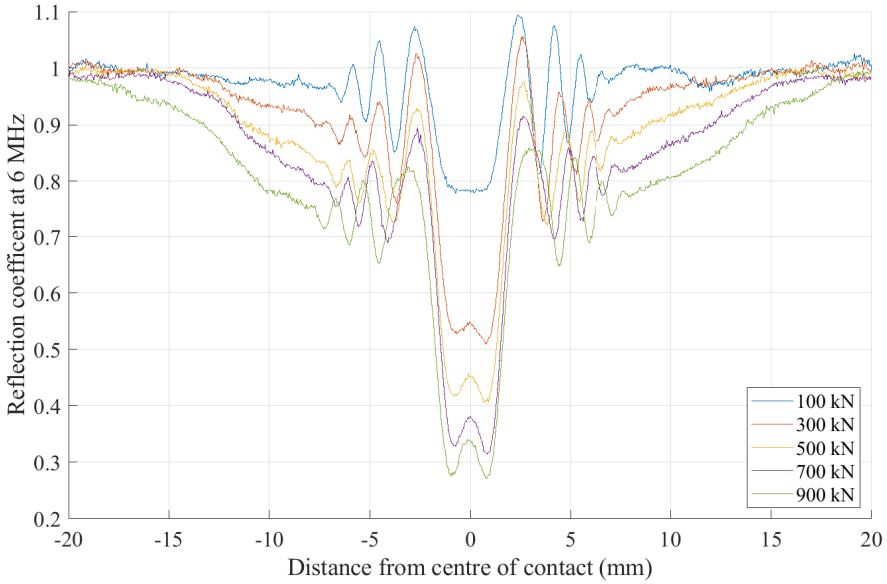

Figure 6.32: Example data to show the trend in reflection coefficient for a single roller pass with changing lubricant. 60 rpm, 500 kN, repeat 2, channel 3.

The features were present across approximately the -6 dB bandwidth (5-8 MHz) of the sensors, as shown in Figure 6.33. The presence of this feature across such a broad range of frequencies suggests that it was not caused by some resonance effect at a particular film thickness.

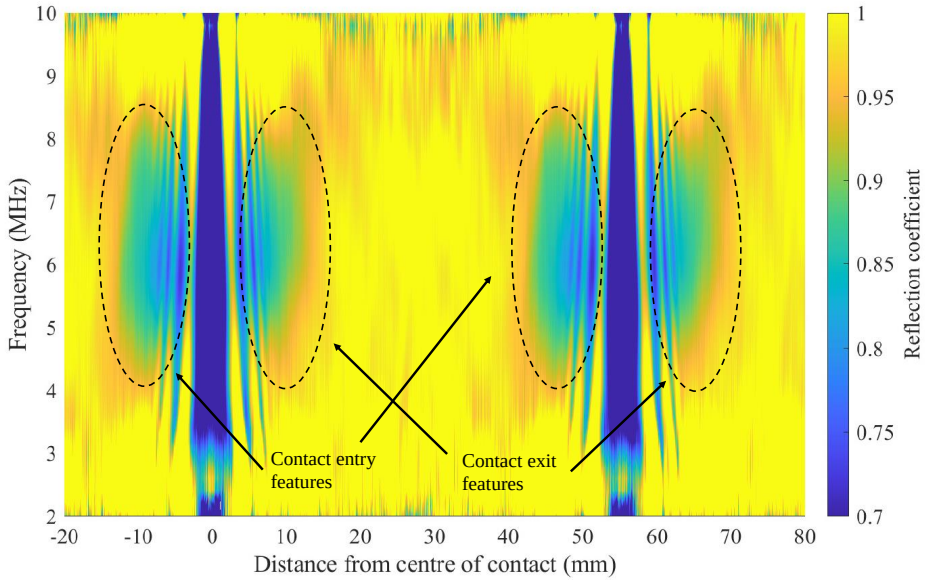

Figure 6.33: Example data to show the trend in reflection coefficient for a single roller pass with changing lubricant. 60 rpm, 500 kN, repeat 2, channel 3.

There is a possibility that this feature is caused by solidification of the lubricant in the contact as this is close to the location of maximum pressure of the contact (as shown in Section 6.7), however at this point in time there is no further evidence this to support this. They may also be caused by some other unknown phenomenon including the cause(s) of fringe effects.

6.6.3 Contact Stiffness

Due to the presence of fringe effects in signals, and the high probability of sensor beam width being larger then the contact patch sizes, there was no value in estimation of contact stiffness values and subsequently film thickness values. However, it was thought that the trends in, and the ratios between, liquid and solid stiffnesses may give some insight into contact behaviour.

Conversion of minimum reflection coefficient values to stiffnesses and application of the theory for mixed lubricant film measurement outlined in Section 3.7.8 created Figure 6.34(a), (b) and (c) for VG32, VG150 and VG320 data respectively, all at a bearing speed of 60 rpm. Reflection coefficient was converted to stiffness using Equation 3.9 for both the longitudinal and the shear sensors and liquid stiffness was calculated using Equation 3.20.

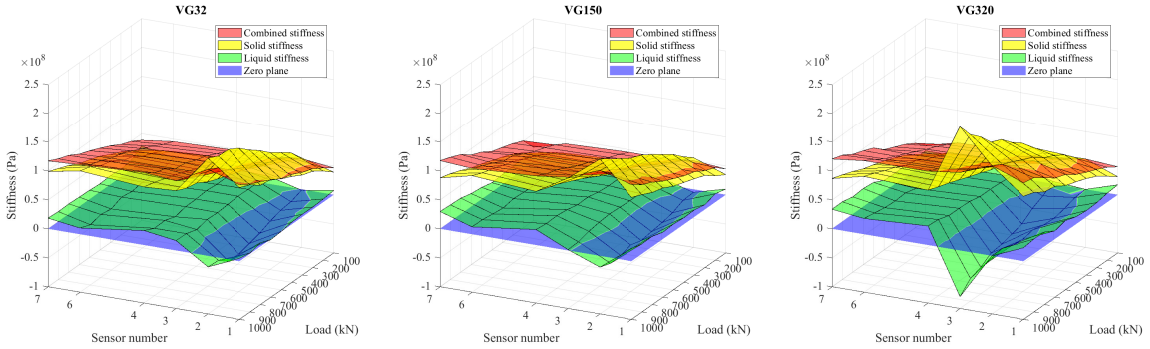

(a) (b) (c)

Figure 6.34: Contact stiffness with varying load across the roller axis at 60rpm bearing speed and with (a) VG32, (b) VG150 and (c) VG320 lubricant. The liquid stiffness is the combined stiffness minus the solid stiffness for each of the surface points.

These figures show that negative values of liquid stiffness were obtained for some sensor 2 and 3 measurements. A negative liquid stiffness is a not physically possible, which is a clear indication that Equation 3.20 was not applicable in this case. These negative regions were likely a result of the features seen at the contact entry and exit in Section 6.6.2.2. These features likely reduced the minimum shear reflection coefficients and so increased the predicted shear stiffness, which was assumed to be the solid stiffness. If solidification of the lubricant occurred this would actually be a measure of both the metal-to-metal and the lubricant stiffness, invalidating Equation 3.20. The fact that the measured shear stiffness was larger than the longitudinal stiffness was likely due to the value of 0.824 in Equation 3.20 being based on a steel-steel interface, and not a combined steel-steel / steel-oil-steel interface, which would be much more difficult to account for.

Outside of sensor 2 and 3, liquid stiffness showed a very slight increasing trend with increasing load, which was expected as the film would be thinner and therefore stiffer at higher loads. Figure 6.35 shows the ratio of liquid to shear stiffness across these channels.

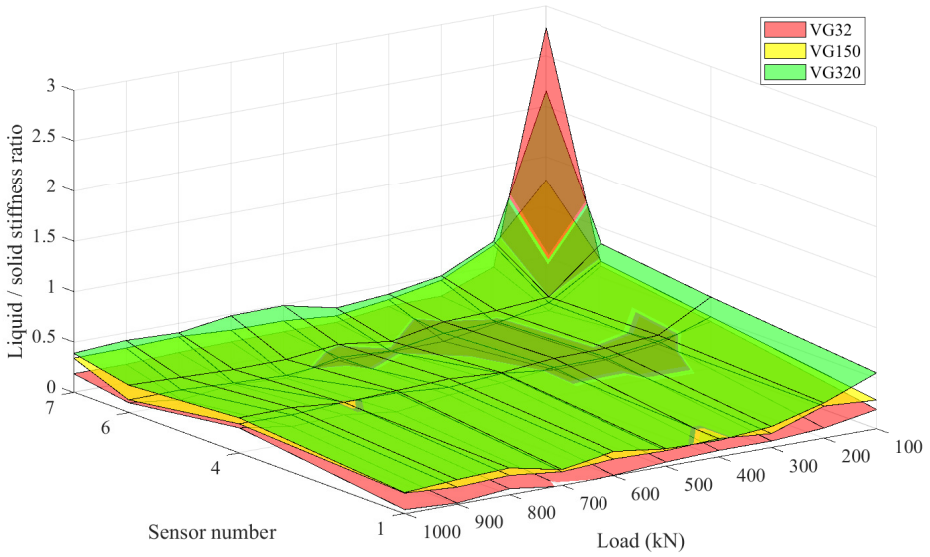

Figure 6.35: Liquid / solid stiffness ratios outside of sensor 2 and 3 for all three lubricant viscosities across all tested loads and at 60rpm bearing speed.

Other than at channel 7 with a 100 kN load, all data shows a ratio of less than 1, indicating that liquid stiffness was lower than solid stiffness. The exemptions at channel 7 were likely caused by light loading at this end of the contact due to misalignment. The general trend of decreasing ratio with increasing load matches with the expected trend that the lubricant film thickness was reduced at higher load. For the majority of data points there was a trend of increasing ratio with lubricant viscosity, although there were some exceptions to this trend. Nevertheless, a general trend of increasing ratio with increasing lubricant viscosity was promising as it matched with predicted behaviour. An increased ratio indicated that the proportion of liquid stiffness reduced with increasing viscosity, and so a thicker lubricant film was present, and thus a larger Λ ratio. Increasing lubricant viscosity is know to produce a thicker film.

These trends show that combined shear and longitudinal measurement of mixed films is likely to be possible provided that solidification of lubricant does not occur (or whatever phenomenon which caused the features in Section 6.6.2.2), fringe effects can be removed from signals and beams are sufficiently focussed so that the spot size is smaller than the contact width.

They also show that the ratio of liquid and solid stiffness can indicate changes in lambda ratio. That being said, trends with speed will not match with expectations (as there was no trend with MRC) and observation of full transition of the contact

from mixed lubrication to a fully separated contact has not been seen. Observation of transition would be necessary to validate this process and the value of 0.824 in Equation 3.20.

6.7 Misalignment Detection

This section investigates whether current bonded ultrasonic techniques can give insight into the state of misalignment in a rolling element bearing. Nicholas [41] has shown that the longitudinal dataset showed misalignment across the full range of loads and was apparently more evident in VG320 than VG32 tests. As a reminder, Figure 6.3 shows the relative positioning of the sensors on the raceway.

6.7.1 Minimum Reflection Coefficient

Figures 6.36, 6.37 and 6.38 show how MRC values for VG32, VG150 and VG320 data decrease with increasing load across the entire length of the contact. As discussed previously, this was expected.

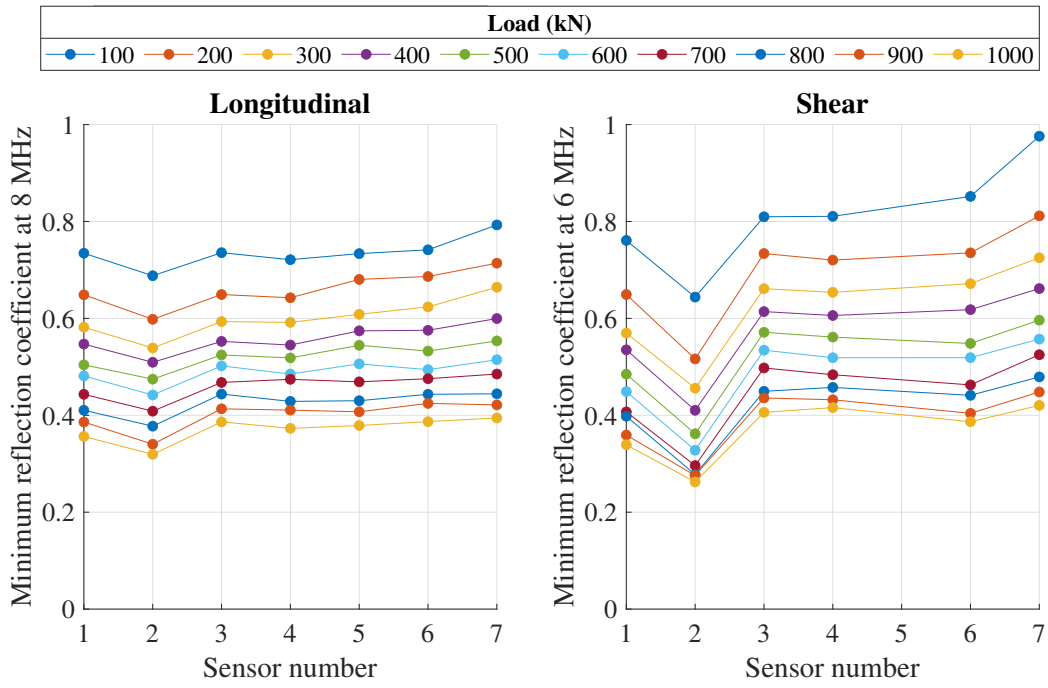

Figure 6.36: Load, VG32, longitudinal 8 MHz, shear 6 MHz.

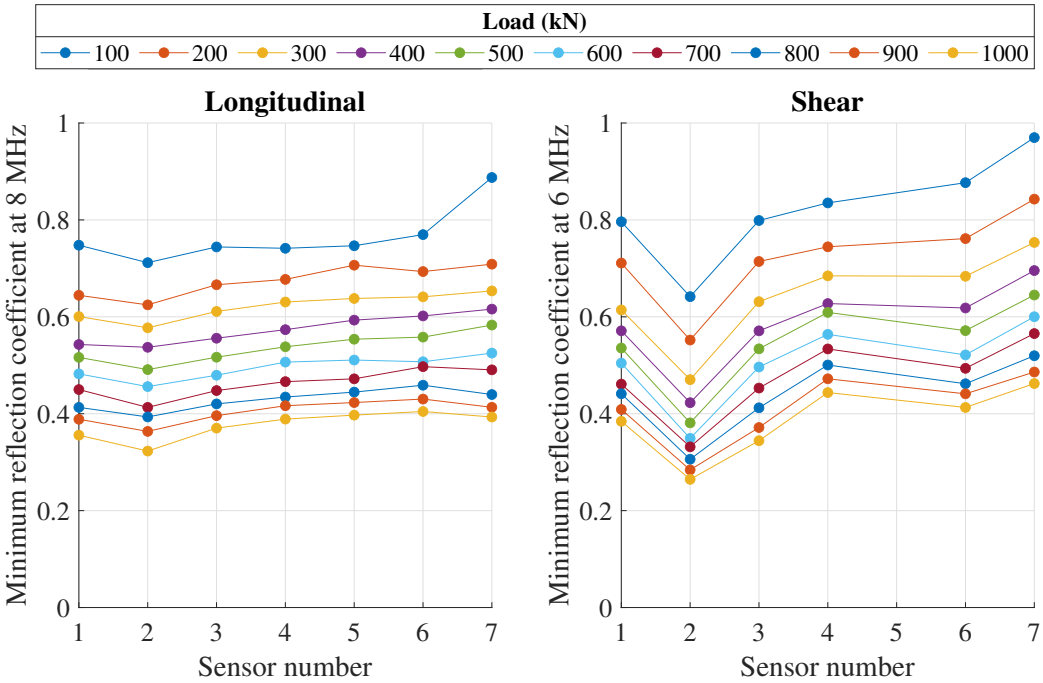

Figure 6.37: Load, VG150, longitudinal 8 MHz, shear 6 MHz.

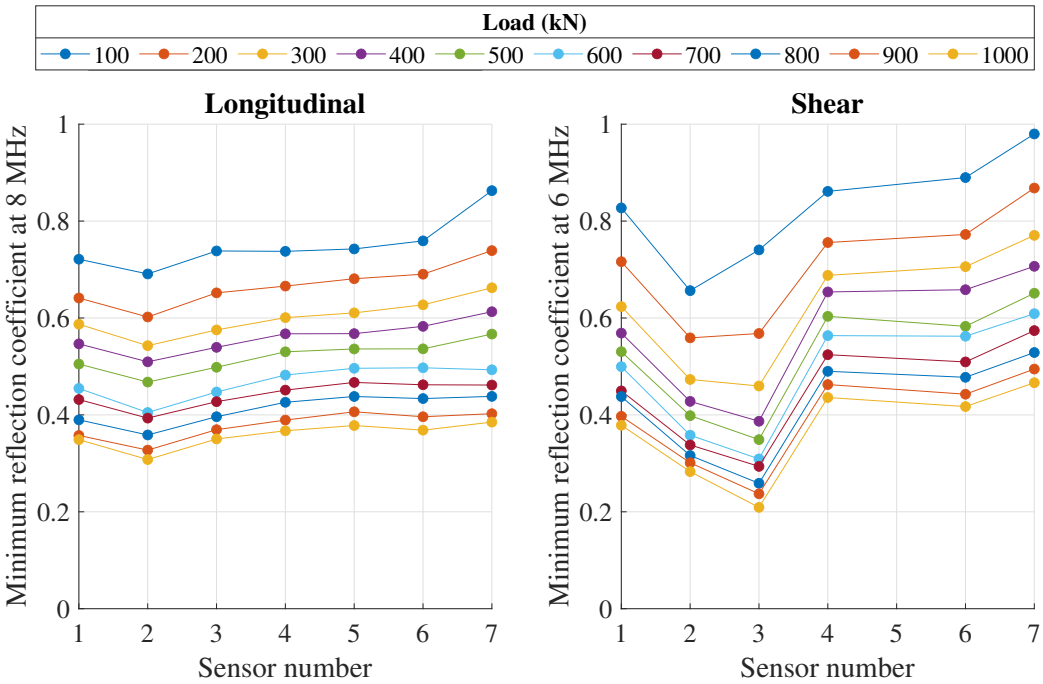

Figure 6.38: Load, VG320, longitudinal 8 MHz, shear 6 MHz.

In all cases, these figures indicated misalignment towards sensor 1 and the profiles remained relatively consistent across all loads. One exception was that the MRC

value of sensor 7 came closer to that of sensor 6 with increasing load, indicating that the length of the contact patch increased with load. Misaligned loading of the rig was not intentional. The rig has had misalignment issues in the past which were thought to be corrected in 2016 [41], however results here show that it is clearly still an issue.

In the shear data channels 2 and 3 likely gave artificially low values due to the features discussed in Section 6.6.2.2. This means that longitudinal data is likely preferable to shear data for monitoring misalignment, although the presence and magnitude of these features may indicate the areas of highest pressure in the contact, if they are indeed caused by solidification of the lubricant.

6.7.2 Reflection Coefficient Contact Width Estimations

In much the same way as Figure 4.15, Figure 6.39 shows estimations of contact widths for each sensor across the measured loads for a sample dataset with VG150 lubricant and 60 rpm bearing speed. The contact width was estimated by finding the two points at which the minimum reflection coefficient value returned halfway from its minimum in Figure 6.12(a) but across all channels. The values were found through linear interpolation between the two neighbouring data points at the half-minimum values (calculated using Equation 3.18), as shown in Figure 4.16. Figure 6.39 also shows predictions from line contact width calculations using Equation 2.5.

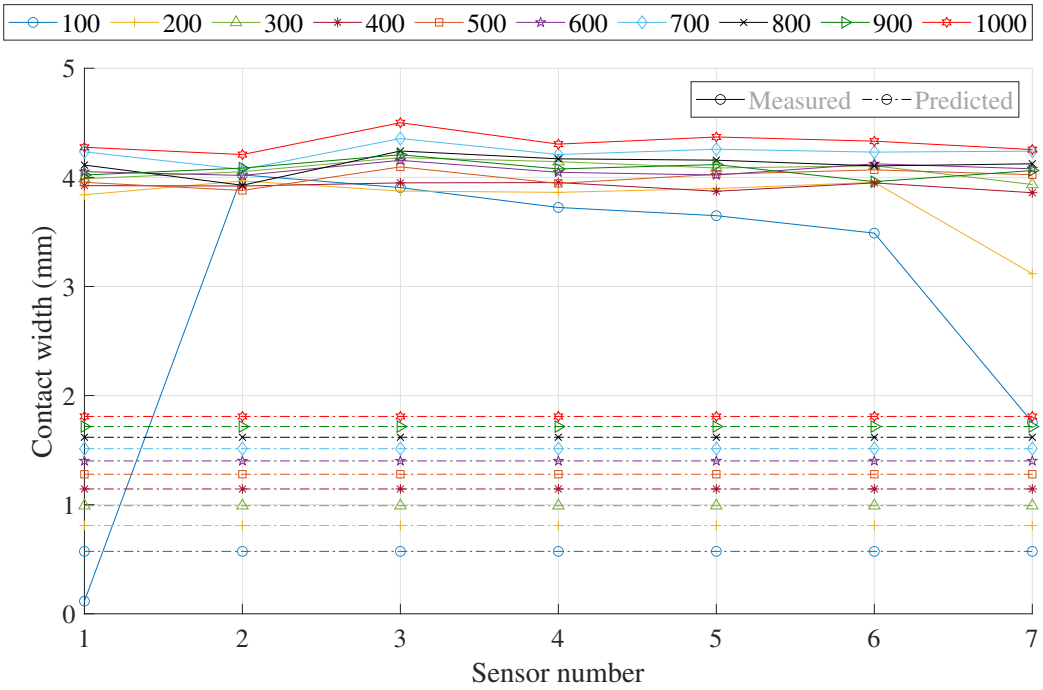

Figure 6.39: Estimated contact width across all sensor locations and bearing loads compared width predictions from line contact calculations. Bearing loads from 100 to 1000 kN. VG150 lubricant, 60 rpm bearing speed, repeat 2 data sets.

Measurements showed contact widths in the region of 3.5 to 4.5 mm and Hertzian calculations estimate that the contacts should have been in the region of 0.5 to 2.0 mm (see Appendix B). Measurement approximations were therefore more than double the expected value, as with those in Chapter 4. The most likely cause of over-prediction in contact width is the cause of fringe effects compromising the results.

A trend of increasing contact width with load was shown which was an improvement from Chapter 4, although still not completely consistent. For example, the 700 kN profile was consistently higher then 800 and 900 kN profiles. This improvement was likely due to the increased resolution in the rolling direction.

The profile appeared lengthen from 100 to 200 kN and again to 300 kN. This is shown by the increased contact width at sensors 1 and 7. This matched the MRC trends at sensor 7 shown in Section 6.7.1. However, the contact misalignment seen in MRC results was not particularly evident in contact width results. This was likely a result of the cause of fringe effects distorting the contact width predictions.

6.7.3 Maximum Change in Time of Flight

Figures 6.40, 6.41 and 6.42 show how the maximum ΔToF changes for VG32, VG150 and VG320 data with increasing load.

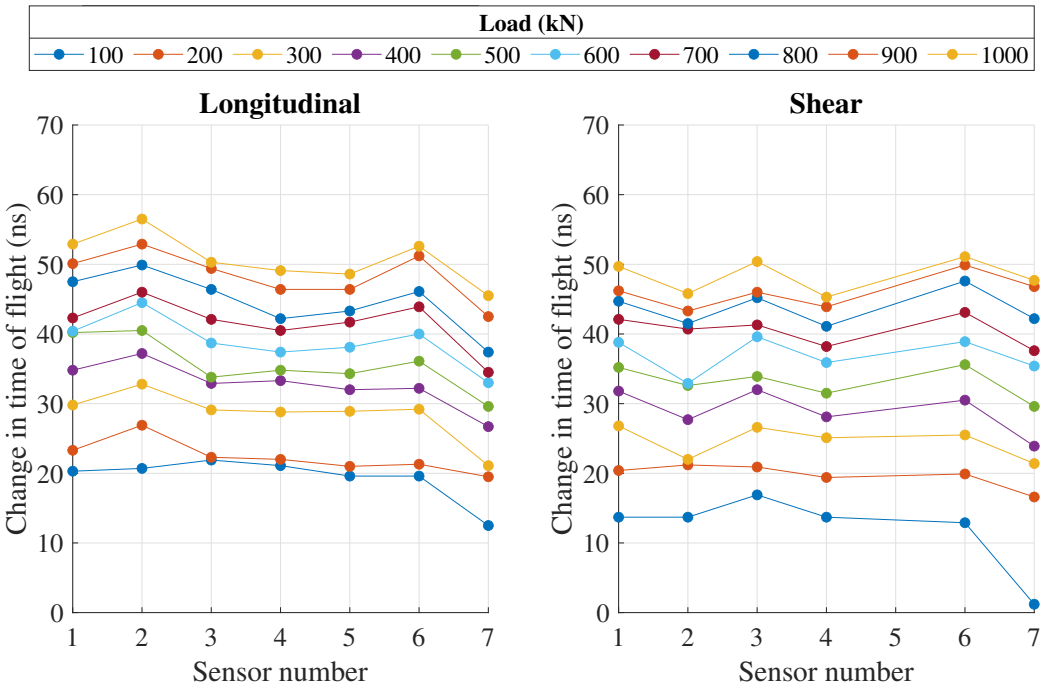

Figure 6.40: Maximum change in time of fight with changing load. VG32 lubricant, 60 rpm, repeat 2.

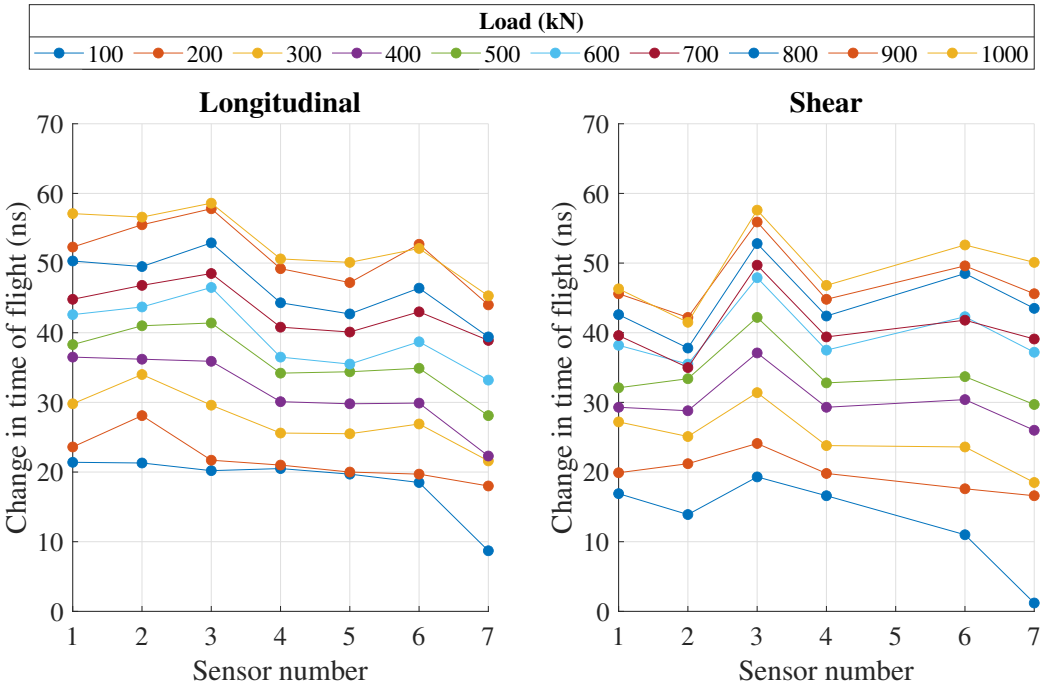

Figure 6.41: Maximum change in time of fight with changing load. VG150 lubricant, 60 rpm, repeat 2.

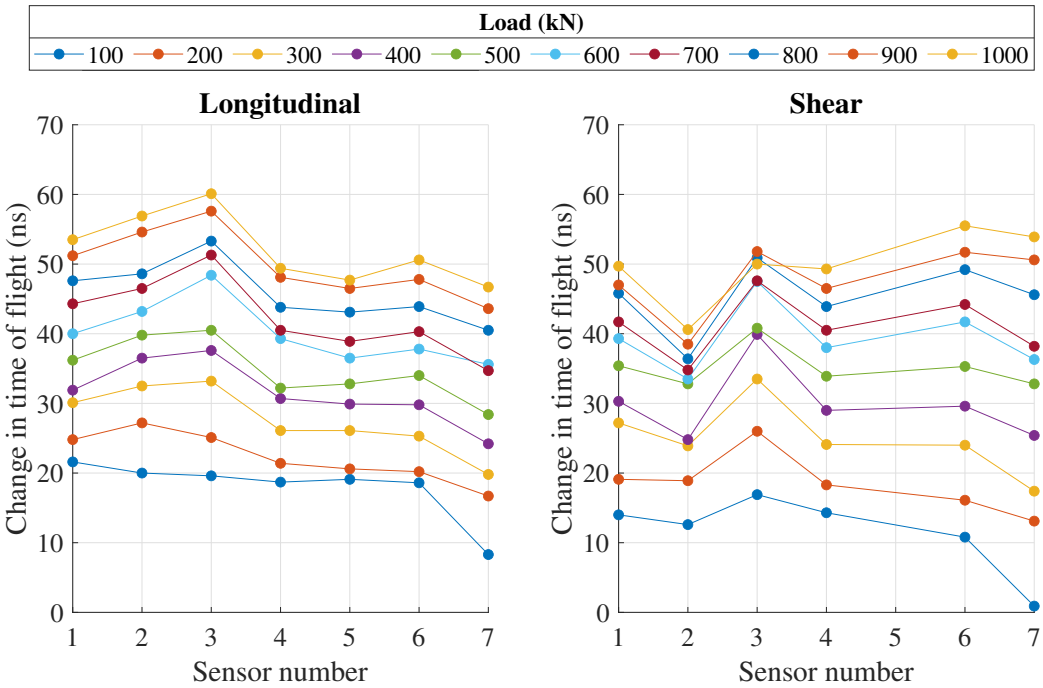

Figure 6.42: Maximum change in time of fight with changing load. VG320 lubricant, 60 rpm, repeat 2.

As with MRC, the longitudinal profiles indicated misalignment towards sensor 1 with

sensor 2 having the maximum value for VG32 and sensor 3 having the maximum value for VG150 and VG320. Data did seem to show a sub-peak at channel 6 but the reason for this is unclear. The shear data did not indicate any clear trend in misalignment for VG32 and VG150 data, and for VG320 data it showed misalignment towards sensor 7 in most cases, conflicting with trends shown by longitudinal data. This suggests that shear maximum ΔToF was unreliable for contact misalignment monitoring, although the cause of this is unknown. The profiles largely stayed the same across all loads for both shear and longitudinal sensors.

6.7.4 Summary

With current bonded sensor techniques, misalignment prediction appears to be possible through use of longitudinal sensors and monitoring both MRC and maximum ΔToF across the contact. Shear sensors do not appear to give good estimations of contact misalignment.

At present, ultrasound appears to be able to identify whether a contact is misaligned, and observe changes in severity of misalignment, but is not able to quantify misalignment. The presence of fringe effects in results limited the amount of insight into contact misalignment; both the contact stiffness and contact width predictions were not accurate as a result of the interference.

6.8 Conclusions

6.8.1 Fringe Effect Investigation

Investigation into fringe effects has shown that the width of the overall shape was affected by frequency which was likely to be a result of the link between frequency and changing beam width; an increase in frequency narrows the beam width. This chapter has also shown that fringe effects increase in severity with a larger first reflection window. This also showed that fringe effects were likely to be caused by beam spread of the transducer and the resulting interference when the beam width was wider than the contact width. The processing technique was not able to remove the underlying interference from results.

Fringe effects were also observed in shear results which contained less side fringes than equivalent longitudinal results, for unknown reasons. The central W shape in shear results was also more symmetrical than longitudinal, which was likely due to some difference between the lubricant inlet and outlet menisci. Overall fringe effects

were very similar in both longitudinal and shear results, suggesting that the same mechanism caused interference patterns in both sensor types.

The strong similarity of interference patterns in ΔToF with fringe effects in reflection coefficient plots is compelling evidence that the same phenomena cause both sets of interference. The overall shape and changes with load speed and lubricant were the same and any differences were small. The use of shear sensors to monitor deflection gave conflicting results to longitudinal sensors. Shear results predicted deflections around 1.4 times longitudinal results. This, along with similarities in fringe effects in reflection coefficient cast serious doubt on ΔToF measurements. It has been shown that fringe effects seriously distort reflection coefficient measurements so it is very likely that ΔToF measurements are distorted by the cause of fringe effects too. From previous studies there is clearly some correlation between signals and load. Perhaps, instead of measuring deflection, these methods relate to some other contact parameter that directly influences the magnitude of fringe effects. The most likely contender is contact width.

Fringe effects in both reflection coefficient and ΔToF did not significantly change with bearing speed or lubricant viscosity however they did change with load. These changes in fringe effects with load have been detailed in this chapter for comparison to model results in Chapter 7. The uncertainty in results containing fringe effects demonstrates a clear need for further understanding of the phenomena and a method to remove their effects from bonded transducers.

6.8.2 Use of Shear Sensors

The combined use of shear and longitudinal sensors to monitor rolling elements suggested that all of the observed data was in a mixed lubrication regime although both longitudinal and shear reflection coefficient data did not entirely behave as expected. This was likely a result of the cause of fringe effects. Shear ultrasound was transmitted through the contacts at all but the edge of the contact at very low loads meaning that contacts were very likely to be in a mixed lubrication regime. The scenario where this conclusion would be wrong is if the lubricant supported shear waves. There was some data at very low load where no shear ultrasound was transmitted into the roller where longitudinal ultrasound was. This gives some confidence in this technology being able to detect a transition from mixed to fully separated contacts in future testing. Transitions in this data set were likely not seen as a result of bearing misalignment and subsequent higher contact pressures.

New phenomena at the contact inlet and outlet with shear sensors show the possible observation of lubricant under high pressure reaching a semi-solid state where it is capable of supporting a shear wave. The phenomena increased in magnitude with increasing bearing load and lubricant viscosity but showed no trend with changing bearing speed. This phenomena, along with the presence of fringe effects meant that mixed lubrication film thickness predictions were not possible. Trends in contact stiffness where these phenomena were not present showed sensible trends with bearing load and contact stiffness, suggesting that combined shear and longitudinal measurement of mixed films should be possible provided that solidification of lubricant does not occur (or whatever phenomenon which caused the features in Section 6.6.2.2), fringe effects can be removed from signals and beams are sufficiently focussed so that the spot size is smaller than the contact width.

6.8.3 Misalignment

This work, in collaboration with Nicholas [41], was the first to observe misalignment in a rolling element bearing using ultrasound. Nicholas showed that misalignment with longitudinal ΔToF and reflection coefficient could be seen at one load, however this work has analysed data in more detail.

It was shown that shear data was not suitable for contact misalignment, most likely due to the solidification phenomena in shear signals previously described. It is recommended that misalignment monitoring should use a combination of reflection coefficient and ΔToF analysis techniques with longitudinal sensors.

In the longitudinal data, profiles largely remained the same with increasing load, however greater changes at sensor 7 (edge sensor) in some instances indicated lengthening of the contact. Lengthening of the contact was also observable in contact width estimations, although actual contact widths were over predicted between 2-4 times those predicted by Hertzian equations. This over-prediction was likely a result of the cause of fringe effects.

Current bonded techniques are able to detect the presence of misalignment and changes in severity but not quantify it. For further insight into misalignment, fringe effects need to be removed from signals.

Chapter 7

Modelling of Fringe Effects

7.1 Introduction

In this chapter, a modelling approach to investigate the cause of fringe effects in ultrasonic signals will be developed. As shown throughout the previous chapters of this thesis, the cause of fringe effects result in issues in bonded ultrasound measurements, however the added benefits that come with bonded transducers mean that they are still an attractive option. Fringe effects are evident in both reflection coefficient and deflection measurements which causes some in results and reduces the value of these measurement techniques. To measure lubrication and load with bonded ultrasonic transducers, reduction, or removal of fringe effects is therefore necessary. It is clear that reducing or removing fringe effects would make ultrasonic measurement techniques more attractive to both industry and research for rolling bearing monitoring. In order to remove or reduce fringe effects they first need to be properly understood. Therefore, modelling techniques are used in this work to provide further insight into the problem.

7.2 Modelling Approach

Across the literature, fringe effects have been attributed to several causes. These, along with other possibilities, are listed below:

- Acoustoelastic effects [39, 77].
- Interaction of the sound field with a feature of similar size to the wavelength.
- Spot size of the transducer being larger than the contact [88, 41].

- Geometry effects from raceway curvature [39].
- Varying stiffness across the contact.

Ideally, all of these causes should be investigated independently, however the problem can be initially investigated with a more simple model and built upon thereafter. A plan to create models of increasing complexity to try to recreate fringe effects was therefore generated, which is summarised in Figure 7.1.

A basic model was created as a first step, which had simplified bearing geometry, did not incorporate deflection of the contact, transmitted 100% of acoustic energy through the contact, and neglected the effect of the stress field due to the contact. The model would be increased in complexity as defined by the stages in Figure 7.1 until the presence of fringe effects which behaved in the same way as experimentally observed fringe effects were reproduced, or the modelling stages were exhausted. It was expected that this would allow the cause of fringe effects to be narrowed to a particular modelling stage.

In order to simulate a roller passing an ultrasound sensor, successive iterations of the model were required with varying position of the contact in relation to the sensor. In a very similar fashion to the quasi-static experiments in Section 4, rolling in the model was simulated by moving the sensor location in the model and keeping the contact location constant, as shown in Figure 7.2. Iteration of other aspects of the model, like contact geometry and sensor frequency, were also required.

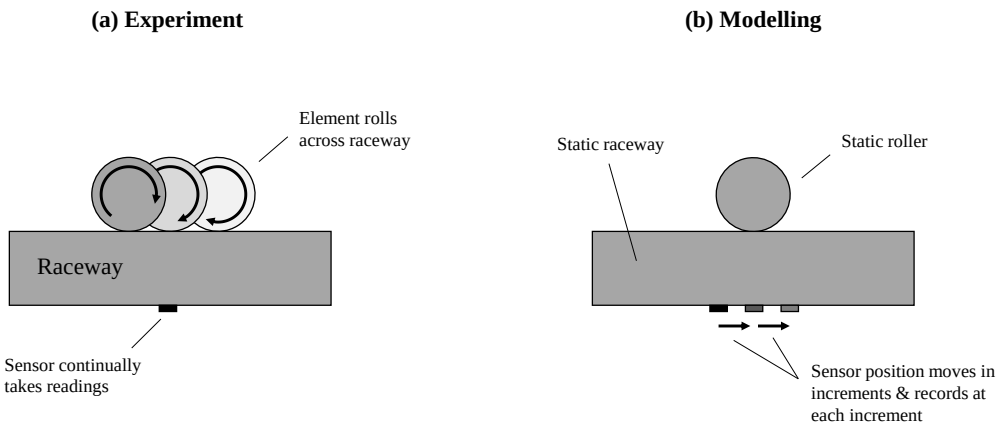

Figure 7.2: A schematic of how rolling was reproduced in the model (b) in comparison to experimental rolling contacts (a).

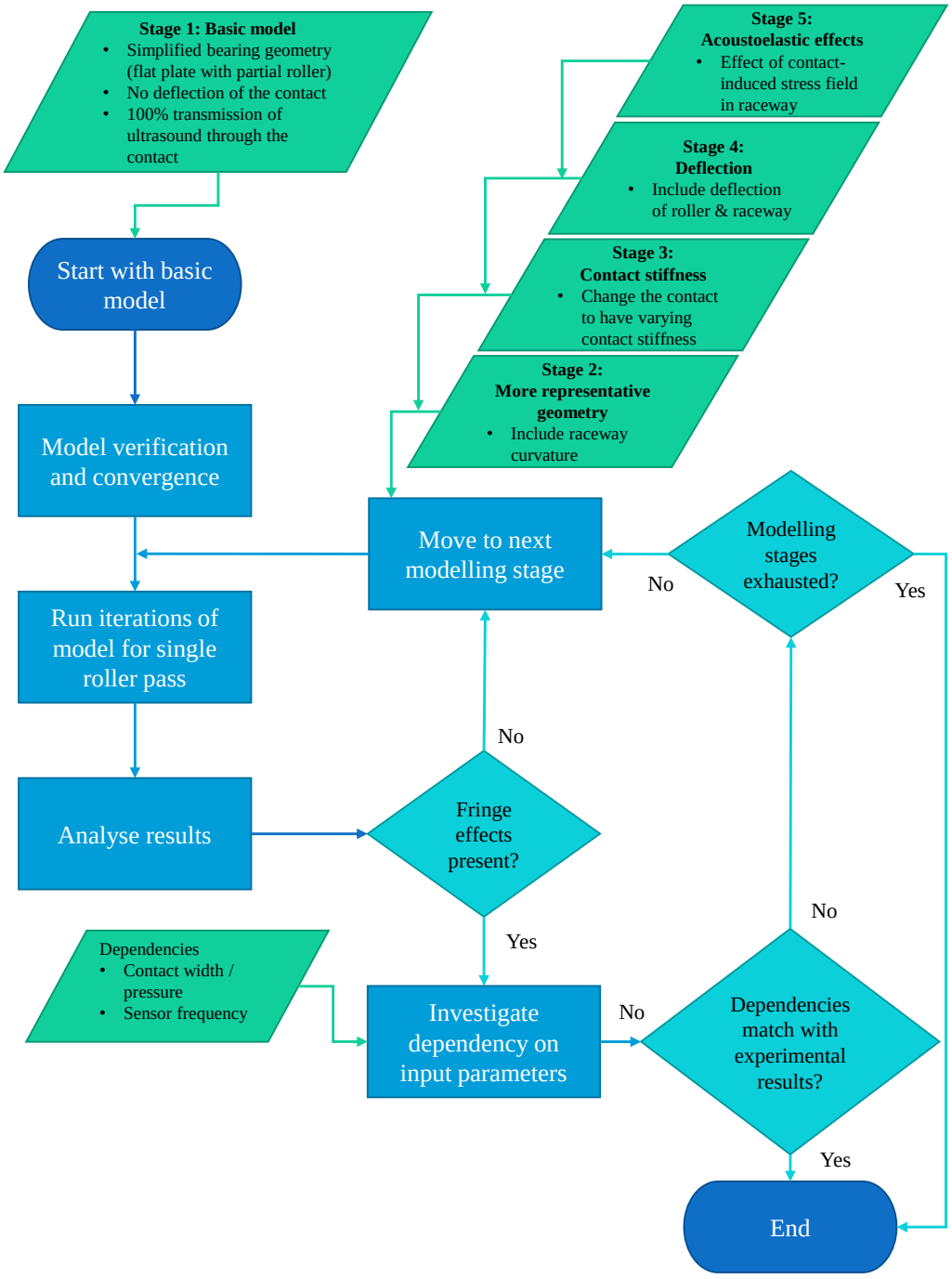

Figure 7.1: Fringe effect modelling approach flow diagram.

7.3 Software Selection

The model was initially created using *Abaqus CAE 2018* finite element analysis (FEA) software as a readily available package that would allow all stages of the modelling plan to be created. Unfortunately, three aspects of this approach held back progress: long solve times, time consuming model iteration and reliability. Even though model iteration with *Abaqus* was possible using Python scripts, aspects of the data extraction process contained bugs and were difficult to automate which resulted in significant amounts of data loss on multiple occasions. Ultimately a combination of the results from the first stage of modelling and difficulties faced using *Abaqus* meant that further modelling was completed in a different software package.

An open source and free *MATLAB* resource called *k-Wave* was chosen to replace *Abaqus* as it had quicker solve times and was easier to run iteratively. *k-Wave* uses the k-space method to solve the system of partial differential equations as opposed to the finite element method. The k-space method "combines the spectral calculation of spatial derivatives (in this case using the Fourier collocation method) with a temporal propagator expressed in the spatial frequency domain" [108]. As the functions are sinusoidal only two grid pints per wavelength are required as opposed to the requirement of approximately 10 grid points per acoustic wavelength for finite element methods (used by *Abaqus*). This results in much faster solve times for models than with *Abaqus*. *k-Wave*'s interface with *MATLAB* made it very easy to run iterative models to reproduce the intended problem. *MATLAB* support on Sheffield's High Performance Computing clusters [109] meant that solving models was even quicker than on a single computer.

7.4 Model Definition

As data from Section 6 was already available for comparison it was decided that the model geometry would be representative of the NU2244 cylindrical roller bearing that was tested in the *MultiLife* rig. Contact widths and deflections were also based on the capabilities of the rig. These were calculated for each of the load conditions conducted in Section 6, which were first converted to maximum roller load using Equation 2.28 where $K_d = 4.08$. These maximum roller loads were used to calculate contact widths and deflections using Hertzian contact mechanics for rollers, as shown in Appendix B. Resulting contact widths are shown in Table 7.1. Deflections were not required

for the first model iteration. The estimated contact width of 1.28 mm when the rig was under 500 kN of applied load was selected for the first model iteration.

Bearing load (kN)	Contact width (mm)
100	0.57
200	0.81
300	0.99
400	1.14
500	1.28
600	1.40
700	1.51
800	1.61
900	1.71
1000	1.81

Table 7.1: Estimated contact widths for different *MultiLife* rig loads.

The instrumented longitudinal sensors used on the *MultiLife* rig were also to be recreated in the model. These were 1 mm wide in the rolling direction and had a design centre frequency of 10 MHz. Only longitudinal sensors were modelled, as shear waves were not possible to model in *k-Wave* - a limitation of using an acoustic package.

Here the priority was to investigate the effect of changing contact size, due to the availability of comparable data from Section 6, but other factors like sensor size, sensor frequency and ultrasound path length (raceway thickness) were also of interest.

7.5 Model Creation

The first iteration of the model was two dimensional and only the steel roller and raceway were modelled. The first step was to create a k-grid. The required model area was calculated based on a raceway length of 50 mm, and a composite raceway and part-roller thickness of 24.4 mm. This area was divided by a universal increment based on the wavelength of the ultrasound in the steel. This increment is defined in Section 7.7. The modelled contact width was 1.28 mm and raceway thickness was 19.4 mm.

Model geometry was created using two material property grids as matrices: density and speed of sound. An example grid can be seen in Figure 7.3 which shows the raceway and roller in blue and the gap in yellow. Their material properties are

summarised by Table 7.2. The entire gap was filled with oil and not air as the smaller wavelength in air would require a much smaller grid size. The roller and raceway were defined as the same material and so 100% of ultrasonic energy was transmitted through the contact giving a reflection coefficient of 0.

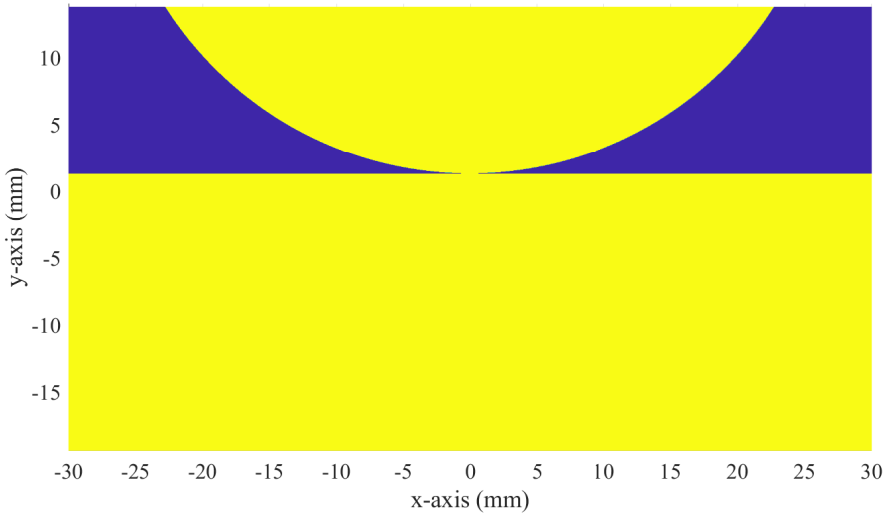

Figure 7.3: The model geometry as a *k-Wave* material properties grid.

Area of model	Based on	Density (kg/m^3)	Speed of sound (m/s)
Roller and raceway	Bearing steel	7810	5900
Gap	VG32 lubricant	870	1456 [39]

Table 7.2: Material properties used in the *k-Wave* simulation.

Sensor excitation was simulated using a pressure pulse along the nodes of the simulated sensor location. A Hanning toneburst with the desired centre frequency of 10 MHz was set as the amplitude profile, as shown in Figure 7.4. Pressure magnitude was set to unity as results were scalable with input pressure due to the assumption of linear-elastic behaviour in the model. A sensor width of 1.0 mm was defined. A perfectly matched layer was also incorporated at the edges of the model to prevent any reflections from these boundaries interfering with results.

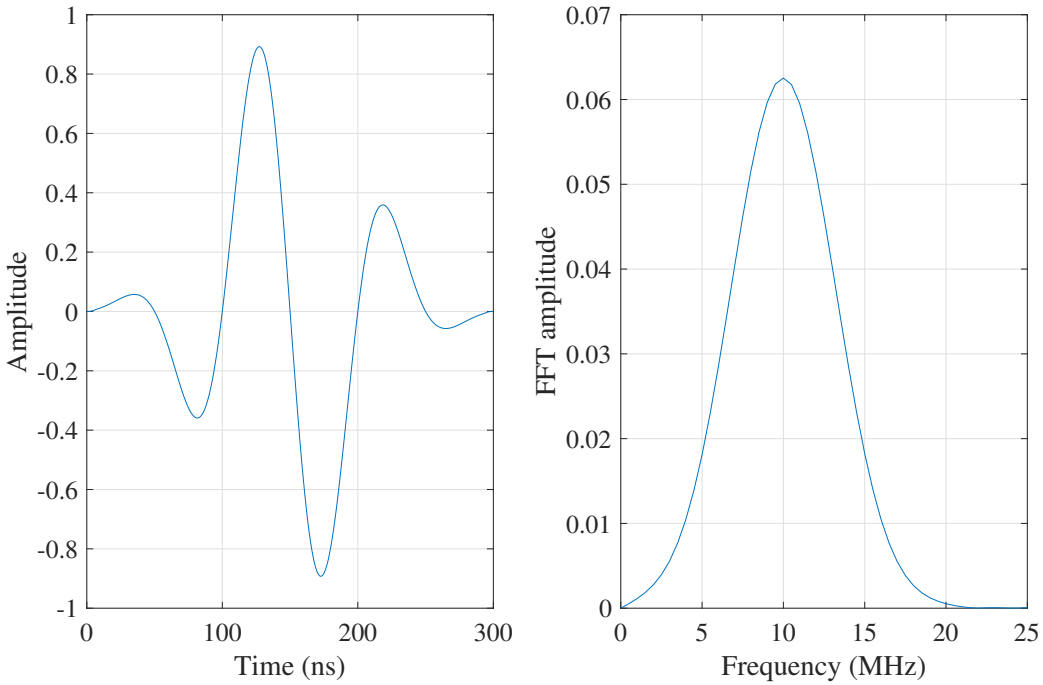

Figure 7.4: *k-Wave* excitation pulse in the time (left) and frequency (right) domains.

In order to give an idea of the accuracy of the replicated sensor beam, the maximum pressure at each grid point in a solid steel block was monitored for a simulate 1.5 mm transducer. Results are shown in Figure 7.5 which allowed comparison to data for beam width obtained by Howard [39] previously discussed in Chapter 3 and calculation using Equations 3.16 and 3.17. Simulation results gave a -6 dB beam width of 8.7 mm. Howard's experimental results (shown in Figure 3.11) show a 3.8 mm beam width at -6 dB. Beam width calculations for this sensor size predict a beam width of 9.7 mm at -6 dB. Simulation results are therefore much closer to beam width calculations, but this was the best approximation of the sensor available at this point in time. In any case, the effect of changing beam width will be investigated later in this work and so will be accounted for.

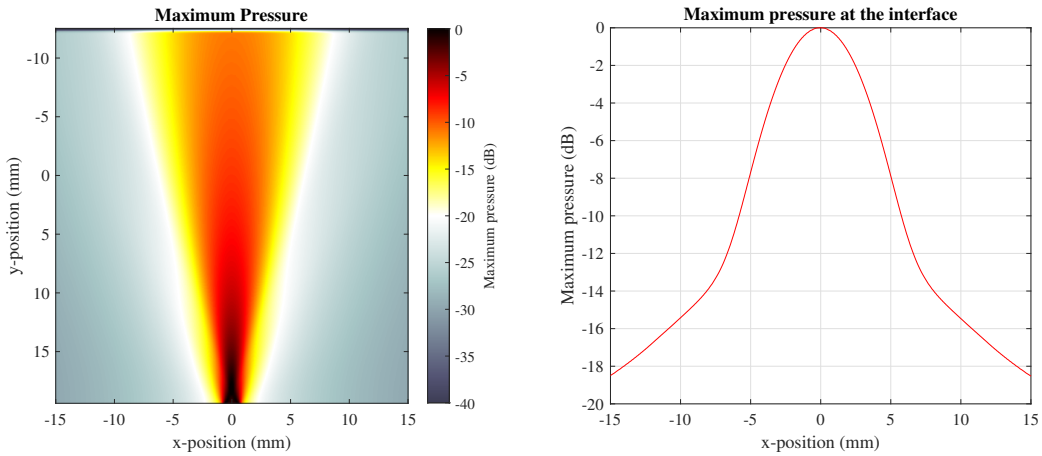

Figure 7.5: Simulated beam width of a 1.5 mm wide transducer for comparison with experimental data.

7.6 Data Processing

Model data resulted in deflection A-scans across each of grid points in the sensor. The mean of these A-scans was taken and subsequently processed in the same manner as raw data from previous sections. Data was processed to obtain reflection coefficient and change in time of flight as described in Section 3.6. Other processing methods are described as they are introduced in the results.

7.7 Convergence Study

Model grid density was evaluated through a convergence study based on peak-to-peak amplitude of the reflected signal when there was no roller present against the raceway. Displacement amplitude in the direction of wave travel was extracted from the results across the sensor nodes to produce the A-scans. The resulting convergence graph can be seen in Figure 7.6. The model was deemed to be converged at a steel wavelength to element ratio of 18. The increment between grid points at this grid density was approximately 0.03 mm and the grid size was rounded to the nearest factor of 2 which resulted in a 2048 x 1024 grid. Grid size was rounded to the nearest factor of 2 in order to speed up solve times, as *k-Wave* is heavily reliant on the FFT. All subsequent modelling was conducted at this grid density.

Convergence at this mesh density makes sense when considering that the wavelength in the simulated oil was approximately 4 times smaller than that in the steel, and the simulated pressure pulse had frequency content up to around 21 MHz (see Figure

7.4). The maximum supported frequency of the model in the oil at this grid density was just over 22 MHz with a little more than two grid points per wavelength.

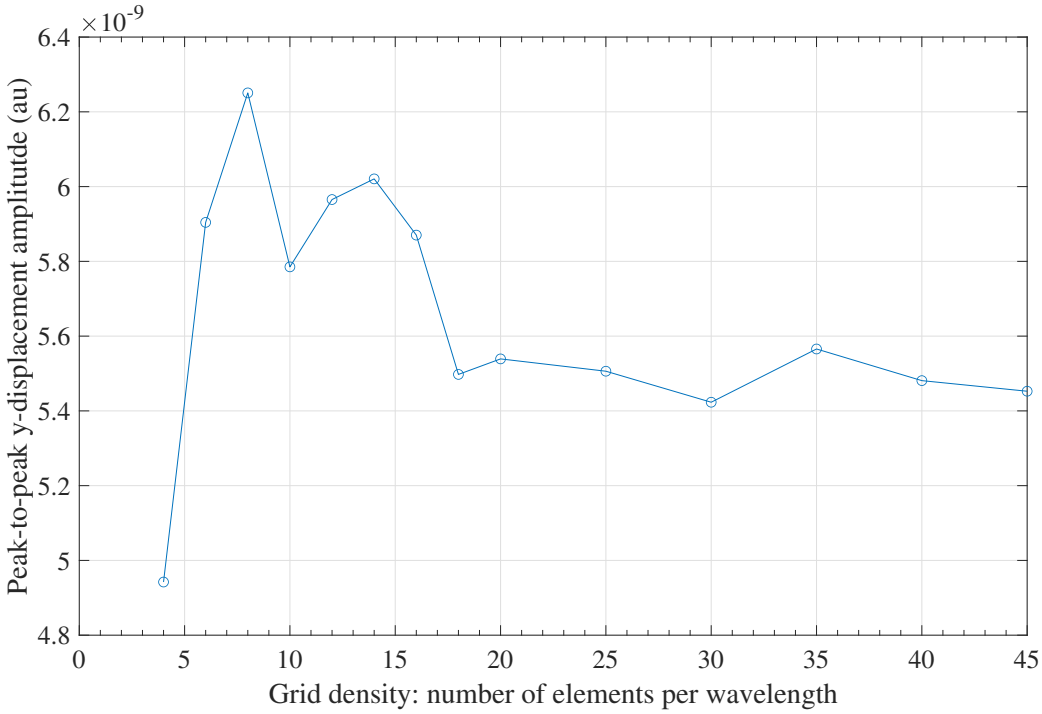

Figure 7.6: An example screen capture of the pressure wave approaching from a single iteration model result.

Results from this convergence study at the selected grid density were used as a thick film reference for calculating reflection coefficient in the following results, as summarised by Equation 7.1, where $R_{thickfilm}$ was theoretically calculated as 0.95 using the properties in Table 7.2 and Equation 3.3.

$$R = \frac{A_{meas}}{A_{thickfilm}} R_{thickfilm} \tag{7.1}$$

7.8 Results for a Single Roller Pass

These results will be our 'base model' for comparisons in the following sections. A spectrogram for a single simulated roller pass with a 1.28 mm contact is shown in Figure 7.7(a). This is remarkably similar to those shown in Chapters 4 and 6 from real data, an example of which is shown in Figure 7.7(b).

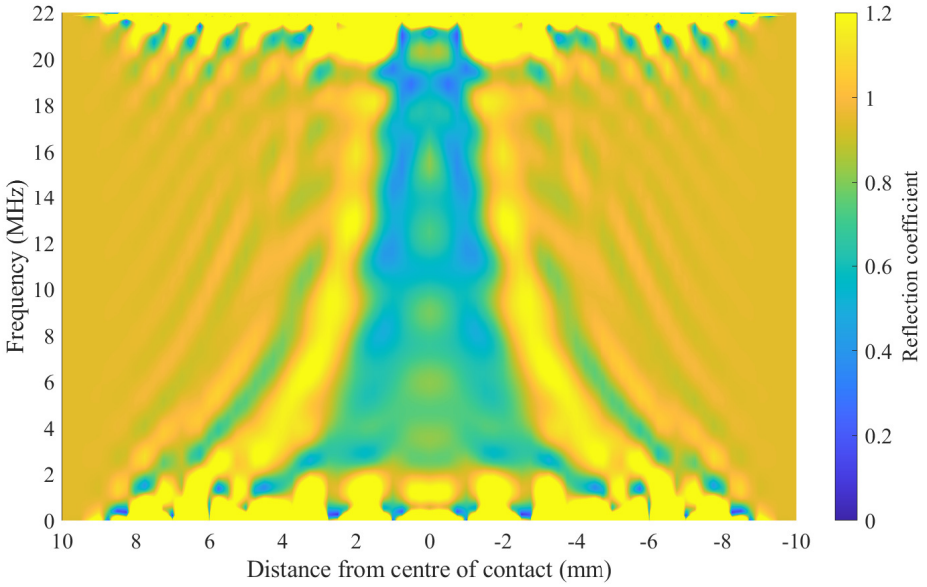

(a)

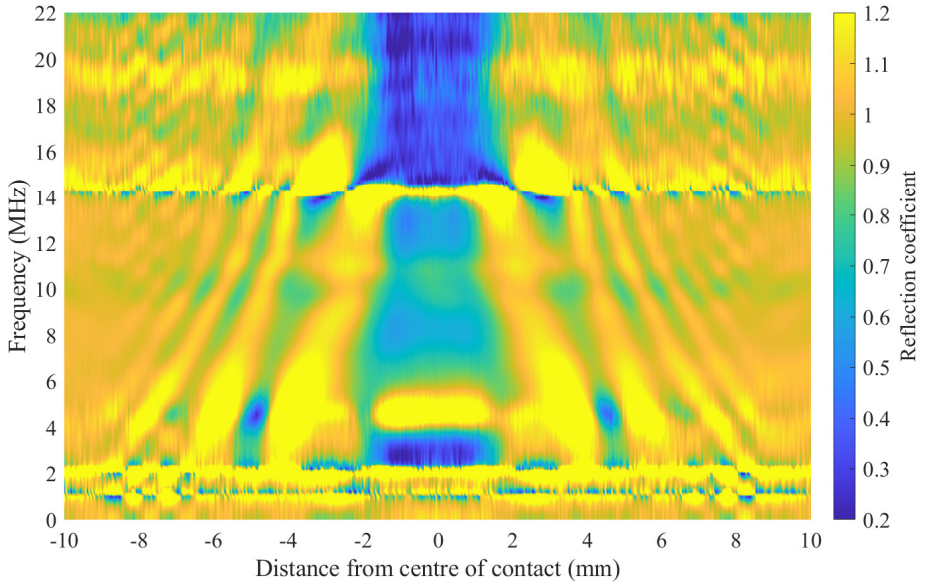

(b)

Figure 7.7: Reflection coefficient results for (a) the base model and (b) experimental data from Chapter 6, VG150 lubricant, 500 kN, 60 rpm, repeat 2, channel 2 across the full bandwidth of the simulated transducer. The bandwidth of the transducer from Chapter 6 was approximately 2 - 14 MHz.

Figure 7.8(a) shows base model reflection coefficient at 10 MHz and change in time of flight. When compared to 7.8(b) there were more similarities in the reflection coefficient plot than the ΔToF plot when compared to real data, although both were

very comparable. The larger difference with ΔToF was likely due to the actual contact deflection, which was not modelled.

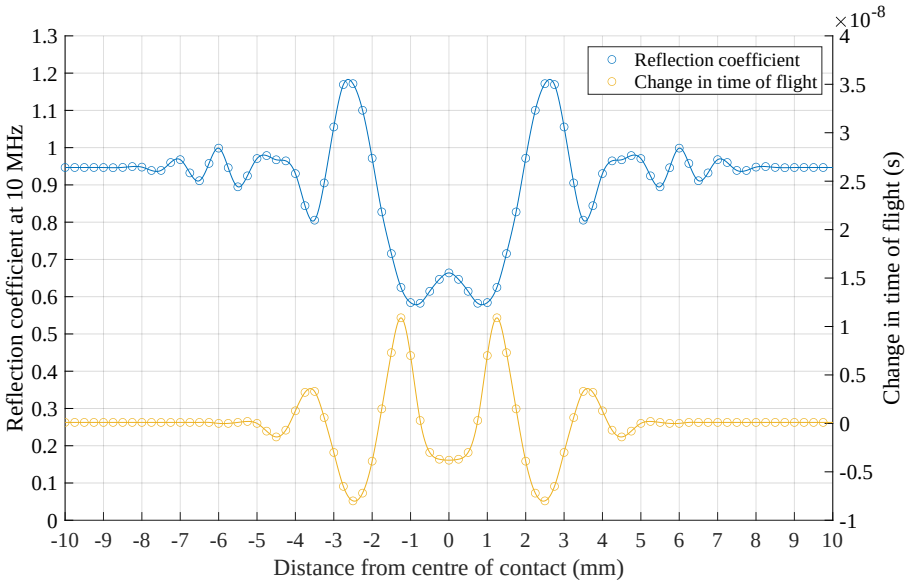

(a)

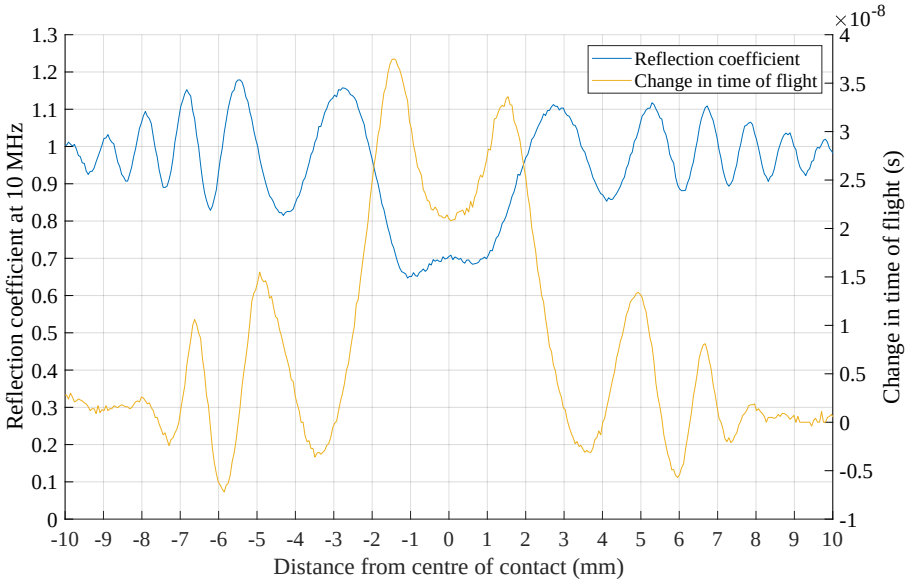

(b)

Figure 7.8: Reflection coefficient and ΔToF results for (a) the base model (cubic splines have been fitted to the data) and (b) for experimental data from Chapter 6, VG150 lubricant, 500 kN, 60 rpm, repeat 2, channel 4.

The results in Figures 7.7 and 7.8 indicated that this simple model reproduced the effect causing fringe effects in real results, and so the effect of changing different model parameters were investigated, as planned. At this stage it is possible to narrow down the cause of fringe effects to interaction of the ultrasonic beam with the small contact. It is likely that reflections from either side of the contact interfere, or that some scattering at the contact edges, resulting in fringe effects.

7.9 The Effect of Different Model Parameters on Fringe Effects

The following sections show the effects of modifying contact width, raceway thickness, sensor width, sensor frequency and roller material properties on both reflection coefficient and change in time of flight across a single roller pass.

In all cases the base model was used as a starting point and one variable was changed. That is: contact width of 1.28 mm, raceway thickness of 19.4 mm, sensor width of 1.0 mm, sensor frequency of 10 MHz and steel material properties.

7.9.1 Contact Width

Figure 7.9(a) shows that MRC was dependent on contact width, as was the magnitude of the central peak. The width of the W shape at R=1 was consistent across all contact widths.

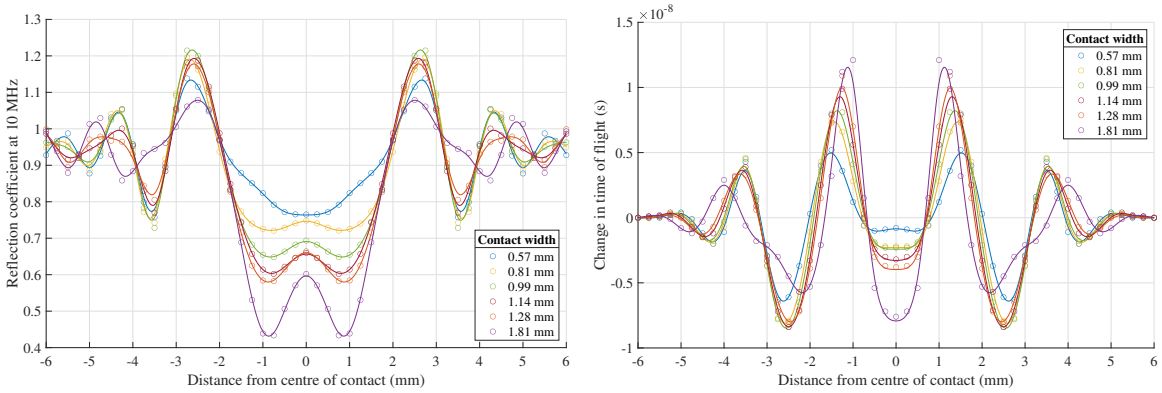

(a) (b)

Figure 7.9: Effect of contact width on *k-Wave* model (a) reflection coefficient and (b) change in time of flight results. Cubic splines have been fitted to the data.

Figure 7.9(b) showed similar trends with changing raceway thickness and change in

time of flight across a roller contact as with reflection coefficient. The central M feature magnitudes increased with contact width. In contrast to reflection coefficient, the width of the M shape appeared to narrow with increasing contact width.

7.9.2 Raceway Thickness

Figure 7.10(a) shows that reflection coefficient was dependent on raceway thickness (i.e. the distance between the sensor and the contact). Reducing the distance both increased MRC and narrowed the central W shape.

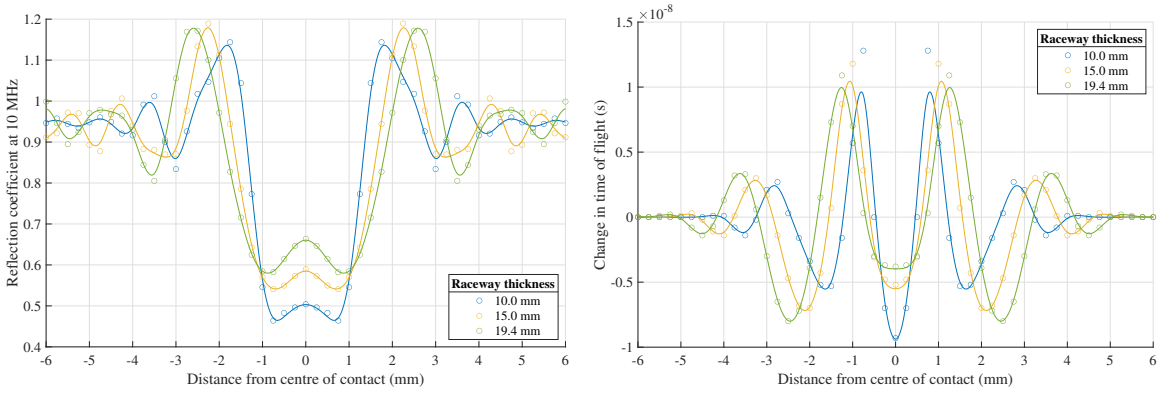

(a) (b)

Figure 7.10: Effect of raceway thickness on *k-Wave* model (a) reflection coefficient and (b) change in time of flight results. Cubic splines have been fitted to the data.

Figure 7.10(b) showed similar trends with changing raceway thickness and change in time of flight across a roller contact as with reflection coefficient. The feature both narrowed and the central magnitude increased with decreasing raceway thickness.

7.9.3 Sensor Width

Figure 7.11(a) showed some dependence between sensor width and reflection coefficient. The magnitude of the side fringes reduced with increased sensor size. The MRC also showed a small reduction with increased sensor size. The width of the W shape did not significantly change with sensor size.

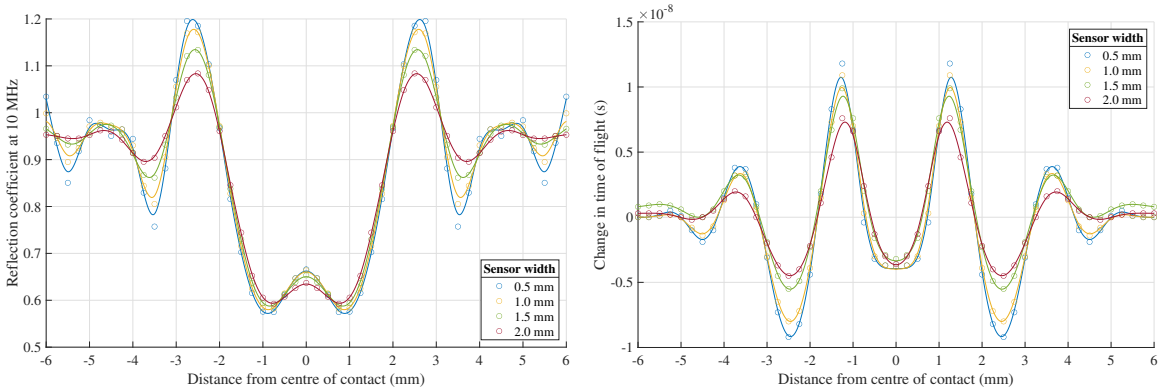

(a) (b)

Figure 7.11: Effect of sensor width on *k-Wave* model (a) reflection coefficient and (b) change in time of flight results. Cubic splines have been fitted to the data.

Figure 7.11(b) showed similar trends with changing raceway thickness and change in time of flight across a roller contact as with reflection coefficient. The side fringes, as well as the peaks of the M shape, reduced in magnitude with increasing sensor size. The central dips and peaks of the W shape showed a trend of slightly reducing in magnitude with increased sensor size too.

7.9.4 Sensor Frequency

Figure 7.12(a) shows that reflection coefficient was strongly dependent on sensor frequency. Reducing the frequency reduced MRC, widened the central W shape and increased the magnitude of the side fringes.

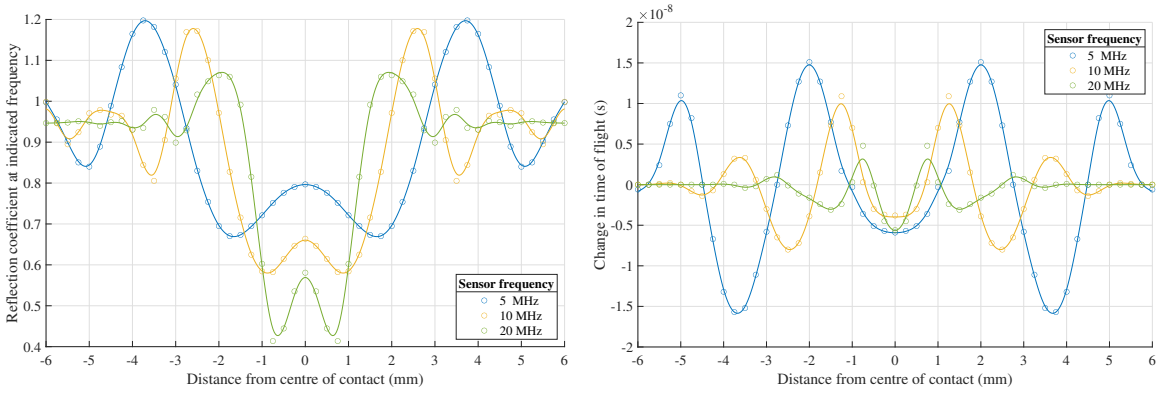

(a) (b)

Figure 7.12: Effect of sensor frequency on *k-Wave* model (a) reflection coefficient and (b) change in time of flight results. Cubic splines have been fitted to the data.

Figure 7.12(b) showed similar trends with changing raceway thickness and change in time of flight across a roller contact as with reflection coefficient. The features all narrowed with increasing sensor frequency and the magnitude of the side fringes and M peaks reduced with increasing sensor frequency. In contrast to reflection coefficient, the magnitude of the central dip did not show a trend with sensor frequency.

7.9.5 Modelling Different Roller Materials

In order to view the effect of differing levels of transmission though the contact the material properties of the roller were changed. The properties of aluminium and rubber were selected to give a range of reflection coefficient values and are shown in Table 7.3. Calculated using Equation 3.3, this should have given reflection coefficients of 0.45 and 0.89 respectively.

Material	Density (kg/m^3)	Speed of sound (m/s)	R with steel
Aluminium	2710	6410	0.45
Rubber	1200	2300	0.89

Table 7.3: Alternative roller material properties used in the *k-Wave* simulation.

Figure 7.13(a) shows that reflection coefficient was strongly dependent on roller material. Reducing the theoretical reflection coefficient reduced the MRC, increased the magnitude of the central peak and increased the magnitude of the side fringes. The width of the W shape was not strongly affected.

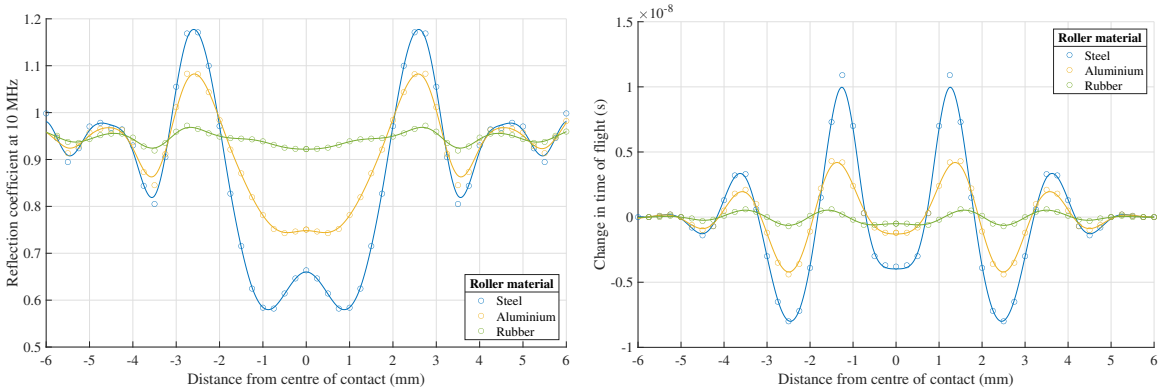

(a) (b)

Figure 7.13: Effect of roller material on *k-Wave* model (a) reflection coefficient and (b) change in time of flight results. Cubic splines have been fitted to the data.

Figure 7.13(b) showed similar trends with changing roller material and change in time of flight across a roller contact as with reflection coefficient. Reducing the theoretical reflection coefficient increased the magnitude of the central dip and the magnitude of the side fringes. The width of the M shape was not strongly affected.

7.9.6 Summary

From Figure 6.12 a decrease in MRC and an increase in the magnitude of the central peak (feature C) in reflection coefficient with increasing load can be expected. Likewise, with ΔToF an increase in the maximum ΔToF and the magnitude of the central dip (feature C2) with increasing load can be expected. A combination of both changing modelled contact width (Figure 7.9)and changing the proportion of ultrasound transmitted through the contact (or roller material, see Figure 7.13) gave these expected changes without additional changes.

Changing modelled sensor frequency also matched with experimental results. The width of the W shape (Features A and B) in modelled reflection coefficient trends increased in width with reduced frequency as shown in Figures 7.7 and 7.12, which can also be seen in experimental data in Figures 6.10 and 6.11. The larger changes in side fringe (feature D) and MRC in Figure 7.12 were not seen in experimental data as only single frequency transducers were used.

At this stage the modelling plan has concluded as the reproduced fringe effects behave in the same manner as those seen experimentally. There was no need to continue onto stage 2 and beyond of the planned modelling.

The remaining model parameters, raceway thickness and sensor width point towards dependence on beam width and therefore knowledge of beam width may enable these relationships to be better understood. The following section does just that.

7.10 Modelling Beam Width

The following figures show the simulated beam shape when changed for different sensor sizes and frequencies. Beam shape was determined through recording maximum pressure at each grid point in an entirely steel grid.

7.10.1 Sensor size

Figure 7.14 shows the effect of increasing sensor width on the resulting beam shape at a frequency of 10 MHz. Figure 7.15 shows the resulting spot size at an interface 19.4 mm from the sensor. Spot size decreased with increasing sensor width up to a width of around 5 mm, after which it increased again. At the larger sensor widths the spot size was close to the sensor size, but not at the smaller sensor widths.

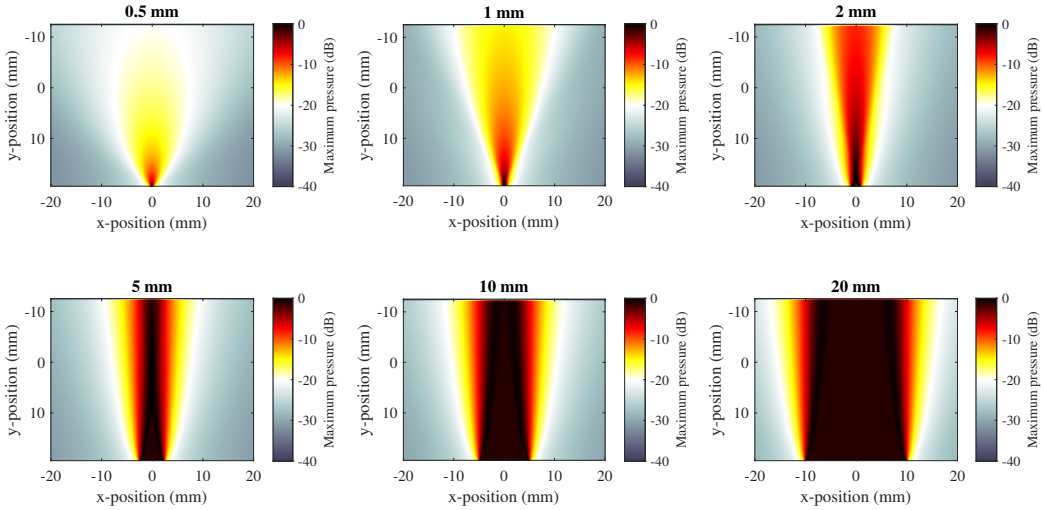

Figure 7.14: Effect of sensor width on *k-Wave* simulated sensor field (maximum pressure).

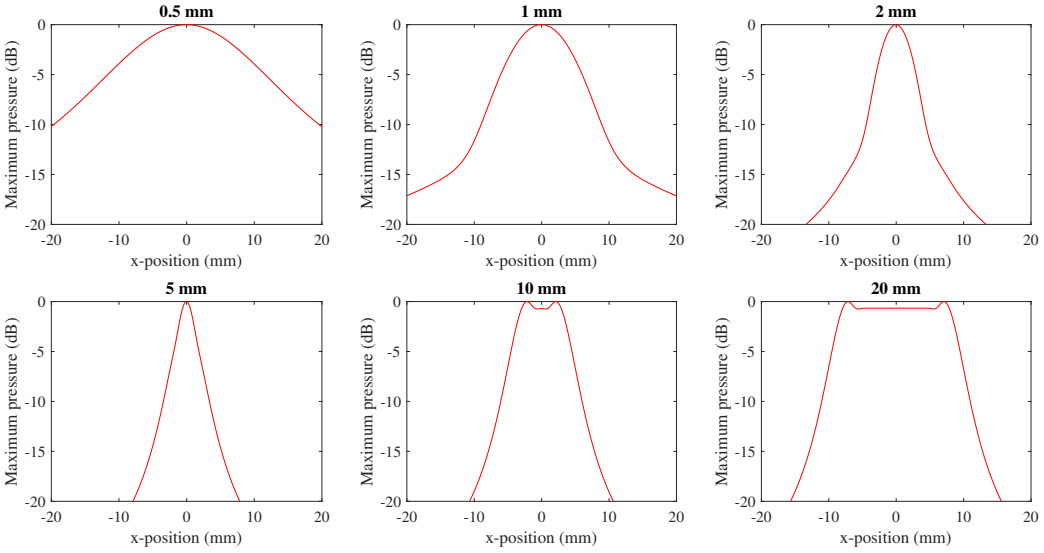

Figure 7.15: Effect of sensor width on *k-Wave* simulated sensor spot size at the interface (maximum pressure).

7.10.2 Sensor frequency

Figure 7.16 shows the effect of increasing sensor frequency on the resulting beam shape at a sensor width of 1 mm. Figure 7.17 shows the resulting spot size at an interface, 19.4 mm from the sensor. It can be seen that spot size decreased with increasing frequency.

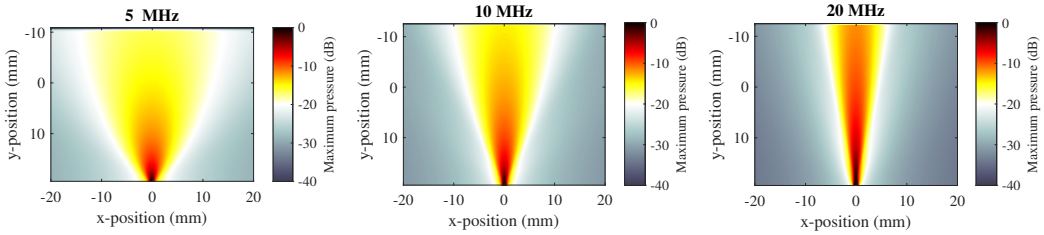

Figure 7.16: Effect of sensor frequency on *k-Wave* simulated sensor field (maximum pressure).

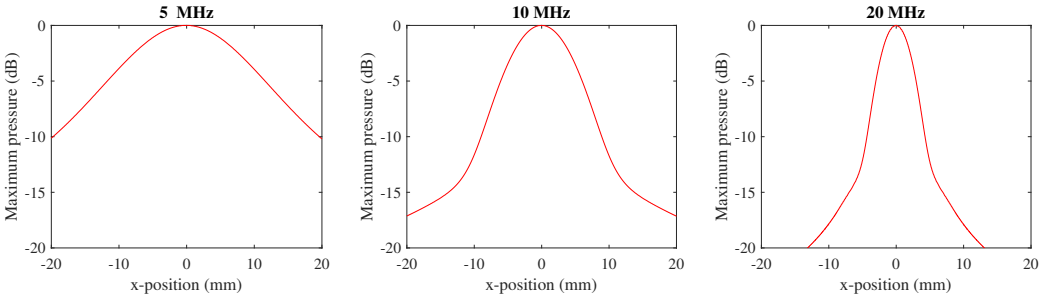

Figure 7.17: Effect of sensor frequency on *k-Wave* simulated sensor spot size at the interface (maximum pressure).

7.10.3 Raceway thickness

Figure 7.18 shows the effect of changing the distance from the sensor to the interface (raceway thickness) at a sensor frequency of 10 MHz and a sensor width of 1 mm. To a lesser effect than changing sensor width and frequency, spot size reduced with decreasing raceway thickness.

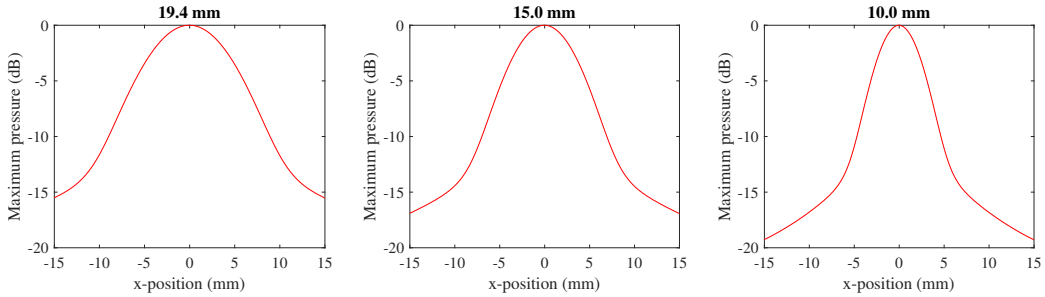

Figure 7.18: Effect of raceway thickness on *k-Wave* simulated sensor spot size at the interface (maximum pressure).

7.10.4 Summary

The magnitude changes in spot size with relation to model parameters, from largest to smallest were: sensor frequency, sensor width and raceway thickness. This was not the same order as the overall magnitude changes in reflection coefficient with relation to model parameters and so a more complex relationship between the fringe patterns and model parameters than the ratio between spot size and beam width was deemed likely.

At this point it was speculated that the fringe effects were a result of the spot size being too large in relation to the contact. The resulting reflections from either side of the contact likely interfered with each other, distorting the sensor signal. This interference pattern would be dependent on the wavelength of the ultrasound and the differences in magnitude between the reflected signal from the left and right sides of the contact. The level of distortion of the signal from the resultant fringe effects would likely be dependent on the difference in magnitude of the reflected signal from the contact and from the free surface.

7.11 Modelling Focussed Transducers

The sensor beam of a focussed transducer can be modelled in *k-Wave* by adding curvature to the sensor using the *k-Wave* function *makeArc*. Figure 7.19 shows the progression of focussed sensor beam shape with increasing sensor width, with the same sensor widths as in Section 7.10.1. Figure 7.20 shows the resulting spot size at an interface 19.4 mm from the sensor. Through comparison to Figures 7.14 and 7.15 it can be seen that smaller spot sizes were created with focussed transducers, increasing in effectiveness as the size of the transducer increased.

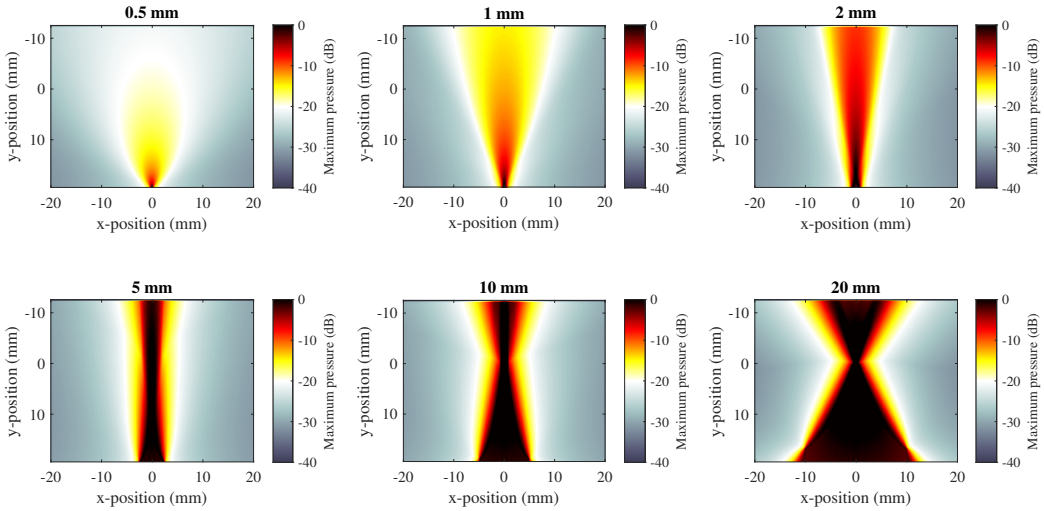

Figure 7.19: Effect of sensor width on *k-Wave* simulated sensor field (maximum pressure).

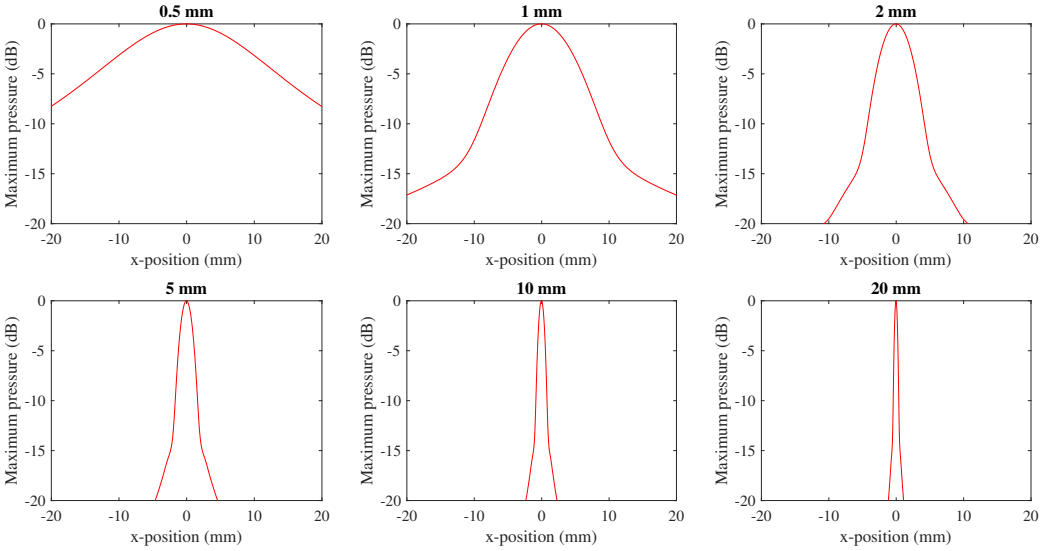

Figure 7.20: Effect of sensor width on *k-Wave* simulated sensor field (maximum pressure).

Figures 7.21 and 7.22 show results for a single roller pass of the base model but with a 10 mm and 20 mm focussed transducer. When compared to Figure 7.8 both of the reflection coefficient results can be seen to be vastly improved.

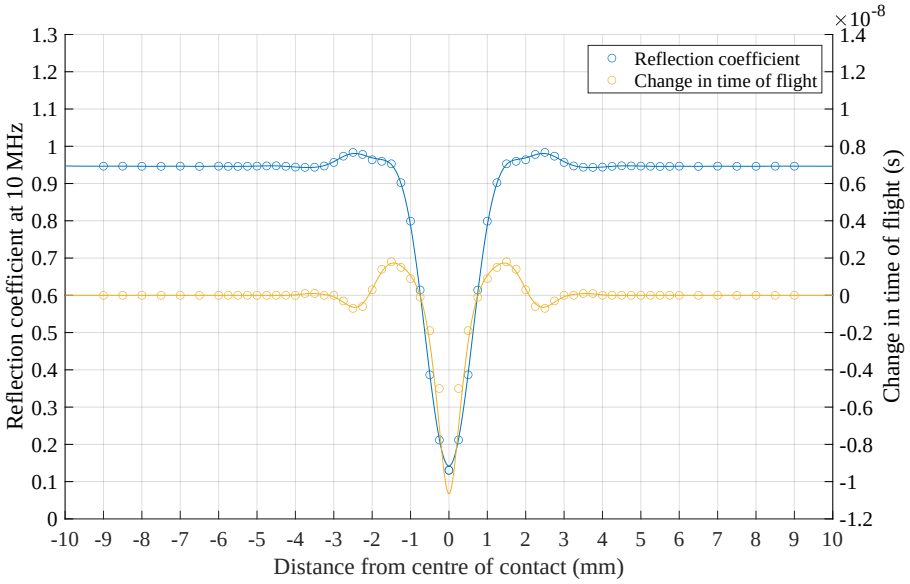

Figure 7.21: 10 MHz reflection coefficient and change in time of flight results for the base model with a 10 mm focussed transducer.

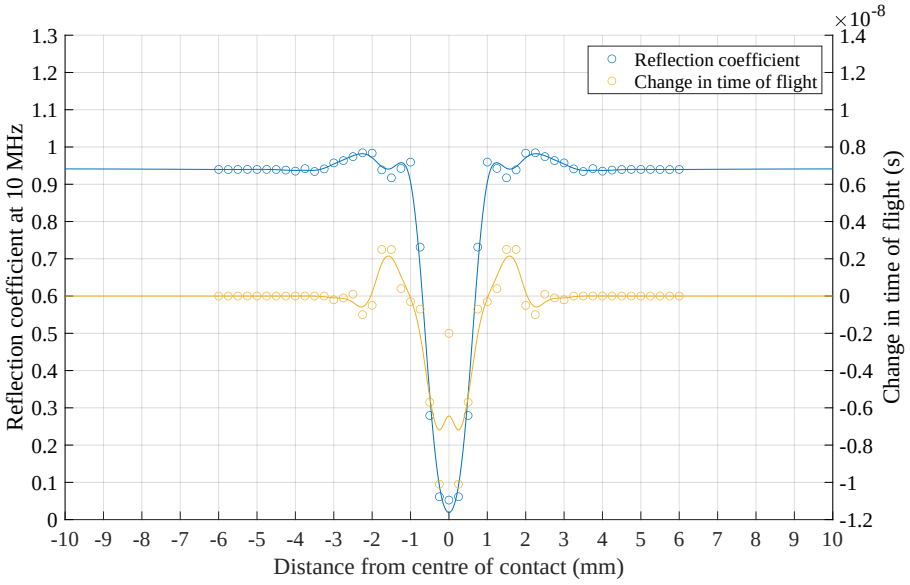

Figure 7.22: 10 MHz reflection coefficient and change in time of flight results for the base model with a 20 mm focussed transducer.

If we look at the central measurements for both the focussed transducers, the 10 mm transducer had one measurement close to 0.1 and the 20 mm transducer had three measurements close to 0.05. As the beam spot reduced in size the MRC value approached the correct value of 0 and the number of measurements within the contact increased. Both focussed transducers also gave an almost perfect contact width estimation of 1.28 mm at a reflection coefficient value of 0.5. Interestingly, the 20 mm result did, however, show more severe side fringes in the signal than the 10 mm result. To further understand why this happened we will introduce the spectrograms for the two results, shown in Figures 7.23 and 7.24.

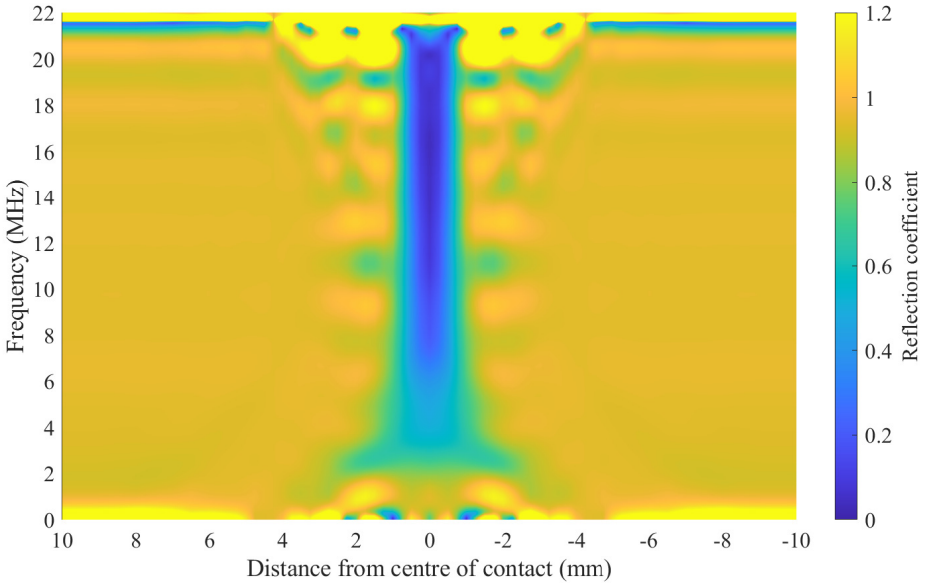

Figure 7.23: Reflection coefficient results for the base model across the full bandwidth of the simulated transducer. Sensor modified to a 10 mm focussed transducer.

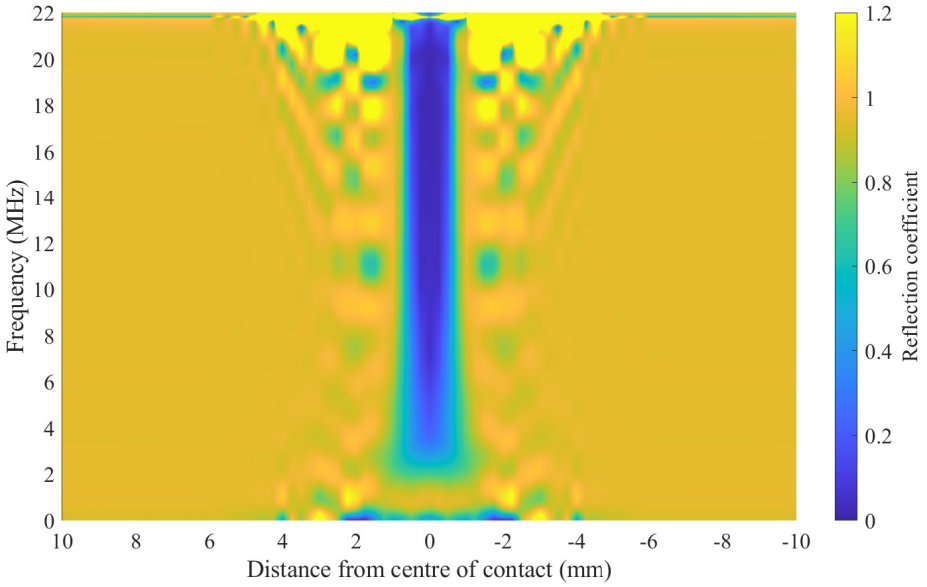

Figure 7.24: Reflection coefficient results for the base model across the full bandwidth of the simulated transducer. Sensor modified to a 20 mm focussed transducer.

These spectrograms no longer show curved side fringes, in a curtain shaped pattern, as seen in Figure 7.7, and the width of the central dip was no longer strongly dependent on frequency. They did, however still show fringes either side of the contact, which alternated between peaks and troughs, depending on frequency. Coincidentally, for the 10 mm sensor, 10 MHz fell between one of these peaks and troughs. To further illustrate this point, Figure 7.25 shows reflection coefficient results from the 20 mm focussed transducer at several frequencies. These aspects of side fringes were likely caused by scattering of the ultrasound at the edges of the contact and appear to be dependent on both the sensor width and the frequency of the ultrasound.

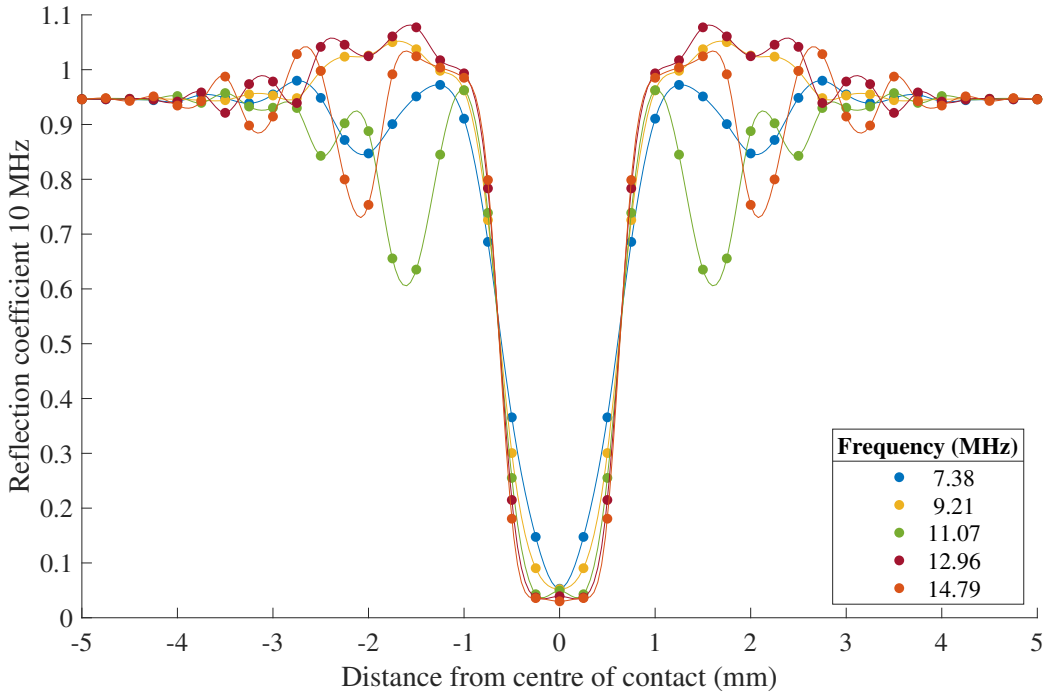

Figure 7.25: 10 MHz reflection coefficient and change in time of flight results for the base model with a 20 mm focussed transducer.

Even with the presence of these side fringes, these models indicate that with focussed transducers we can monitor both the contact width and reflection coefficient fairly accurately. The maximum error in contact width from these frequencies was 0.02 mm. All of the errors are summarised in Table 7.4. The error for a specific application will be dependent on transducer spot size (affected by transducer frequency, size, shape, focussing, distance from the sensor to the contact and bonding) and contact width.

Frequency (MHz)	MRC	Ultrasound predicted contact width (mm)	Error in contact width (mm)
7.38	0.053	1.24	0.02
9.21	0.052	1.26	0.01
11.07	0.050	1.28	0.00
12.96	0.039	1.28	0.00
14.79	0.030	1.28	0.00

Table 7.4: Summary of results from changing frequency with a simulated 20mm focussed transducer. Data extracted from Figure 7.25.

The vast improvements that sensor focussing showed on reflection coefficient measurements did not translate to change in time of flight measurements and so further

investigation was deemed necessary. This result coincides well with early work on focussed immersion transducers which did not see fringe effects in their results.

Figure 7.26 shows how reflection coefficient trends changed with contact width when the simulated transducer was focussed. This shows the limits of this particular sensor size and frequency. The transducer was adequate for monitoring contacts of around 1.2 mm and above but below this the MRC over-predicted more significantly and the contact width also began to over-predict, as can be seen in Table 7.5.

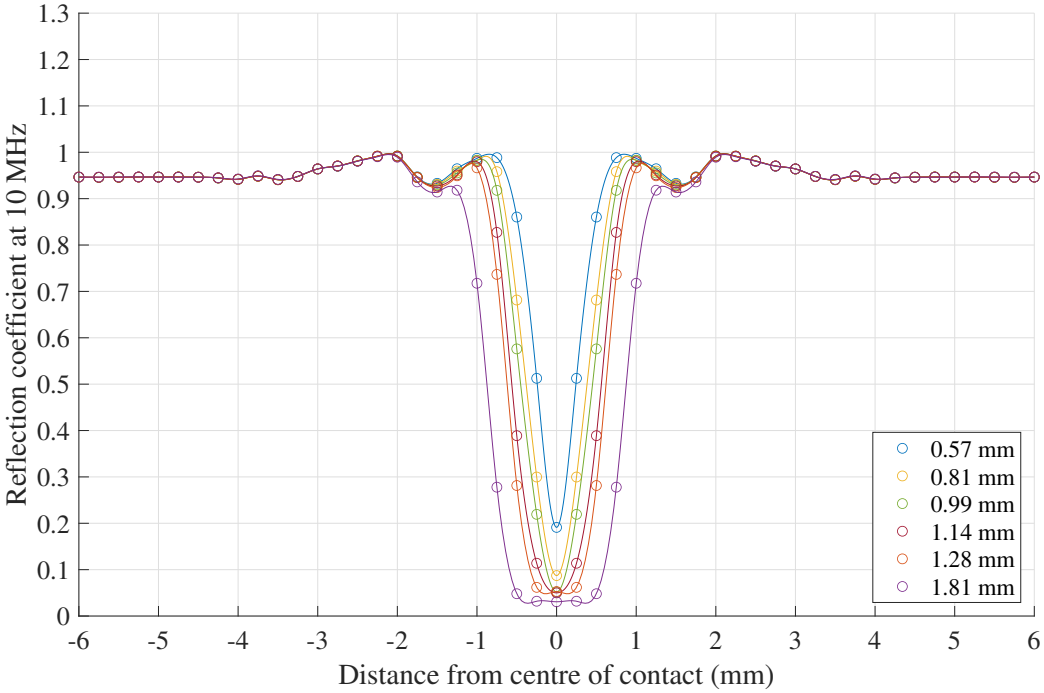

Figure 7.26: 10 MHz reflection coefficient results for the base model with a 20 mm focussed transducer and varying contact width.

Contact width (mm)	MRC	Ultrasound predicted contact width (mm)
1.81	0.013	1.8
1.28	0.037	1.3
1.14	0.056	1.2
0.99	0.117	1.1
0.81	0.194	0.8
0.57	0.370	0.6

Table 7.5: Summary of results from changing contact width with a simulated 20mm focussed transducer. Data extracted from Figure 7.26.

7.12 Investigating Change in Time of Flight Processing Methods

The following figures show comparison of three different methods for comparing change in time of flight. The first is as previously described: the normalised Hilbert envelope of the measurement and reference signals were cross correlated in order to obtain change in time of flight. The second used the difference in time between the (non-normalised) maxima of the two Hilbert envelopes. The third monitored one of the locations (in a specific time interval) at which the A-scan signal crossed zero and compared this time value to the reference signal. The results for the base model are shown in Figure 7.27 and results with a 20 mm focussed transducer are shown in Figure 7.28.

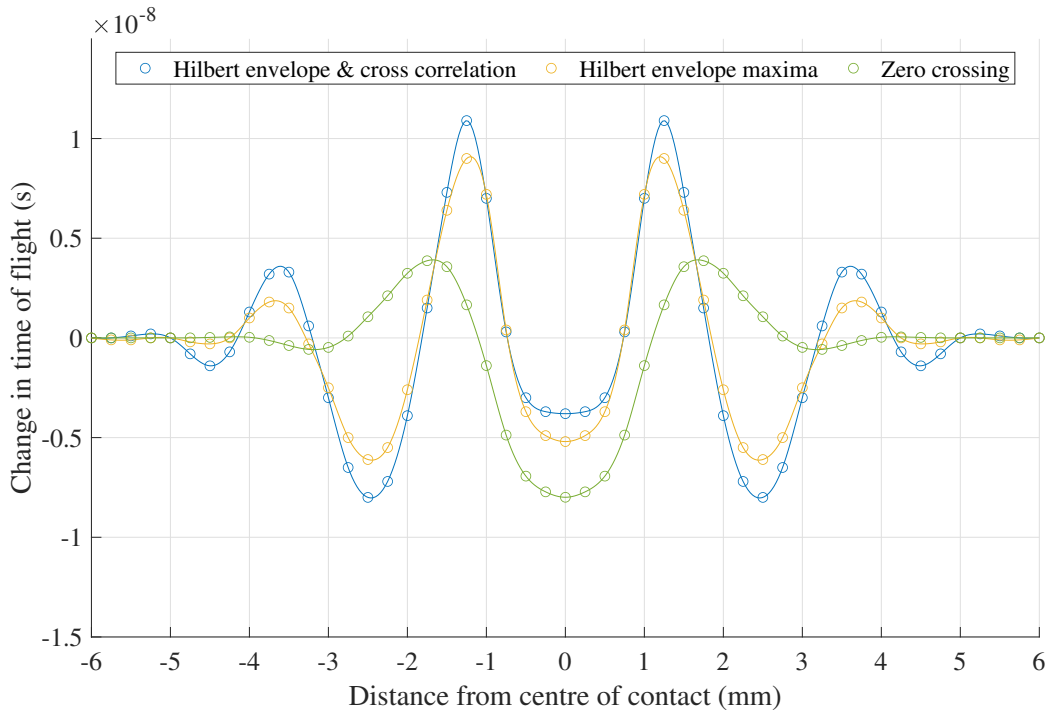

Figure 7.27: Change in time of flight results for the base model with three different methods for monitoring change in time of flight.

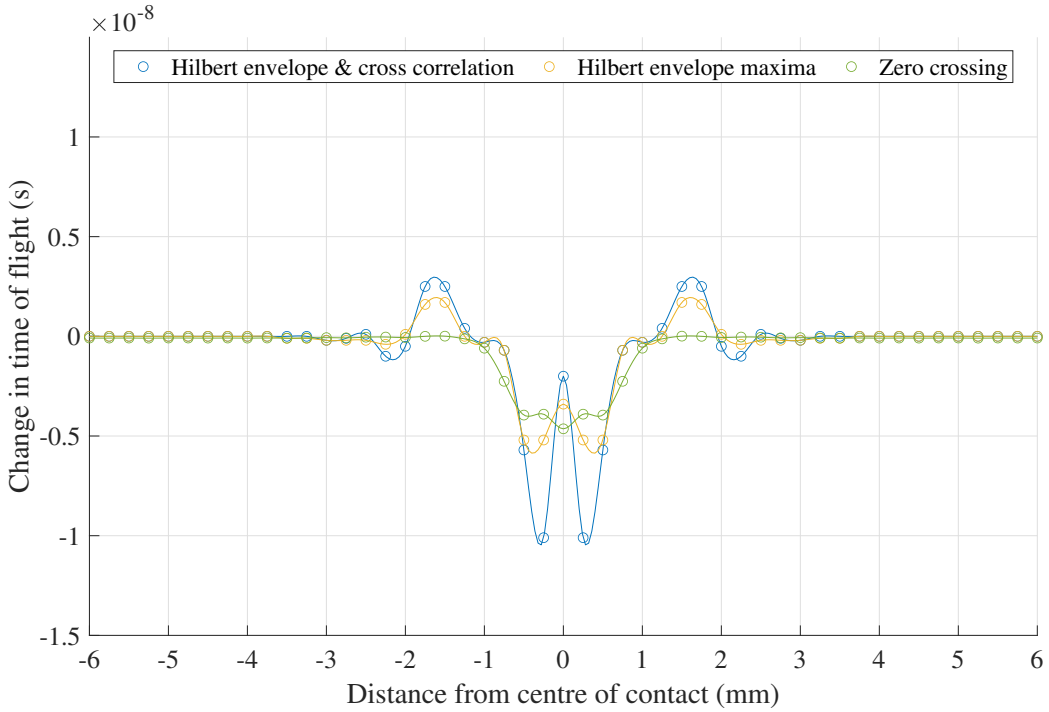

Figure 7.28: Change in time of flight results for the base model, modified with a 20 mm focussed transducer, with three different methods for monitoring change in time of flight.

Results in the base model showed the most distortion with the Hilbert cross correlation method, a small reduction in distortion using the Hilbert maxima method and a significant reduction using the zero crossing method. Results with the focussed model showed the same trend and an overall reduction in distortion. They also showed a different trend, with a peak in the middle. Even so, there was still distortion present in the signal with the focussed transducer and the use of the Hilbert transform with real data is necessary to remove phase shifts in the signal due to varying contact stiffnesses.

Ideally a flat line of change in time of flight of zero across the contact is desired as there was no deflection in this model. With this in mind, all three methods showed some distortion of the signal, even with a focussed transducer. It should therefore be considered that change in time of flight measurements have too much distortion in them to be a reliable measurement technique. Interference patterns in change in time of flight signals are most likely a result of interaction of the sensor beam with the edges of the contact. The overall trends shown in Chapters 4 and 6 are likely a combination of the interference modelled here and a measurement of actual deflection,

but it does not appear to be possible to separate the two in order to monitor actual deflection, at least not with sensor focussing.

Whilst changes in deflection could be monitored using change in time of flight, actual values are likely to be quite inaccurate. It is surprising that the technique has given sensible results thus far. The author suggests that, instead of measuring deflection with time of flight and converting to load, the contact width should be measured through reflection coefficient using focussed ultrasonic techniques and this value used to calculate contact load instead.

7.13 Confirmation of the Causes of Fringe Effects

7.13.1 Reflection from either side of the contact

In order to verify that reflections from either side of the contact were partially to blame for fringe effects the base model was adapted so that only the reflected signal was simulated. The reflected signal was generated by creating two point sources at the interface spaced 1.28 mm apart. The entire raceway was simulated as a sensor in order to record a B-scan of the resulting wavefront. The resulting B-scan can be seen in Figure 7.29. If we look at this figure from the front, the resulting interference pattern is more obvious, as shown in Figure 7.30.

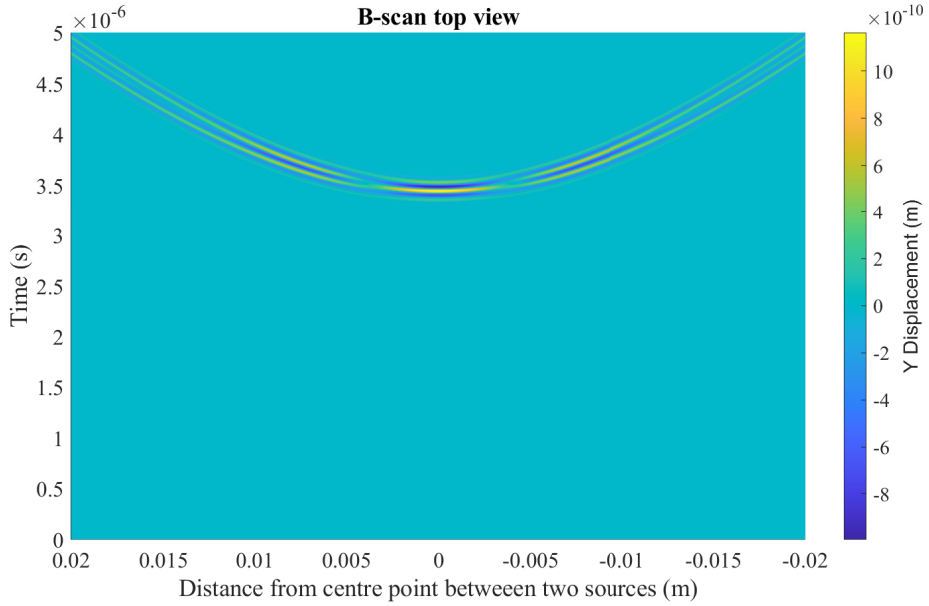

Figure 7.29: *k-Wave* simulated B-scan from two equal point sources, top view.

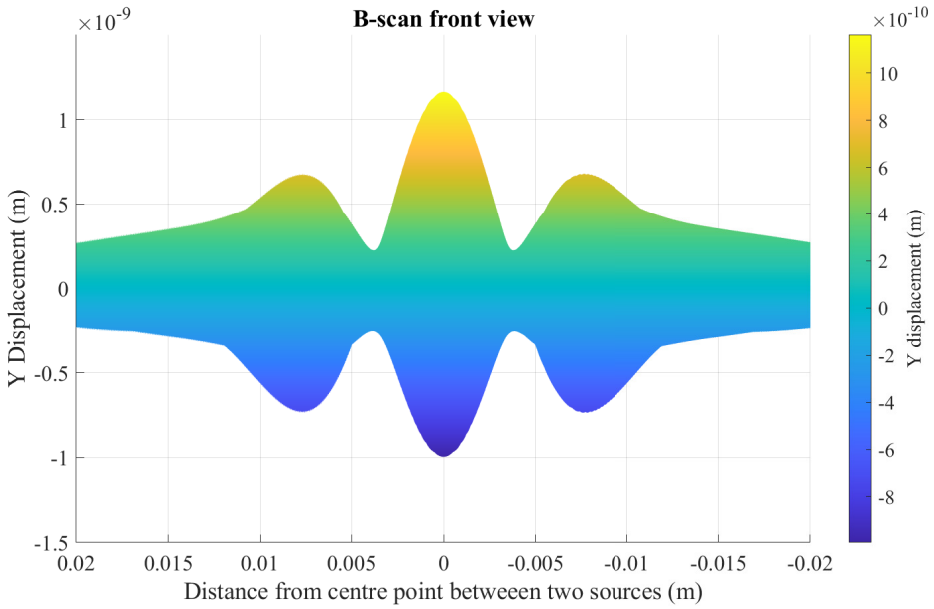

Figure 7.30: *k-Wave* simulated B-scan from two equal point sources, front view.

This was only representative of the wavefront when the sensor was aligned with the contact. When it was not aligned one of the reflections was slightly delayed and lower in amplitude. The effect of lowering amplitude of one source by 50% is shown in Figure 7.31 and the effect of a short delay on the same sensor is shown in Figure 7.32.

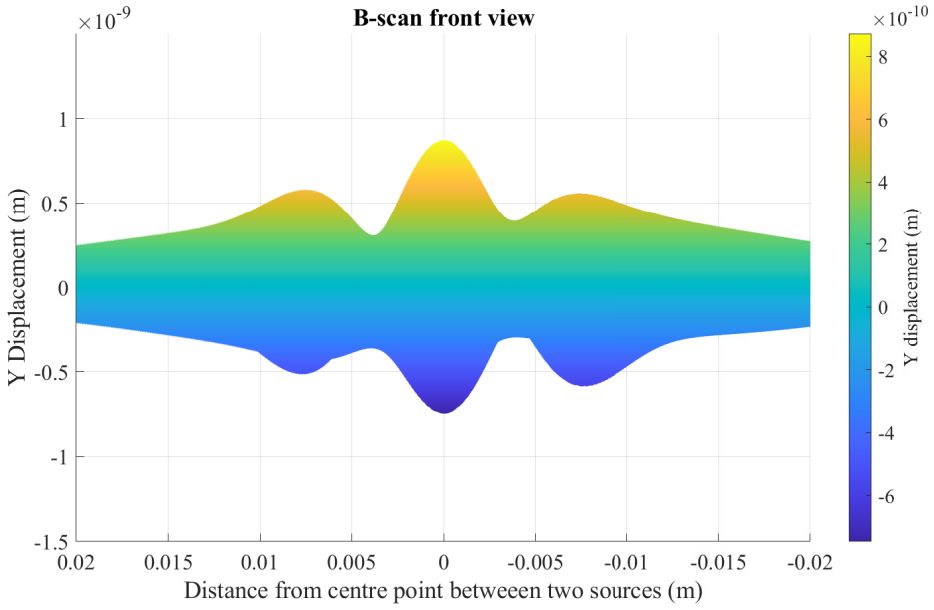

Figure 7.31: *k-Wave* simulated B-scan from two point sources, one of which had half the amplitude of the other. Front view.

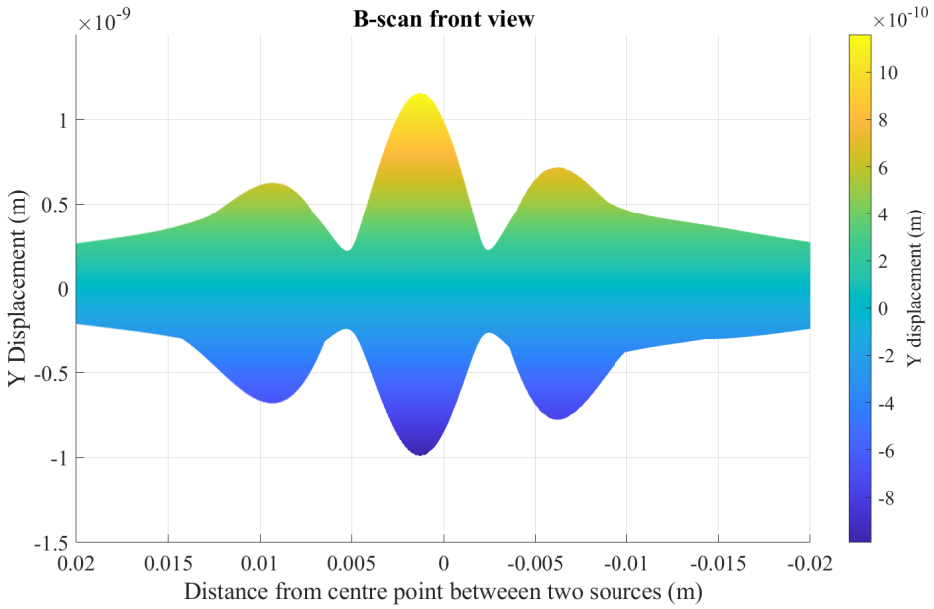

Figure 7.32: *k-Wave* simulated B-scan from two point sources, one of which was slightly delayed. Front view.

One can see the how the resulting interference pattern would lead to the interference in the signals shown in previous results as fringe effects.

7.13.2 Scatter from a contact edge

Another source of interference fringe features was thought to be scatter from the contact edge. In order to verify this, another modified model was created with only one contact edge, as shown in Figure 7.33.

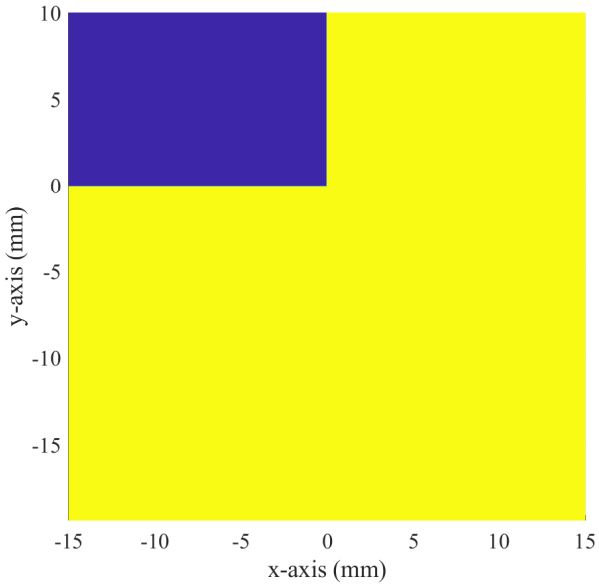

Figure 7.33: Edge model geometry as a *k-Wave* material properties grid.

The resulting reflection coefficient and change in time of flight results are shown in Figure 7.34.

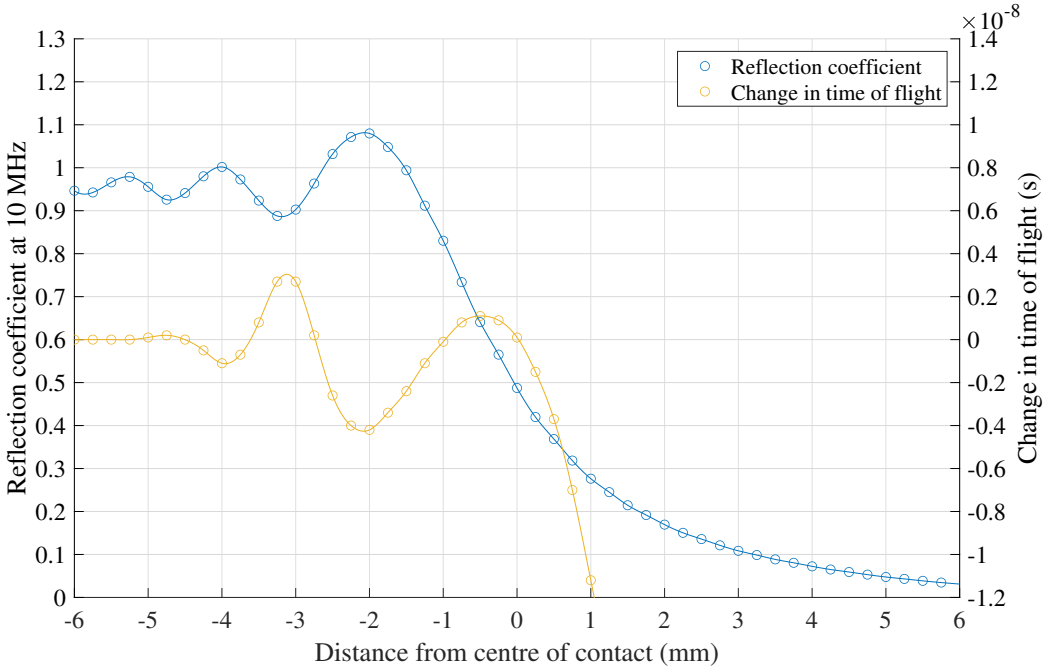

Figure 7.34: 10 MHz reflection coefficient and change in time of flight results for the single edge model.

This clearly shows how side fringes can be a result of interaction of the sensor beam with the contact edge.

7.14 Conclusions

This work has used *k-Wave* acoustic modelling software to recreate fringe effects seen in real measurement of roller contacts using bonded ultrasonic sensors. Model results suggested that:

- Fringe effects were partially caused by reflection from both sides of the contact when sensor spot size is larger than the contact and partially caused by interaction of the sensor beam with the contact edge.
- The stage at which modelling was concluded also suggested that fringe effects were not dominated by the effect of raceway curvature, varying stiffness across the contact, deflection of the contact or acoustoelastic effects.
- The measurement area of a bonded transducer is not equal to its footprint in all cases, particularly for small sensors.
- Focussing can vastly improve reflection coefficient signals to the point where MRC and contact width values are sufficiently accurate. The best case modelled gave 0% error in contact width and a 1.3% error in MRC.
- The error for a specific application will be dependent on transducer spot size and contact width. Increasing transducer frequency and transducer size will reduce error, as will perfect curvature for focussing and reducing the distance from the sensor to the contact (up to a minimum focal distance defined by sensor size). Bonding of the transducer also appeared to have a focussing effect which has not been quantified.
- Focussing cannot be used to remove interference from change in time of flight signals. Whilst changes in deflection could be monitored using change in time of flight, actual values are likely to be quite inaccurate. It is surprising that the technique has given sensible results thus far.
- It is suggested that, instead of measuring deflection with time of flight and converting to load, the contact width should be measured through reflection coefficient using focussed ultrasound techniques and the measured contact width to calculate contact load.

Chapter 8

Ultrasonic Monitoring of Small Contacts Using the Total Focussing Method

8.1 Selection of an Ultrasonic Focussing Method

There have been several attempts to increase the accuracy of ultrasound methods without focussing where the focal spot size is larger than the contact. Prediction of the contact width using Hertzian contact calculations, along with ray tracing modelling of the contact, have been used with some success to correct film thickness measurements [89, 91]. This technique assumed that the measurement width of the contact was equal to the size of the transducer which we have seen from Sections 3.7.4 and 7.10 is an contended assumption with bonded transducers. This also does not alleviate any challenges from contact patch size and shape monitoring in the presence of fringe effects.

Other techniques have attempted to improve accuracy using the non-overlapping sections of successive spot sizes to increase resolution of reflection coefficient measurements [90]. These experiments made use of focussed immersion transducers and required knowledge of the focal spot size of the transducer. With bonded transducers this is clearly not simple to predict, as discussed in Section 3.7.4, and measurement of sensor spot size is not a simple undertaking.

With the confirmation that fringe effects are caused by large beam spread of bonded transducers, the question now becomes: how can we focus ultrasound at the contact without losing the small form factor and repeatability of bonded transducers?

The most common passive techniques use ultrasonic transducers with curved faces. Commercially available probes are all designed for immersion transducers and thus it would be difficult to obtain the correct curvature for focussing in steel. It would also be extremely difficult to permanently couple such a transducer with a steel component as the steel surface would require very precise machining to be conformal. Other methods of passive focussing include apodization cones and Fresnel zone plates [110] although these techniques cause significant amplitude losses in the resultant signal. This leaves the use of arrays of transducers.

Active focussing uses an array of transducers together with time delayed pulsing and receiving to artificially create the curved wavefront of a focussed transducer, as shown in Figure 8.1. This figure also introduces some standard terminology for arrays of transducers, including the aperture, element pitch and element width of a 2D array. The beam width at the focal point can be approximated by Equations 3.16 and 3.17 when replacing the transducer width with the array aperture and the distance from the source by the intended focal length. The focal length must be less than the near field distance, calculated with Equation 3.15, also replacing transducer width with the array aperture.

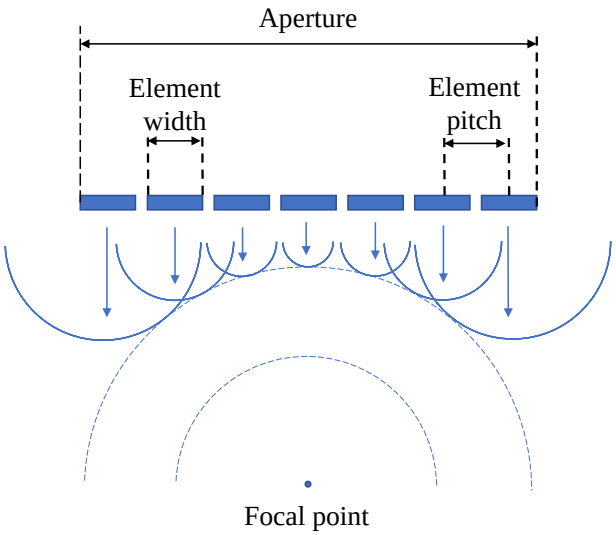

Figure 8.1: A diagram to show how an array of transducers can replicate a curved transducer.

This technique is promising for use on rolling element bearings however the specialist and relatively expensive equipment required for simultaneous delayed pulsing of sev-

eral elements with active time delays and multi-channel digitisation was not available at the University of Sheffield at the time of this work.

8.1.1 Total Focussing Method Concept

The final option was therefore to use full matrix capture (FMC) in combination with the total focussing method (TFM). As previously described FMC involves capturing reflections for the full range of transducer pairs of an array. i.e. transducer 1 is pulsed and data is received from transducer 1 and then each of the other transducers in the array. This is repeated, pulsing each of the transducers. The result is a 'full matrix' of captured data. Essentially this allows the focussing effect of delaying pulse excitation and digitisation to be undertaken in post processing, meaning that the focus is adjustable. An example post processing focussing method is the total focussing method [81].

The TFM defines a grid of an area of interest that is a known distance from the array. For each point in the grid the known speed of sound in a material is used to calculate the time of flight from each of the sensors to this grid point and back to each of the sensors, resulting in a matrix of time of flights, equal in size to the number of A-scans captured by FMC. The amplitude of each A-scan in the FMC is then summed at each of these corresponding time of flights in order to define the FMC amplitude at this location. This is repeated for each point in the grid. Figure 8.2 illustrates this. Increasing array aperture increases the resolution of the image produced by the TFM and decreasing the element pitch (i.e. increasing the number of elements in the array) reduces the amount of artefacts in the image [111, 112]. Reducing the pitch should remove artefacts at half the wavelength of the ultrasound so there is no additional benefit to reducing it further than this. Medical imaging typically uses one wavelength pitch distance.

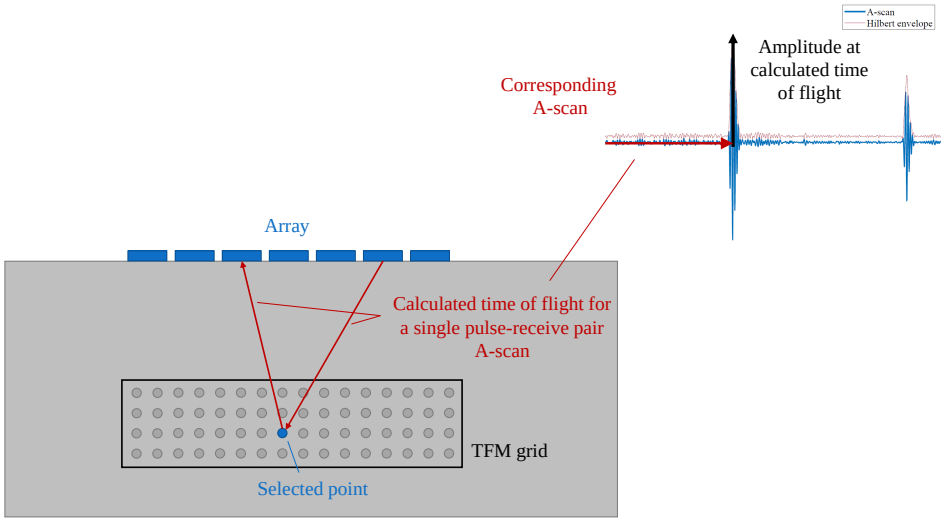

Figure 8.2: A diagram to illustrate the TFM.

Arguably, for a rolling element bearing only a fixed focal location was required due to the fixed raceway thickness, however, with the equipment available at the University of Sheffield FMC was possible and active focussing was not. This was achieved using a multiplexer which allowed the PRF of a single channel UPR to be split across all the channel combinations. The result, depending on the number of sensors was a fairly slow overall pulse delay, in the order of magnitude of seconds, rather than microseconds for a single sensor. This was mainly limited by the speed of the multiplexer. With an infinitely fast multiplexer, the overall pulse delay would be in the order of magnitude of milliseconds, or a PRF of 100s of Hz. This would still be too low for monitoring most roller bearings under normal operational speeds as low numbers of measurements within the contact would be taken. Nevertheless, an investigation using TFM techniques was deemed valuable in order to see if focussing was sufficient for the removal of fringe effects. Results may also be useful for the study of other small tribological contacts where longer measurement durations are not an issue.

Prior to the COVID pandemic, development of ultrasonic data acquisition hardware, as well as improved array instrumentation techniques was planned. This may have enabled active focussing techniques or high speed FMC capture to be employed on actual bearings, however work plans had to be adapted as lab access was not possible for such development. A more model focussed approach was therefore adopted for the remainder of this work.

8.2 Modelling the Total Focussing Method

In order to investigate the suitability of the total focussing method on tribological contacts an adapted *k-Wave* model from Chapter 7 was used. The model was similar to the base model from the previous chapter but with different source and sensor definitions. That is: contact width of 1.28 mm, raceway thickness of 19.4 mm, sensor width of 1.0 mm, sensor frequency of 10 MHz and steel material properties.

A transducer array width was defined and split up into a number of elements. A single model was solved for each of the defined source positions. The pulse was simulated across the simulated element and the results were recorded across the entire length of the array. The recorded results across the array were then split into element A-scans in post processing.

Due to the success of the 20 mm focussed transducer in removing signal distortion in Chapter 7, a 20 mm array was first modelled.

8.2.1 Data Processing

In order to obtain a reflection coefficient from the data, both a reference and measurement roller were used. The reference model had no roller present and the measurement model had a contact width of 1.28 mm. TFM processing used a modified script and functions in *MATLAB* provided by Jie Zhang from the University of Bristol. TFM grid spacing was set at 0.1 mm and TFM amplitude was calculated for the grid. The resulting amplitudes for each model are shown in Figure 8.3.

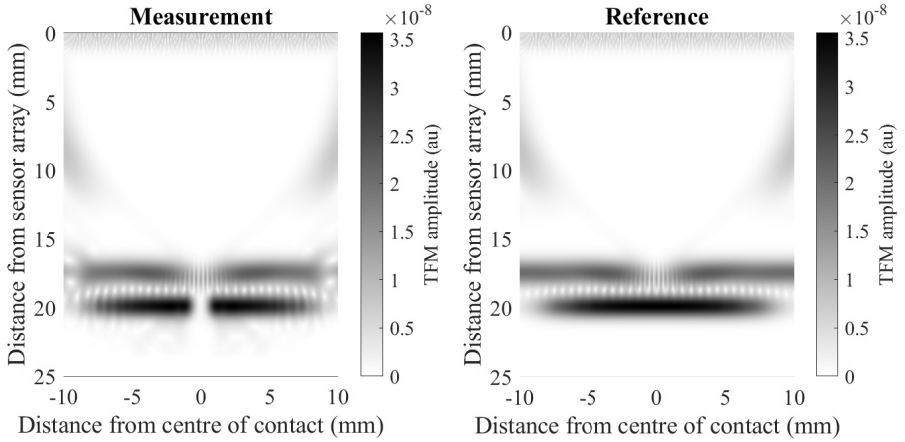

Figure 8.3: TFM grids for a 20mm array split into 16 sensors. Left was for a 1.28 mm contact. Right was for a reference model with no contact.

The amplitude at the contact interface was extracted for each model, as shown in Figure 8.4 (left). Reflection coefficient can be seen in Figure 8.4 (right) which was calculated using Equation 7.1.

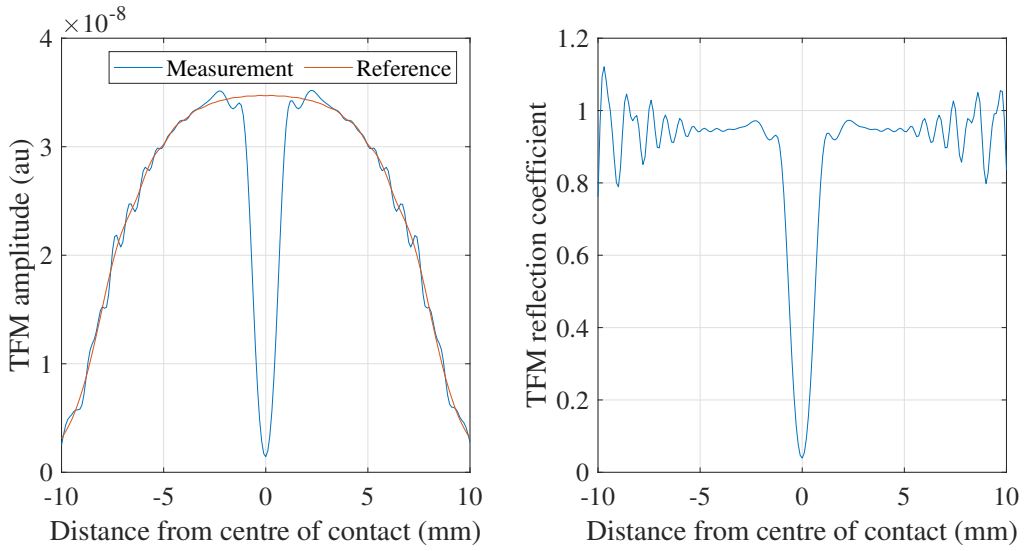

Figure 8.4: TFM amplitudes at the interface for measured and reference models (left) and the resulting TFM reflection coefficient (right).

8.2.2 Results

8.2.2.1 Number of Elements

Figure 8.5 shows the effect of changing the number of elements in the array. The 16 and 32 element array show sufficient focussing but in the 8 element array artefacts in the TFM images distorted the results, as shown in Figure 8.6. Artefacts in the TFM image became less prominent with a increasing number of elements in the array, as shown through the progression of Figures 8.6, 8.7 and 8.8.

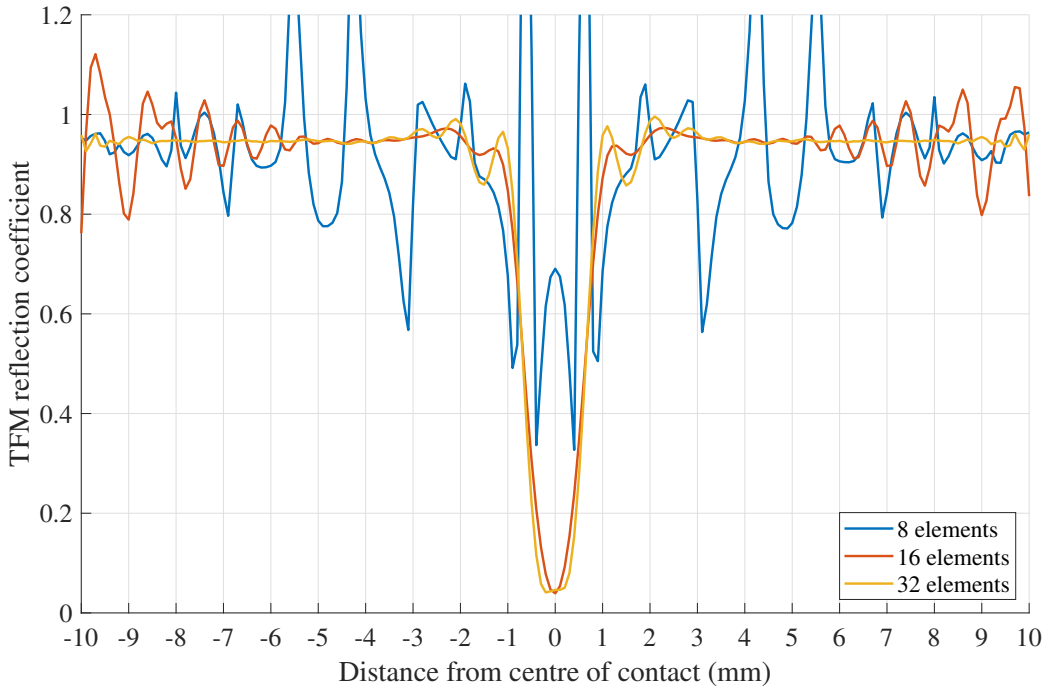

Figure 8.5: The modelled effect of number of elements on TFM reflection coefficient results. All arrays had an aperture of 20 mm, with differing number of elements and element size.

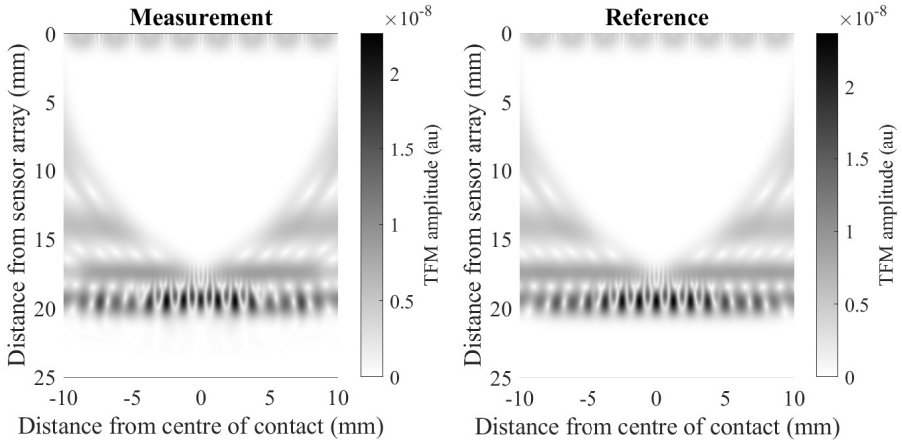

Figure 8.6: TFM grids for a 20 mm array split into 8 sensors. Left was for a 1.28 mm contact. Right was for a reference model with no contact.

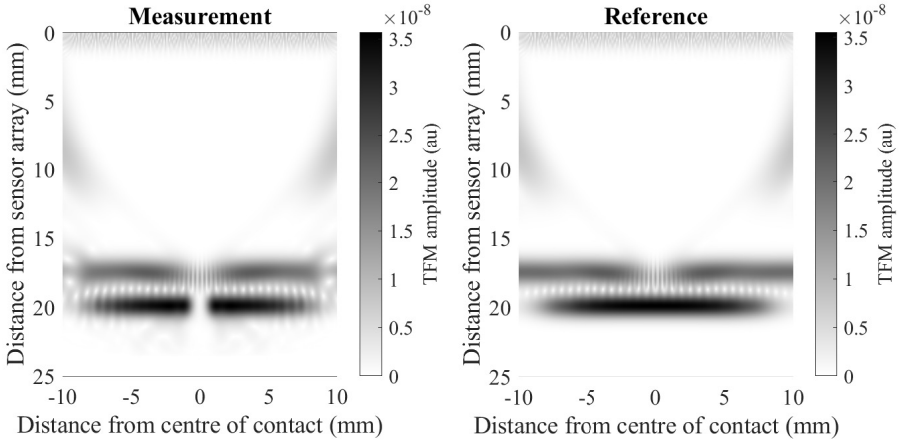

Figure 8.7: TFM grids for a 20 mm array split into 16 sensors. Left was for a 1.28 mm contact. Right was for a reference model with no contact.

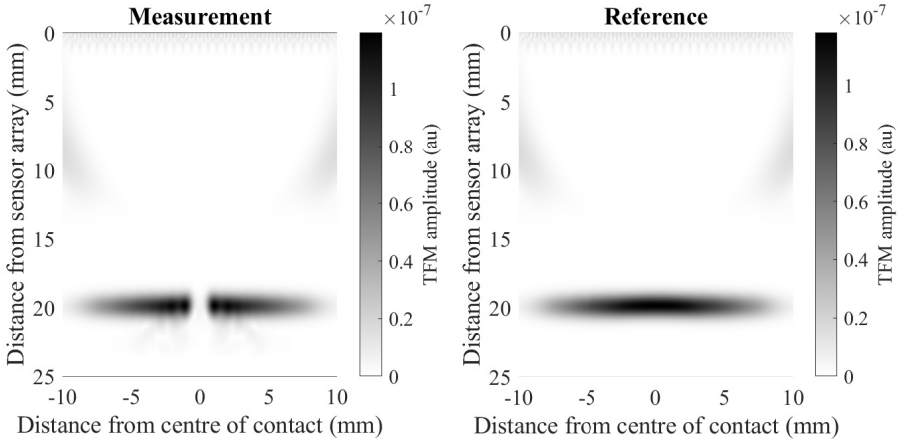

Figure 8.8: TFM grids for a 20 mm array split into 32 sensors. Left was for a 1.28 mm contact. Right was for a reference model with no contact.

8.2.2.2 Aperture

Figure 8.9 shows the effect of changing the aperture of the array, keeping the number of elements constant. From 11.2 to 16 mm the increased aperture improved the focussing ability of the array. The array was sufficiently focussed at 16 mm, as shown by the small change in signal between 16 and 20 mm apertures. At 24 mm, artefacts began to distort the signal due to the increased element size, as shown in Figure 8.13. Figures 8.10 - 8.13 show how the TFM images change with increasing aperture without changing the number of elements.

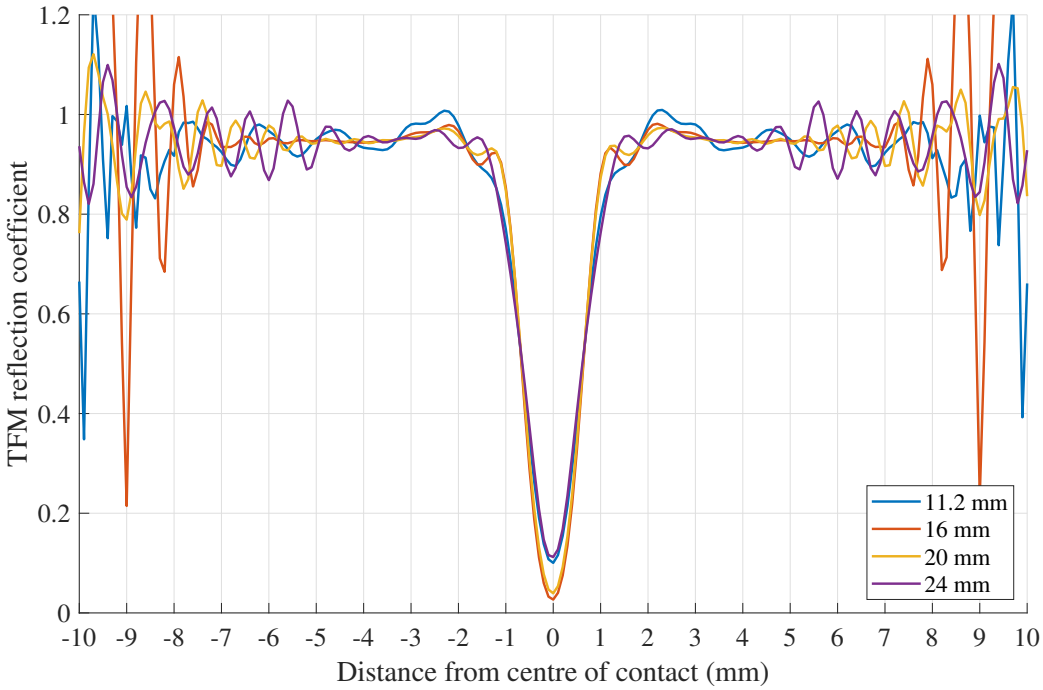

Figure 8.9: The modelled effect of aperture on TFM reflection coefficient results. All arrays had an aperture 16 elements, with differing number of elements and element size.

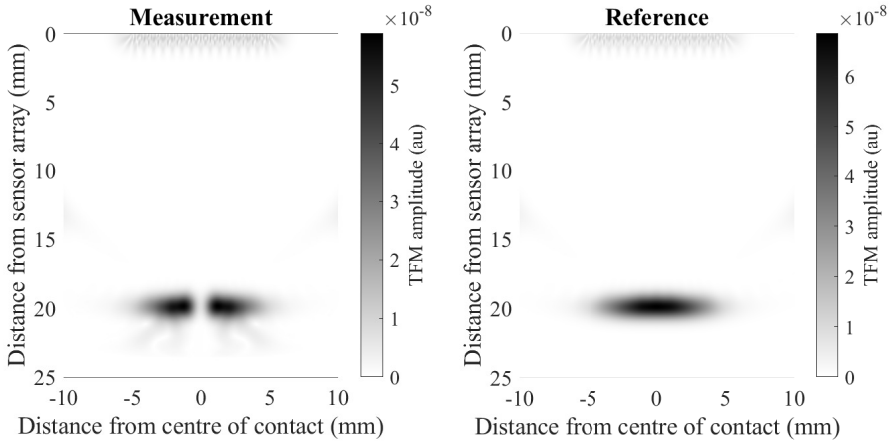

Figure 8.10: TFM grids for an 11.2 mm array split into 16 sensors. Left was for a 1.28 mm contact. Right was for a reference model with no contact.

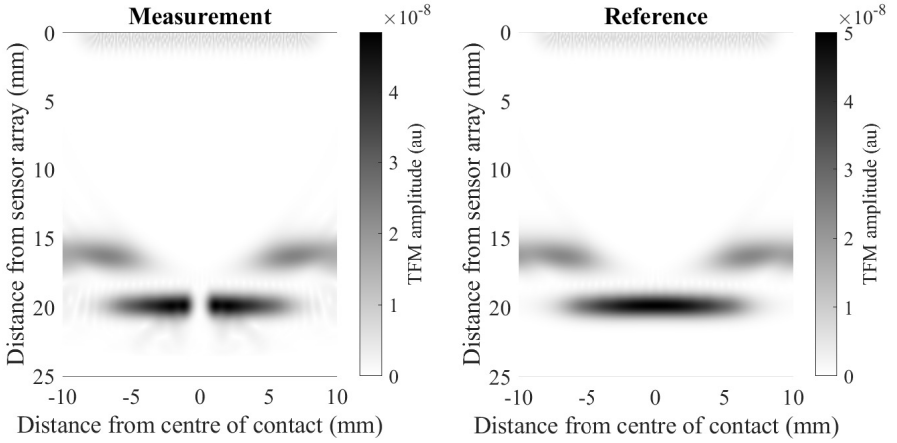

Figure 8.11: TFM grids for a 16 mm array split into 16 sensors. Left was for a 1.28 mm contact. Right was for a reference model with no contact.

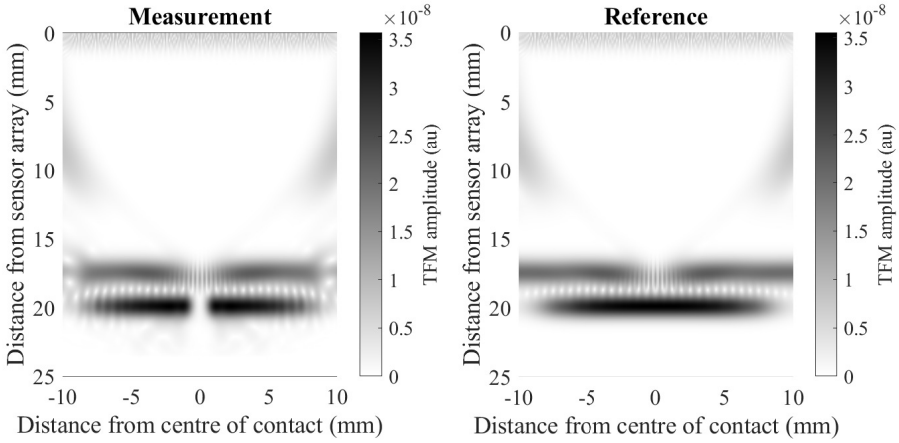

Figure 8.12: TFM grids for a 20 mm array split into 16 sensors. Left was for a 1.28 mm contact. Right was for a reference model with no contact.

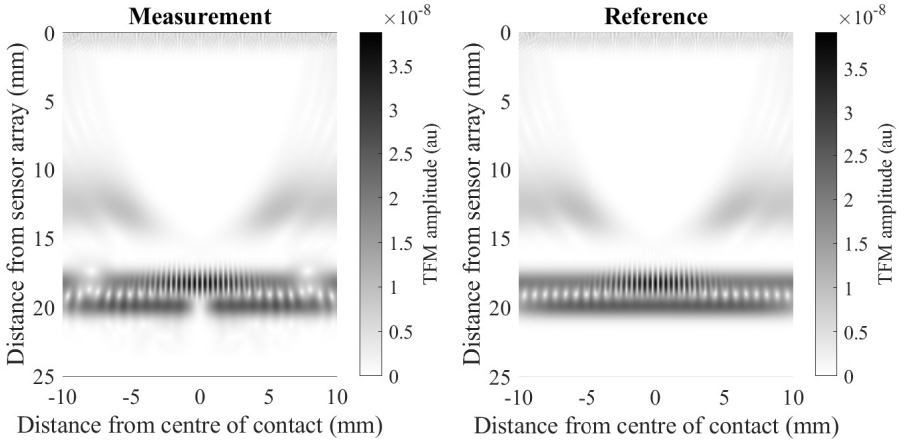

Figure 8.13: TFM grids for a 24 mm array split into 16 sensors. Left was for a 1.28 mm contact. Right was for a reference model with no contact.

Results so far suggest that increasing aperture increases focussing capability and decreasing element size and pitch reduces the presence of artefacts in TFM images, which was expected from literature [111, 112]. This modelling has given us some insight into what artefacts in images and sufficiently focussed TFM images are likely to look like at an interface.

8.2.2.3 Contact Width

The effectiveness of a 20 mm 16 element array of ultrasonic transducers used in combination with the TFM across several contact widths is shown in Figure 8.14. The transducer was adequate for monitoring contacts of around 1.1 mm and above but below this the MRC over-predicted more significantly and the contact width also began to over-predict, as can be seen in Table 8.1. Overall the results were very similar to those seen in Figure 7.26 with the equivalent simulated focussed transducer.

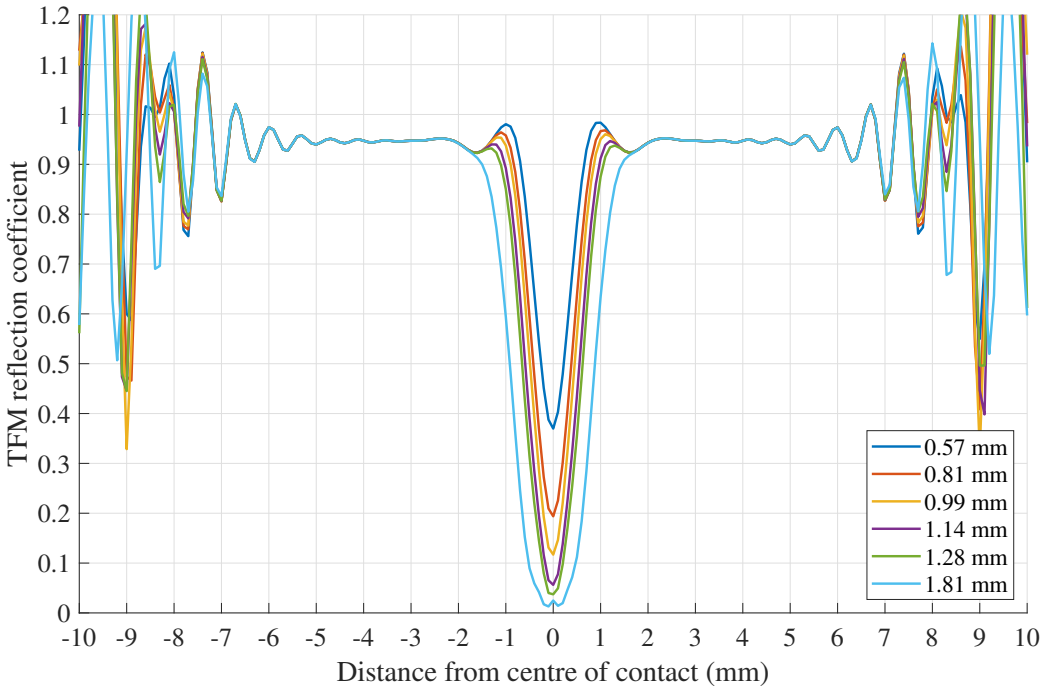

Figure 8.14: The modelled effect of changing contact width on TFM reflection coefficient results. All arrays had an aperture of 20 mm, with 16 elements.

Contact width (mm)	MRC	Ultrasound predicted contact width (mm)
1.81	0.013	1.8
1.28	0.037	1.3
1.14	0.056	1.2
0.99	0.117	1.0
0.81	0.194	1.0
0.57	0.370	0.8

Table 8.1: Summary of results from changing contact width with a simulated 20mm 16 element array. Data extracted from Figure 8.14.

8.2.2.4 Focussing Convergence

Now that we have seen that the TFM is applicable to contacts provided there is a sufficient array aperture and element pitch, the next question is: how do we know when there is sufficient focussing?

A proposed 'convergence' technique is presented here. It involves gradually reducing the number of elements used in an array and can be done in post processing. The convergence of the reflection coefficient signal should be checked at both the half-minimum predicted contact width and MRC using an increasing number of sensors

in the array. In order to maintain array alignment with the centre of the contact the number of array elements used must change by 2 for each step in the convergence study. Figure 8.15 shows this process for a 20 mm aperture 32 element array which showed convergence at 24 elements and above.

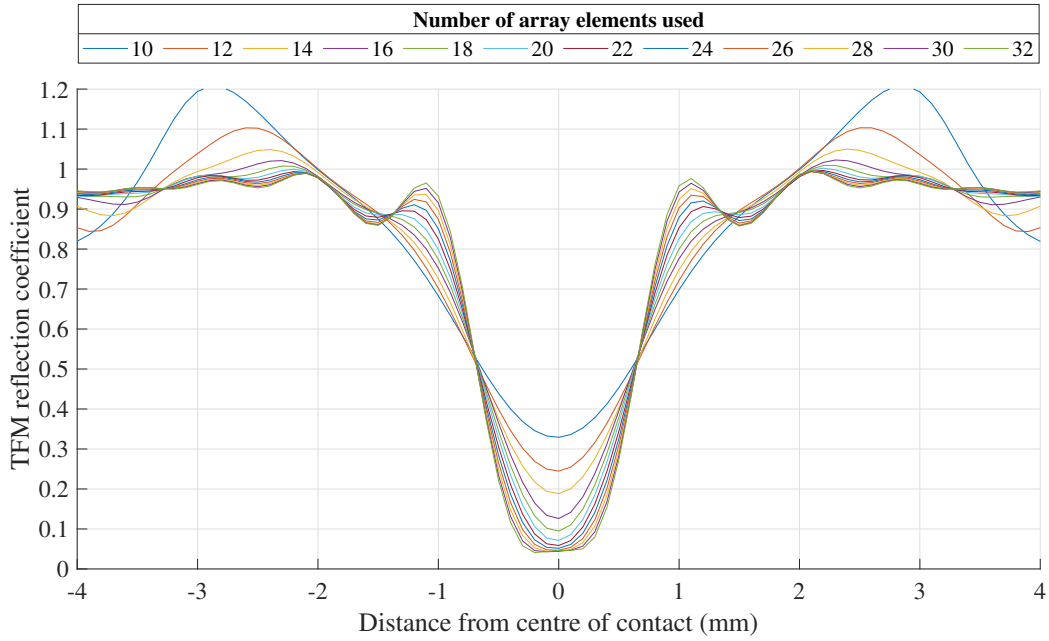

Figure 8.15: Convergence method tested on simulated 20 mm 32 element array with a 1.28 mm contact.

Similarly, Figure 8.16 shows this process for a 20 mm aperture 16 element array which showed convergence at 14 elements and above.

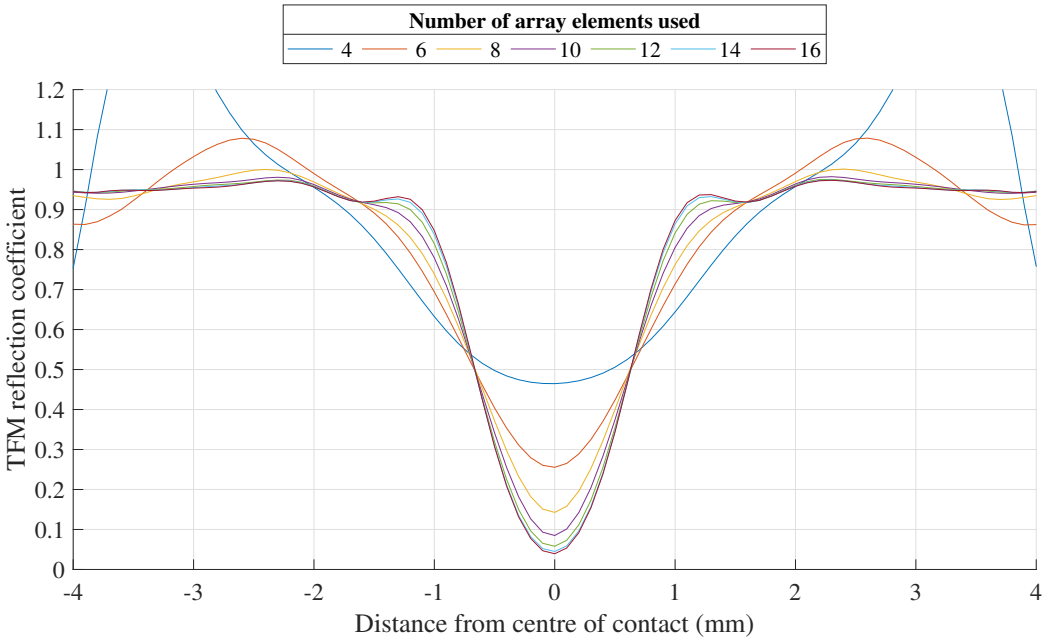

Figure 8.16: Convergence method tested on simulated 20 mm 16 element array with a 1.28 mm contact.

It was noticed that the contact width prediction converged much quicker if the two points at which the current profile overlaps the next profile with increased number of elements was used. These points converge at an R value of 0.5 at 12 elements in Figure 8.15 and 6 elements in Figure 8.16. This may be used to predict contact width even when focussing is not sufficient to accurately measure MRC. It may also be used to infer actual MRC value through doubling of the converged R value at the two crossing points, although a non-symmetrical contact would likely cause error in this method.

8.3 Conclusions

This chapter has developed techniques to apply FMC and TFM methods to tribological contacts and has shown how different array variables effect the performance of the TFM for monitoring small contacts. Increased array aperture and decreased element pitch improved the effectiveness of array performance. The increase in array aperture allowed increased focussing and the reduction in element pitch removed artefacts from TFM images.

k-Wave modelling has predicted that with sufficient array aperture and sufficiently small sensor size the contact width and MRC of rolling element sized contacts can

be monitored using reflection coefficient. The form factor of signal distortion due to artefacts in the signal has been shown which allows assessment of their presence in real data.

Convergence methods to assess whether the array is sufficiently focussed was also proposed for both contact width and MRC. The convergence methods involved gradually reducing the number of elements used in an array and could be done in post processing. In order to maintain array alignment with the centre of the contact the number of array elements used must change by 2 for each step in the convergence study. The convergence of MRC and contact width at the half minimum (using Equation 3.18) using an increasing number of sensors in the array should be seen to verify sufficient focussing.

An alternative 'crossing convergence' method required around half the elements to the previous method. This was achieved by monitoring the two points at which the current profile overlaps the next profile with increased number of elements was used. These points converged at a particular R value which was approximately half of the actual MRC. The distance between these two points was the contact width. This may be used to predict contact width even when focussing is not sufficient to accurately measure MRC. It may also be used to infer actual MRC value through doubling of the converged crossing point value. Non-symmetrical contacts would likely cause error in this method and therefore use of the convergence method in the previous paragraph is preferable where possible.

Chapter 9

Pilot Study of the Total Focussing Method Application to a Contact

An opportunity to experimentally verify the use of the TFM on small contacts was presented to the author through use of a previously instrumented test platform for inspection of rubber seals. This was developed by by Peak to Peak Measurement Solutions Ltd. [113] and was the first iteration of their test platform.

9.1 Experimental Setup

The test platform is shown in Figure 9.1. The rubber seal was placed between the upper perspex and steel plates, as shown in Figure 9.1(b). The perspex plate allowed estimation of the ultrasonically inspected steel-rubber contact width through measurement of the perspex-rubber contact width from above. This assumed the contact width was largely determined by the deflection of the rubber. Load was applied to the contact through rotation of the central threaded screw propped up by the steel block at the bottom of Figure 9.1(a). This applied load to the top steel plate through deflection of the three springs of know stiffness. Measurement of spring deflection allowed calculation of applied load to the contact.

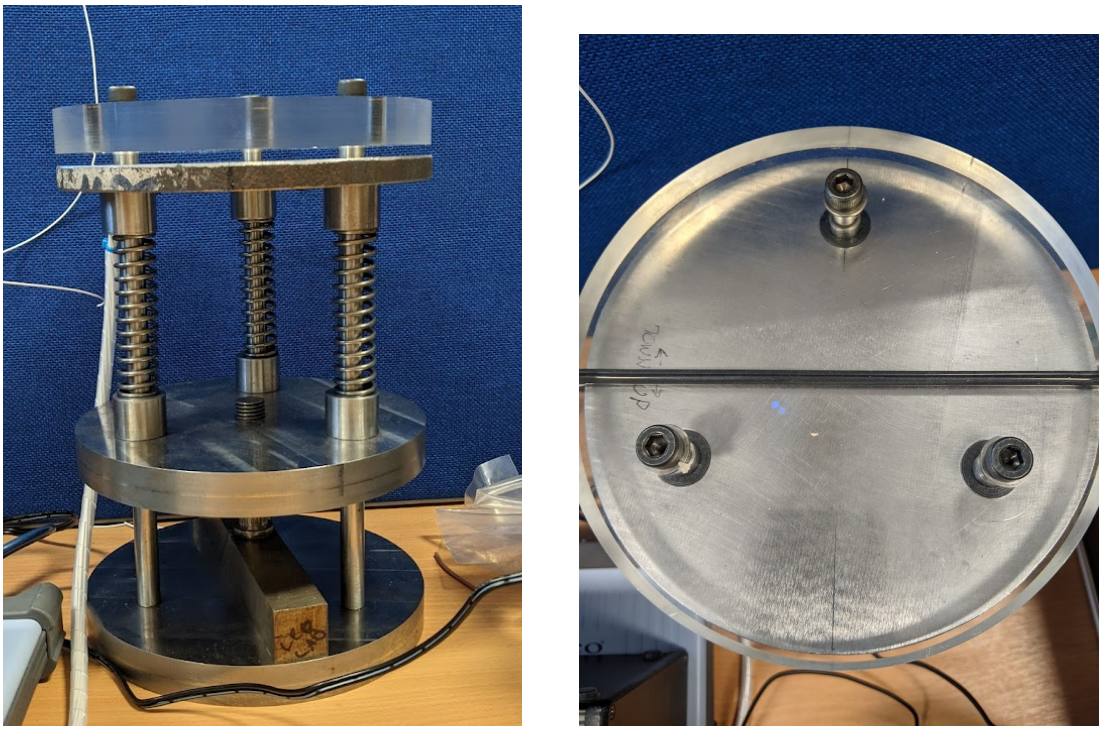

(a) Side view (b) Top view

Figure 9.1: Test rig setup for experimental TFM trials (a) side view (b) top view.

An array of ultrasonic transducers was instrumented on the underside of the top steel plate for inspection of the contact. The array ran perpendicular to the direction of the rubber seal for inspection of the contact width. The array had an aperture of 11.2 mm, with 16 elements and an element pitch of 0.7 mm. Elements were 0.6 by 3 mm in size and an intended central frequency of 10 MHz. 0.6 mm is around the lower width limit for a 10 MHz sensor whilst still operating in its desired oscillatory mode. The instrumented steel plate was approximately 11 mm thick.

Figure 9.2 shows the data acquisition hardware used. Sensors were plugged into a custom 16 channel multiplexer developed by Peak to Peak Measurement Solutions [113] . Signals were generated and received by a Picoscope 5000 series UPR. The multiplexer and UPR were controlled through a custom LabVIEW interface developed at the University of Sheffield, which allowed control of the hardware as well as data capture and storage on a laptop.

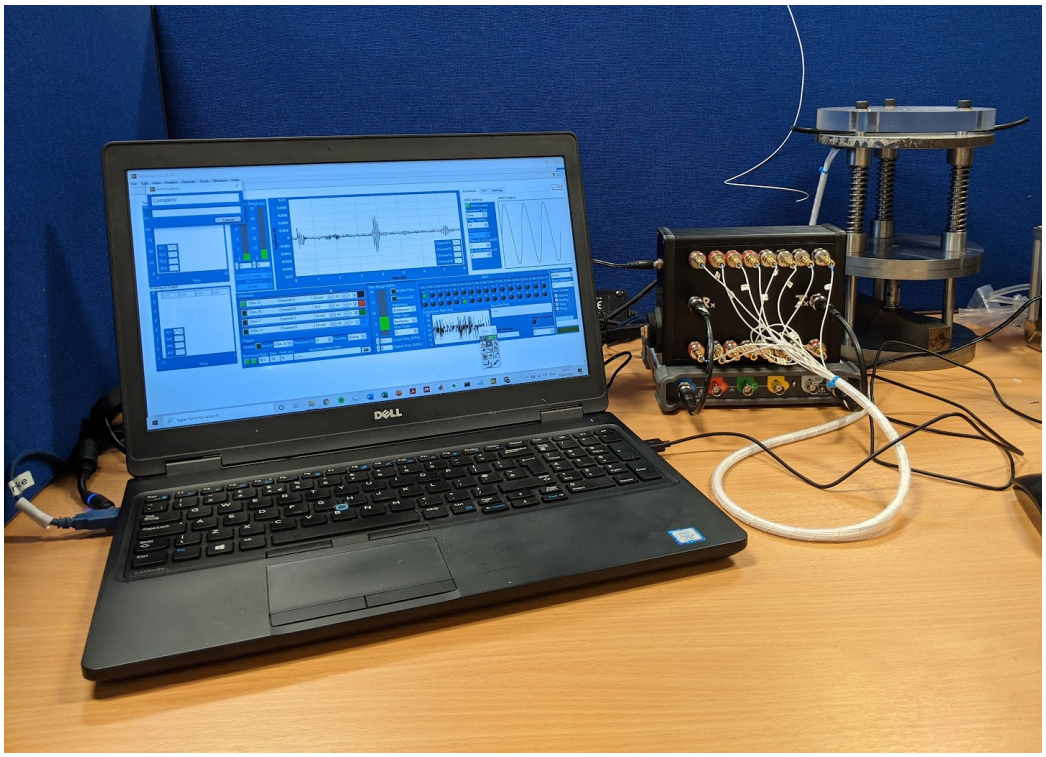

Figure 9.2: Testing setup for experimental TFM trials including data acquisition hardware.

9.2 Model Predictions

Figure 9.3 shows a *k-Wave* predicted sensor beam for an 11.2 mm focussed wide sensor with a focal distance of 11 mm, using the techniques outlined in Chapter 7. This suggests that the sensor would not be capable of sufficient focussing with active pulsing techniques.

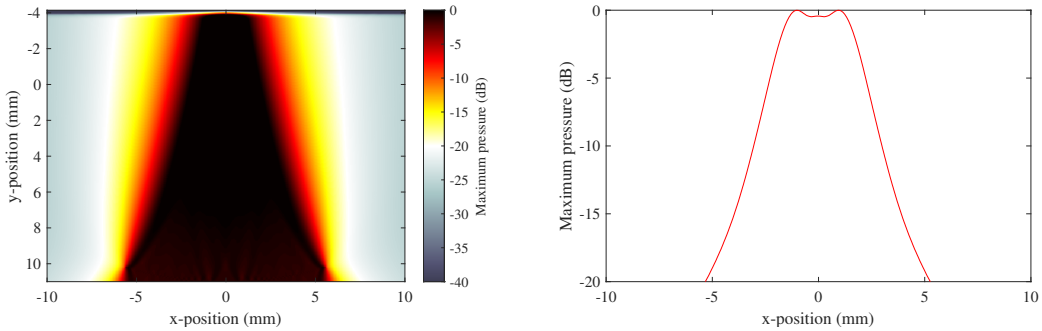

Figure 9.3: *k-Wave* predicted sensor field and beam width at the interface for an 11.2 mm curved sensor, with a plate thickness of 11 mm.

A *k-Wave* model of the intended contact was created using the respective geometry and array dimensions. The resulting FMC images are shown in Figure 9.4 which predicted very few artefacts would be present in the results.

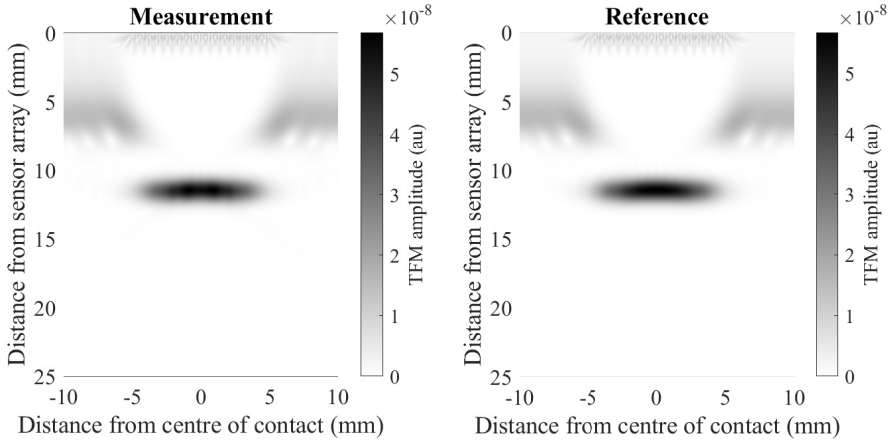

Figure 9.4: TFM grids for an 11.2 mm array split into 16 sensors. Left was for a 1.27 mm contact with a rubber roller. Right was for a reference model with no contact. Raceway thickness was 11 mm.

The resulting TFM reflection coefficient is shown in Figure 9.5. This gave a good approximation of MRC and a slight over-estimate of contact width, but was still a vast improvement on pulse echo (PE) results, also shown in Figure 9.5. Figure 9.6 shows that with 16 elements the MRC and contact width appeared to be close to convergence.

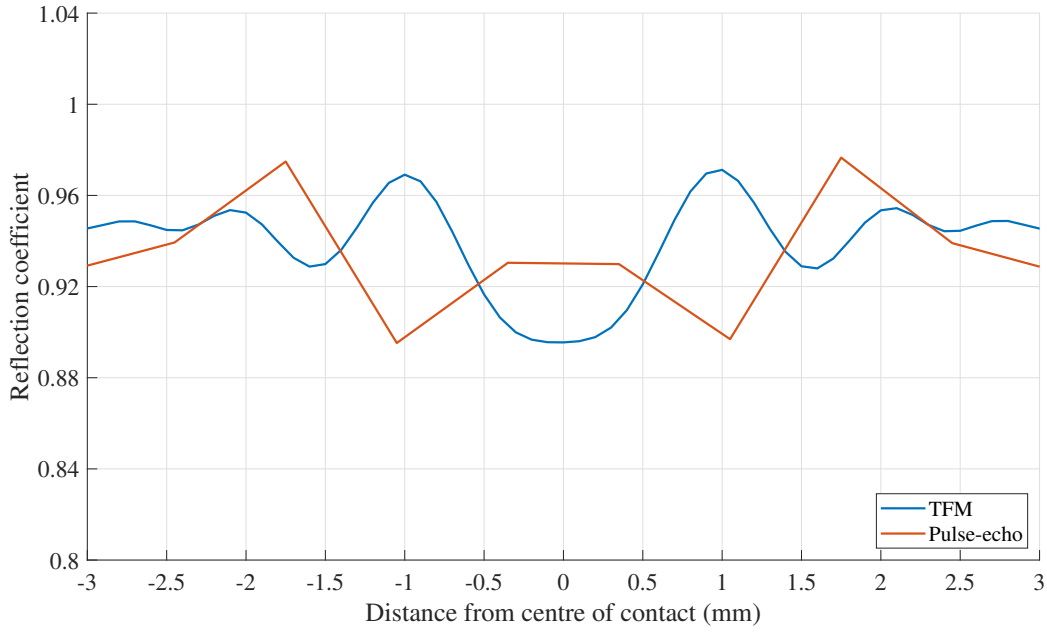

Figure 9.5: Reflection coefficient results. Array had an aperture of 11.2mm and 16 elements. A 1.28 mm wide rubber contact.

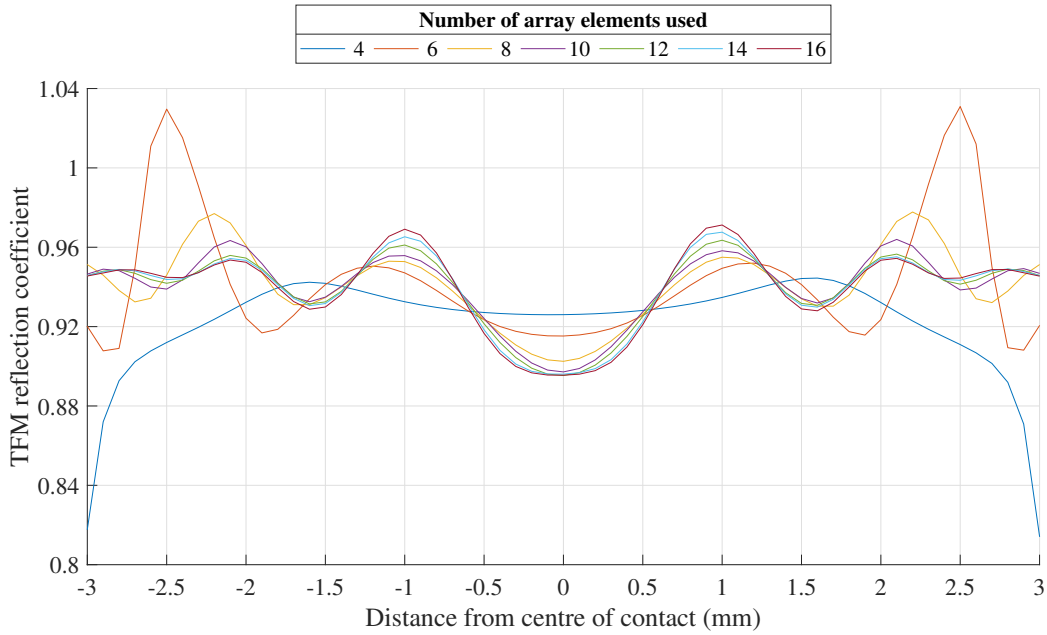

Figure 9.6: Convergence method tested on simulated 11.2 mm 16 element array with a 1.28 mm wide rubber contact.

9.3 Results

Figure 9.7 shows the TFM image for both a loaded measurement and an air reference from the instrumented array. Both the first reflection and second reflection can be seen approximately 11 and 22 mm form the sensor array. On first inspection the image appears to heavily affected by artefacts. This was thought to be due to uneven sensor response from each element in the array. Even though all sensors were the same size, the quality of the bond can affect the sensor response quite significantly.

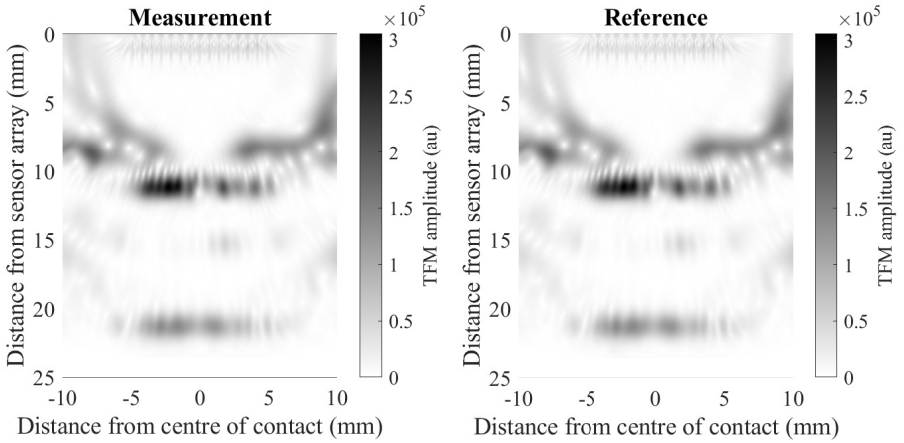

Figure 9.7: TFM grids for the experimental data.

To attempt to correct this some pre-processing of data was trialled which involved obtaining the maximum Hilbert envelope amplitude from each of the first reflection pulse echo results in the reference signals. Each of these maximum amplitudes was divided by the maximum value of the 16 maxima to give an amplitude factor for each channel. Each A-scan result in the FMC matrix was then divided by an amplitude factor twice before processing. The first factor was for which sensor the signal was transmitted from and the second was for which sensor received the signal. The resulting TFM images are shown in Figure 9.8 which shows only a very slight change in TFM images. It is still likely that the different sensor responses had an effect on the image but cannot be corrected by such a simple algorithm. It is likely that different sensors had different beam shapes which would need to be accounted for. Nevertheless, these differences should not be a significant issue as we are comparing the measurement signal with a reference, and both the measurement and reference have the same array footprint.

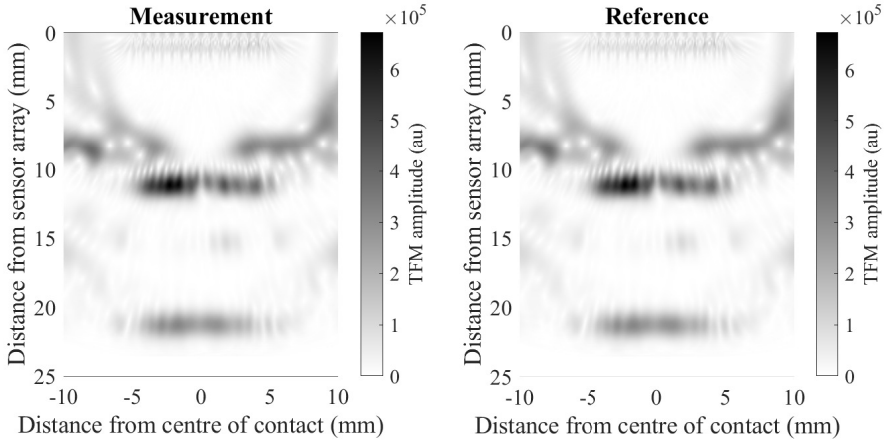

Figure 9.8: TFM grids for the experimental data, with normalised amplitudes prior to processing.

Figure 9.9 shows reflection coefficient results for the original TFM data, normalised TFM data and pulse-echo data. There was very little difference between the original and normalised TFM reflection coefficient predictions but there was a vast improvement over the pulse echo plot.

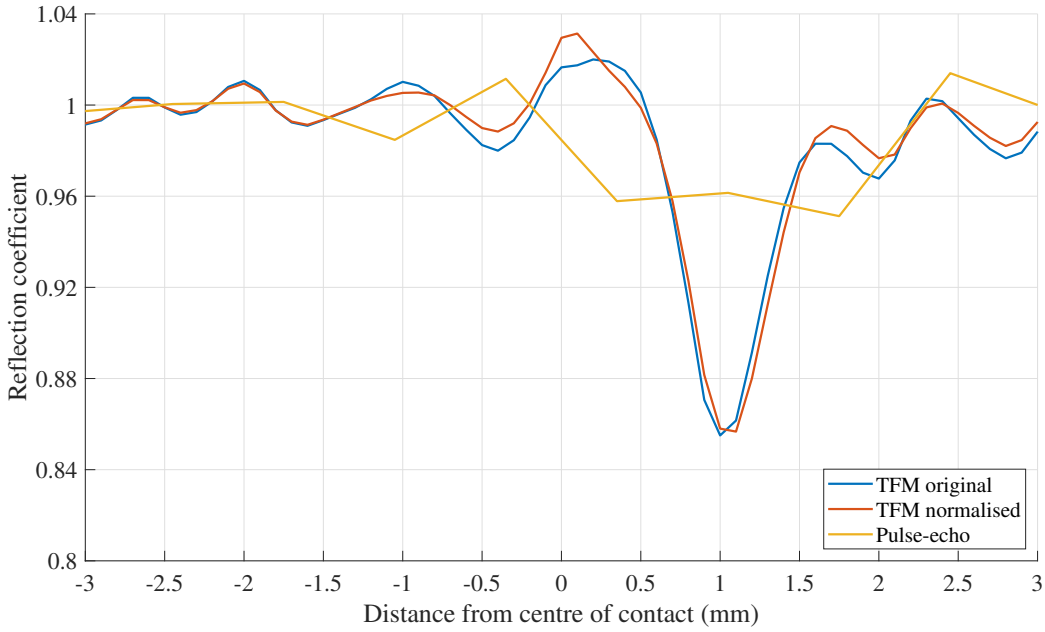

Figure 9.9: Experimental TFM (both original and normalised) and PE reflection coefficient results.

Figure 9.10 shows results for two contacts, one with a higher load and one with a lower load. Both had contact widths between 0.5 and 1 mm on the perspex side but

the higher loaded contact was slightly wider than the lower loaded one.

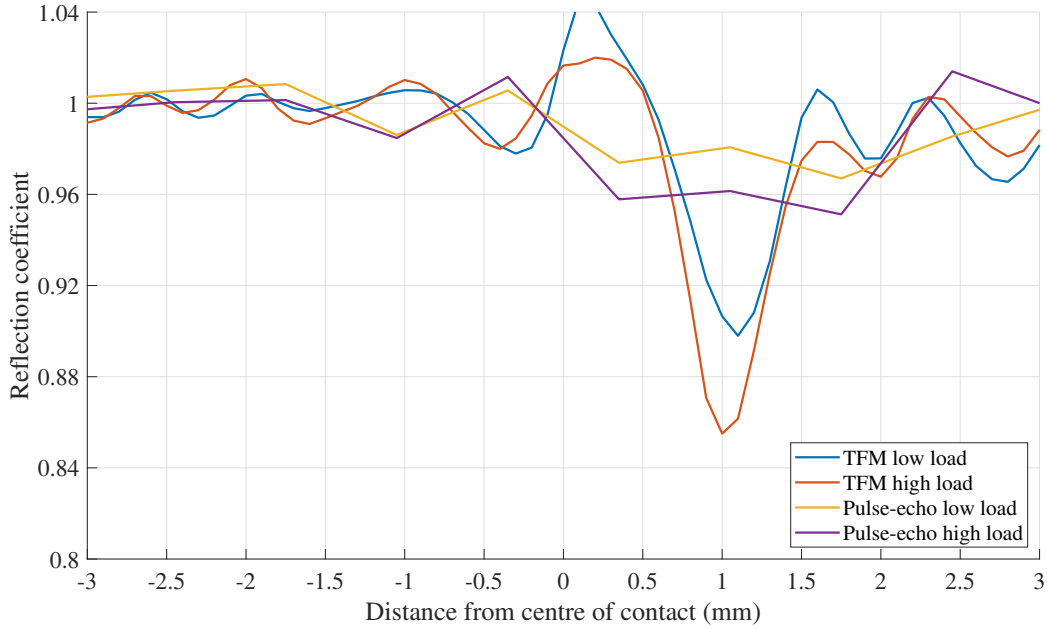

Figure 9.10: Experimental TFM (original) and PE reflection coefficient results.

The TFM results gave a MRC of 0.898 and a contact width of approximately 0.6 mm for the lower load contact. For the higher loaded contact, results gave a MRC of 0.855 and a contact width of approximately 0.7 mm. Both results seemed sensible; contact widths matched with observations and MRC values were around the predicted value of 0.89 using Equation 3.3 and the rubber values in Table 7.3.

Figure 9.11 shows the convergence of the array for the higher load contact and Figure 9.12 shows the convergence of the array for the lower load contact. In both cases, where less than 12 sensors were used the results were distorted by artefacts in the image. At 12 sensors and above the results began to but did not completely converge.

The alternative 'crossing convergence' method gave a contact width of 0.7 mm for both the higher and lower load data, an MRC of 0.7926 for the lower load data and an MRC of 0.7961 for the higher load data. These result make less sense than the previous ones. With increasing load contact width should increase and MRC should decrease, neither of which happened. This, along with the much less clear convergence points in the real data compared to modelled data, suggest that this method is less applicable to real contact than the standard convergence method.

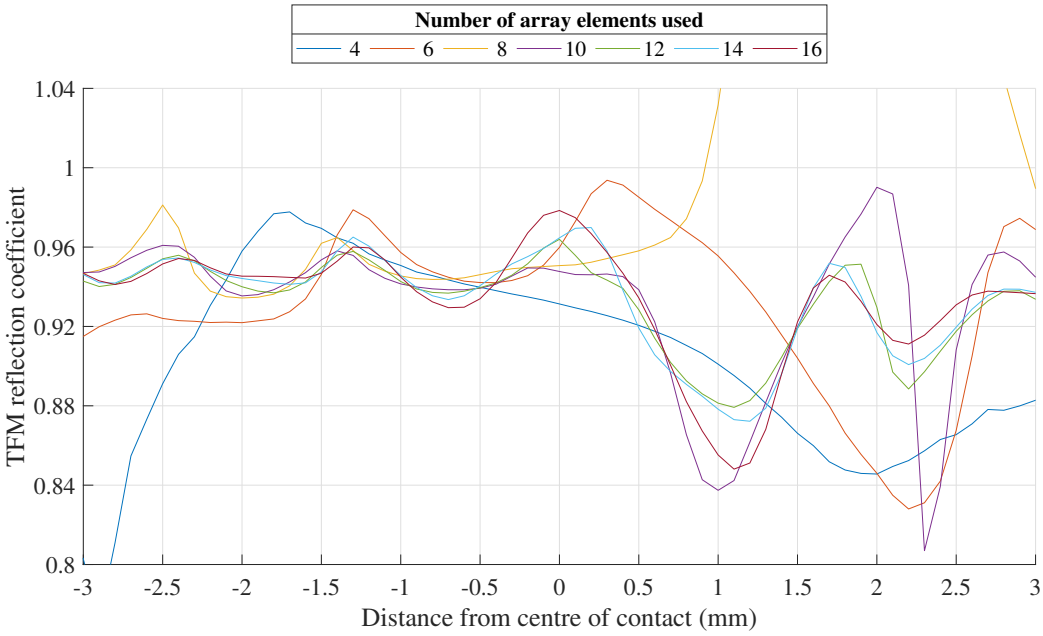

Figure 9.11: Convergence method tested on the higher load data.

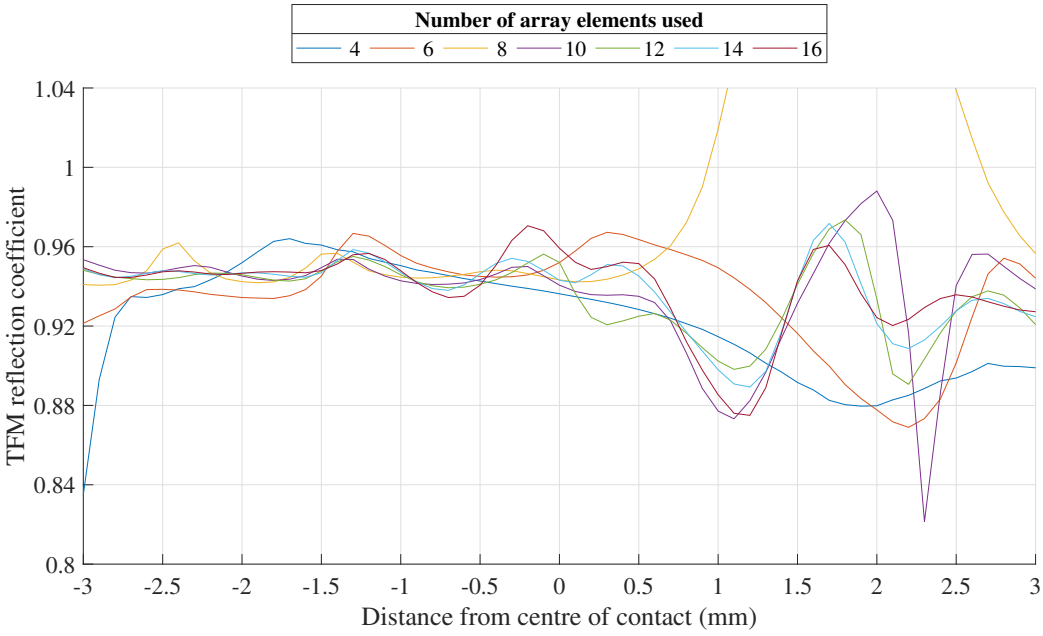

Figure 9.12: Convergence method tested on the lower load data.

9.4 Discussion

This experiment has shown that the TFM is applicable to real contacts and can vastly improve insight into contacts in comparison with pulse-echo inspection. It has,

however shown that there are additional challenges when working with real bonded arrays. Additional artefacts in the image were present that were not predicted by modelling of the contact. These were likely due to different sensor responses from each of the elements in the array, which were probably due to differences in the bond layer between sensors and also slight differences in sensor sizes. Another possibility is that signal to noise ratio played a role in the distortion. If excitation voltage was not sufficient for some pulse-receive pairs to register reflections this could have been the cause of artefacts in the image. The sensors here were excited with sine waves of 4V peak to peak voltage which was the maximum of the Picoscope function generator, but is fairly low compared to other ultrasonic hardware such as the FMS (used in Chapters 4 and 6) which can apply square wave pulse voltages of up to 300V. The use of an in-line amplifier could improve results, or even a different acquisition system.

9.5 Conclusions

In this chapter the techniques developed in Chapter7 were applied experimentally to a rubber-on-steel contact. These experiments showed that the TFM is applicable to real contacts and can vastly improve insight into contacts in comparison with pulse-echo inspection. The standard convergence method showed that the array was not sufficiently focussed for full convergence and therefore accurate MRC and contact width measurements. The alternative 'crossing convergence' method did not perform well on this real data.

The real array showed more artefacts in the TFM image than predicted by the *k-Wave* model. Suggested causes for these artefacts were differing sensor responses from elements within the array and low excitation voltage. Improvements in array instrumentation consistency, as well as hardware capability were recommended for future experiments.

Chapter 10

Conclusions

To conclude this thesis, a summary of key findings split into development areas, recommendations for future research and original contributions of research are presented below.

10.1 Key Findings

The aim of this work was to develop ultrasonic rolling bearing techniques in the following ways:

- Understand the current error in ultrasonic measurement techniques on a rolling bearing.
- Assess the error of roller load measurements on an operational wind turbine bearing through comparison to a simple model, with knowledge of measurement error.
- Create a detection mechanism for misalignment of rolling bearings through ultrasonic measurements.
- Develop a method to detect a transition from mixed to fully separated lubricant regimes in a rolling bearing through use of shear sensors.
- Understand how finite sensor size and resulting fringe effects affect ultrasonic measurements.
- Develop bonded sensor technologies to enable more robust measurement.

Key findings from this work have been split into their areas of development are summarised in the following sections.

10.1.1 Error in Ultrasonic Rolling Element Bearing Measurements

A statistical approach was used in Chapter 4 to analyse variability in ultrasonic signals was estimated using prediction intervals. The variation in each of these data points incorporated several sources of error. The sources of error were not exhaustive and did not include those which would offset data, such as the acoustoelastic constant. The errors in the analysis included noise in the signal, digitisation error, error implicit in processing methods and variation in load during the 2 s test capture period. The error caused by load variation was calculated to be approximately 3-13% and therefore the prediction intervals of measurement variability were slight overestimates.

Error in reflection coefficient measurements was generally good with 95% prediction intervals giving between $\pm$ 0.7 and 2.6% error between reflection coefficients of 0.2 to 1. Error in change in time of flight (ΔToF) measurements was significantly higher than reflection coefficient with 95% prediction intervals giving between $\pm$ 1 and 39% error, between ΔToF of 46 to 1 ns. The increase in error was likely caused by a combination of decreased digitisation interval in relation to the measured change in the time as well as a more complex data processing routine.

The variability error analysis in Chapter 4 was used in combination with a multi-body static model in Chapter 5. This was to estimate the proportion of the variability in ultrasonic load measurements from an operational wind turbine that was due to measurement variability.

A significant portion of load variation was attributed to error in ultrasonic load measurement. The high level of scatter in measurements was shown to be partially due to the fact that the bearing was under a light load. The measurement variability as a percentage of the mean would decrease when measuring more heavily loaded bearings. This percentage error would also likely decrease with improved measurement hardware.

Quantification of error in ultrasonic measurements was used to identify possible transient events in data. These events were most likely caused by wind gusts as no grid disconnection or braking events were observed in the data.

10.1.2 Distribution of Bearing Load

This work, in collaboration with Nicholas [41], has shown that it is possible to measure misalignment in rolling element bearings through the use of an array of sensors

along the axis of a raceway. This was demonstrated in both Chapter 4 and Chapter 6. Misalignment was detected through observation of a non-symmetrical reflection coefficient profile across the axis of the roller. Direction of misalignment was identified by the position of the minimum reflection coefficient (MRC) or maximum ΔToF. Changes in misalignment severity were also observed by the position of this point: the further form the centre point, the more severe. In the longitudinal data in Chapter 6, profiles largely remained the same with increasing load, however greater changes at sensor 7 (edge sensor) in some instances indicated lengthening of the contact. Lengthening of the contact was also observable in contact width estimations.

In Chapter 4 reflection coefficient measurements may have been distorted by surface damage or distress. In Chapter 6 ΔToF measurements also appeared to be slightly distorted by some unknown phenomenon. A combination of the two processing techniques was therefore recommended for a thorough analysis of the contact. Shear data from Chapter 6 showed that shear sensors should not be used for misalignment monitoring as their profiles were prone to distortion by lubricant effects. At present it is only possible to qualitatively monitor misalignment - to tell if it is present and if it changes in severity. Qualitative measurement is limited by distortion of signals known as fringe effects.

It has also been shown that changes in the load distribution around a bearing can be seen using multiple sensors around the bearing circumference. This was demonstrated on an operational wind turbine in Chapter 5 and was, again, qualitative partially due to only two data points around the circumference being available but also due to the cause of fringe effects. Instances where the load distribution of the bearing shifted were linked with transient events in the turbine operation, most likely wind gusts. For a better understanding of movement of the loaded zone in future bearing testing, more than two circumferential measurement sensors would be required to give insight into the changed load distribution.

10.1.3 The Use of Shear Sensors for Monitoring Rolling Element bearings

The combined use of shear and longitudinal sensors to monitor rolling elements in Chapter 6 suggested that all of the observed data was in a mixed lubrication regime although both longitudinal and shear reflection coefficient data did not entirely behave as expected. This was likely a result of the cause of fringe effects. Shear ultrasound was transmitted through the contacts at all but the edge of the contact at

very low loads meaning that contacts were very likely to be in a mixed lubrication regime. The scenario where this conclusion would be wrong is if the lubricant supported shear waves. There was some data at very low load where no shear ultrasound was transmitted into the roller where longitudinal ultrasound was. This gives some confidence in this technology being able to detect a transition from mixed to fully separated contacts in future testing. Transitions in this data set were likely not seen as a result of bearing misalignment and subsequent higher contact pressures.

The experiment in Chapter 6 also showed that shear sensors may be able to identify instances where lubricant solidification occurs in contacts. New phenomena at the contact inlet and outlet with shear sensors show the possible observation of lubricant under high pressure reaching a semi-solid state where it is capable of supporting a shear wave. The phenomena, shown in Section 6.6.2.2, increased in magnitude with increasing bearing load and lubricant viscosity but showed no trend with changing bearing speed. This phenomena, along with the presence of fringe effects meant that mixed lubrication film thickness predictions were not possible. Trends in contact stiffness where these phenomena were not present showed sensible trends with bearing load and contact stiffness, suggesting that combined shear and longitudinal measurement of mixed films should be possible provided that solidification of lubricant does not occur (or whatever phenomenon which caused the features in), fringe effects can be removed from signals and beams are sufficiently focussed so that the spot size is smaller than the contact width.

10.1.4 Investigation of the Cause of Fringe Effects

Chapter 4 showed that fringe effects were not caused by dynamic effects, high PRFs or lubricant in the contact. It also showed that fringe effects were present in change in time of flight, as well as reflection coefficient results. Chapter 6 showed that fringe effects were present in shear sensors too. The use of shear sensors to monitor deflection gave conflicting results to longitudinal sensors. Shear results predicted deflections around 1.4 times those predicted by longitudinal results. This, along with similarities in fringe effects in reflection coefficient cast serious doubt on ΔToF and subsequent load measurements. From previous studies there is clearly some correlation between signals and load. Perhaps, instead of measuring deflection, these methods relate to some other contact parameter that directly influences the magnitude of fringe effects. The most likely contender is contact width.

Chapters 4 and 6 showed that the cause of fringe effects results in overestimation of contact widths of between 2-4 times those predicted by Hertzian equations. A more detailed study into how fringe effects are effected by experimental variables was conducted in Chapter 6. The overall shape of fringe effects was affected by frequency which was likely to be a result of the link between frequency and changing beam width; an increase in frequency narrows the beam width. More severe fringe effects were also observed with a larger first reflection window. This showed that fringe effects were likely to be caused by beam spread of the transducer too. The processing technique was not able to remove the underlying interference from results. Fringe effects in both reflection coefficient and ΔToF did not significantly change with bearing speed or lubricant viscosity however they did change with load. These changes in fringe effects with load were detailed in Chapter 6 and used to confirm model replication of fringe effects in Chapter 7.

Modelling in Chapter 7 showed that fringe effects were most likely a result of both reflections from either side of the contact interfering with each other when the beam width was larger than the contact and scattering of the beam at the edges of the contact. The stage at which modelling was concluded also suggested that fringe effects were not dominated by the effect of raceway curvature, varying stiffness across the contact, deflection of the contact or acoustoelastic effects. This modelling showed that the measurement area of a bonded transducer is not equal to its footprint in all cases, particularly for small sensors. Modelling suggested that focussing of the beam could reduce these effects to the point where minimum reflection coefficient and contact width values are sufficiently accurate. The best case gave 0% error in contact width and a 1.3% error in MRC. Modelling also showed that distortion of change in time of flight measurements would still be present, even with focussing. Whilst changes in deflection could be monitored using change in time of flight, actual values are likely to be quite inaccurate. It is surprising that the technique has given sensible results thus far. It is suggested that, instead of measuring deflection with time of flight and converting to load, the contact width should be measured through reflection coefficient using focussed ultrasound techniques and the measured contact width to calculate contact load.

The error in ultrasonic MRC and contact width measurements for a specific application will be dependent on transducer spot size and contact width. Increasing transducer frequency and transducer size will reduce error, as will perfect curvature

for focussing and reducing the distance from the sensor to the contact (up to a minimum focal distance defined by sensor size). Bonding of the transducer also appeared to have a focussing effect which has not been quantified.

10.1.5 Ultrasonic Focussing Using Bonded Sensors

Use of the total focussing method (TFM) to improve reflection coefficient measurements of rolling contacts was investigated using k-space modelling in Chapter 8. The modelling showed promising results and also enabled development of techniques to ensure the performance of the array was sufficient.

Increased array aperture and decreased element pitch improved the effectiveness of array performance. The increase in array aperture allowed increased focussing and the reduction in element pitch removed artefacts from TFM images. *k-Wave* modelling has predicted that with sufficient array aperture and sufficiently small sensor size the contact width and MRC of rolling element sized contacts can be monitored using reflection coefficient. The form factor of signal distortion due to artefacts in the signal has been shown which allows assessment of their presence in real data.

Convergence methods to assess whether the array is sufficiently focussed was also proposed for both contact width and MRC. The convergence methods involved gradually reducing the number of elements used in an array and could be done in post processing. In order to maintain array alignment with the centre of the contact the number of array elements used must change by 2 for each step in the convergence study. The convergence of MRC and contact width at the half minimum (using Equation 3.18) using an increasing number of sensors in the array should be seen to verify sufficient focussing.

An alternative 'crossing convergence' method required around half the elements to the previous method. This was achieved by monitoring the two points at which the current profile overlaps the next profile with increased number of elements was used. These points converged at a particular R value which was approximately half of the actual MRC. The distance between these two points was the contact width. This may be used to predict contact width even when focussing is not sufficient to accurately measure MRC. It may also be used to infer actual MRC value through doubling of the converged crossing point value. Non-symmetrical contacts would likely cause error in this method and therefore use of the convergence method in the previous paragraph is preferable where possible.

The TFM was also used experimentally, with some success, to improve reflection coefficient measurement of a small contact in Chapter 8 but also showed additional signal distortion which requires further investigation.

In this chapter the techniques developed in Chapter7 were applied experimentally to a rubber-on-steel contact. These experiments showed that the TFM is applicable to real contacts and can vastly improve insight into contacts in comparison with pulse-echo inspection. The standard convergence method showed that the array was not sufficiently focussed for full convergence and therefore accurate MRC and contact width measurements. The alternative 'crossing convergence' method did not perform well on this real data.

The real array showed more artefacts in the TFM image than predicted by the *k-Wave* model. Suggested causes for these artefacts were differing sensor responses from elements within the array and low excitation voltage. Improvements in array instrumentation consistency, as well as hardware capability were recommended for future experiments.

10.2 Further Work

Overall, this work has developed ultrasonic techniques in several areas. Capabilities have been expanded and better defined. Hopefully this will lead to further industry interest and wider adoption of the technique for monitoring rolling element bearings. That being said, there are still areas where the technique could be improved.

The use of focussing methods to monitor contacts in operational bearings is the recommended ultimate goal for further work. The test platform used in Section 9 could be adapted to create contact patches of known width, ideally with steel-on-steel contacts and experiment with different array configurations, instrumentation techniques and different acquisition hardware to optimise the process. The next step would then be to repeat these tests on an actual roller bearing contact. This could be achieved in a configuration similar to that shown in Chapter 4 but with a small circumferential array (or several) to examine the contact width at one or more locations along the roller. TFM scripts would need to be adapted in order to account for the curvature of the array if it were bonded directly to the raceway surface. Active focussing techniques could also be trialled on the same arrays with access to the correct acquisition hardware. The final step would be the application of these techniques to an operational bearing. This would require more expensive equipment

than that used in this work for fast capture rates and measurements would be more suited to low speed bearings.

If focussing techniques became successful then mapping of contact patches would be possible and conversion to contact pressures and loads could be done through Hertzian models such as those presented in Section 2.3. Contact loads and pressures can be estimated from contact width or length through knowledge of contact materials properties and geometries. Sufficient focussing would enable film thickness measurements in fully separated contacts and may also enable mixed film thickness measurements with the use of a combination of shear and longitudinal arrays. Stiffness trends in Chapter 6 certainly suggest that this would be possible provided there is no solidification of the lubricant. Focussing of both shear and longitudinal sensors would also enable clearer observation of lubricant behaviour between contacts and any solidification of lubricants, particularly at the inlet out outlet.

Work should also be undertaken to allow ultrasonic monitoring around the full circumference of a rolling bearing. This could be achieved by instrumentation at several points around the full circumference (or an area of interest) of the static raceway or instrumentation at a single point on the rotating raceway and the use of a slip ring.

10.3 Original Contributions of Research

Throughout this work, several areas of novel work have been completed which have contributed to widening knowledge in the use of ultrasonic sensors to monitor performance of rolling element bearings. These are summarised in the following list:

- A method for statistical measurement of error due to variation in ultrasonic measurements has been devised and used to quantify error for both reflection coefficient and change in time of flight measurements.
- Movement of the loaded zone in a tapered roller bearing in an operational wind turbine has been identified, as well as identification of transient events in ultrasonic load data.
- In collaboration with Nicholas [41], measurement of misaligned rollers using ultrasonic techniques has been undertaken for the first time.
- Shear ultrasonic transducers have been used to monitor rolling element bearings

  - An indication of solidification of lubricant in contacts was seen with these sensors.
  - Results showed transition from full separation to mixed lubrication but only at the contact edge and not for the entirety of the contact.

- A new cause for the fringe effects and central W shape in reflection coefficient plots for a single roller pass with bonded transducers has been proposed, supported by k-space modelling.
- The presence of fringe effects in change in time of flight results has been acknowledged and investigated for the first time.
- k-space models have predicted that signal distortion causing fringe effects can be removed from reflection coefficient, but not change in time of flight data, through focussing of the ultrasonic beam.
- Full matrix capture and the total focussing method have been used to inspect tribological contacts.
  - Convergence methods to ensure sufficient focussing of the array using these techniques have also been devised.

Appendices

Appendix A

MulitLife Instrumentation Jig Drawings

Drawings for the custom jigs used in the instrumentation of ultrasound sensors on the bearing for the MultiLife rig. Figure A.1 shows the jig for the outer surface of the raceway and Figure A.2show the jig for the inner surface.

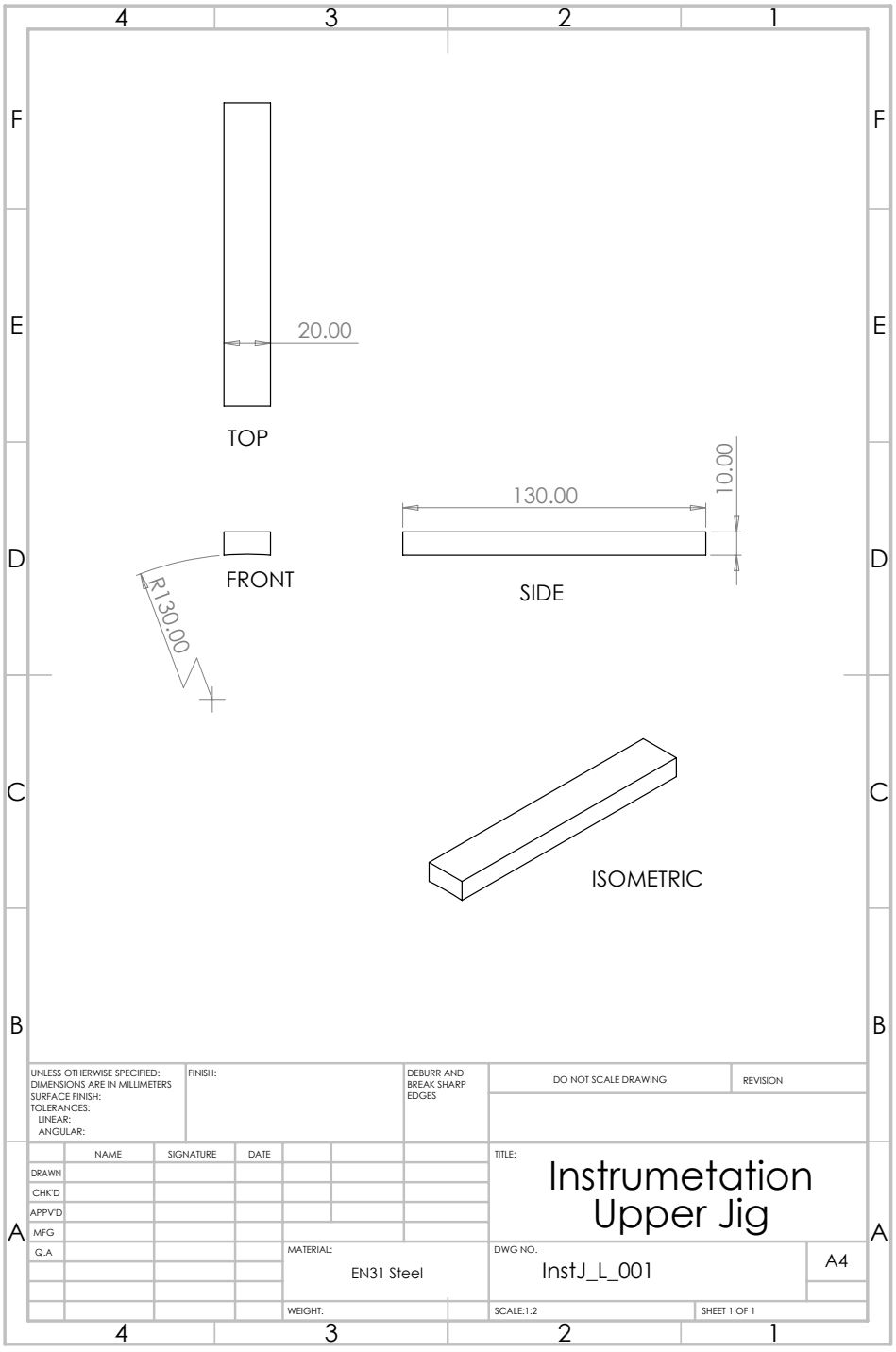

Figure A.1: Jig for the outer surface of the MultiLife inner raceway

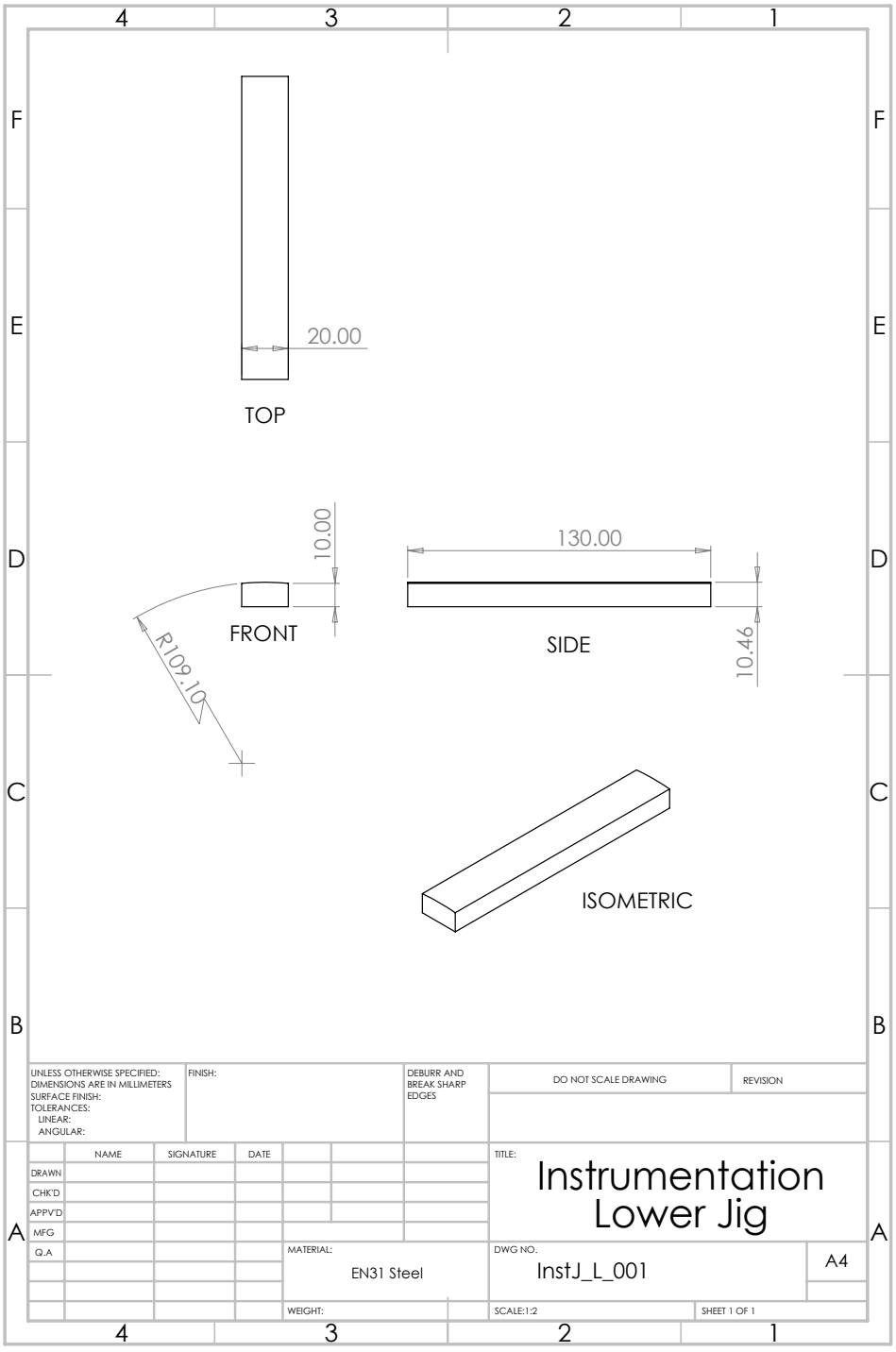

Figure A.2: Jig for the inner surface of the MultiLife inner raceway

Appendix B

Roller Load and Contact Calculations for the *MultiLife* rig

The geometry and other design parameters of the NU2244 bearing tested in the *MultiLife* rig can be found in Table 4.1.

B.1 Equations, Geometries and Material Properties

To convert bearing load to maximum roller load Equation 2.28 was used. For the NU2244 bearing $Z = 15$ and $\gamma = 0$deg.

B.1.1 Line Contact

Contact width was calculated using Equation 2.5. Material properties and line contact geometries used are shown in Table B.1:

Material property / geometry	Symbol	Value
Young's modulus (GPa)	$E_A = E_B$	210
Poisson's ratio (1)	$\upsilon_A = \upsilon_B$	0.3
Roller radius (mm)	R_{Ax}	27
Raceway radius (mm)	R_{Bx}	129.5
Axial radii (mm)	$R_{Ay} = R_{By}$	∞
Roller length (mm)	l	82

Table B.1: Material properties and geometries for *MultiLife* Hertzian line contact calculations

Line contact pressures were calculated with Equations 2.8 and 2.9 and deflections were calculated using Equations 2.10, 2.19 and 2.20 - 2.27.

B.1.2 Elliptical Contact

For an elliptical contact the material properties and geometries in Table B.1 were used with the exception of the alterations shown in Table B.2. Equations 2.6 and 2.7 were still applicable.

Material property / geometry	Symbol	Value
Axial roller curvature (m)	R_{Ay}	17.15 [44]
Axial raceway curvature (mm)	R_{By}	-198.81 [44]

Table B.2: Altered geometries from Table B.1 for *MultiLife* Hertzian elliptical contact calculations

Contact half widths in both the axial direction (a) and rolling direction (b) were calculated using Equations 2.11 and 2.12: Elliptical contact pressures were calculated with Equations 2.15 and 2.16 and deflections were calculated using Equations 2.17 and 2.20 - 2.27.

B.1.3 Other Deflection Equations

Deflection was converted to change in time of flight (ΔToF) using Equation 3.19 where L = -2.26 and c_0 = 5960 m/s [44].

B.2 Calculations for Seeding Jig Experiment Comparison

Contact size and pressure results for the NU2244 bearing are shown in Tables B.3 and B.4 for line and elliptical point contacts respectively. The elliptical contacts use approximated circular roller and raceway profile R_y values from [44]. Clearly these calculations are not valid as most $2a$ values are larger than the roller length of 82 mm. This is due to the actual roller profile being logarithmic as is industry standard and not circular. The actual values are likely to be in between those shown in Tables B.3 and B.4.

Q (kN)	$2b$ (mm)	p_{max} (GPa)	p_{avg} (GPa)
50	0.775	1.001	0.786
100	1.097	1.416	1.112
150	1.343	1.734	1.362
200	1.551	2.002	1.573
250	1.734	2.239	1.758
300	1.899	2.452	1.926

Table B.3: *MultiLife* Hertzian line contact calculation results for 50 - 300 kN roller load

Q (kN)	$2a$ (mm)	$2b$ (mm)	p_{max} (GPa)	p_{avg} (GPa)
50	74.618	0.995	1.286	0.580
100	94.013	1.254	1.620	0.820
150	107.618	1.436	1.854	1.005
200	118.449	1.580	2.041	1.160
250	127.595	1.702	2.198	1.297
300	135.590	1.809	2.336	1.421

Table B.4: *MultiLife* Hertzian elliptical contact calculation results for 50 - 300 kN roller load

Maximum contact deflection results for the NU2244 bearing are shown in Table B.5. Table B.6 shows these results converted into change in time of flight (ΔToF) and table B.7 shows the effect that 0.1kN variance in load would have on the ΔToF value. Values of deflection were largest for the Houpert calculations and also gave the greatest variance in ΔToF with a 0.1 kN change in load.

Q (kN)	δ_{line} (μm)	$\delta_{elliptical}$ (μm)	$\delta_{Palmgren}$ (μm)	$\delta_{Houpert}$ (μm)
50	20.410	30.968	19.158	34.603
100	38.484	49.159	35.750	54.928
150	55.675	64.417	51.495	68.430
200	72.294	78.035	66.712	85.147
250	88.486	90.552	81.550	101.622
300	104.339	102.255	96.092	117.901

Table B.5: *MultiLife* deflection contact calculation results for 50 - 300 kN roller load

Q (kN)	ΔToF_{line} (ns)	$\Delta ToF_{elliptical}$ (ns)	$\Delta ToF_{Palmgren}$ (ns)	$\Delta ToF_{Houpert}$ (ns)
50	11.185	16.962	10.498	18.952
100	21.069	26.907	19.572	30.065
150	30.472	35.250	28.183	37.448
200	39.561	42.698	36.507	46.592
250	48.418	49.543	44.622	55.603
300	57.089	55.944	52.576	64.507

Table B.6: *MultiLife* change in time of flight results for 50 - 300 kN roller load

Q (kN)	ΔToF_{line} (ns)	$\Delta ToF_{elliptical}$ (ns)	$\Delta ToF_{Palmgren}$ (ns)	$\Delta ToF_{Houpert}$ (ns)
$50.1 - 50$	0.0205	0.0226	0.0189	0.0252
$100.1 - 100$	0.0192	0.0179	0.0176	0.0200
$150.1 - 150$	0.0185	0.0157	0.0169	0.0184
$200.1 - 200$	0.0179	0.0142	0.0164	0.0181
$250.1 - 250$	0.0175	0.0132	0.0161	0.0179
$300.1 - 300$	0.0172	0.0124	0.0158	0.0177

Table B.7: The effect of 0.1 kN load variance on *MultiLife* change in time of flight results for 50 - 300 kN roller load

B.3 Calculations for Contact Modelling

Results for bearing load between 100 and 1000 kN are shown in the following Tables. Table B.8 shows results where $K_d = 4.08$ (with no bearing clearance) and B.9 shows results where $K_d = 5$ (with nominal bearing clearance). In actuality the load is likely to be distributed such that the value of K_d is somewhere between these values. Due to the smaller contact values being thought to be more challenge to measure using ultrasound the case where $K_d = 4.08$ was used for modelling.

F_r (kN)	Q_{max} (kN)	$2b$ (mm)	p_{max} (GPa)	p_{avg} (GPa)	$\delta_{Palmgren}$ (μm)
100	27.2	0.572	0.738	0.580	11.076
200	54.4	0.809	1.044	0.820	20.669
300	81.6	0.991	1.279	1.005	29.772
400	108.8	1.144	1.477	1.160	38.570
500	136.0	1.279	1.651	1.297	47.148
600	163.2	1.401	1.809	1.421	55.556
700	190.4	1.513	1.954	1.534	63.823
800	217.6	1.618	2.089	1.640	71.974
900	244.8	1.716	2.215	1.740	80.022
1000	272.0	1.809	2.335	1.834	87.982

Table B.8: *MultiLife* Hertzian contact calculation results for 100 - 1000 kN load and $K_d = 4.08$

F_r (kN)	Q_{max} (kN)	$2b$ (mm)	p_{max} (GPa)	p_{avg} (GPa)	$\delta_{Palmgren}$ (μm)
100	33.3	0.633	0.817	0.642	13.301
200	66.7	0.895	1.156	0.908	24.820
300	100.0	1.097	1.416	1.112	35.750
400	133.3	1.266	1.635	1.284	46.315
500	166.7	1.416	1.828	1.436	56.617
600	200.0	1.551	2.002	1.573	66.712
700	233.3	1.675	2.163	1.699	76.641
800	266.7	1.791	2.312	1.816	86.428
900	300.0	1.899	2.452	1.926	96.092
1000	333.3	2.002	2.585	2.030	105.650

Table B.9: *MultiLife* Hertzian contact calculation results for 100 - 1000 kN load and $K_d = 5$

Appendix C

Roller Load and Contact Calculations for the *MultiLife* rig

Much of the beginning of these calculations was the same as those outlined in Appendix B. The geometry and other design parameters of the NU2244 bearing tested in the *MultiLife* rig can be found in Table 4.1. Values for roller load were calculated from bearing load using Equation 2.28 where $Z = 15$, $\gamma = 0°$ and K_d =5. Elliptical contact parameters were calculated as in Section B.1.2.

Central and minimum lubricant film thickness were calculated from Equations 2.33 and 2.34 respectively. Mean lubricant entrainment speed was calculated through Equation 2.35 where $u_i = 0$ m/s as the inner raceway was static and u_r was calculated from Equation 2.2 and converted to linear speed through knowledge of the roller radius. The lubricant dynamic viscosity and the lubricant pressure-viscosity coefficient can be found in Table 6.1. Results for lubricant viscosity at 40°C are shown in Table C.1:

Lubricant	min h_c (μm)	max h_c (μm)	min h_0 (μm)	max h_0 (μm)
VG32	0.037	0.125	0.028	0.098
VG150	0.117	0.401	0.089	0.314
VG320	0.206	0.708	0.158	0.557

Table C.1: Film thickness calculations for lubricants at 40°C

With an estimated composite surface roughness of 0.19 μm [39], Lambda ratios can be predicted:

Lubricant	min Λ from h_c (μm)	max Λ from h_c (μm)	min Λ from h_0 (μm)	max Λ from h_0 (μm)
VG32	0.19	0.65	0.14	0.51
VG150	0.61	2.08	0.46	1.63
VG320	1.07	3.68	0.82	2.89

Table C.2: Lambda ratio calculations for lubricants at 40°C

This predicts that we should have seen a transition from mixed to fully separated lubrication in the VG150 data and in the VG320 data.

References

[1] Zaopartrzenie24, "Cylindrical roller bearing." [Online]. Available: https://pixabay.com/photos/bearing-bearings-basket-brass-brass-3460127/

[2] ——, "Tapered roller bearing." [Online]. Available: https://pixabay.com/photos/tapered-roller-bearing-bearings-3460126/

[3] T. A. Harris and M. N. Kotzalas, *Rolling bearing analysis: Essential concepts of bearing technology*, 5th ed. CRC Press, 2007.

[4] ISO, "ISO 76:2006+A1:2017 Rolling bearings — Static load ratings," ISO, Tech. Rep., 2017.

[5] ——, "ISO 281: Rolling bearings — Dynamic load rating and rating life," ISO, Tech. Rep., 2008.

[6] ——, "DD ISO/TS 16281: Rolling bearings - methods for calculating the modified reference rating life for universally loaded bearings," ISO, Tech. Rep., 2009.

[7] Pasja1000, "Wind turbine." [Online]. Available: https://pixabay.com/photos/clouds-windmill-wind-nature-figure-3643255/

[8] Renewables First, "How much does a wind turbine cost?" [Online]. Available: https://www.renewablesfirst.co.uk/windpower/windpower-learning-centre/how-much-does-a-wind-turbine-cost/

[9] J. Carroll, A. McDonald, and D. McMillan, "Failure rate, repair time and unscheduled O&M cost analysis of offshore wind turbines," *Wind Energy*, vol. 17, no. April 2013, pp. 657–669, 2014. [Online]. Available: http://onlinelibrary.wiley.com.sheffield.idm.oclc.org/doi/10.1002/we.1887/epdf

[10] Y. Gong, J. L. Fei, J. Tang, Z. G. Yang, Y. M. Han, and X. Li, "Failure analysis on abnormal wear of roller bearings in gearbox for wind turbine,"

Engineering Failure Analysis, vol. 82, no. July, pp. 26–38, 2017. [Online]. Available: http://dx.doi.org/10.1016/j.engfailanal.2017.08.015

[11] S. Sheng, "Report on Wind Turbine Subsystem Reliability - A Survey of Various Databases," National Renewable Energy Laboratory, Tech. Rep., 2013. [Online]. Available: https://www.nrel.gov/docs/fy13osti/59111.pdf

[12] H. D. M. De Azevedo, A. M. Araújo, and N. Bouchonneau, "A review of wind turbine bearing condition monitoring: State of the art and challenges," *Renewable and Sustainable Energy Reviews*, vol. 56, pp. 368–379, 2016. [Online]. Available: http://dx.doi.org/10.1016/j.rser.2015.11.032

[13] Office for National Statistics, "Wind energy in the UK: June 2021," 2021. [Online]. Available: https://www.ons.gov.uk/economy/environmentalaccounts/articles/windenergyintheuk/june2

[14] National Grid, "Britain's clean energy system achieves historic milestone in 2019," 2019. [Online]. Available: https://www.nationalgrid.com/group/news/britains-clean-energy-system-achieves-historic-milestone-2019

[15] Department for Business Energy and Industrial Strategy, "Statistical Press Release: UK Energy Statistics 2018 and Q4 2018," National Statistics, London, Tech. Rep. March, 2019. [Online]. Available: https://assets.publishing.service.gov.uk/government/uploads/system/uploads/attachment_d consumption of electricity was,2017%2C up 0.1 per cent.&targetText=Renewable electricity generation was a,c

[16] The European Parliament and The Council of the European Union, "Directive (EU) 2018/2001 of the European Parliament and of the Council of 11 December 2018 on the promotion of the use of energy from renewable sources (recast)," *Official Journal of the European Union*, vol. L 328/82, no. 21.12.2018, pp. 82 – 209, 2018. [Online]. Available: https://eur-lex.europa.eu/legal-content/EN/TXT/?uri=uriserv:OJ.L_.2018.328.01.0082.01.ENG&toc=OJ:L:2018:328:TOC

[17] UK Government, "Climate Change Act 2008," 2008. [Online]. Available: http://www.legislation.gov.uk/ukpga/2008/27/contents

[18] H. Chauvaud De Rochefort and M. Valls, "Industrial flexibility and competitiveness in a low carbon world," RenewableUK, Tech. Rep. June, 2018. [Online].

Available: https://www.theade.co.uk/assets/docs/resources/Industrial flexibility and competitiveness report_v10 web.pdf

[19] J. Lee and F. Zhao, "Gobal Wind Report 2021," Global Wind Energy Council, Tech. Rep., 2021. [Online]. Available: http://www.gwec.net/global-figures/wind-energy-global-status/

[20] R. Wiser and M. Bolinger, "2018 Wind Technologies Market Report," U.S. Department of Energy, Tech. Rep., 2018. [Online]. Available: papers://19d3a2af-8636-448c-acad-e5205d8697e4/Paper/p93

[21] J. F. Manwell, J. G. McGowan, and A. L. Rogers, *Wind Energy Explained*, 2nd ed. Chichester, UK: John Wiley and Sons, Ltd, dec 2009. [Online]. Available: http://doi.wiley.com/10.1002/9781119994367

[22] P. Anderson, "Rotor hub and pitch bearing without mounted rotor blades," 2008. [Online]. Available: https://en.wikipedia.org/wiki/Pitch_bearing#/media/File:Hub_secured_to_Turbine_Tower_N_geograph.org.uk_-_787507.jpg license: https://creativecommons.org/licenses/by-sa/2.0/deed.en

[23] E. Hart, A. Turnbull, J. Feuchtwang, D. McMillan, E. Golysheva, and R. Elliott, "Wind turbine main-bearing loading and wind field characteristics," *Wind Energy*, vol. 22, no. 11, pp. 1534–1547, 2019.

[24] P. Anderson, "Scout moor gearbox, rotor shaft and brake assemblye," 2008. [Online]. Available: https://commons.wikimedia.org/wiki/File:Scout_moor_gearbox,_rotor_shaft_and_brake_assen license: https://creativecommons.org/licenses/by-sa/2.0/deed.en

[25] H. Cen and P. M. Lugt, "Film thickness in a grease lubricated ball bearing," *Tribology International*, vol. 134, no. October 2018, pp. 26–35, 2019. [Online]. Available: https://doi.org/10.1016/j.triboint.2019.01.032

[26] L. Rasolofondraibe, B. Pottier, P. Marconnet, and X. Chiementin, "Capacitive sensor device for measuring loads on bearings," *IEEE Sensors Journal*, vol. 12, no. 6, pp. 2186–2191, 2012.

[27] G. W. Stachowiak and A. W. Batchelor, *Engineering Tribology*, 4th ed. Oxford: Elsevier, 2014.

[28] R. Larsson, "EHL Film Thickness Behavior," in *Encyclopedia of Tribology*, Q. J. Wang and Y.-W. Chung, Eds. Boston, MA: Springer US, 2013, pp. 817–827. [Online]. Available: https://doi.org/10.1007/978-0-387-92897-5_639

[29] A. Hamilton and F. Quail, "Detailed state of the art review for the different online/inline Oil analysis techniques in context of wind turbine gearboxes," *Journal of Tribology*, vol. 133, no. 4, pp. 1–18, 2011.

[30] X. Zhu, C. Zhong, and J. Zhe, "Lubricating oil conditioning sensors for online machine health monitoring – A review," *Tribology International*, vol. 109, no. January, pp. 473–484, 2017. [Online]. Available: http://dx.doi.org/10.1016/j.triboint.2017.01.015

[31] T. J. Harvey, R. J. Wood, and H. E. Powrie, "Electrostatic wear monitoring of rolling element bearings," *Wear*, vol. 263, no. 7-12 SPEC. ISS., pp. 1492–1501, 2007.

[32] P. D. McFadden and J. D. Smith, "Vibration monitoring of rolling element bearings by the high-frequency resonance technique - a review," *Tribology International*, vol. 17, no. 1, pp. 3–10, 1984.

[33] A. Rai and S. H. Upadhyay, "A review on signal processing techniques utilized in the fault diagnosis of rolling element bearings," *Tribology International*, vol. 96, pp. 289–306, 2016. [Online]. Available: http://dx.doi.org/10.1016/j.triboint.2015.12.037

[34] D. Yang, H. Li, Y. Hu, J. Zhao, H. Xiao, and Y. Lan, "Vibration condition monitoring system for wind turbine bearings based on noise suppression with multi-point data fusion," *Renewable Energy*, vol. 92, pp. 104–116, 2016. [Online]. Available: http://dx.doi.org/10.1016/j.renene.2016.01.099

[35] N. Tandon and A. Choudhury, "Review of vibration and acoustic measurement methods for the detection of defects in rolling element bearings," *Tribology International*, vol. 32, no. 8, pp. 469–480, 1999.

[36] J. R. Naumann, "Acoustic emission monitoring of wind turbine blades," PhD, The University of Sheffield, 2016. [Online]. Available: https://core.ac.uk/reader/42605700

[37] J. S. Chen and K. W. Chen, "Bearing load analysis and control of a motorized high speed spindle," *International Journal of Machine Tools and Manufacture*, vol. 45, no. 12-13, pp. 1487–1493, 2005.

[38] Y. Guo and J. Keller, "Investigation of high-speed shaft bearing loads in wind turbine gearboxes through dynamometer testing," *Wind Energy*, vol. 21, no. 2, pp. 139–150, feb 2018. [Online]. Available: https://onlinelibrary.wiley.com/doi/10.1002/we.2150

[39] T. Howard, "Development of a Novel Bearing Concept for Improved Wind Turbine Gearbox Reliability," PhD thesis, University of Sheffield, 2016.

[40] G. Nicholas, T. Howard, H. Long, J. Wheals, and R. Dwyer-Joyce, "Measurement of roller load, load variation, and lubrication in a wind turbine gearbox high speed shaft bearing in the field," *Tribology International*, no. March, 2020. [Online]. Available: https://doi.org/10.1016/j.triboint.2020.106322

[41] G. Nicholas, "Development of Novel Ultrasonic Monitoring Techniques for Improving the Reliability of Wind Turbine Gearboxes," PhD thesis, University of Sheffield, 2021.

[42] H. Brunskill, P. Harper, and R. Lewis, "The real-time measurement of wear using ultrasonic reflectometry," *Wear*, vol. 332-333, pp. 1129–1133, 2015. [Online]. Available: http://linkinghub.elsevier.com/retrieve/pii/S0043164815001581

[43] J. Zhang, B. W. Drinkwater, and R. S. Dwyer-Joyce, "Monitoring of Lubricant Film Failure in a Ball Bearing Using Ultrasound," *Journal of Tribology*, vol. 128, no. 3, p. 612, 2006. [Online]. Available: http://dx.doi.org/10.1115/1.2197848%5Cnhttp://tribology.asmedigitalcollection.asme.org/a http://tribology.asmedigitalcollection.asme.org/article.aspx?articleid=1467585

[44] G. Nicholas, B. P. Clarke, and R. S. Dwyer-Joyce, "Detection of Lubrication State in a Field Operational Wind Turbine Gearbox Bearing Using Ultrasonic Reflectometry," *Lubricants*, vol. 9, no. 1, p. 6, jan 2021. [Online]. Available: https://www.mdpi.com/2075-4442/9/1/6

[45] T. Brenchley, "Viscosity Measurements Using a Multiple Frequency Matching Layer Viscometer," PhD thesis, The University of Sheffield, 2021. [Online]. Available: https://etheses.whiterose.ac.uk/29501/1/Thesis_Brenchley_CleanVersion.pdf

[46] R. Glovnea, M. Furtuna, Y. Nagata, and J. Sugimura, "Electrical Methods for the Evaluation of Lubrication in Elastohydrodynamic Contacts," *Tribology Online*, vol. 7, no. 1, pp. 46–53, 2012.

[47] F. Bogard, S. Murer, L. Rasolofondraibe, and B. Pottier, "Numerical determination of the mechanical stiffness of a force measurement device based on capacitive probes: Application to roller bearings," *Journal of Computational Design and Engineering*, vol. 4, no. 1, pp. 29–36, 2017. [Online]. Available: http://dx.doi.org/10.1016/j.jcde.2016.08.003

[48] W. Wang, J. V. I. Timonen, A. Carlson, D. M. Drotlef, C. T. Zhang, S. Kolle, A. Grinthal, T. S. Wong, B. Hatton, S. H. Kang, S. Kennedy, J. Chi, R. T. Blough, M. Sitti, L. Mahadevan, and J. Aizenberg, "Multifunctional ferrofluid-infused surfaces with reconfigurable multiscale topography," *Nature*, vol. 559, no. 7712, pp. 77–82, 2018.

[49] J. Keller, Y. Guo, and B. Mcniff, "Gearbox Reliability Collaborative High Speed Shaft Tapered Roller Bearing Calibration," National Renewable Energy Laboratory, Tech. Rep. NREL/TP-5000-60319, 2013. [Online]. Available: https://www.nrel.gov/docs/fy14osti/60319.pdf

[50] Y. Guo and J. Keller, "Investigation of high-speed shaft bearing loads in wind turbine gearboxes through dynamometer testing," *Wind Energy*, vol. 21, no. 2, pp. 139–150, 2018.

[51] H. Hertz, "On the contact of elastic solids," *Journal für die Reine und Angewandte Mathematik*, vol. 92, pp. 156–171, 1881.

[52] J. H. Tripp, "Hertzian Contact in Two and Three Dimensions," NASA Technical Paper, Tech. Rep. 2473, 1985.

[53] A. Palmgren, *Ball and roller bearing engineering*, 3rd ed. Philadelphia: SKF Industries, 1959.

[54] L. Houpert, "An Engineering Approach to Hertzian Contact Elasticity—Part I," *Journal of Tribology*, vol. 123, no. 3, p. 582, 2001. [Online]. Available: http://tribology.asmedigitalcollection.asme.org/article.aspx?articleid=1466490

[55] B. J. Hamrock and D. Dowson, "Minimum Film Thickness in Elliptical Contacts for Different Regimes of Fluid-Film Lu-

brication," NASA, Tech. Rep. 1342, 1978. [Online]. Available: https://ntrs.nasa.gov/archive/nasa/casi.ntrs.nasa.gov/19780025504.pdf

[56] T. E. Tallian, Y. P. Chiu, D. F. Huttenlocher, J. A. Kamenshine, L. B. Sibley, and N. E. Sindlinger, "Lubricant films in rolling contact of rough surfaces," *Wear*, vol. 8, no. 2, p. 147, 1965. [Online]. Available: https://linkinghub.elsevier.com/retrieve/pii/0043164865902814

[57] T. A. Harris and M. N. Kotzalas, *Rolling bearing analysis: Advanced concepts of bearing technology*, 5th ed. CRC press, 2007.

[58] M. H. Evans, "An updated review: white etching cracks (WECs) and axial cracks in wind turbine gearbox bearings," *Materials Science and Technology*, vol. 32, no. 11, pp. 1133–1169, 2016.

[59] M. N. Kotzalas and G. L. Doll, "Tribological advancements for reliable wind turbine performance," *Philosophical Transactions of the Royal Society A: Mathematical, Physical and Engineering Sciences*, vol. 368, no. 1929, pp. 4829–4850, 2010. [Online]. Available: http://rsta.royalsocietypublishing.org/cgi/doi/10.1098/rsta.2010.0194

[60] J. Krautkrämer and H. Krautkrämer, *Ultrasonic Testing of Materials*, 4th ed. Springer-Verlag Berlin Heidelberg, 1990. [Online]. Available: http://link.springer.com/10.1007/978-3-662-10680-8

[61] NDT Resource Center, "Wave Propagation." [Online]. Available: https://www.nde-ed.org/EducationResources/CommunityCollege/Ultrasonics/Physics/wavepropagation.htm

[62] R. S. Dwyer-Joyce, T. Reddyhoff, and B. Drinkwater, "Operating limits for acoustic measurement of rolling bearing oil film thickness," *Tribology Transactions*, vol. 47, no. 3, pp. 366–375, 2004.

[63] R. S. Dwyer-Joyce, P. Harper, and B. W. Drinkwater, "A method for the measurement of hydrodynamic oil films using ultrasonic reflection," *Tribology Letters*, vol. 17, no. 2, pp. 337–348, 2004.

[64] NDT Resource Center, "Modes of Sound Wave Propagation." [Online]. Available: https://www.nde-ed.org/EducationResources/CommunityCollege/Ultrasonics/Physics/modepropagation.htm

[65] L. E. Kinsler, A. R. Frey, A. B. Coppens, and J. V. Sanders, *Fundamentals of Acoustics*, 4th ed. New York: John Wiley and Sons, 2000.

[66] D. M. Egle and D. E. Bray, "Measurement of acoustoelastic and third-order elastic constants for rail steel," *The Journal of the Acoustical Society of America*, vol. 60, no. 3, pp. 741–744, 1976. [Online]. Available: http://asa.scitation.org/doi/10.1121/1.381146

[67] NDT Resource Center, "Attenuation of Sound Waves." [Online]. Available: https://www.nde-ed.org/EducationResources/CommunityCollege/Ultrasonics/Physics/attenuation.htm

[68] H. G. Tattersall, "The ultrasonic pulse-echo technique as applied to adhesion testing," *Journal of Physics D : Applied Physics*, vol. 6, pp. 819–832, 1973.

[69] B. W. Drinkwater, R. S. Dwyer-Joyce, and P. Cawley, "A Study of the Interaction between Ultrasound and a Partially Contacting Solid–Solid Interface," *Proceedings of the Royal Society A: Mathematical, Physical and Engineering Sciences*, vol. 452, no. 1955, pp. 2613–2628, 1996. [Online]. Available: http://rspa.royalsocietypublishing.org/cgi/doi/10.1098/rspa.1996.0139

[70] R. S. Dwyer-Joyce, B. W. Drinkwater, and C. J. Donohoe, "The measurement of lubricant-film thickness using ultrasound," *Proceedings of the Royal Society A: Mathematical, Physical and Engineering Sciences*, vol. 459, pp. 957–976, 2003. [Online]. Available: http://rspa.royalsocietypublishing.org/cgi/doi/10.1098/rspa.2002.1018

[71] NDT Resource Center, "Refraction and Snell's Law." [Online]. Available: https://www.nde-ed.org/EducationResources/CommunityCollege/Ultrasonics/Physics/refractionsnells.htm

[72] W. Chen, R. Mills, and R. S. Dwyer-Joyce, "Direct load monitoring of rolling bearing contacts using ultrasonic time of flight," *Proceedings of the Royal Society A: Mathematical, Physical and Engineering Science*, vol. 471, 2015. [Online]. Available: http://rspa.royalsocietypublishing.org/lookup/doi/10.1098/rspa.2015.0103

[73] H. P. Brunskill, "The Real-Time Characterisation of Dry Machine Element Contacts Using Ultrasonic Reflectometry," PhD thesis, University of Sheffield, 2013.

[74] Science Direct, "Piezoelectric Effect." [Online]. Available: https://www.sciencedirect.com/topics/engineering/piezoelectric-effect

[75] ——, "Curie Temperature." [Online]. Available: https://www.sciencedirect.com/topics/chemistry/curie-temperature

[76] NDT Olympus, "Ultrasonic transducers technical notes," Olympus, NDT, Waltham, MA, Tech. Rep., 2006. [Online]. Available: http://www.olympus-ims.com/pt/knowledge/%5Cnhttp://scholar.google.com/scholar?hl=en&btnG=Search&q=i

[77] A. K. Hunter, "Ultrasonic Measurements of the Strip Thickness, Lubricant Film Thickness, Roll Deflection and Roll Stress in the Roll Bite in the Cold Rolling of Steel," PhD thesis, University of Sheffield, 2018.

[78] NDT Resource Center, "Couplant." [Online]. Available: https://www.nde-ed.org/EducationResources/CommunityCollege/Ultrasonics/EquipmentTrans/Couplant.htm

[79] P. Harper, "Measurement of Film Thickness in Lubricated Components using Ultrasonic Reflection," PhD thesis, University of Sheffield, 2008.

[80] FDominec, "Coaxial cable cut." [Online]. Available: https://commons.wikimedia.org/wiki/File:Coaxial_cable_cut.jpg license: https://creativecommons.org/licenses/by-sa/3.0/deed.en

[81] C. Holmes, B. W. Drinkwater, and P. D. Wilcox, "Post-processing of the full matrix of ultrasonic transmit-receive array data for non-destructive evaluation," *NDT and E International*, vol. 38, no. 8, pp. 701–711, 2005.

[82] W. Chen, R. Mills, and R. S. Dwyer-Joyce, "Direct load monitoring of rolling bearing contacts using ultrasonic time of flight," *Proceedings of the Royal Society A: Mathematical, Physical and Engineering Science*, vol. 471, 2015. [Online]. Available: http://rspa.royalsocietypublishing.org/lookup/doi/10.1098/rspa.2015.0103

[83] R. S. Dwyer-Joyce, B. W. Drinkwater, and C. J. Donohoe, "The measurement of lubricant-film thickness using ultrasound," *Proceedings of the Royal Society A: Mathematical, Physical and Engineering Sciences*, vol. 459, no. 2032, pp. 957–976, 2003.

[84] J. Zhang, B. W. Drinkwater, and R. S. Dwyer-Joyce, "Calibration of the ultrasonic lubricant-film thickness measurement technique," *Measurement Science and Technology*, vol. 16, no. 9, pp. 1784–1791, 2005.

[85] ——, "Acoustic measurement of lubricant-film thickness distribution in ball bearings," *The Journal of the Acoustical Society of America*, vol. 119, no. 2, p. 863, 2006.

[86] A. Takeuchi, "Observation of lubrication conditions using an ultrasonic technique," *Lubrication Science*, vol. 21, no. 10, pp. 397–413, 2009.

[87] B. W. Drinkwater, J. Zhang, K. J. Kirk, J. Elgoyhen, and R. S. Dwyer-Joyce, "Ultrasonic Measurement of Rolling Bearing Lubrication Using Piezoelectric Thin Films," *Journal of Tribology*, vol. 131, no. 1, p. 011502, 2009. [Online]. Available: http://tribology.asmedigitalcollection.asme.org/article.aspx?articleid=1468167

[88] M. K. Wan Ibrahim, D. Gasni, and R. S. Dwyer-Joyce, "Profiling a Ball Bearing Oil Film with Ultrasonic Reflection," *Tribology Transactions*, vol. 55, no. 4, pp. 409–421, 2012.

[89] K. Zhang, Q. Meng, and W. Zhao, "Measurement of oil film thickness in cylindrical roller bearings by ultrasound," *Proceedings of the ASME 2014 12th Biennial Conference on Engineering Systems Design and Analysis*, 2014.

[90] M. Li, M. Jing, Z. Chen, and H. Liu, "An improved ultrasonic method for lubricant-film thickness measurement in cylindrical roller bearings under light radial load," *Tribology International*, vol. 78, 2014.

[91] K. Zhang, Q. Meng, W. Chen, J. Li, and P. Harper, "Ultrasonic measurement of oil film thickness between the roller and the inner raceway in a roller bearing," *Industrial Lubrication and Tribology*, 2015.

[92] E. Avcioglu, "Measurement of Surface Deflection in Rolling Bearing by Ultrasonic Reflection," Ph.D. dissertation, PhD thesis, University of Sheffield, 2018.

[93] R. Mills, "Ultrasonic measurement of lubricant films generated at the piston-cylinder interface of internal combustion engines," PhD thesis, University of Sheffield, 2012.

[94] R. S. Dwyer-Joyce and B. W. Drinkwater, "In situ measurement of contact area and pressure distribution in machine elements," *Tribology Letters*, vol. 14, no. 1, pp. 41–52, 2003.

[95] S. Kasolang and R. S. Dwyer-Joyce, "Viscosity measurement in thin lubricant films using shear ultrasonic reflection," *Proceedings of the Institution of Mechanical Engineers, Part J: Journal of Engineering Tribology*, vol. 222, no. 3, pp. 423–429, 2008.

[96] M. Schirru, R. Mills, R. Dwyer-Joyce, O. Smith, and M. Sutton, "Viscosity Measurement in a Lubricant Film Using an Ultrasonically Resonating Matching Layer," *Tribology Letters*, vol. 60, no. 3, 2015.

[97] X. Li, "Measuring Friction at an Interface Using Nonlinear Ultrasonic Response," PhD thesis, University of Sheffield, 2018. [Online]. Available: https://etheses.whiterose.ac.uk/22514/

[98] R. Dwyer-Joyce, T. Reddyhoff, and J. Zhu, "Ultrasonic Measurement for Film Thickness and Solid Contact in Elastohydrodynamic Lubrication," *Journal of Tribology*, vol. 133, no. 3, p. 031501, 2011. [Online]. Available: http://tribology.asmedigitalcollection.asme.org/article.aspx?articleid=1468734 http://dx.doi.org/10.1115/1.4004105

[99] M. Gonzalez-Valadez, R. S. Dwyer-Joyce, and R. Lewis, "Ultrasonic reflection from mixed liquid-solid contacts and the determination of interface stiffness," *Tribology and Interface Engineering Series*, vol. 48, no. 05, pp. 313–320, 2005.

[100] D. Ferguson, "Installation of Wind Turbine Condition Monitoring Equipment at Barnesmore Wind Farm," University of Strathclyde, Tech. Rep., 2015.

[101] Ricardo, "SABR." [Online]. Available: https://software.ricardo.com/products/sabr

[102] J. Tamura, "Calculation Method of Losses and Efficiency of Wind Generators," in *Wind Energy Conversion Systems*. London: Springer, 2012, ch. 2, pp. 25–51. [Online]. Available: http://link.springer.com/10.1007/978-1-4471-2201-2_2

[103] V. Sohoni, S. C. Gupta, and R. K. Nema, "A Critical Review on Wind Turbine Power Curve Modelling Techniques and Their Applications in Wind Based Energy Systems," *Journal of Energy*, vol. 2016, no. region 4, pp. 1–18, 2016.

[104] C. Carrillo, A. Obando Montaño, J. Cidrás, and E. Díaz-Dorado, "Review of power curve modelling for wind turbines," *Renewable and Sustainable Energy Reviews*, vol. 21, pp. 572–581, may 2013. [Online]. Available: https://linkinghub.elsevier.com/retrieve/pii/S1364032113000439

[105] C. E. Rasmussen and C. K. I. Williams, *Gaussian Processes for Machine Learning*. MIT Press, 2006. [Online]. Available: http://www.gaussianprocess.org/gpml

[106] Castrol, "Castrol Hyspin VG Range Product Data," Castrol Limited, Tech. Rep., 2016.

[107] ——, "Castrol Alpha SP Range Product Data," Castrol Limited, Tech. Rep., 2016.

[108] B. Treeby, B. Cox, and J. Jaros, "k-wave Toolbox: Simulation of Acoustic Wave Fields," k-Wave, Tech. Rep., 2016.

[109] The University of Sheffield, "High Performance Computing at Sheffield." [Online]. Available: https://docs.hpc.shef.ac.uk/en/latest/

[110] T. E. Gómez Álvarez-Arenas, J. Camacho, and C. Fritsch, "Passive focusing techniques for piezoelectric air-coupled ultrasonic transducers," *Ultrasonics*, vol. 67, pp. 85–93, 2016.

[111] B. Drinkwater, *Ultrasonic Array Imaging for Non-Destructive Testing*. FESI Publishing, 2021.

[112] P. D. Wilcox and J. Zhang, "Quantification of the Effect of Array Element Pitch on Imaging Performance," *IEEE Transactions on Ultrasonics, Ferroelectrics, and Frequency Control*, vol. 65, no. 4, pp. 600–616, 2018.

[113] Peak to Peak Measurment Solutions, "Peak to Peak Measurment Solutions." [Online]. Available: https://pktopk.co.uk/